Targeting Notch Signalling in the EMT Dynamics of Triple-Negative Breast Cancer Cells

A Thesis

Submitted in Partial Fulfilment of the Requirements for the award of the degree of

DOCTOR OF PHILOSOPHY

By

Plaboni Sen

(Roll No. - 186106009)

Department of Biosciences and Bioengineering

Indian Institute of Technology Guwahati

Guwahati, 781039, Assam, India

May 2023

Dedicated to my Family

Declaration

I, hereby, declare that the research embodied in this thesis entitled "**Targeting Notch Signalling in the EMT Dynamics of Triple-Negative Breast Cancer Cells**" is the result of investigations carried out by me under the supervision of Prof. Siddhartha Sankar Ghosh, Department of Biosciences and Bioengineering, Indian Institute of Technology Guwahati, India for the award of Degree of Doctor of Philosophy. This work has not been submitted elsewhere for any degree, diploma, etc. of any Institute or University to the best of my knowledge and belief.

Date: 29.05.2023

Place: Guwahati

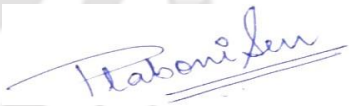

Plaboni Sen

Roll No. 186106009

Indian Institute of Technology Guwahati

Department of Biosciences and Bioengineering

Certificate

This is to certify that the thesis entitled **"Targeting Notch Signalling in the EMT Dynamics of Triple-Negative Breast Cancer Cells"** being submitted to the **Indian Institute of Technology Guwahati** by **Plaboni Sen** (Roll No. **186106009)** for the award of the degree of **Doctor of Philosophy** in Department of Biosciences and Bioengineering, is a bonafide record of research work carried out by her. The contents of thisthesis have not been submitted to any other University or Institute for theaward of any degree or diploma.

Date: 29.05.2023
Place: Guwahati

Prof. Siddhartha Sankar Ghosh
(Thesis Supervisor)

Acknowledgement

"We are so often caught up in our destination that we forget to appreciate the journey, especially the goodness of the people we meet on the way"

Hence, I would like to express my heartfelt gratitude to the people, who have been a part of my life. I consider myself blessed to have had a wonderful journey of PhD at the Indian Institute of Technology Guwahati. This was all made possible by the guidance, motivation and love of a lot of people who hold immense value in my life.

To begin with, I would initially like to thank my guide, Prof. Siddhartha Sankar Ghosh for providing me with this wonderful opportunity to work in his lab. I thank him for taking care of all the facilities to carry out my research work. It was his constant support and guidance that helped me to nurture the finest qualities of being an independent researcher. I whole heartedly thank him for being the inspiration I will always look forward to in my life.

I would also like to thank my doctoral committee members: Dr. Biplab Bose, Dr. Priyadarshi Satpati, and Prof. Gurvinder Kaur for evaluating my work and for giving critical suggestions from time to time. I acknowledge all the staff and faculty members of the Department of Biosciences and Bioengineering and the Centre for Nanotechnology. I am highly indebted to the Department of Biosciences and Bioengineering, Centre for Nanotechnology, Central Instrumentation Facility, and Param-Ishan, IIT Guwahati for providing the state-of-art facilities to conduct my research work.

I sincerely thank Prof. Roy P. Paily, Prof. Debasis Manna, Prof. Amaresh Dalal and Dr. Rajkumar P. Thummer for providing me with the opportunity to work in collaboration and explore the possibility of application of my work in multidisciplinary fields.

I would also like to thank all my teachers for their support and guidance in my academic life. I would also extend my acknowledgement to the staff and faculty members of Maulana Abul Kalam Azad University of Technology (MAKAUT), West Bengal and Jamshedpur Women's College, Jamshedpur, for teaching me the basics of science and research.

I sincerely appreciate the help, guidance and love of all my labmates, Dr. Neha Arora, Dr. Upashi Goswami, Dr. Anil Bidkar, Dr. Srirupa Bhattacharyya, Dr. Rajib Shome, Dr. Anitha T. Simon, Muktashree, Debashree, Konika, Hirak, Thiru, Shilpi, Arisha, Sayantani, Sawna,

Basab, Sayantani, Sujisha, Suchandra, Parijat, and Dheepika. I thank every one of them for being there for me always and for providing me with love, support and an amicable environment. I also thank all the members of the DBT program support facility.

"There are friends, there is family and then there are friends that become family." I am fortunate to find some great friends, hence, I would like to extend my deepest gratitude and love to Suraj, Konika, Yvonne, Bibrita and Narayani for their love, care and support.

No words are enough to thank the love, affection, care and encouragement that I have received from my family, especially my parents and my brother. They have always been the pillars of my life and I owe them everything that I am today. Moreover, I will always be indebted to the Almighty God for being the guiding light at all times.

It was indeed an experience of a lifetime, besides having a lovely and pleasant stay at this splendid campus of IIT Guwahati.

"I have no a clue how my story will end, but that's all right. When you set out on a journey and night covers the road, that's when you discover the stars"

- Plaboni Sen

Table Of Contents

Abstract

In contrast to the other subtypes, the basal-like also known as Triple-Negative Breast Cancer (TNBC) is a heterogenous collection of breast cancers, which constitutes about 20% of all cancer. TNBC is biologically aggressive, and metastatic and is associated with a worse prognosis. Therefore, the treatment of TNBC is complex and involves a combination of different modalities including surgery, radiotherapy, hormonal therapy, chemotherapy, or biological therapies delivered in diverse sequences. People with advanced metastatic cancers often undergo combination therapy, a treatment module combining two or more therapeutic agents. The rationale is to encourage the usage of drugs at a significantly lower dosage to minimize their dose-dependent adverse effects. Moreover, the amalgamation of two or more drugs enhances the efficacy of the treatment in comparison to mono-therapy, since it targets the pivotal signalling pathways in a synergistic or additive manner. Among the various evolutionary conserved developmental pathways, the Notch is one of the pivotal pathways that are generally responsible for the development and differentiation of embryonic and adult tissues. Since, the Notch is associated with cell fate determination, aberrant signalling results in triggering the aggressiveness of numerous malignancies.

Therefore, it is hypothesized in the current thesis that: (i) targeting the proteases of the Notch pathway would efficiently and effectively abrogate the harmful effects of Notch, and (ii) combining the already existing therapies with the inhibition of the Notch signalling pathway would suffice the gap and enhance the efficacy of the treatment in profound ways.

This work mainly focuses on exploring the effects of the Notch signalling pathway in the metastatic domain of TNBC. **Section 1** comprises the **Introduction and Review of the Literature,** which endows us with information about the complexity of the Notch signalling pathway and its role in cancer progression and dissemination. In this section, the detailed molecular aspect of the Notch signalling pathway is depicted. Additionally, the implications of the Notch in cancer, and its cross talks with some of the major oncogenic signals have been described. Moreover, the association of the Notch with EMT, and the numerous aggressiveness (such as drug resistance, maintenance of stemness, angiogenesis, circulating tumour cells (CTCs), etc.) thus inflicted, are elucidated in this section. Furthermore, the objectives of the thesis have been fabricated to study the dynamics of the Notch signalling pathway in metastatic TNBC. Finally, the salient features of this thesis have been delineated. **Section 2** describes the detailed procedures for the methodologies (both *in vitro* and *in silico*) that have been employed throughout the study. It also contains the details of the materials utilized in this study. **Section 3** describes the **Results and Discussions**. In this section, a summary depicting the identification of the major signalling nodes to targeting, along with the therapeutic outcome on TNBC cell lines has been portrayed.

The Notch pathway is a major regulator of the aggressive characteristics of metastatic triple-negative breast cancer. Hence, a lack of effective therapies often contributes to poor clinical outcomes associated with aberrant Notch signalling, which further facilitates drug resistance, angiogenesis and metastasis.

The initial study focuses on the identification of the pivotal molecules that can be therapeutically targeted to tweak the aberrant Notch pathway in metastatic TNBC (in other words, EMT-induced TNBC). Initially, literature mining portrayed the major role of ADAM17 in cancer and inflammatory diseases. However, it is quite challenging to design a candidate drug for targeting ADAM17 due to its structural similarity with the catalytic domain of the matrix metalloproteases (MMPs). Hence, the present study reports the protein-protein interaction analysis of ADAM17, which confirms the association of ADAM17 with numerous oncogenes that facilitate cancer progression and inflammation, especially the members of the Notch, receptor tyrosine kinase (RTK) and TNFα pathways. The outcome provides evidence that the prevalent protease ADAM17 could attribute to cancer signalling regulation through the shedding of various inflammatory and oncogenic molecules. Therefore, owing to the effects of ADAM17 in promoting the major oncogenic pathways, we exploited the analogs of the existing inhibitors, with an aim of discovering a potent molecule, which could be used as an inhibitor against ADAM17-inflicted cancer progression. Upon stringent screening, we delineated our choice into two specific compounds (I6 and I9; analogs of IK862, a type of γ-lactam hydroxamates), possessing the lowest binding energy (–9.1 Kcal/mol), stable MD-simulation studies and superior pharmacodynamic properties. The current information illustrates the avenue to persuade further research on targeting ADAM17 with small molecular compounds (I6 and I9) in cancer therapeutics.

Additionally, a Polypharmacology approach was employed to target the pivotal proteases of the Notch signalling pathway. Herein, we identified TACE/ADAM protease and the γ-secretase complex to be the major regulatory proteases that are required for the activation of the Notch pathway. Initially, a library of FDA-approved drugs (obtained from the Guide to Pharmacology server) was screened against these proteases. In this study, Lomitapide was chosen based on its binding score (-305.108 kJ/mol and -173.174 kJ/mol) against TACE and γ-secretase, respectively. Further, the remarkable antitumor properties of Lomitapide were established on the TNBC cell lines (MDA-MB-231 and MDA-MB-468), along with the EMT-induced MDA-MB-468 cells. Apart from inducing ~2-fold to 2.5-fold increase in the cellular ROS levels, Lomitapide induced apoptosis, arrested cell cycle progression and reduced sphere and colony forming abilities of the TNBC cells. Differentiated epithelial phenotype with diminished CD44-stem cell marker was also observed upon treatment. Furthermore, reduction of migration potential, decrease in the gene expression profile of the EMT markers, along with downregulation of the Notch signalling genes were evident in the treated TNBC cells. Altogether, the present study attributes the repurposing of Lomitapide as an effective therapeutic agent against the major proteases of the Notch pathway to combat TNBC progression and dissemination.

In the subsequent endeavour, the role of Notch inhibition was examined to facilitate the efficacy of SAHA (Suberoylanilide hydroxamic acid; also known as 'Vorinostat'), an HDAC inhibitor (HDACI). It is evident from the literature that HDACIs, possess great therapeutic value for numerous malignancies. However, their inherent capability to induce EMT in some cases has been of greater concern. Therefore, in the present study, it was hypothesized that SAHA facilitates EMT via the activation of the Notch pathway. Further, PPI analysis depicts that HDAC1/2 mediates the formation of the repressor complex upon interacting with the DNA binding domain, CSL. This in turn results in the inhibition of the transcriptional activation of the Notch downstream genes. Hence, the use of HDACIs (such as SAHA) facilitates the transcriptional activation of the Notch target genes, by disrupting the corepressor complex and recruiting the coactivator complex, thereby facilitating EMT. In this study it is evident that SAHA upregulates the protein expression profile of the Notch ligands (such as JAG1, and JAG2), thereby aberrantly activating the Notch pathway. Therefore, the focus was on combination therapy using a γ-secretase inhibitor, LY411575 that would enhance the efficacy of SAHA by blocking the canonical Notch pathway mediated via NICD. It was observed that co-treatment synergistically mediates apoptosis, generates ROS, depolarizes mitochondria, and diminishes the stemness properties. Besides, it also mediates autophagy-independent cell death, and decreases the expression of inflammatory cytokines, along with the downregulation in the expression of the Notch downstream genes, EMT markers and EMT-TFs. Altogether, our study provides a mechanistic basis for combating EMT potentiated by SAHA, which could be utilized as a rational strategy for the treatment of solid tumours, especially TNBC.

Finally, the associations of the Notch pathway with the major oncogenic pathways that are responsible for inducing EMT, angiogenesis, drug resistance and survival were delineated. In this study, Axitinib was used in combination with LY411575 to establish the combined effect of two drugs on TNBC cells. It is interesting to note that besides the acquisition of mesenchymal properties, EMT also imparts pericyte-like properties to the TNBC cells. This in turn gives rise to a phenomenon known as epithelial to pericyte transition. In this study, Axitinib was selected to establish the connections between the oncogenic RTKs such as VEGFs, EGFR and Notch in TNBC progression and dissemination. Moreover, Axitinib was used in combination with LY411575 (a potent Notch pathway inhibitor) and it was observed that the co-treatment synergistically induced apoptosis (by 35.73% in MB-231 and 27.7% in MB-468), arrests cells at the G2/M phase, decreases the stemness properties of the TNBC cells. Also, it diminishes the capability of cells to form spheroids, enhances the expression of epithelial markers, such as E-cadherin (by 2.2-fold in MDA-MB-231 and 2.51-fold in MDA-MB-468) and downregulated the expression of mesenchymal genes and proteins. Additionally, the protein expression profile of the pro-oncogenic and pro-survival genes also reduced significantly after the administration of co-therapy, which was highlighted by a reduction in the levels of pEGFR, pFAK, pMAPK, NF-κB, etc. Moreover, the expression of pericyte markers (such as PDGFRs, α-SMA, c-kit and NG2) was also found to be downregulated following combination therapy. Especially, the protein expression levels of NG2 (a potent pericyte marker) were

found to be diminished significantly by 1.69-fold in MDA-MB-231 and 2.1-fold in MDA-MB-468 cells, thereby hinting towards the inhibition of epithelial-to-pericyte transition (EPT). The current work endows us with the effectiveness of the co-therapy on the EMT and EPT dynamics of TNBC upon inhibition of the major cross-talk between the VEGF and Notch pathway.

Section 4 comprises the **Conclusion and Future prospects,** which summarize the key findings of the current thesis. Conclusively, the insights gained in the present study reveal the associations of the Notch signalling pathway with the aggressiveness of metastatic TNBC. Altogether, the results obtained from the present study emphasize a potential therapeutic target along with the idea of implementing a combined therapeutic module in the treatment of TNBC.

Abbreviations

AD	Alzheimer's Disease
ADAM	A Disintegrin and Metalloprotease
ADC	Antibody Drug Conjugate
AIP4	Aryl Hydrocarbon Receptor-Interacting Protein 4
AKT	Ak strain transforming
ALDH	Aldehyde Dehydrogenase
AML	Acute Myeloid Leukemia
ANK	Ankyrin
APH	Anterior Pharynx-Defective
APP	Amyloid Protein Precursor
ASI	Alpha-Secretase Inhibitors
Aβ	Amyloid-B
BC	Breast Cancer
bs-Ab	Bispecific Antibody
CAR	Chimeric Antigen Receptor
CART	Chimeric Antigen Receptor Therapy
CBF1	C Promoter-Binding Factor
CCN3	Cellular Communication Network Factor 3
CDC10	Cell Division Cycle
CDK8	Cyclin Dependant Kinase 8
CIAP	Cellular Inhibitor Of Apoptosis Proteins
CIR	Corepressor Interacting With RBPJ 1
CLL	Chronic Lymphocytic Leukemia
CR	Cysteine-Rich
CSCs	Cancer stem cells
CSL	CBF1, Suppressor of Hairless, Lag-1
CtBP	Carboxy-terminal-binding protein 1
DCFDA	dichlorodihydrofluorescein diacetate
Dlg-1	Drosophila disc large tumour suppressor
Dlk	human Delta-like
DLL	Delta Like Canonical Notch Ligand 1
DNER	Delta/Notch-like EGF-related receptor
DOS	Delta and OSM-11 motif
DSL	Delta, Serrate and LAG-2

E(spl)	Enhancer of Split1
EDTA	Ethylenediaminetetraacetic Acid
EGFR	Epidermal Growth Factor Receptors
EGTA	ethylene glycol-bis(β-aminoethyl ether)-N,N,N′,N′-tetraacetic acid
EMT	Epithelial To Mesenchymal Transition
EMT-TF	Epithelial To Mesenchymal Transition
EPT	Epithelial To Pericyte Transition
EPS15	Epidermal Growth Factor Receptor Pathway Substrate 15
FGF	Fibroblast Growth Factor
FITC	Fluorescein isothiocyanate
GAPDH	Glyceraldehyde 3-phosphate dehydrogenase
GEPIA	Gene Expression Profiling Interactive Analysis
GCN5	General Control Non-Derepressible 5
GlcNAc	O-linked N-acetylglucosaminyltransferase
Glp-1	Glucagon-like peptide 1
GSI	Gamma-Secretase Inhibitor
GSK-3β	Glycogen synthase kinase 3 beta
GSM	Gamma-Secretase Modulator
GTEx	Genotype-Tissue Expression
h	Hour
HAT	Histone Acetyltransferase
HCC	Hepatocellular Carcinoma
HD	Heterodimerization Domain
HDAC1	Histone Deacetylase I
HER2	Human Epidermal Growth Factor Receptor 2
HES	Hairy and Enhancer of Split1
HEY2	Hairy/enhancer-of-split related with YRPW motif protein 2
HGF	Hepatocyte Growth Factor
HIF-1	Hypoxia Inducible Factor -1
i-CliPs	intramembrane Cleaving Protease
IC	Inhibitory Concentration
IGF	Insulin-Like Growth Factor 1
IKK	inhibitor of nuclear factor-κB (IκB) kinase
Itch	Itchy E3 Ubiquitin Protein Ligase
JC-1	Tetraethyl-benzimidazolylcarbocyanine Iodide
KBF2	Kappa-Binding Factor 2
kDa	kilo Dalton

LAG-1	Longevity-Assurance Gene-1
LC3	Microtubule-associated protein 1A/1B-light chain 3
LDM	Lidamycin
LEF	Lymphoid Enhancer Factor
LNR	LIN12/Notch Related Region
mAbs	monoclonal antibodies
MAGP	Microfibril-Associated Glycoproteins
MAML	Mastermind-like
MAPK	Mitogen-Activated Protein Kinase
mRNA	Messenger Ribonucleic acid
mTOR	Mammalian target of rapamycin
MTT	(3-(4,5-Dimethylthiazol-2-yl)-2,5-diphenyltetrazolium bromide)
NAS	Notch1 Antisense Oligonucleotide
NCCS	National Centre for Cell Scienc
NCT	Nicastrin
NF-κB	Nuclear factor kappa-light-chain-enhancer of activated B
NICD	Notch Intracellular Domain
NECD	Notch Extracellular Domain
NEXT	Notch Extracellular Truncation
NF-κB	Nuclear factor kappa B
NLS	Nuclear Localisation Signalling
NRR	Negative Regulatory Region
NSCLC	Non-Small Cell Lung Cancer
NSIAD	Non-Steroidal Anti-Inflammatory Drug
O-fut	O-fucosyltransferase1
OSM	Oncostatin M
PBS	Phosphate Buffer Saline
PBST	Phosphate Buffer Saline with 0.1% Tween
PCR	Polymerase Chain Reaction
PCAF	p300/CPB Associated Factor
PDZ	PSD-95/Dlg/ZO-1
PDGF	Platelet derived growth factor
PDGFR	Platelet derived growth factor receptor
PE	Phycoerythrin
PEN	Presenilin Enhancer
PEST	proline (P), glutamic acid (C), serine (S) and threonine (T)
P-GP	P-glycoprotein

PI	Propidium Iodide
PI3K	Phosphoinositide 3-Kinase
Poglut1	Protein O-glucosyltransferase 1
PSD95	Post Synaptic Density protein (PSD95) binding motif
PSEN	Presenilin
PVDF	Polyvinylidene Difluoride
qRT-PCR	Quantitative reverse transcription Polymerase Chain Reaction
RAM	RBPJ Associated Molecule
RBPJ	Recombination signal Binding Protein for Immunoglobulin kappa J region
RES	Resveratrol
RIPA	Radioimmunoprecipitation Assay Buffer
RITA	RBPJ interacting and tubulin associated
RNAi	Ribonucleic Acid interference
ROS	Reactive Oxygen Species
SAHA	Suberoylanilide hydroxamic acid
SDS PAGE	Sodium Dodecyl Sulphate Polyacrylamide Gel Electrophoresis
SKIP	Skeletal muscle and kidney-enriched inositol phosphatase
SHARP	SMRT/HDAC-associated repressor protein
shRNA	short-hairpin RNA
SKP2	S-Phase Kinase Associated Protein 2
SMRT	Silencing Mediator of Retinoid and Thyroid hormone receptors
SUH	Suppressor of Hairless
TACE	TNF-α converting enzyme
TAD	Transcription Activation Domain
T-ALL	T-cell acute lymphoblastic leukemia
TCGA	The Cancer Genome Atlas
TEMED	Tetramethylethylenediamine
TGF-β	Transforming growth factor beta
TMD	Trans Membrane Domain
TMP	Tumor-associated Membrane Protein
TNBC	Triple Negative Breast Cancer
TNFα	Tumour Necrosis Factor-alpha
Tris	Trizma Base
VEGF	Vascular Endothelial Growth Factor
VEGFR	Vascular Endothelial Growth Factor Receptor
vWFC	von-Willebrand factor type-C
ZO-1	Zonula Occludens-1

List of Schemes

Schematic 1.5 The NICD (Notch intracellular domain) regulates the expression of various downstream genes that induces proliferation, aid in EMT (epithelial to mesenchymal transition) and inhibits apoptosis, thereby promoting tumorigenesis.

Schematic 1.6 The mutational profile among the gene sequence of the Notch receptors.

Schematic 1.7 The Notch pathway crosstalk facilitating EMT: The Notch pathway is intertwined with numerous oncogenic pathways (such as Hypoxia, TGFβ, Rho-RACK, MAPK, FAK, AKT/mTOR, Wnt) that facilitate the transcription of several transcription factors (such as ZEB, Snail, Slug, Twist) which in turn potentiates the epithelial to mesenchymal transition. *(Concept source: KEGG pathway database)*

Schematic 1.8 Schematic representation of the epithelial to mesenchymal transition. (A) The tumour architecture; (B) upon external stimuli from the tumour niche, there is an alteration in the gene expression that results in the phenotypic change of the epithelial tumour cell; (C) following EMT, the epithelial cells acquire migratory mesenchymal characteristics; upon the secretion of matrix metalloproteases (MMPs) by the mesenchymal cells the basement membrane gets degraded (1), the mesenchymal cells then traverse the stromal cellular layers (2); the tumour cells possess PDGFR (platelet derived growth factor receptors), therefore, are chemo-attracted by the endothelial cells of the blood vessels secreting PDGF (3); following chemotaxis, the tumour cells intravasate into the blood vessels (4); (5) they travel to a distant site in the body either alone or in clusters, after being surrounded by the platelets which help them escape immune recognition, (6) the extravasation of the tumour cells through the blood vessels engenders secondary tumours (7), whereby, following the process of mesenchymal to epithelial transition (MET), the migratory cells acquire epithelial characteristics and give rise to an entirely new cluster of tumours (8). *(Concept source: https://doi.org/10.1039/D0MA00455C)*

Schematic 1.9 The formation of the Circulating tumour cells (CTCs). (A) the Jagged mediated Notch pathway activation gives rise to the phenomenon of lateral induction. As a result of which the surrounding cells acquire the same cellular fate, thereby giving rise to a cluster of circulating tumour cells. (B) the Delta mediated Notch pathway activation gives rise to the phenomenon of lateral inhibition. As a result,

List of Figures

Figure 3.2.3 STRINGS network depicting the network of ADAM and γ-secretase enzyme. Briefly, ADAM and the components of γ-secretase (NCSTN, APH-1A, APH1B, PSENEN, PSEN1 and PSEN2) for Homo Sapiens was fed as the query molecule. The interacting network was restricted to the first shell, with a confidence score of 0.7 that is indicated to be of significant reliability.

Figure 3.2.4 Root means square deviation of protein backbone upon binding of drugs over 100 ns simulation for **(A)** TACE and **(E)** γ-secretase. Root means square fluctuation of each residue of target proteins upon drug binding over 100 ns in **(B)** TACE and **(F)** γ-secretase. Number of H-bonds formed between the target protein and drug over 10 ns simulation for **(C)** TACE and **(G)** γ-secretase. Pair distance between the target protein and drugs for 100 ns for **(D)** TACE and **(H)** γ-secretase. Binding conformation of FDA-approved drugs in the binding pocket of the target proteins with 20 ns time interval for **(I)** TACE and **(J)** γ-secretase. Each colour represents the different time period of the simulation. Red- 0th ns, green-20th ns, blue- 40th ns, magenta- 60th ns, cyan- 80th ns, orange- 100th ns.

Figure 3.2.5 Determination of cell viability by MTT assay following treatment with **(A)** Lomitapide, **(B)** LY411575, **(C)** TMI-1 for a time period of 48 h in MDA-MB-231. Determination of cell viability by MTT assay following treatment with **(D)** Lomitapide, **(E)** LY411575, **(F)** TMI-1 for a time period of 48 h in MDA-MB-468. The results are expressed as the mean ± SEM for three independent experiments. The statistical significance was assessed in comparison to the untreated cells. The significance level was set at $p < 0.5$ (*), $p < 0.1$ (**), $p < 0.01$ (***) and $p < 0.001$ (****).

Figure 3.2.6 Graphical representation of the cellular ROS detection using DCFDA based flow cytometry in **(A)** MDA-MB-231, **(B)** MDA-MB-468. **(C)** Fold-change generation of ROS in TNBC cells. Flow cytometric analysis of apoptotic population by annexin-V_FITC PI assay, following 48 h of treatment in **(D)** MDA-MB-231, **(E)** MDA-MB-468. The results are expressed as the mean ± SEM on the basis of three independent experiments. The statistical significance was obtained in comparison to the untreated control cells. The significance level was set at $p < 0.05$ (*), $p < 0.01$ (**), $p < 0.001$ (***) and $p < 0.0001$ (****).

Figure 3.2.7 Assessment of the spheroid formation ability following treatment with the respective inhibitors in **(A)** MDA-MB-231 and **(B)** MDA-MB-468 cells.

Graphical representation of changes in the diameter of the spheroids, following treatment with the respective inhibitors in comparison to the untreated samples in **(C)** MDA- MB-231 and **(D)** MDA-MB-468 cells. The results are expressed as the mean ± SEM on the basis of three independent experiments. The statistical significance was obtained in comparison to the untreated control cells. The significance level was set at $p < 0.05$ (*), $p < 0.01$ (**), $p < 0.001$ (***) and $p < 0.0001$ (****).

Figure 3.2.8 Scratch wound-healing assays of **(A)** MDA-MB-231 and **(B)** MDA-MB-468 cells. Graphical representation of changes in the wound healing capacity following treatment with the respective inhibitors in comparison to the untreated samples in **(C)** MDA-MB-231 and **(D)** MDA-MB-468 cells. The results are expressed as the mean ± SEM on the basis of three independent experiments. The statistical significance was obtained in comparison to the untreated control cells. The significance level was set at $p < 0.05$ (*), $p < 0.01$ (**), $p < 0.001$ (***) and $p < 0.0001$ (****).

Figure 3.2.9 The pseudo-plot representation of the CD44/CD24 population in **(A)** MDA-MB-231 and **(B)** MDA-MB-468 cells.

Figure 3.2.10 Evaluation of cell cycle profile of **(A)** MDA-MB-231 and **(B)** MDA-MB-468 cells.

Figure 3.2.11 Mitochondrial membrane potential detection of **(A)** MDA-MB-231 and **(B)** MDA-MB-468 cells, using JC-1 staining.

Figure 3.2.12 Representative western blot showing HES-1, NICD, Beclin-1 and p21 levels in **(A)** MDA-MB-231 and **(F)** MDA-MB-468 cells. β-actin serves as the loading control. The graphs are a representation of the changes in the expression level of the proteins **(B)** HES-1, **(C)** NICD, **(D)** Beclin-1 and **(E)** p21 in MDA-MB-231 cells, and **(G)** HES-1, **(H)** NICD, **(I)** Beclin-1 and **(J)** p21 in MDA-MB-468 cells with respect to the untreated samples. The changes in the level of protein expression were deduced using the ImageJ software. The results are expressed as the mean ± SEM on the basis of three independent experiments. The statistical significance was obtained in comparison to the untreated control cells. The significance level was set at $p < 0.05$ (*), $p < 0.01$ (**), $p < 0.001$ (***) and $p < 0.0001$ (****).

Figure 3.2.13 Immunocytochemistry of LC3 (left) MDA-MB-231 cells and (right) MDA-MB-468 cells. The formation of the LC3B puncta (red) in cells was observed

significance level was set at $p < 0.05$ (*), $p < 0.01$ (**), $p < 0.001$ (***) and $p < 0.0001$ (****).

Figure 3.2.21 Graphical representation of the changes in the expression level of the EMT markers: E- cadherin, Fibronectin and Vimentin, following treatment for a time period of 24 h **(A)** and 48 h **(B)**; Graphical representation of the changes in the expression level of the EMT transcription factors: Snai1 and Twist1, following treatment for a time period of 24 h **(C)** and 48 h **(D). (E)** Graphical representation of the changes in the expression level of the EMT marker: N-cadherin, following treatment for a period of 24 h and 48 h. The results are expressed as the mean ± SEM on the basis of three independent experiments. The statistical significance was obtained in comparison to the untreated control cells. The significance level was set at $p < 0.05$ (*), $p < 0.01$ (**), $p < 0.001$ (***) and $p < 0.0001$ (****).

Figure 3.2.22 **(A)** Representative western blot showing HES-1, NICD and Beclin-1 in EMT-induced MDA- MB-468 cells. β-actin serves as the loading control. Graphical representation of the changes in the expression level of the proteins **(B)** HES-1, **(C)** NICD and **(D)** Beclin-1 in EMT-induced MDA-MB-468 cells. The results are expressed as the mean ± SEM on the basis of three independent experiments. The statistical significance was obtained in comparison to the untreated control cells. The significance level was set at $p < 0.05$ (*), $p < 0.01$ (**), $p < 0.001$ (***) and $p < 0.0001$ (****).

Figure 3.2.23 Graphical depiction in the fold change alteration in the expression profile (following ICC) of autophagy marker, LC3 in **(A)** MDA-MB-231, **(B)** MDA-MB-468 and **(C)** EMT induced MDA-MB-468. Based on three independent experiments, the results are represented as mean ± SEM, along with a statistical significance denoting $p < 0.5$ (*), $p < 0.1$ (**), $p < 0.01$ (***) and $p < 0.001$ (****).

Figure 3.2.24 Immunocytochemistry of LC3 in EMT-induced MDA-MB-468 cells (left). The formation of the LC3B puncta (red) in cells was observed under confocal microscopy. The nuclei are counterstained with DAPI (blue). The scale bar represents 20 µM.

Figure 3.2.25 Nile Red staining of EMT-induced MDA-MB-468. The scale bar represents 20 µm.

Figure 3.3.1 STRINGs image of the interacting proteins with the query protein RBPJ (CSL). Briefly, RBPJ for Homo Sapiens was fed as the query molecule. The interacting network was restricted to the first shell, with a confidence score of 0.7 that is indicated to be of significant reliability.

Figure 3.3.2 Graph depicting the **(A)** biological processes; **(B)** KEGG pathway enrichment graph illustrating the association of these genes in a particular signalling pathway; **(C)** drug used against them obtained from the Drug Bank, using Web Gestalt database.

Figure 3.3.3 HDAC activity assay in **(A)** MDA-MB-231 and **(B)** MDA-MB-468 cells. The results are expressed as the mean ± SEM based on three independent experiments. The statistical significance was assessed in comparison to the untreated cells. The significance level was set at $p < 0.05$ (*), $p < 0.01$ (**), $p < 0.001$ (***) and $p < 0.0001$ (****).

Figure 3.3.4 Determination of viability of EMT-induced TNBC cell lines (MDA-MB-231 and MDA-MB-468) monolayer cultures by MTT assay, upon treatment with inhibitors for a period of 48 h. **(A), (B)**, and **(C)** refer to the treatment with SAHA, LY411575 and SAHA+LY411575, respectively in MDA-MB-231. **(D)** depicts the dose-effect curve, **(E)** depicts Median-Effect Plot, and **(F)** depicts Combination Index Plot for MDA-MB-231 following combination treatment. Similarly, **(G), (H),** and **(I)** refer to the treatment with SAHA, LY411575 and SAHA+LY411575, respectively in MDA-MB-468. **(J)** depicts the dose-effect curve, **(K)** depicts Median-Effect Plot, and **(L)** depicts Combination Index Plot for MDA-MB-468 following combination treatment. Drug combinations with CI < 1 are considered synergistic, while CI=1 is considered additive, and CI > 1 is considered synergistic. The results are expressed as the mean ± SEM based on three independent experiments. The statistical significance was assessed in comparison to the untreated cells. The significance level was set at $p < 0.05$ (*), $p < 0.01$ (**), $p < 0.001$ (***) and $p < 0.0001$ (****).

Figure 3.3.5 Determination of viability by MTT assay, upon treatment with inhibitors for a period of 48 h. **(A), (B)**, and **(C)** refer to the treatment with SAHA, LY411575 and SAHA+LY411575, respectively in MCF7. **(D), (E)**, and **(F)** refer to the treatment with SAHA, LY411575 and SAHA+LY411575, respectively in HEK293. The results are expressed as the mean ± SEM based on three independent experiments. The statistical significance was assessed in

comparison to the untreated cells. The significance level was set at $p < 0.05$ (*), $p < 0.01$ (**), $p < 0.001$ (***) and $p < 0.0001$ (****).

Figure 3.3.6 Dose effect curve of the breast cancer cells **(A)** MCF7 and **(C)** human embryonic kidney cells (HEK293) treated with SAHA (s), LY411575 (ly), and their combination (sl) respectively. Combination Index plot for **(B)** MCF7 and **(D)** HEK293 cells.

Figure 3.3.7 Graphical representation of the generation of ROS following respective treatments in **(A)** MDA-MB-231 and **(B)** MDA-MB-468. The results are expressed as the mean ± SEM based on three independent experiments. The statistical significance was assessed in comparison to the untreated cells. The significance level was set at $p < 0.05$ (*), $p < 0.01$ (**), $p < 0.001$ (***) and $p < 0.0001$ (****).

Figure 3.3.8 **(A)** Assessment of Mitochondrial membrane potential using JC-1 based flow cytometry in **(a)** MDA-MB-231 and **(b)** MDA-MB-468 cells. Graphical representation of the green vs red fluorescence following mitochondrial depolarization in **(B)** MDA-MB-231 and **(C)** MDA-MB-468. The results are expressed as the mean ± SEM based on three independent experiments. The statistical significance was assessed in comparison to the untreated cells. The significance level was set at $p < 0.05$ (*), $p < 0.01$ (**), $p < 0.001$ (***) and $p < 0.0001$ (****).

Figure 3.3.9 Flow cytometric analysis of the apoptotic and necrotic populations probed by Annexin V-FITC/PI based assay following treatment with the respective inhibitors in **(a)** MDA-MB-231 and **(b)** MDA-MB-468 cells. The results are expressed as the mean ± SEM based on three independent experiments. The statistical significance was assessed in comparison to the untreated cells. The significance level was set at $p < 0.05$ (*), $p < 0.01$ (**), $p < 0.001$ (***) and $p < 0.0001$ (****).

Figure 3.3.10 Evaluation of the cell cycle profile of **(A)** MDA-MB-231 and **(B)** MDA-MB-468.

Figure 3.3.11 Graphical representation of changes in gene expression levels following treatment with the inhibitors in monotherapy as well as in combination therapy as quantified by qRT-PCR analysis. **(A)** and **(B)** show gene expression levels obtained from MDA-MB-231 and MDA-MB-468 monolayer cultures, respectively. The results are expressed as the mean ± SEM based on three independent experiments. The statistical significance was assessed in

comparison to the untreated cells. The significance level was set at $p < 0.05$ (*), $p < 0.01$ (**), $p < 0.001$ (***) and $p < 0.0001$ (****).

Figure 3.3.12 Representative immunoblots showing the expression of the Notch downstream genes in MDA-MB-231 cells, Graphical representation of the fold change in **(A)** Cyclin-D3, **(B)** c-Myc, **(C)** HES-1, **(D)** NICD-1, **(E)** Jagged-2, **(F)** Notch1, **(G)** p21, **(H)** RBPSUH and **(I)** Jagged-1 in MDA-MB-231 cells. The results are expressed as the mean ± SEM based on three independent experiments. The statistical significance was assessed in comparison to the untreated cells. The significance level was set at $p < 0.05$ (*), $p< 0.01$ (**), $p < 0.001$ (***) and $p < 0.0001$ (****).

Figure 3.3.13 Representative immunoblots showing the expression of the Notch downstream genes in MDA-MB-468 cells, Graphical representation of the fold change in **(A)** Cyclin-D3, **(B)** c-Myc, **(C)** HES-1, **(D)** NICD-1, **(E)** Jagged-2, **(F)** Notch1, **(G)** p21, **(H)** RBPSUH and **(I)** Jagged-1 in MDA-MB-468 cells. The results are expressed as the mean ± SEM based on three independent experiments. The statistical significance was assessed in comparison to the untreated cells. The significance level was set at $p < 0.05$ (*), $p < 0.01$ (**), $p < 0.001$ (***) and $p < 0.0001$ (****).

Figure 3.3.14 Graphical representation of changes in gene expression levels following treatment with the inhibitosr in monotherapy as well as in combination therapy as quantified by qRT-PCR analysis. **(A)** and **(B)** shows the gene expression levels obtained from MDA-MB-231 and MDA-MB-468 monolayer cultures, respectively. The results are expressed as the mean ± SEM based on three independent experiments. The statistical significance was assessed in comparison to the untreated cells. The significance level was set at $p < 0.05$ (*), $p < 0.01$ (**), $p < 0.001$ (***) and $p < 0.0001$ (****).

Figure 3.3.15 Graphical representation of changes in gene expression levels following treatment with the inhibitors in monotherapy as well as in combination therapy as quantified by qRT-PCR analysis. **(A)** and **(B)** shows the gene expression levels obtained from MDA-MB-231 and MDA-MB-468 monolayer cultures, respectively. The results are expressed as the mean ± SEM based on three independent experiments. The statistical significance was assessed in comparison to the untreated cells. The significance level was set at $p < 0.05$ (*), $p < 0.01$ (**), $p < 0.001$ (***) and $p < 0.0001$ (****).

Figure 3.3.16 Representative immunoblots showing the expression of the EMT markers and EMT-TFs in **(A)** MDA-MB-231 cells, and **(D)** MDA-MB-468 cells. Graphical representation of the fold change in **(B)** Snail, **(E)** Zeb, **(G)** E-cadherin, **(I)** Vimentin, **(K)** Slug, and **(L)** Twist-1 in MDA-MB-231 cells; while **(C)** Snail, **(F)** Zeb, **(H)** E-cadherin, **(J)** Vimentin, **(M)** Slug, **(N)** Claudin-1, and **(O)** Twist-1 in MDA-MB-468 cells. β-actin serves as a loading control. The results are expressed as the mean ± SEM based on three independent experiments. The statistical significance was assessed in comparison to the untreated cells. The significance level was set at $p < 0.05$ (*), $p < 0.01$ (**), $p < 0.001$ (***) and $p < 0.0001$ (****).

Figure 3.3.17 Confocal images of **(A)** MDA-MB-231 and **(B)** MDA-MB-468 monolayer cultures immune- stained with anti-ZEB and anti-SNAI1 antibody visualized by Alexa Fluor-488 and Alexa Fluor-647. Nuclei were stained with DAPI. Cells were treated with individual inhibitors and drugs as well as in combination therapy for 48 h. The scale bar represents 20 µm. Graphical depiction in the fold change alteration in the expression profile (following ICC) of mesenchymal marker, Vimentin in **(C)** MDA-MB-231 and **(D)** MDA-MB-468, respectively. Based on three independent experiments, the results are represented as mean ± SEM, along with a statistical significance denoting $p < 0.5$ (*), $p < 0.1$ (**), $p < 0.01$ (***) and $p < 0.001$ (****).

Figure 3.3.18 Confocal images of **(A)** MDA-MB-231 and **(B)** MDA-MB-468 monolayer cultures immune- stained with anti-ZEB and anti-SNAI1 antibody visualized by Alexa Fluor-488 and Alexa Fluor-647. Nuclei were stained with DAPI. Cells were treated with individual inhibitors and drugs as well as in combination therapy for 48 h. The scale bar represents 20 µm. Graphical depiction in the fold change alteration in the expression profile (following ICC) of mesenchymal marker (such as Snail **(C)** and **(E)**, and Zeb-1 **(D)** and **(F)**) in MDA-MB-231 and MDA-MB-468, respectively. Based on three independent experiments, the results are represented as mean ± SEM, along with a statistical significance denoting $p < 0.5$ (*), $p < 0.1$ (**), $p < 0.01$ (***) and $p < 0.001$ (****).

Figure 3.3.19 Confocal images of MDA-MB-231 monolayer cultures immune-stained with anti-E-cadherin antibody visualized by Alexa Fluor-488. The Actin cytoskeleton was stained with Phalloidin-555. Nuclei were stained with DAPI.

Cells were treated with individual inhibitors and drugs as well as in combination therapy for 48 h. The scale bar represents 20 µm.

Figure 3.3.20 Confocal images of MDA-MB-468 monolayer cultures immune-stained with anti-E-cadherin antibody visualized by Alexa Fluor-488. The Actin cytoskeleton was stained with Phalloidin-555. Nuclei were stained with DAPI. Cells were treated with individual inhibitors and drugs as well as in combination therapy for 48 h. The scale bar represents 20 µm.

Figure 3.3.21 Determination of Boyden-chamber invasion assay of **(A)** MDA-MB-231 and **(B)** MDA-MB-468 cells. Graphical representation of changes in invasiveness following treatment with respect to untreated samples in **(C)** MDA-MB-231 and **(D)** MDA-MB-468 cells. The results are expressed as the mean ± SEM based on three independent experiments. The statistical significance was assessed in comparison to the untreated cells. The significance level was set at $p < 0.05$ (*), $p < 0.01$ (**), $p < 0.001$ (***) and $p < 0.0001$ (****).

Figure 3.3.22 Scratch wound-healing assays of **(A)** MDA-MB-231 and **(B)** MDA-MB-468 monolayer cultures. Graphical representation of changes in wound healing capacity following treatment with respect to untreated samples in **(C)** MDA-MB-231 and **(D)** MDA-MB-468 cells. The results are expressed as the mean ± SEM based on three independent experiments. The statistical significance was assessed in comparison to the untreated cells. The significance level was set at $p < 0.05$ (*), $p < 0.01$ (**), $p < 0.001$ (***) and $p < 0.0001$ (****).

Figure 3.3.23 A pseudo-plot representation of the CD44/CD24 population in **(a)** MDA-MB-231 and **(b)** MDA-MB-468, respectively.

Figure 3.3.24 Evaluation of sphere formation ability following respective treatments for 48 h in **(A)** MDA-MB-231 cells, and **(B)** MDA-MB-468 cells. Graphical representation of the sphere-forming ability of **(C)** MDA-MB-231 cells, and **(D)** MDA-MB-468 cells. The results are expressed as the mean ± SEM based on three independent experiments. The statistical significance was assessed in comparison to the untreated cells. The significance level was set at $p < 0.05$ (*), $p < 0.01$ (**), $p < 0.001$ (***) and $p < 0.0001$ (****).

Figure 3.3.25 **(A)** Assessment of colony formation assay in **(a)** MDA-MB-231 and **(b)** MDA-MB-468 cells. Graphical representation of the fold change in colony forming ability of the cells of **(B)** MDA-MB-231 and **(C)** MDA-MB-468 cells, respectively. The results are expressed as the mean ± SEM based on three independent experiments. The statistical significance was assessed in

comparison to the untreated cells. The significance level was set at $p < 0.05$ (*), $p < 0.01$ (**), $p < 0.001$ (***) and $p < 0.0001$ (****).

Figure 3.3.26 Graphical representation of changes in gene expression levels following treatment with the inhibitors in monotherapy as well as in combination therapy as quantified by qRT-PCR analysis. **(A)** and **(B)** shows the gene expression levels obtained from MDA-MB-231 and MDA-MB-468 monolayer cultures, respectively. The results are expressed as the mean ± SEM based on three independent experiments. The statistical significance was assessed in comparison to the untreated cells. The significance level was set at $p < 0.05$ (*), $p < 0.01$ (**), $p < 0.001$ (***) and $p < 0.0001$ (****).

Figure 3.3.27 Representative immunoblots showing the expression of autophagic markers: Beclin-1 and LC3 in **(A)** MDA-MB-231 cells, and **(B)** MDA-MB-468 cells. β-actin serves as a loading coantrol. Graphical representation of the fold change in Beclin-1 in **(C)** MDA-MB-231 and **(D)** MDA-MB-468; and LC3 in **(E)** MDA-MB-231 and **(F)** MDA-MB-468. The results are expressed as the mean ± SEM based on three independent experiments. The statistical significance was assessed in comparison to the untreated cells. The significance level was set at $p < 0.05$ (*), $p < 0.01$ (**), $p < 0.001$ (***) and $p < 0.0001$ (****).

Figure 3.3.28 Representative immunoblots showing the expression of MDR-1 and PDL-1 in **(A)** MDA-MB-231 cells, and **(B)** MDA-MB-468 cells. β-actin serves as a loading control. Graphical representation of the fold change in MDR-1 in **(C)** MDA-MB-231 and **(D)** MDA-MB-468; and PDL-1 in **(E)** MDA-MB-231 and **(F)** MDA-MB-468. The results are expressed as the mean ± SEM based on three independent experiments. The statistical significance was assessed in comparison to the untreated cells. The significance level was set at $p < 0.05$ (*), $p < 0.01$ (**), $p < 0.001$ (***) and $p < 0.0001$ (****).

Figure 3.3.29 Representative immunoblots showing the expression of the acetylated histones in **(A)** MDA-MB-231 cells, and **(B)** MDA-MB-468 cells. β-actin serves as a loading control. Graphical representation of the fold change in H3K9ac in **(C)** MDA-MB-231 and **(F)** MDA-MB-468; H3K14ac in **(D)** MDA-MB-231 and **(G)** MDA-MB-468; while H3K27ac in **(E)** MDA-MB-231 and **(H)** MDA-MB-468. Results are expressed as mean ± SEM based on at least 3 independent experiments. The statistical significance was assessed vs. that of the untreated cells. The significance level was set at $p < 0.5$ (*), $p < 0.1$ (**), $p < 0.01$ (***) and $p < 0.001$ (****).

Figure 3.3.30 Graphical representation of changes in gene expression levels following treatment with the inhibitors in monotherapy as well as in combination therapy as quantified by qRT-PCR analysis. **(A)** and **(B)** show gene expression levels obtained from MDA-MB-231 monolayer cultures, while **(C)** and **(D)** show gene expression levels obtained from MDA-MB-468 monolayer cultures. Results are expressed as mean ± SEM based on at least 3 independent experiments. The statistical significance was assessed vs. that of the untreated cells. The significance level was set at $p < 0.5$ (*), $p < 0.1$ (**), $p < 0.01$ (***) and $p < 0.001$ (****).

Figure 3.4.1 Pictorial representation of the cohort of multiple pathways that facilitates the major hallmarks of cancer *(Adapted and redrawn from https://doi.org/10.1039/D0MA00455C and KEGG pathway database)*

Figure 3.4.2 Determination of cell viability of monolayer cells, using MTT-based cytotoxic assay. The viability of the TNBC cells was observed after 48 h of treatment with **(A)** Axitinib, and its combination with LY411575 **(B)** in MDA-MB-231; while the viability obtained after treatment with **(C)** Axitinib, and its combination with LY411575 **(D)** in MDA-MB-468 cells. **(E)** and **(F)** represents the combination index of the treatment MDA-MB-231 and MDA-MB-468 cells, respectively. Based on three independent experiments, the results are represented as mean ± SEM, along with a statistical significance denoting $p < 0.5$ (*), $p < 0.1$ (**), $p < 0.01$ (***) and $p < 0.001$ (****).

Figure 3.4.3 Determination of cell viability of 3D-Tumours spheroids, using alamarBlue based cytotoxic assay. The viability of the TNBC cells were observed after 48 h of treatment with **(A)** Axitinib, **(B)** LY411575 and **(C)** a combination of Axitinib and LY411575 in MDA-MB-231 3D Tumours spheroids; while **(D), (E)** and **(F)** denotes treatment with Axitinib, LY411575 and combination of Axitinib and LY411575 in MDA-MB-468 3D Tumours spheroids, respectively. Based on three independent experiments, the results are represented as mean ± SEM, along with a statistical significance denoting $p < 0.5$ (*), $p < 0.1$ (**), $p < 0.01$ (***) and $p < 0.001$ (****).

Figure 3.4.4 Visualization of the z-stack projections of Live-dead cells of MDA-MB-468 3D Tumours spheroids, after staining with Calcein-AM/Propidium Iodide (PI). The green fluorescence obtained from the Calcein-stained cells represents the

Figure 3.4.11 Assessment of Scratch (or wound healing) assay after subsequent treatment with respective inhibitors in monotherapy and their combination in **(A)** MDA-MB-231 and **(B)** MDA-MB-468 cells. Graphical illustration of fold-change in migration and/or wound healing assay in **(C)** MDA-MB-231 and **(D)** MDA-MB-468 cells. The results are expressed as the mean ± SEM based on three independent experiments. The statistical significance was assessed in comparison to the untreated cells. The significance level was set at $p < 0.05$ (*), $p< 0.01$ (**), $p < 0.001$ (***) and $p < 0.0001$ (****).

Figure 3.4.12 **(A)** Boyden-chamber-based Matrigel invasion assay to obtain the migratory and/or invasive properties of **(i)** MDA-MB-231 and **(ii)** MDA-MB-468 cells. **(B)** and **(C)** are the graphical presentation of the fold-change in intensity to determine the number of migratory cells in MDA-MB-231 and MDA-MB-468, respectively. The results are expressed as the mean ± SEM based on three independent experiments. The statistical significance was assessed in comparison to the untreated cells. The significance level was set at $p < 0.05$ (*), $p < 0.01$ (**), $p < 0.001$ (***) and $p < 0.0001$ (****).

Figure 3.4.13 Graphical depiction of the alteration in the gene expression profile of epithelial marker: E-cadherin, and mesenchymal markers: Fibronectin, N-cadherin, Vimentin, Snail, and Twist in MDA-MB-231 **(A)** and **(B);** and MDA-MB-468 cells **(C)** and **(D),** obtained by qRT-PCR analysis. Based on three independent experiments, the results are represented as mean ± SEM, along with a statistical significance denoting $p < 0.5$ (*), $p < 0.1$ (**), $p < 0.01$ (***) and $p < 0.001$ (****).

Figure 3.4.14 **(A)** and **(B)** represents the western blots showing Notch ligand (Jagged-1), Notch target gene (HES-1 and p21), along with the epithelial marker (E-cadherin) and mesenchymal marker (Vimentin, Snail, and Twist-1) obtained from the treated MDA-MB-231 cells. Graphs depicting the alterations in the protein expression profile of **(C)** Jagged-1, **(D)** Vimentin, **(E)** HES-1, **(F)** Twist-1, **(G)** E-cadherin, **(H)** Snail and **(I)** p21. β-actin was used as a loading control. Based on three independent experiments, the results are represented as mean ± SEM, along with a statistical significance denoting $p < 0.5$ (*), $p < 0.1$ (**), $p < 0.01$ (***) and $p < 0.001$ (****).

Figure 3.4.15 **(A)** and **(B)** represents the western blots showing Notch ligand (Jagged-1), Notch target gene (HES-1 and p21), along with the epithelial marker (E-cadherin) and mesenchymal marker (Vimentin, Snail, and Twist-1) obtained

from the treated MDA-MB-468 cells. Graphs depicting the alterations in the protein expression profile of **(C)** Jagged-1, **(D)** Vimentin, **(E)** HES-1, **(F)** Twist-1, **(G)** E-cadherin, **(H)** Snail and **(I)** p21. β-actin was used as a loading control. Based on three independent experiments, the results are represented as mean ± SEM, along with a statistical significance denoting $p < 0.5$ (*), $p < 0.1$ (**), $p < 0.01$ (***) and $p < 0.001$ (****).

Figure 3.4.16 Immune staining of MDA-MB-468 cells with anti-E-cadherin antibody as visualized by Alexa Fluor 488. The actin cytoskeletons were counterstained with Phalloidin-555, while the nuclei were stained with DAPI. Cells were treated with the aforementioned inhibitors and their combinations for 48 h. The scale bar represents 20 μM.

Figure 3.4.17 Graphical depiction of the alteration in the gene expression profile Notch pathway genes in **(A)** MDA-MB-231 and **(B)** MDA-MB-468 cells, obtained by qRT-PCR analysis. Based on three independent experiments, the results are represented as mean ± SEM, along with a statistical significance denoting $p < 0.5$ (*), $p < 0.1$ (**), $p < 0.01$ (***) and $p < 0.001$ (****).

Figure 3.4.18 **(A)** and **(B)** represents the western blots showing the protein expression profile of the nodal essential genes of the angiogenic pathway, obtained from the treated MDA-MB-231 cells. Graphs depicting the alterations in the protein expression profile of **(C)** p-EGFR, **(D)** p-AKT, **(E)** CD9, **(F)** MDR-1, **(G)** p-FAK and **(H)** p-MAPK. **(I)** and **(J)** represents the western blots showing the protein expression profile of the nodal essential genes of the angiogenic pathway, obtained from the treated MDA-MB-468 cells. Graphs depicting the alterations in the protein expression profile of **(K)** p-EGFR, **(L)** p-FAK, **(M)** p-AKT, **(N)** CD9, **(O)** MDR-1, and **(P)** p-MAPK. β-actin was used as a loading control. Based on three independent experiments, the results are represented as mean ± SEM, along with a statistical significance denoting $p < 0.5$ (*), $p < 0.1$ (**), $p < 0.01$ (***) and $p < 0.001$ (****).

Figure 3.4.19 Graphical depiction of the alteration in the gene expression profile of TCF and LEF **(A)**, and ABC transporter genes such as BCRP, MRP-1 and MDR-1 **(B)** in MDA-MB-231 cells, obtained by qRT-PCR analysis. Similarly, a graphical depiction of the alteration in the gene expression profile of TCF and LEF **(C),** and ABC transporter genes such as BCRP, MRP-1 and MDR-1 **(D)** in MDA-MB-468 cells, obtained by qRT-PCR analysis.

Figure 3.4.20 Representative histograms depicting the alteration in expression of NF-κB assessed by immune- flow cytometry in MDA-MB-231 **(A)** and MDA-MB-468 **(B)** cells. Graphical representation of fold-change in the protein expression profile of NF-κB in **(C)** MDA-MB-231 and **(D)** MDA-MB-468 cells. The results are expressed as the mean ± SEM based on three independent experiments. The statistical significance was assessed in comparison to the untreated cells. The significance level was set at $p < 0.05$ (*), $p < 0.01$ (**), $p < 0.001$ (***) and $p < 0.0001$ (****).

Figure 3.4.21 Graphical depiction of the alteration in the gene expression profile of **(A)** VEGF and VEGFRs, along with RTKs such as **(C)** α-SMA and c-Kit, **(E)** PDGFRα and PDGFRβ in treated MDA-MB-231 cells, obtained by qRT-PCR analysis. Similarly, a graphical depiction of the alteration in the gene expression profile of **(B)** VEGF and VEGFRs, along with RTKs such as **(D)** α-SMA and c-Kit, **(F)** PDGFRα and PDGFRβ in treated MDA-MB-468 cells, obtained by qRT-PCR analysis. Based on three independent experiments, the results are represented as mean ± SEM, along with a statistical significance denoting $p < 0.5$ (*), $p < 0.1$ (**), $p < 0.01$ (***) and $p < 0.001$ (****).

Figure 3.4.22 Representative histograms depicting the alteration in expression of NG2 assessed by immune-flow cytometry in MDA-MB-231 **(A)** and MDA-MB-468 **(B)** cells. **(C)** Immune staining of MDA-MB-468 cells with anti-NG2 antibody as visualized by Alexa Fluor 488. The actin cytoskeletons were counterstained with Phalloidin-555, while the nuclei were stained with DAPI. Cells were treated with the aforementioned inhibitors and their combinations for 48 h. The scale bar represents 20 μM.

Figure 3.4.23 Graphical depiction in the fold change alteration in the expression profile (following ICC) of epithelial marker (such as E-cadherin **(A)** and **(F)**), pericyte marker (such as NG2 **(B)** and **(C)**) and mesenchymal marker (such as Snail **(C)** and **(H)**, Viemntin **(D)** and **(I)** and Zeb-1 **(E)** and **(F)**) in MDA-MB-231 and MDA-MB-468, respectively. Based on three independent experiments, the results are represented as mean ± SEM, along with a statistical significance denoting $p < 0.5$ (*), $p < 0.1$ (**), $p < 0.01$ (***) and $p < 0.001$ (****).

List of Tables

Section 1

Introduction and Review of Literature

1.1. The Intricate Notch Signalling Dynamics in Therapeutic Realms of Cancer

- ***ACS Pharmacology and Translational Science*** *2023, 6, 5, 651−670*

DOI: 10.1021/acsptsci.2c00239

[ACS Publishing group]

Introduction and Review of Literature

Cancer is a plethora of diseases that share a fundamental feature i.e., the abnormal, uncontrollable growth of cells. Besides the unpredicted origin of the disease, the ability of the malignant cells to disseminate to distant parts of the body makes it highly menacing. Among the various subtypes of cancer, breast cancer remains one of the most prevalent cancers in women worldwide. Its incidences and mortality have faced a huge surge over the last three decades on account of the alteration in the risk factor profiles, with about 80% of the patients being aged above 50. Based on the gene expression profile, breast cancer is divided into four molecular subtypes: (i) Luminal A (ER^+, PR^+ and $HER2^-$), Luminal B (ER^+, PR^+ and $HER2^+$), HER2-enriched (ER^-, PR^- and $HER2^+$) and basal-like (ER^-, PR^- and $HER2^-$). In contrast to the other subtypes, the basal-like also known as Triple-Negative Breast Cancer (TNBC) is a heterogenous collection of breast cancers, which constitutes about 20% of all cancer. TNBCs are biologically aggressive, metastatic and are associated with a worse prognosis.

Treatment of breast cancer is complex and involves a combination of different modalities including surgery, radiotherapy, hormonal therapy, chemotherapy or biological therapies delivered in diverse sequences. People with advanced metastatic cancers often undergo combination therapy, a treatment modality combining two or more therapeutic agents. The rationale is to encourage the usage of drugs at a significantly lower dosage so as to minimize the dose-dependent adverse effects of the drugs. Moreover, the amalgamation of two or more drugs enhances the efficacy of the treatment in comparison to monotherapy, since it targets the pivotal signalling pathways in a synergistic or additive manner.

1.1 Signal transduction pathway in cancer

Disruption in the signal-transducing pathways in cancer is responsible for numerous specific characteristics of tumour cells that distinguish them from 'normal' cells – these features are known as 'The Hallmarks of Cancer'. A Signal transduction pathway defines the flow of information in a cell and converts extracellular stimuli into specific cellular responses. It begins extracellularly when a ligand binds to the receptor and ends intracellularly, with a change in the function of the cells, either by altering the DNA expression in the nucleus or by altering the activity of the enzymes in the cytoplasm. Mainly, the Wnt, Hedgehog and Notch signalling pathways are responsible for the development and differentiation of embryonic and adult tissues.Since, these are the evolutionarily conserved pathways that are associated with cell fate determination, aberrant signalling of any one of these pathways has the capability of triggering aggressive malignancies.

Research evidence suggests that among the numerous signalling pathways that facilitate breast cancer progression and dissemination, the Notch signalling pathway has been a prime concern. The Notch signalling pathway plays a pivotal role in facilitating the proliferation and dissemination of breast cancer by imparting the phenomena such as epithelial to mesenchymal transition (EMT), drug resistance, angiogenesis, maintenance of cancer stemness, etc. [1][2].

1.2 The Notch pathway

The Notch is an evolutionarily conserved pathway in both vertebrates and invertebrates, that is responsible for the specific cellular events during embryogenesis and tissue homeostasis [1]. This pathway was first studied in Drosophila in the process of neurogenesis [2]. The Notch pathway is pleiotropic in nature, i.e. it not only affects cell specifications across a wide variety of species (both unicellular and multicellular) but also across a broad range of cell types and at different steps during cell lineage progression [3]. At all stages of development, Notch signalling along with other cell factors influences differentiation, proliferation and apoptosis, which is found to be upregulated in many malignancies.

1.2.1 Structure of the Notch receptors and Ligands

The vertebrates possess four Notch receptor genes (Notch1, Notch2, Notch3 and Notch4), which are synthesized individually from independent mRNA as a single protein precursor **(Schematic 1.1: A).** The activity of the Notch receptor is modulated by Fringe modification of receptors or ligands, co-expression of receptors with ligands, mode of ligand presentation and cell surface area in contact. The Notch receptor possesses an extracellular domain containing multiple EGFR (Epidermal growth factor receptors) like repeats that assist in ligand binding; three LNR (LIN12/Notch related region) repeats, which negatively regulates receptor activation by preventing ligand-independent signalling; followed by a transmembrane domain that facilitates receptor dimerization [4]. However, the cytoplasmic domain of the Notch receptor, also known as the Notch intracellular domain (NICD) comprises a RAM (RBPJ associated molecule) motif that interacts with the DNA binding domain, CSL, six copies of the ANK (CDC10-ankyrin like) repeats that are involved in the protein-protein interaction of cytoskeleton and transcription factors. The ANK repeats are spanned by two nuclear localization signalling (NLS) domains and a C-terminal PEST domain [rich in proline (P), glutamic acid (E), serine (S) and threonine (T)] that facilitates the rapid proteolytic degradation of the Notch proteins. Additionally, Notch1 and Notch2 possess an extra TAD (transcription activation domain) domain. Generally, the variable number of the amino acids between the ANK repeats and PEST domain among the different Notch proteins are responsible for the variable-sized cytoplasmic domain.

Furthermore, vertebrates exhibit structural homology with the two *Drosophila* ligands (Delta and Serrate), as depicted in **Schematic 1.1: B**.They are designated as either Delta-like (DLL1, DLL3 and DLL4) or serrate (Jagged1 and Jagged2) ligands. The Serrate ligands have more EGF repeats, a von-Willebrand factor type-C (vWF-c) domain and an additional cysteine-rich (CR) region, in comparison to the Delta-like ligands. Interestingly, DLL1 and DLL4 have an almost similar structure with approximately 60% similarity in their protein sequence. The intracellular regions of Jagged1, DLL1 and DLL4, have a C-terminal domain that contains a PDZ binding motif, which aids in the intracellular protein-protein interactions and also facilitates the anchoring of membrane proteins to the cytoskeleton [5]. Additionally, the DLL1, Jagged domains contain EGF-like repeats termed the Delta and OSM-11(DOS) motif that enhances the ligand affinity for the Notch receptors [6].

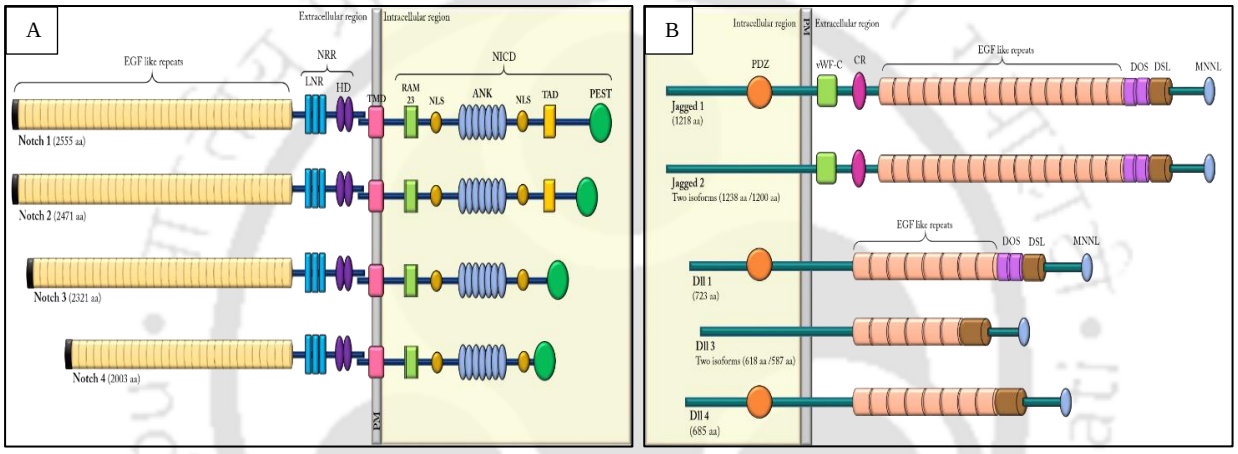

Schematic 1.1: (A) *Schematic representation of mammalian Notch receptor proteins &* ***(B)*** *the Notch ligands.* ***(****Concept source: https://doi.org/10.1016/j.cell.2009.03.045)*

1.2.2 Activation of the Notch pathway

The activation of the Notch receptors involves a series of proteolytic events (details are illustrated in **Schematic 1.2** and **Schematic 1.3)**. Initially, S1 cleavage occurs in the trans-Golgi network by a furin-like convertase, which aids in the functionalization of the receptors. The initiation of Notch signalling takes place by the secondary proteolytic cleavage (S2 cleavage), facilitated upon ligand binding to the extracellular Notch receptors, accredited to the metalloprotease TACE (TNF-a Converting Enzyme, also known as ADAM 17). Upon ligand binding, an E3 ubiquitin ligase, adds a ubiquitin to the intracellular domain, triggering ligand endocytosis. This causes a conformational change in the Notch receptor, resulting in the final proteolytic cleavage (S3 cleavage), by the γ-secretase complex, thereby generating the Notch intracellular domain (NICD). The NICD is then translocated to the nucleus where it forms a complex with the DNA binding subunit RBP-Jk/CBF-1/CSL and acts as a transcription modulator of the Notch target genes of the basic helix loop helix family of proteins such as HES and HEY [5].

The Notch is a 'cell-to- cell' contact pathway, the cells expressing the ligands are called 'signal sender cells' while the ones expressing the Notch receptors are known as 'signal receiving cells'.

In the absence of Notch signalling, the DNA binding domain, CSL protein binds to several transcriptional repressors (histone deacetylase1, HDAC1; silencing mediator of retinoid and thyroid hormone receptors, SMRT, etc.) thereby forming a corepressor complex, which is transcriptionally inactive. Upon NICD binding, several transcriptional activators bind to the CSL protein, replacing the corepressor complex with activators (histone acetyltransferases, HAT; Mastermind-like proteins, MAML; p300, etc.) thereby activating the transcription of the Notch target genes [7]. The Notch is associated with numerous malignancies, such as the development of Hepatocellular carcinoma (HCC) [6], T-cell acute lymphoblastic leukaemia (T-ALL) and aggressive neoplasm of immature T-cells [8], melanoma [9], non-small cell lung carcinoma (NSCLC) [7], etc. There are numerous pathways that are directly linked with the Notch pathway,such as the Ras/MAPK pathway [10], NF-kB pathway [11], PI3/AKT pathway [12] and Wnt pathway [13] thatassist in cancer progression and dissemination.

1.2.3 The non-canonical Notch pathway

The non-canonical Notch pathway, also known as RBPJ/CSL-independent Notch signalling is activated either upon binding of the non-canonical ligands to the Notch receptors or in the absence of ligand [14]. The Notch activation might be γ-secretase dependent or independent, whereby the later exert its function in a membrane-bound form. The non-canonical pathway is also independent of CSL, instead gets activated by interacting with the PI3K/mTOR/Wnt/AKT/NF-kB/HIFα pathways, which might act with the NICD or other regulatory genes, either in the cytoplasm or in the nucleus to exert its function in various biological processes including cancer. The Notch can get activated through R-Ras to promote cell adhesion. Alternatively, it may interact with IKKα in the NF-κB pathway or LEF1 in the Wnt pathway; Notch can also exert its function through its intracellular domain (NICD) which further activates multiple pathways [15].

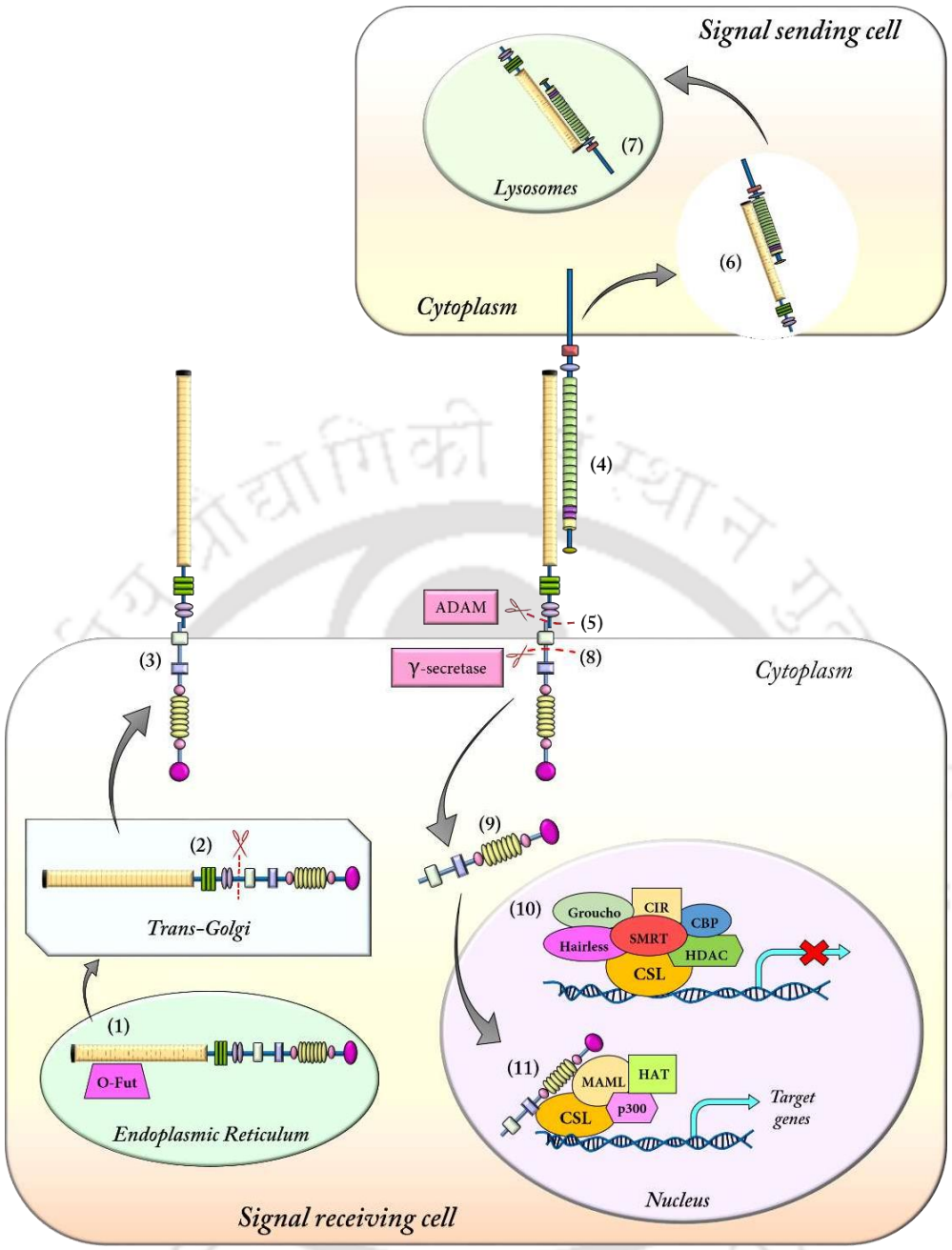

Schematic 1.2: *Detailed representation of the Notch pathway. (1) The Notch receptor processing occurs in the ER, by the enzyme O-Fut (O-fucosyltransferase) that adds fucose to the Notch precursor, followed by Fringe mediated glycosylation (2). In the trans-Golgi network, Furin-like convertase cleaves full-length Notch (S1 cleavage) that generates a heterodimer molecule, which is expressed on the cell membrane (3). (4) The Notch receptors are activated upon binding of the Delta/Serrate family of ligand to the extracellular receptor of Notch (5), facilitating ADAM-protease-mediated S2 cleavage. (6) The ligand bound to the Notch extracellular domain (NECD) gets internalized or cytocyzed by the signal-sending cell, which gets degraded inside the lysosomes (7). (8) S3 cleavage occurs by the γ-secretase enzyme, resulting in the release of the Notch intracellular domain (NICD), which gets internalized into the nucleus (9) and (11) binds to the DNA binding domain, CSL and replaces the corepressors with the coactivators that facilitate the transcription of the Notch targeted genes. (10) In the absence of NICD, the CSL is bound to the corepressor complex, which inhibits the transcription of Notch target genes. (Concept source: https://doi.org/10.1016/j.cell.2009.03.045)*

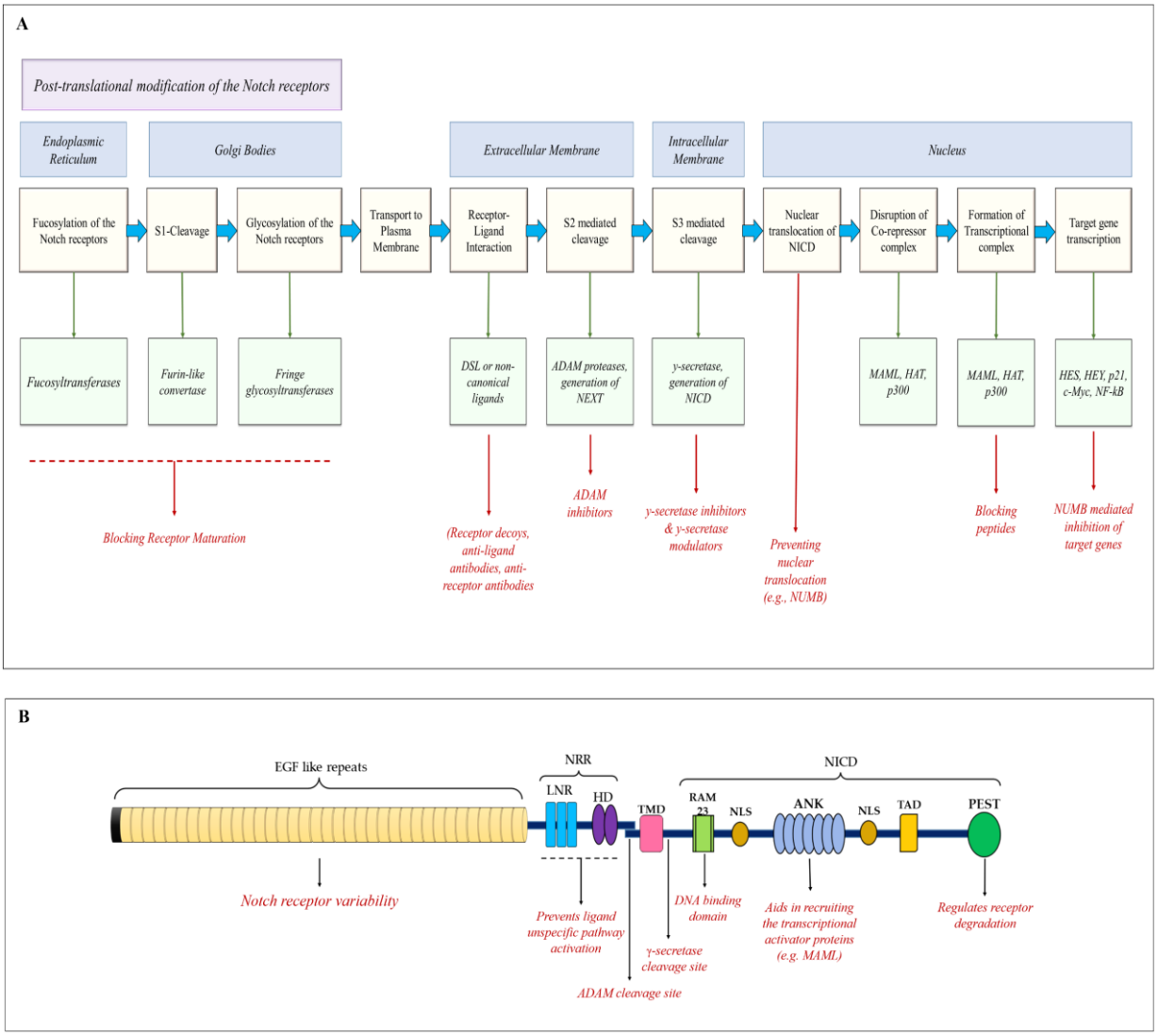

Schematic 1.3: (A) *Detailed overview of the Notch signalling pathway and its possible therapeutic targets.* ***(B)*** *the function domains of the Notch receptor and their corresponding functions. (Concept source: modified and redrawn from Mollen et. al. doi: 10.3389/fonc.2018.00518)*

1.2.4 The NICD

The S3 cleavage of Notch is heterogeneous regarding the position of the cleavage site. The NICD fragments being generated have either an N-terminal valine (Val) or an N-terminal serine/leucine (Ser/Leu). The Ser/Leu-NICD fragments have a shorter half-life than Val-NICD fragments that affect the duration of Notch signalling [16]. The NICD is subjected to a variety of post-translational modifications **(Schematic 1.4),** including phosphorylation, ubiquitylation, hydroxylation and acetylation, which is important for its proper activity, half-life and stability, reviewed by Belle *et al.* [17].

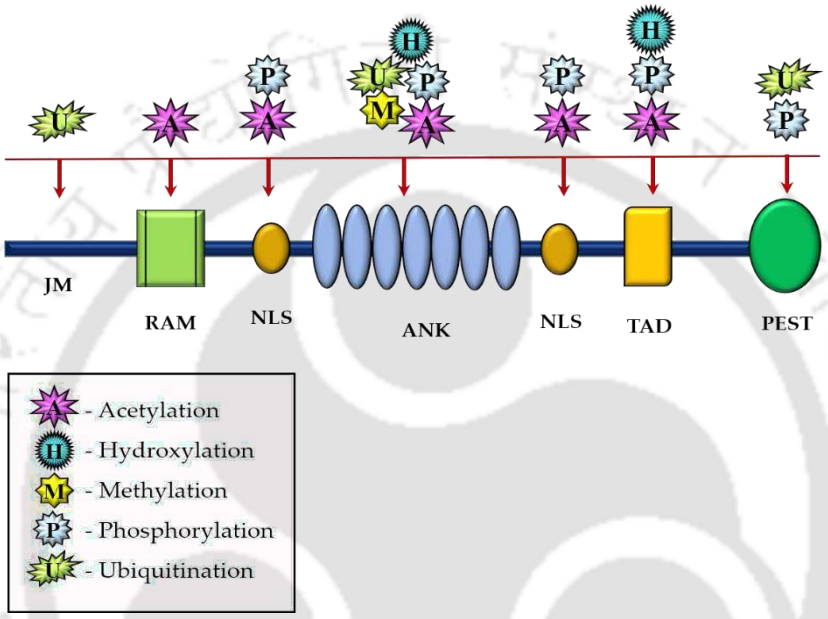

Schematic 1.4: *Post-translational modifications in the NICD: the NICD followed by its cleavage undergoes post-translational modifications like acetylation (responsible for finely tuning the half-life of Notch), hydroxylation (contributes to signalling diversity of NICD), methylation (increases stability and half-life of NICD), phosphorylation (regulates activity and turnover of NICD), ubiquitination (activates Notch signalling, regulatesthe half-life of Notch).*

NICD is a short-lived protein with a half-life of approximately four hours. One molecule of NICD generates one signalling unit. Moreover, the effectiveness of receptor-ligand interaction is directly proportional to the amount of NICD in the nucleus. During transcriptional activation, kinases (such as cyclin dependant kinase 8, CDK8) phosphorylate NICD within its PEST domain which is then targeted for proteasome-mediated degradation by Sel10 (also called Fbw7), an E3 ubiquitin ligase. Thus, limiting the half-life of the NICD that reset the cell for the next pulseof signalling.

Among the different components of the Notch signalling pathway, the cleaved intracellular domain (NICD), has the inherent ability to transduce signals in both healthy and tumour cells. In tumour cells, the pleiotropic effects of NICDupon its interactions with the signalling components of the other pathways result in the enhanced tumorigenesis and dissemination of the cancer cells; depicted in **Schematic 1.5.**

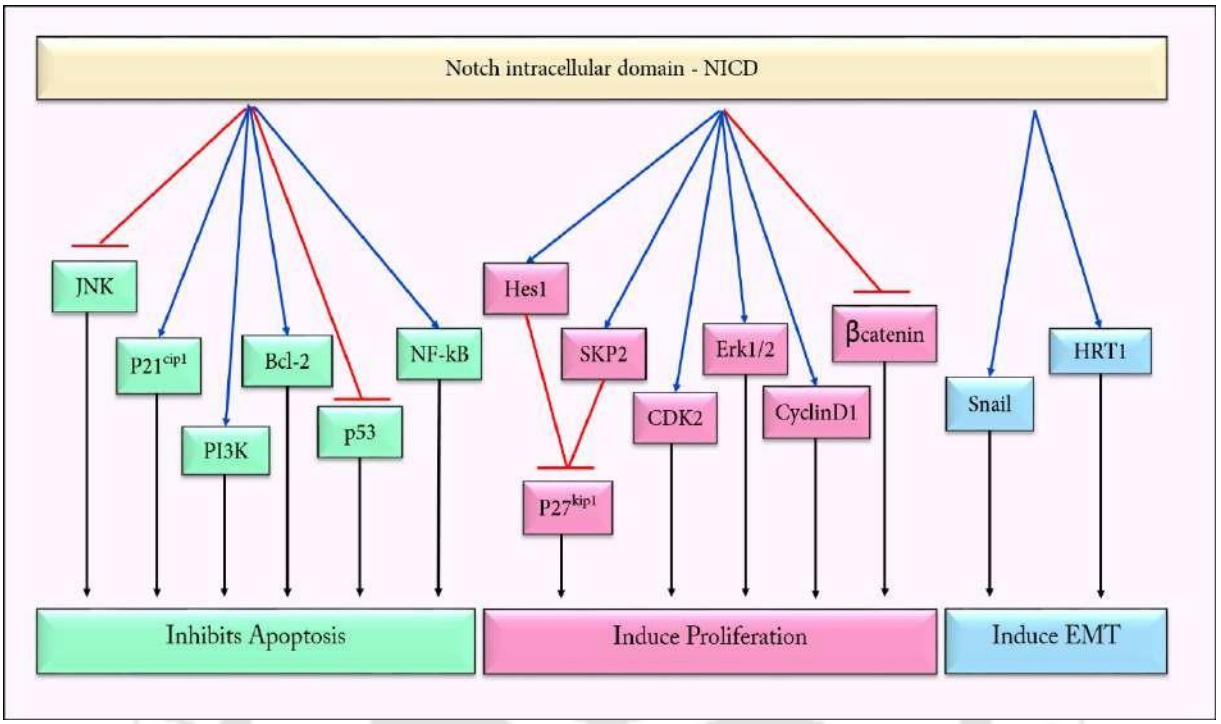

Schematic 1.5: *The NICD (Notch intracellular domain) regulates the expression of various downstream genes that inducesproliferation, aid in EMT (epithelial to mesenchymal transition) and inhibits apoptosis, thereby promoting tumorigenesis.*

1.3 Implications of Notch in cancer

The Notch acts either as an oncogene or a tumour suppressor gene based on the tumour subtype. For example, the Notch ligands and/or receptors possess tumour- suppressive properties in various cancers such as prostate cancer [18], lung cancer [19], skin cancer [20], etc. The Jagged1, DLL1, and DLL4 ligands mediated Notch activation inhibit self-renewal capacity and growth of AML cells [21]. In haematological malignancies, Notch signalling suppresses proliferation and induces apoptosis in B-cell lymphoma and multiple myeloma, following upregulation of $p21^{WAF/Cip}$ expression [22], [23].

Besides, the aberrant expression of Notch ligands is associated with poor prognosis in more than 70 % of hepatocellular carcinoma tissues. The activating mutations of the Notch1 receptors and Jagged1 ligand upregulate the proliferation and dissemination of various leukemia, such as in T-cell acute lymphoblastic leukemia (T-ALL) [24] and acute myeloid leukemia (AML) [25]. Constitutive activations of the Notch1 receptor promote melanoma via β-catenin mediated MAPK and PI3K/AKT activation [26]. Moreover, it also promotes the aggressiveness of non-small cell lung carcinoma (NSCLC) in hypoxic conditions. Additionally, in breast cancer, the Notch pathway plays a pivotal role. For example, the hyperactivation of Jagged1 and Notch1, in cross-talk with the Ras/MAPK pathway correlates to poor prognosis in breast cancer patients [10].

1.4 Causal mutations of Notch in cancer

The role of the Notch pathway in the development of *Drosophila* has been studied since a dominant notched wing phenotype was first reported in 1914. However, its role in human development and disease was recognized only when mutations in the Notch1 gene were associated with a form of T-ALL. Mutations in the Notch signalling pathway genes generally cause defective developmental phenotypes, which affect the heart, kidney, liver, skeleton, eye, and vasculature [27].

Analysis of a cohort of cancer cell lines reveals that genetic alterations (such as mutations, deletions, amplifications, and gain-of-function) in one Notch receptor are mutually exclusive to changes in other receptors and its ligands. Gain-of-function mutations are characteristics of hematopoietic cancers, whereby single cells are affected, such as T-ALL and B-CLL. However, in solid tumours, alteration in the signalling is bi-directional, i.e., the oncogenic or tumour suppressor function of Notch is context-dependent, such as stage, cancer entity tissue of origin, tumour microenvironment, or the genetic background. For example, mutations in all four Notch receptors preferentially act as either a driver mutation that promotes tumour survival and progression or it can also promote progression and survival of a malignancy at the later stages. Similarly, genetically acquired gain-of-function mutations of Notch activity facilitate the initiation and progression of gliomas [28], osteosarcomas [29], or SCLC (small cell lung cancer).

Additionally, gain-of-function mutations in the Notch also aid in EMT progression and invasive phenotypes of NSCLCs [30]. Furthermore, it also promotes the drug-resistant phenotype in lung cancers [31]. Additionally, it has also been observed that mutations in Notch2 facilitate the development of liver metastasis [32]. Also, activating Notch1 mutations or rearrangements in EGF and NRR regions have been observed in TNBC basal-like phenotypes. While, nonsense mutations in the PEST domain of Notch1, Notch2 and Notch3 receptors have been observed in TNBC, which results in an elevated half-life of the NICDand leads to overexpression of the Notch downstream genes [33].

Moreover, the loss-of-function mutations in Notch are equivalently predominant in epithelial cancer types or carcinomas, such as squamous skin carcinoma and basal-cell carcinoma [34], along with pancreatic [35], liver cancers [36], etc. Moreover, loss-of-function mutations in the Notch also reduce the expression of the regulatory genes such as FBXW7, which itself acts as a potent tumour suppressor, thereby resulting in cancer progression and dissemination [37]. Some of the common mutations in the Notch receptors are depicted in **Schematic 1.6**, as obtained from the cBioportal database (https://www.cbioportal.org/).

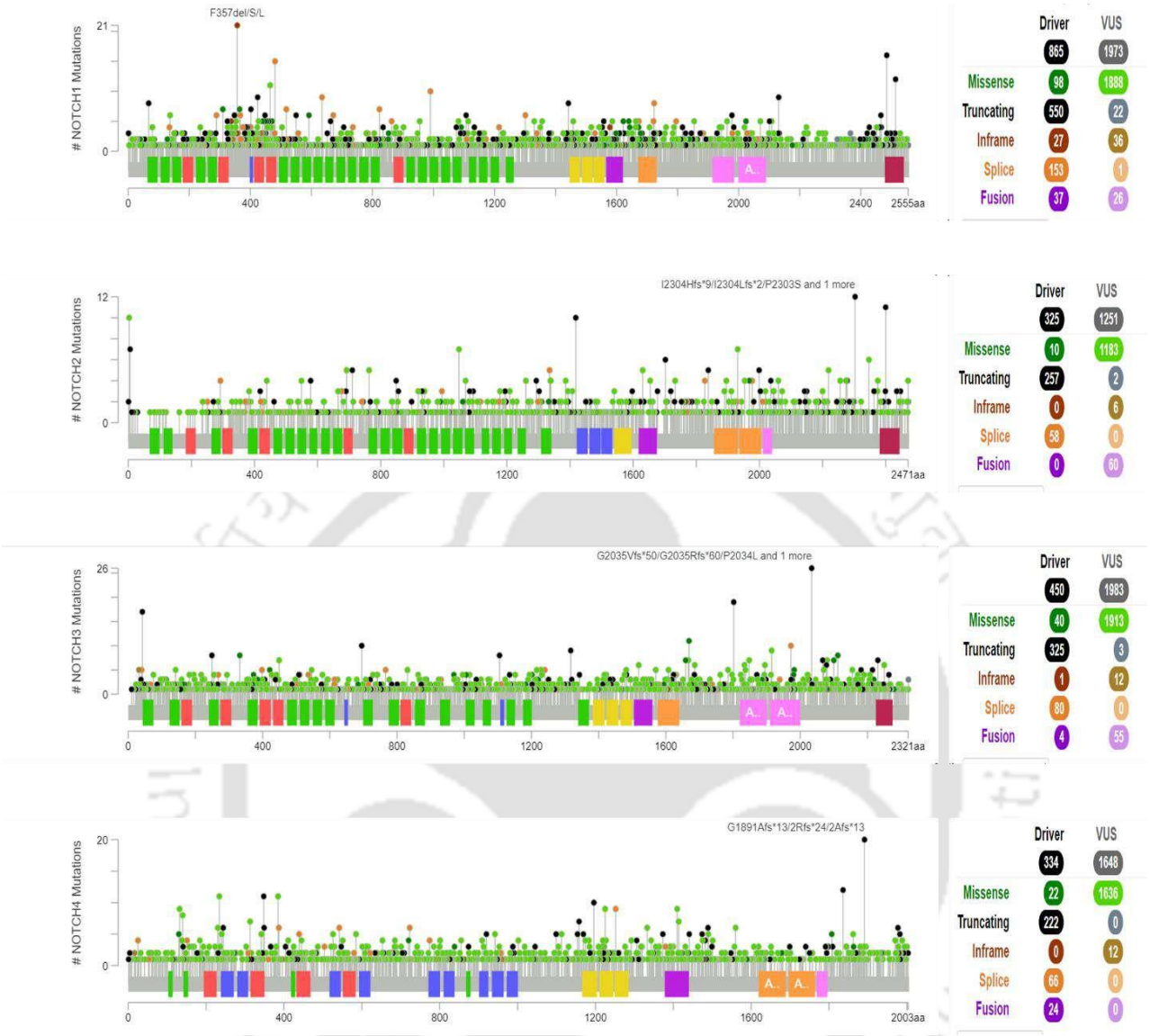

Schematic 1.6: *The mutational profile among the gene sequence of the Notch receptors.*

1.5 Crosstalk of the Notch with some major oncogenic signals

The Notch is a cynosure signalling pathway that is integrated into signalling networks and regulated by otherpathways via its intracellular domain, NICD. The details of the functional relationship among the Notch and other oncogenic pathways are illustrated in **Schematic 1.7**. For example, the Notch ligand, receptor and NICD, confer the activation of NF-kB, therefore leading to the activation of the NF-kB target genes such as MMP-2, MMP-9, VEGF, Survivin, Bcl-xL, etc. that promotes pancreatic cancer [11], breast cancer [38], etc.

In general, the Notch and the Wnt pathway possess contradictory effects on cellular fate determination, whereby the Wnt promotes stem cell fate, while the Notch promotes lineage commitment and differentiation of cells [13]. In molecular level, Wnt pathway inhibits the expression of GSK-3β, which results in the activation of HES-1 promoter by Notch2. However, aberrant expression of Wnt pathway results in the phosphorylation and inhibition of the GSK-3β, which results in constitutive activation of the HES-1 genes in malignant cells, thereby activating the transcription of the downstream genes [39]. Similarly, Hedgehog in combination with the Wnt pathway, induces the expression of HES-1, thereby regulating self-renewal and differentiation of breast cancer stem cells [14]. Further, MAPK-ERK signalling induces the activation of Jagged1, thereby promoting angiogenic properties in head and neck squamous cell carcinoma [40], breast cancer [41], etc. MEK/ERK also promotes the expression of HES-1, which in turn inhibits PTEN, thereby upregulating the PI3K/AKT pathway. Also, PI3K regulated the expression of β-catenin, which also activates the Notch pathway in various cancer [42].

Moreover, the Notch and TGF-β are essential for cellular differentiation. However, TGFβ upregulates the expression of the Notch target genes (such as Hey1, Hey2, Hes1 and Hes5) and Notch ligand Jagged1, therefore, inducing EMT [43]. Further, downstream synergistic interaction of the NICD and SMAD3 results in the activation of the synthetic promoters containing CSL or SMAD3 binding sites, which further facilitates EC migration [44]. Moreover, the activation of TGFβ pathway is also mediated by the Snail and Slug, which are the downstream target genes of the Notch pathway, especially in breast cancer [45]. Similar to TGF-β, there lies a feedback mechanism between the Notch and hypoxia pathway. For example, the cytoplasmic levels of HIF-1α are upregulated during hypoxic conditions, which interacts with the γ-secretase, thereby potentiating its enzymatic activity. This in turn results in the increased NICD expression, and enhanced transcription of the Notch target gene, HES-1. Additionally, the nuclear HIF-1α synergistically interacts with NICD, thus upregulating the expression of the Notch target genes, altogether resulting in the progression of EMT [46].

Altogether, the Notch exhibits established cross-talks with numerous signalling pathways that aids in the aggressiveness of the malignancies. The major hallmarks contributed by the aberrant expression of this pathway are drug resistance, angiogenesis, epithelial to mesenchymal phenotype (EMT), maintenance of stemness, etc. Hence, owing to the oncogenic role of the Notch pathway in a variety of malignancies, therapeutic intervention of this pathway in monotherapy as well as in combination therapy might withhold promising results in ablating cancer.

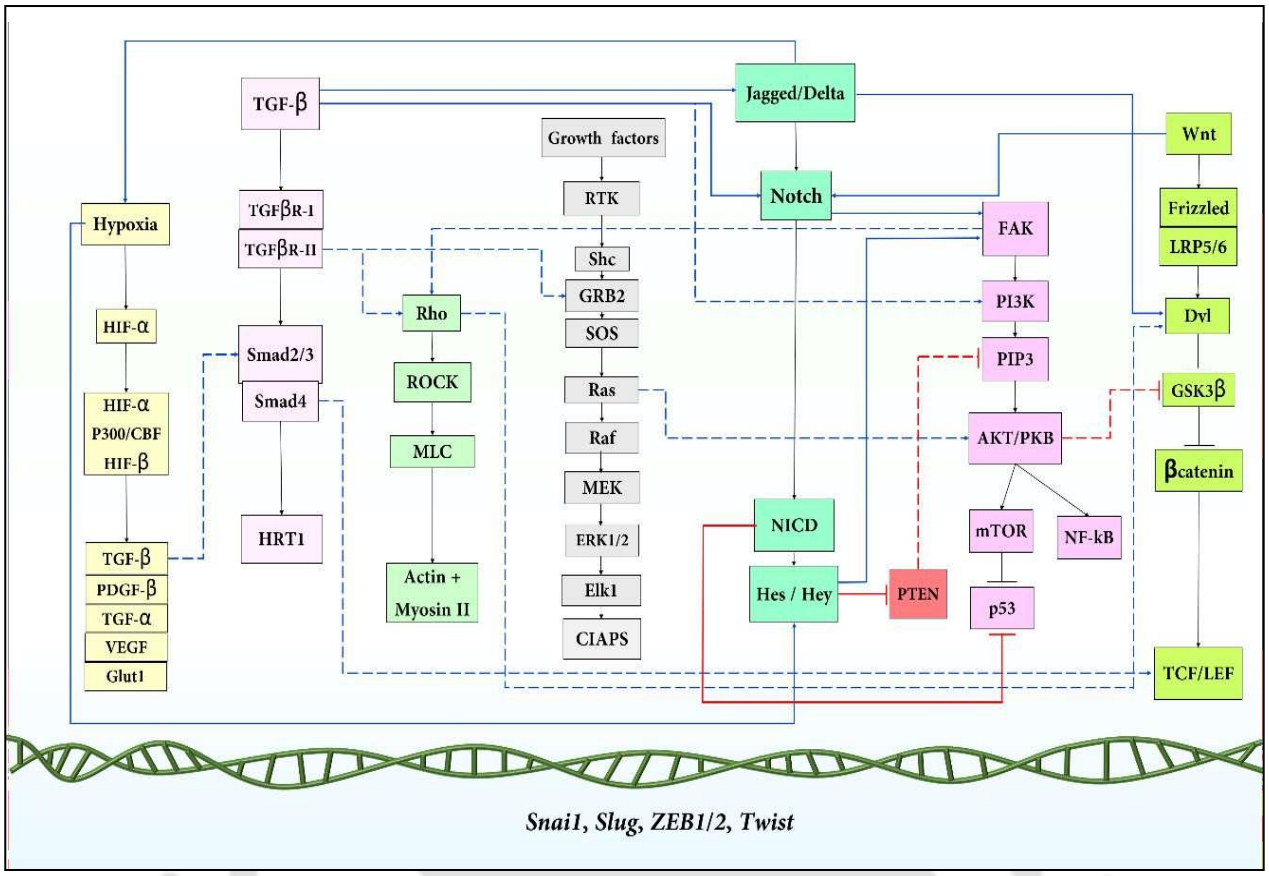

Schematic 1.7: *The Notch pathway crosstalk facilitating EMT: The Notch pathway is intertwined with numerous oncogenic pathways (such as Hypoxia, TGFβ, Rho-RACK, MAPK, FAK, AKT/mTOR, Wnt) that facilitates the transcription of several transcription factors (such as ZEB, Snail, Slug, Twist) which in turn potentiates the epithelial to mesenchymal transition. (Concept source: KEGG pathway database)*

1.6 The Notch facilitates various hallmarks of cancer

The hallmarks of cancer were initially divided into eight subtypes; however, recently it has been renewed into 14 major subtypes by Hanahan in 2022, which are as follows: (i) Sustaining proliferative signalling, (ii) Unlocking phenotypic plasticity, (iii) Deregulating cellular metabolism, (iv) Resisting cell death, (v) Genome instability and mutations, (vi) Senescent cells, (vii) Inducing or accessing vasculature, (viii) Activating invasion and metastasis, (ix) Polymorphic microbiomes, (x) Tumour promoting inflammation, (xi) Enabling replicative immortality, (xii) Avoiding immune destruction, (xiii) non-mutational epigenetic reprogramming, and (xiv) Evading growth suppressors [47].

1.6.1 The Notch and EMT

Metastasis is defined as the spread of the malignant cells from its primary source to a distant area, thereby producing additional tumours. It is one of the most difficult aspects of cancer therapy and the leading cause of mortality in cancer patients. The key molecular mechanism involved in this process is termed as the 'epithelial to mesenchymal transition', most commonly known as EMT.

EMT is a conserved phenomenon that generally occurs during development, tissue regeneration or wound healing. It is one of the pivotal phenomena that potentiates metastasis in cancer, illustrated in **Schematic 1.8** [48]. EMT is induced by several molecular programs facilitated by the transcriptional repressors that results in the loss of epithelial proteins (e.g., E-cadherin, occludin, claudin, etc.), loss of cell-to-cell adhesions, loss of apical-basal polarity, etc., along with the gain of migratory mesenchymal characteristics, such as overexpression of the mesenchymal proteins (e.g., vimentin, fibronectin, N-cadherin, etc.). Moreover, the increased expression of the matrix metalloproteases (MMPs) such as MMP-2, MMP-3, and MMP-9, facilitates the degradation of the basement membranes, thereby allowing the CTCs to traverse through to distant part of the body [49]. Moreover, the zinc finger binding transcription factors (such as Snai1, Slug and ZEB) and the basic helix-loop-helix factors (such as Twist and TCF3) also contributes to the loss of epithelial phenotype. The expression of these transcription factors are facilitated by multiple pathways such as the Wnt pathway [50], TGFβ pathway [51], Notch pathway [52], etc.

The Notch in associations with various oncogenic pathways also induces EMT (depicted in **Schematic 1.7**). For example, overexpression of Notch1 in endothelial cells induces the expression of Snail *in vitro*, which results in the loss of E-cadherinexpression and induces EMT [53]. The Notch signalling pathway upregulates the expression of the Snail by recruiting the NICD to the Snail promoter. Also, the Notch potentiates the recruitment of HIF-1 to the LOX (lysyl oxidase) promoter, which results in the upregulation of the LOX proteins that stabilizes the expression of Snail [54]. Additionally, the Notch pathway upregulates the expression of the Slug promoter via its interaction with CSL in endothelial cells [55]. Overexpression of the Notch1/Jagged1 axis aids in breast cancer progression and metastasis. Furthermore, in NSCLC cells, the Notch-miR200-ZEB1 axis promotes cancer progression and metastasis by promoting EMT [56]. The Notch pathway also interacts with the FAK pathway and mediates changes in the actin-cytoskeletal dynamics of the cells, thus, potentiating EMT [57]. The Notch forms a reciprocal positive regulatory loop with the TGF-β pathway via the SMAD proteins, thereby inducing EMT [58]. In the tumour microenvironment, the Notch pathway synergistically interacts with HIFα and IL6, to facilitate EMT [59]. Moreover, hypoxia induced activation of the Notch pathway results in the enhanced expression of Snail and Slug, which promotes EMT [60]. The Notch pathway also imparts Anoikis resistance to tumour cells, via the activation of the PKB/Akt pathway, a key effector of theactivated Ras in numerous malignancies [61].

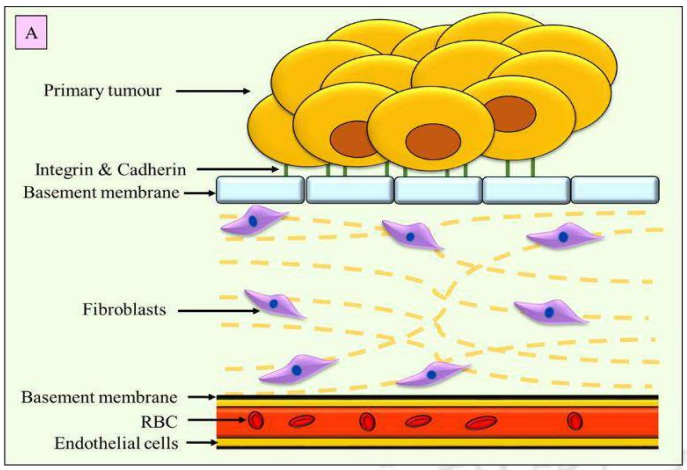

The primary tumour architecture

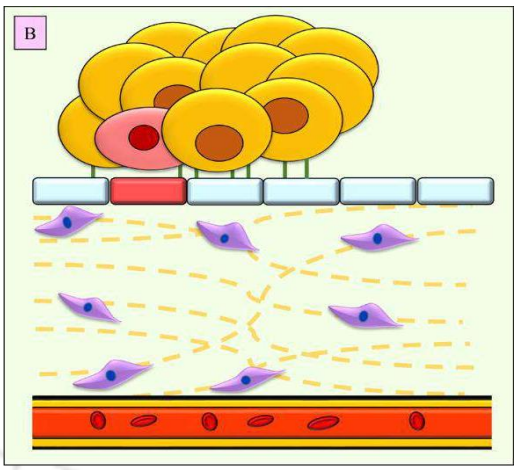

Alteration in the gene expression leads to changes in the cellular structure

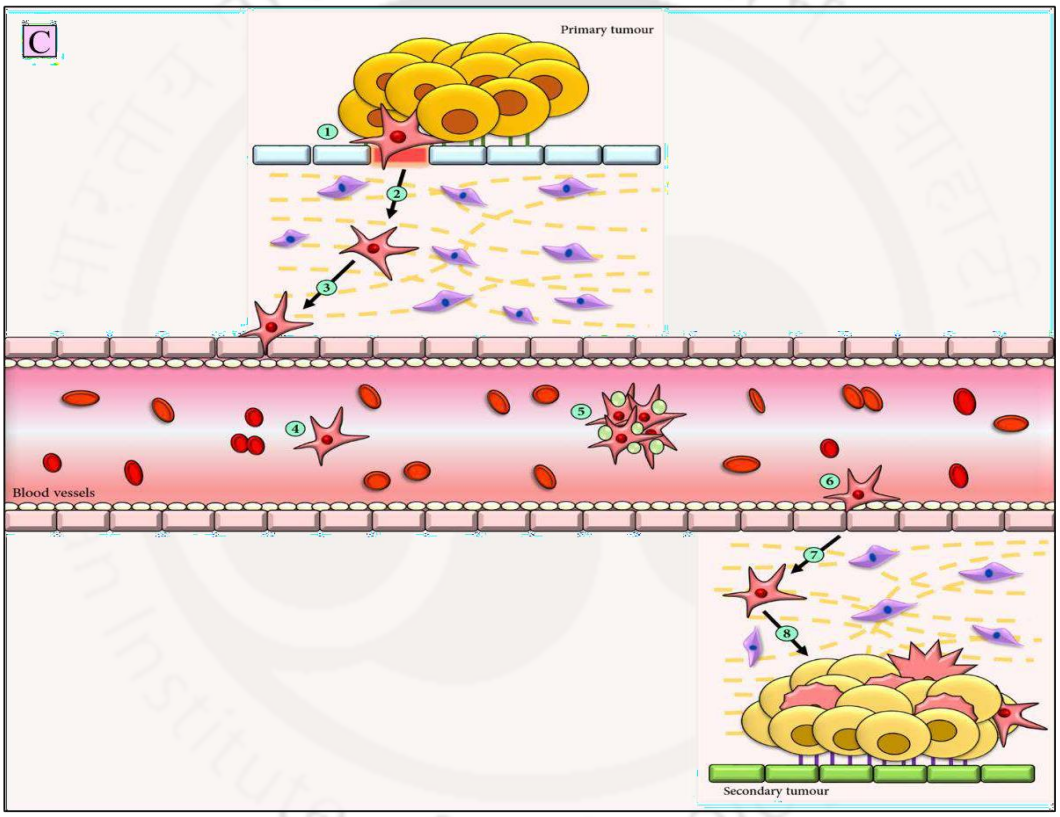

The metastasis of cancer cells from primary tumour site to a secondary tumour site

Schematic 1.8: *Schematic representation of the epithelial to mesenchymal transition.* ***(A)*** *The tumour architecture; (B) upon external stimuli from the tumour niche, there is an alteration in the gene expression that results in the phenotypic change of the epithelial tumour cell****; (C)*** *following EMT, the epithelial cells acquire migratory mesenchymal characteristics; upon the secretion of matrix metalloproteases (MMPs) by the mesenchymal cells the basement membrane gets degraded (1), the mesenchymal cells then traverse the stromal cellular layers (2); the tumour cells possess PDGFR (platelet derived growth factor receptors), therefore, are chemo-attracted by the endothelial cells of the blood vessels secreting PDGF (3); following chemotaxis, the tumour cells intravasate into the blood vessels (4); (5) they travel to a distant site in the body either alone or in clusters, after being surrounded by the platelets which help them escape immune recognition, (6) the extravasation of the tumour cells through the blood vessels engenders secondary tumours (7), whereby, following the process of mesenchymal to epithelial transition (MET), the migratory cells acquire epithelial characteristics and give rise to an entirely new cluster of tumours (8).* *(Concept source: https://doi.org/10.1039/D0MA00455C)*

1.6.2 The Notch, EMT and CTCs (circulating tumour cells)

The migratory and mesenchymal characteristics in cancer cells are imparted following repeated cycles of EMT and MET. Upon induction of EMT, the tumour cells exhibiting epithelial phenotype, lose their epithelial markers and attains partial EMT phenotype, also known as hybrid E/M (epithelial/mesenchymal) state; whereby they still exhibit some residual cell-to-cell interactions and have the potential to migrate as a cluster of circulating tumour cells (CTCs) [62]. Finally, upon complete induction of EMT, the tumour cells acquire mesenchymal characteristics. These mesenchymal cells, possesses the ability to traverse via bloodstream and lymph nodes to the distant part of the body and undergoes metastatic colonization via mesenchymal to epithelial transition (MET); therefore, giving rise to secondary tumours. However, the resulting from the hybrid E/M phenotypes are apoptosis resistant, possesses high metastatic propensity, and are more potent in establishing metastatic colonization and tumour relapse [63]. However, the Notch plays an important role in determining the phenotype of the tumour cells undergoing EMT. The Notch-Jagged signalling axis gives rise to similar type of cell fate (lateral induction), whereas the Notch-Delta signalling axis gives rise to alternative cell fates (lateral inhibition). This in turn results in the generation of either a cluster of cells exhibiting hybrid E/M phenotype during lateral induction, or cells exhibiting complete mesenchymal phenotype during lateral inhibition (depicted in **Schematic 1.9**) [64]. Altogether, these studies suggests that the regulationof EMT-E/M-MET is highly dependent on the cell-to-cell interaction profile via the Notch signalling.

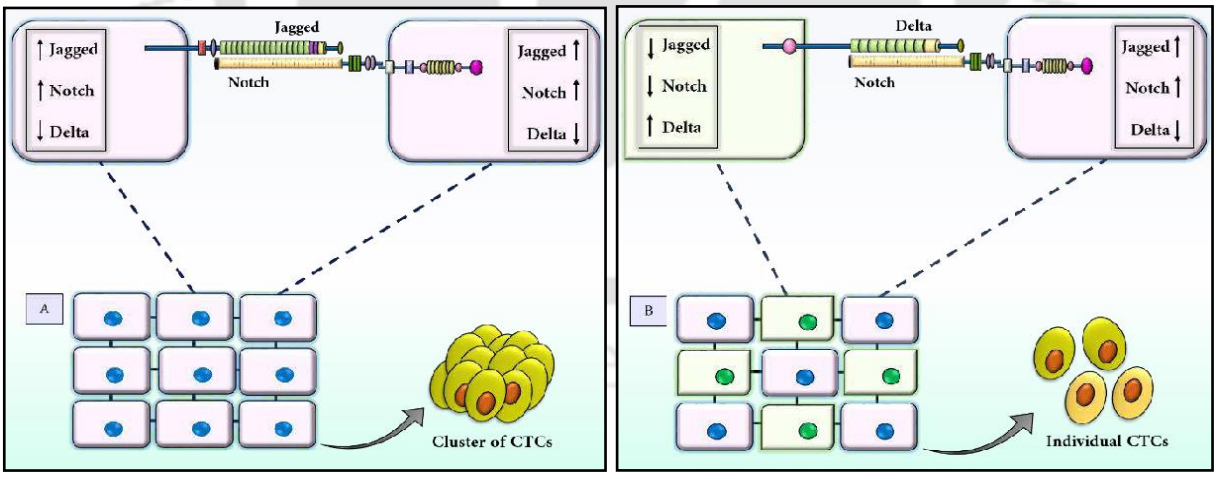

Schematic 1.9: *The formation of the Circulating tumour cells (CTCs). (A) the Jagged mediated Notch pathway activation gives rise to the phenomenon of lateral induction. As a result of which the surrounding cells acquire the same cellular fate, thereby giving rise to a cluster of circulating tumour cells. (B) the Delta mediated Notch pathway activation gives rise to the phenomenon of lateral inhibition. As a result, the surrounding cells acquire different cellular fates, thereby giving rise to individual circulating tumour cells. (Concept source: 10.3389/fonc.2015.00155)*

1.6.3 The Notch and CSCs (cancer stem cells)

Cancer stem cells (CSCs) are defined by their inherent ability of self-renewal and pluripotency. The major difference between a cancer stem cell and a healthy cell is their degree of dependency on their microenvironment niche, which plays an essential role in the maintenance of cancer cells by providing extrinsic factors and regulatory signalling molecules such as HIF-hypoxia inducible factors, BMP-bone morphogenetic proteins, FGF-fibroblast growth factors, Notch, etc. [65].

On account of the heterogeneity in their frequency and functionality, the roles of CSCs are trivial. In stressful conditions, the CSCs divide into daughter progenitor cells, which act as tumour-initiating cells, thereby facilitating metastasis in a more suitable environment [66]. Research evidence suggests that EMT influences cancer cells to develop into CSCs, which results in enhanced relapse, drug resistance and metastasis in numerous malignancies [67]. For example, in breast cancer, the induction of EMT results in the elevation of the gene expression profile, i.e., $CD44^{high}/CD24^{low}$. Additionally, the transcription factors that facilitate EMT (such as ZEB, Snail, Slug, etc.) also help in maintaining stem cells by inducing the expression of stemness genes. Further, multiple pathways have been implicated in the process of EMT and maintenance of CSCs, such as EGFR, Wnt/β-catenin, Hedgehog, Notch, and STAT3 [67]. Amongst them, the Notch is an obligatory self-renewal pathway in both normal and malignant cells. It is required for the establishment of embryonic stem cells. In cancer, the Notch interacts with other pathways and facilitates the maintenance of CSCs and their associations with their microenvironment. The Notch retains CD133+ cells(cancer stem cells) in endometrial cancer and renal cell carcinomas, with enhanced self-renewal ability, drug-resistance, and enhanced EMT [68], [69]. However, downregulation of Notch1 mRNA and proteins suppresses the expression of CD133 in hepatocellular carcinoma, thereby establishing a strong correlation between the Notch pathway, EMT and CSCs [70].

1.6.4 The Notch and angiogenesis

Angiogenesis is defined as the formation of new blood vessels, a process that involves the migration, growth and differentiation of the endothelial cells that outlines the wall of blood vessels. Angiogenesis is controlled by various chemotaxins, such as VEGF (vascular endothelial growth factors), PDGF (platelet-derived growth factor), etc. It plays an important role in the growth, metastasis and maintenance of tumours by initiating the formation of new blood vessels that exchange oxygen and nutrients to the proliferating tumours.

The association of Notch with angiogenesis is ascertained by various researchers. For example, the VEGF-mediated sprouting of the endothelial stalk cells into tip cells, results in the branching of the new blood vessels, whereas the DLL4-mediated Notch1 signalling regulates the selection of tip cells by lateral inhibition, which in turn facilitates the sprouting of the new blood vessels [71]. Moreover, the stromal tumourcells secrete growth factors (such as EGF, TGFα, etc.), which induce the expression of Jagged1 via the

MAPK pathway in the tumour/endothelial cells. This in turn interacts with the Notch receptors in the endothelial cells/tumour cells, respectively. Therefore, activating the Notch downstream genes, which ultimately facilitates angiogenesis [72].

1.6.5 The Notch and drug resistance

Although chemotherapy remains the most successful among cancer therapies, the development of multi-drug resistance (MDR) has hindered its effectiveness. MDR occurs as a result of various mechanisms, for example, enhanced drug efflux via the efflux pumps such as P-glycoproteins, diminished uptake of drugs via the transporters, activation of DNA repair mechanisms, activation of metabolic enzymes such as cytochrome P450 and glutathione S-transferase, induction of EMT, etc. [32]. Moreover, the CSCs confer MDR by upregulating the various transporter proteins, especially the ATP-binding cassette (ABC) family of proteins. Additionally, they also overexpress the ABC transporter proteins on their membranes, thereby pumping out diverse substances and decreasing their biological efficacy [36]. Amongst the various pathways that facilitate MDR, the Notch has been a prime concern. Notch signalling confers drug resistance by inhibiting the p53 pathway through the mTOR-dependent PI3-Akt/PKB pathway [73]. Notch1 is known to regulate the expression of the multidrug resistance gene ABCC1/MRP1. It is also observed that the Notch1-NICD is involved in the transcriptional regulation of ABCC1, thereby contributing to ABCC1-mediated resistance to etoposide [74]. Several such reports depict the involvement of NICD in the resistance of cancer cells to certain chemotherapeutic drugs and inhibitors such as glucocorticoid [75], Enzalutamide[76], etc. A study depicting the enhanced levels of Notch1, Notch2, Jagged1, Jagged2, DLL1 and DLL4 was observed in renal cancer stem cells (CD133+/CD24+) with resistance to Cisplatin and Sorafenib [69].

1.7 Targeting the Notch in Cancer

Owing to the underlying associations of the Notch with various aggressive hallmarks in cancer, it is necessary to efficiently target the pathway to ablate the progression and recurrence of tumours. Moreover, the targeting efficacy could be achieved by contemplating the major facts about the Notch signalling pathway. Firstly, the Notch can act either as a tumour suppressor gene or an oncogene, depending on the tumour type. Hence, a preliminary assessment of its role should be ascertained before moving onto any therapy. Secondly, the half-life of the Notch intracellular domain (NICD) is short-lived, almost about four hours (it might be longer in the case of malignant cells), thus, intermittent inhibition is possible and might be successful. Thirdly, the downstream effects of the Notch activation are dose-dependent, hence, complete inhibition of the pathway is not necessary [77].

In order to effectively inhibit the signalling pathway, various underlying molecular components can be inhibited and/or regulated (depicted in **Schematic 1.10**). Besides, the potent molecular components that confer the activation of the pathway are: (i) the γ-secretase enzyme, (ii) ADAM (a disintegrin and metalloprotease) proteases, (iii) NUMB protein, etc. Therefore, the Notch pathway can be targeted using: (i) anti-ligand/anti-receptor antibodies and/or decoys, (ii) anti-sense oligonucleotides, (iii) ADAM inhibitors, (iv) γ-secretase inhibitors (GSIs), (v) γ-secretase modulators (GSMs), (vi) monoclonal antibodies (mAbs), bs-Ab (bispecific antibody), ADC (antibody-drug conjugate) and CAR-T therapy, etc. [78].

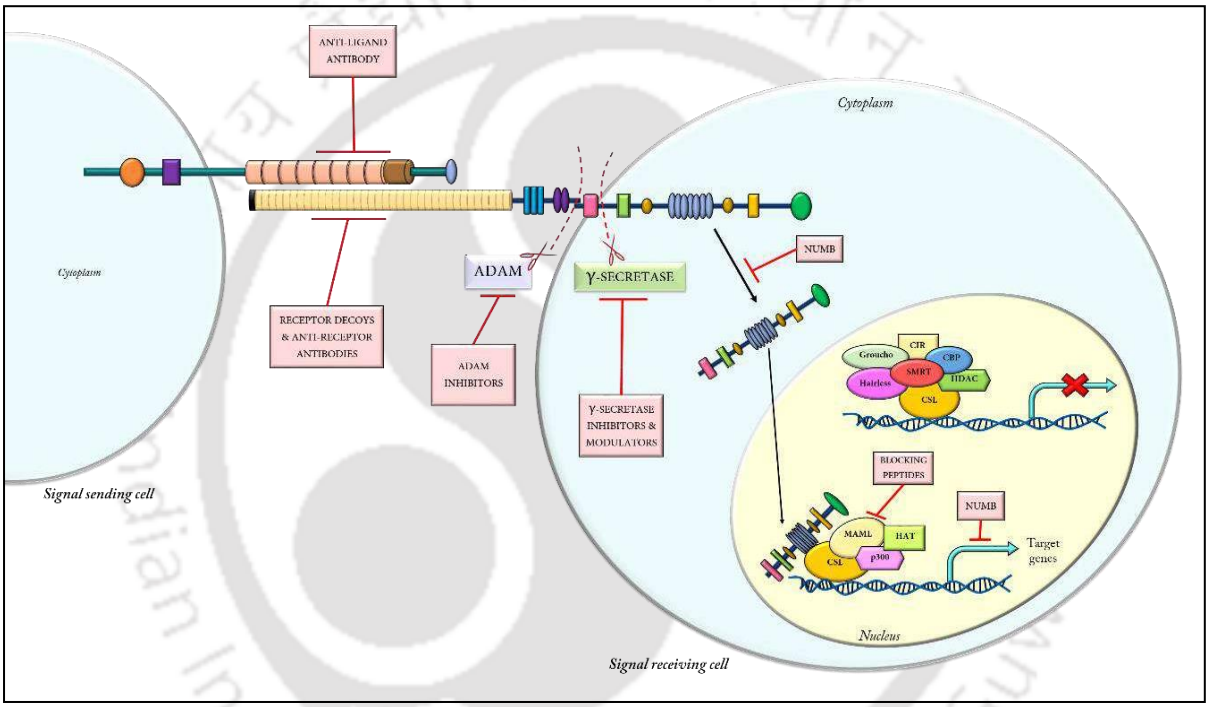

Schematic 1.10: *The possible strategies for Notch inhibition include receptor activation inhibition, modification of receptor-ligand interactions, inhibition by antibodies, disruption of ADAM & γ-secretase cleavage of Notch, alteration of NICD post-translational modifications, inhibition of protein-protein interactions within the nucleus and disruption of assembly of the coactivator NICD–RBPJ complex. (Concept source: 10.1021/acsptsci.2c00239)*

1.8 Key features and Scope of research

The fundamental understanding of molecular mechanism governing the Notch pathway in facilitating the metastatic propensity of the TNBC cells offers substantial therapeutic leverage to effectively abrogate the aggressiveness of breast cancer. The present research investigations is based on the following scopes as potential research areas.

1. Understanding the role of the Notch pathway in potentiating the aggressiveness of the TNBC cells.
2. Identification of the pivotal molecules to regulate the Notch pathway in the EMT dynamics of TNBC cells.
3. Repurposing of the FDA approved drugs for multi-targeting the pivotal proteases of the Notch signalling pathway in TNBC.
4. Exploring the role of the Notch pathway in promoting EMT and metastasis in TNBC cells.
5. Co-targeting the Notch pathway with an HDAC inhibitor to obtain a better therapeutic outcome
6. Co-targeting the pathways to inhibit the EMT and EPT dynamics of the TNBC.

1.9 Objective

- Detecting key molecules of Notch signalling in monolayer, spheroids and EMT cells.
- Therapeutic interception of Notch pathway by small molecule inhibitors and in combination therapy.
- Establishing crosstalk among the Notch pathway and EMT signalling pathways in TNBC

1.10 Salient outcome

- The current study rationalizes the effect of the Notch pathway in EMT dynamics of TNBC cells.
- Co-targeting the Notch pathway reverses the clinical attrition of HDACIs by successfully abrogating their ability to facilitate EMT.
- Similarly, the ability of the Notch pathway in potentiating EPT along with EMT was also ascertained in the TNBC cells.

Section 2

Materials and Methods

Materials and Methods

2.1 Materials

Antibodies used for the protein expression studies are listed below:

Table 2.1.1: *List of antibodies*

Antibodies	Catalogue No.	Manufacturer
β-actin	8457S	Cell Signalling Technology, USA
HES-1	68309	Cell Signalling Technology, USA
NICD (cleaved-Notch)	68309	Cell Signalling Technology, USA
Notch1	68309	Cell Signalling Technology, USA
p21	68309	Cell Signalling Technology, USA
Cyclin D3	68309	Cell Signalling Technology, USA
RBPSUH	68309	Cell Signalling Technology, USA
Jagged-1	8658	Cell Signalling Technology, USA
Jagged-2	8658	Cell Signalling Technology, USA
c-Myc	68309	Cell Signalling Technology, USA
Claudin-1	13255	Cell Signalling Technology, USA
E-cadherin	3195	Cell Signalling Technology, USA
Vimentin	5741	Cell Signalling Technology, USA
Snai1	REF-MA5-14801	Invitrogen
Slug	REF-PA5-73015	Invitrogen
Twist-1	REF-MA5-17195	Invitrogen
Zeb	TA802298	Origene
PDL1	13684	Cell Signalling Technology, USA
MDR1	13342	Cell Signalling Technology, USA
H3K9	9927T	Cell Signalling Technology, USA
H3K14	9927T	Cell Signalling Technology, USA
H3K27	9927T	Cell Signalling Technology, USA
Histone 3	9927T	Cell Signalling Technology, USA
Beclin-1	3495T	Cell Signalling Technology, USA
LC3	12741	Cell Signalling Technology, USA
EGFR	4267	Cell Signalling Technology, USA
pEGFR (Tyr 1068)	3777	Cell Signalling Technology, USA
FAK	9330	Cell Signalling Technology, USA

pFAK (Tyr 576/577)	9330	Cell Signalling Technology, USA
AKT	4691	Cell Signalling Technology, USA
pAKT (Thr)	4060	Cell Signalling Technology, USA
MAPK	4695	Cell Signalling Technology, USA
pMAPK (Thr 202/Tyr 204)	4370	Cell Signalling Technology, USA
NG2	14-6504-80	ThermoFisher Scientific
CD9	13174	Cell Signalling Technology, USA
NF-κβ mAb (Alexa Fluor® 647 Conjugate)	8801	Cell Signalling Technology, USA
CD44 mAb (FITC Conjugate)	903785	Cell Signalling Technology, USA
CD24 mAB (PE Conjugate)	4414S	ThermoFisher Scientific
Anti-Rabbit IgG Fab2 (Alexa Flour® 647 Conjugate)	4414S	ThermoFisher Scientific
Anti-Rabbit IgG Fab2 (Alexa Flour® 488 Conjugate)	4412S	ThermoFisher Scientific
Anti-mouse IgG Fab2 (Alexa Flour® 647 Conjugate)	4418S	ThermoFisher Scientific
Anti-mouse IgG Fab2 (Alexa Flour® 488 Conjugate)	75122S	Cell Signalling Technology, USA

BD Biosciences – FITC Annexin-V Apoptosis Detection Kit

Bio-Rad Laboratories – cDNA synthesis kit, PCR Master Mix, SYBR Green Master Mix for qPCR

Borosil – Glassware

Corning Inc. – Growth factor reduced Matrigel matrix, Boyden chamber trans-well inserts, glass-bottom Petri plates

GE Healthcare – Agarose gel and SDS-PAGE running apparatus

Gibco – Antibiotic-Antimycotic solution

Hi-Media India – Bovine Serum Albumin (BSA), Methanol, Ethanol

Sigma-Aldrich (USA) – Agarose, Dulbecco's modified eagle's medium (DMEM), Ponceau S, Propidium iodide (PI), RIPA buffer, Triton-X-100, Trizma Base (Tris), Tween-20, Tetra-methyl-ethylene-diamine (TEMED), Tri reagent, Ammonium persulphate (APS), Dimethylsulphoxide (DMSO), Sodium pyruvate, Sodium bicarbonate, Epidermal growth factor (EGF), Chemiluminescent reagent, 2',7'-dichlorofluorescein diacetate (DCFDA), DAPI, Phosphate Buffer Saline (PBS), RNAse, Anti-rabbit IgG HRP-linked antibody, Anti-mouse IgG HRP-linked antibody, PVDF membrane, Axitinib, LY411575, SAHA, Lomitapide, TMI-1

Tarsons Products Pvt. Ltd. – Plasticware

Thermo Fisher Scientific – Cell culture plates, DNA and protein ladder, Trypan Blue, alamar blue, Fetal bovineserum (FBS), Penicillin-streptomycin, JC-1 dye, Calcein-AM

Integrated DNA Technologies (IDT) – primers for PCR reactions have been listed in the table below:

Table 2.1.2: *List of primers*

Name	Forward Primer	Reverse Primer
α-SMA	GACGTACAACTGGTATTGTG	TCAGGATCTTCATGAGGTAG
ABCB1	GGGAGCTTAACACCCGACTTA	GCCAAAATCACAAGGGTTAGCTT
ABCC1	CTGAGAAGGAGGCGCCCTG	GTGTCCGGATGGTGGACTG
ABCG2	TGGCTTAGACTCAAGCACAGC	TCGTCCCTGCTTAGACATCC
β-ACTIN	CTGGAACGGTGAAGGTGACA	AAGGGACTTCCTGTAACAATGCA
C-KIT	CACCGAAGGAGGCACTTACACA	TGCCATTCACGAGCCTGTCGTA
E-Cadherin	TGAAGGTGACAGAGCCTCTGGAT	TGGGTGAATTCGGGCTTGTT
EpCAM	GCTGGCCGTAAACTGCTTTG	ACATTTGGCAGCCAGCTTTG
Fibronectin	GGTGACACTTATGAGCGTCCTAAA	AACATGTAACCACCAGTCTCATGTG
Hes1	GTGGGTCCTAACGCAGTGTC	ACAAAGGCGCAATCCAATATG
Hey1	TGGATCACCTGAAAATGCTG	TTGTTGAGATGCGAAACCAG
IL-6	GGCACTGGCAGAAAACAACC	GCAAGTCTCCTCATTGAATCC
Ki-67	AGAGCCTTAGCAATAGCAACG	GTCTCCCGCGATTCCTCTG
N-Cadherin	CCATCAAGCCTGTGGGAATC	GCAGATCGGACCGGATACTG
MMP-1	ACAGCCCAGTACTTATTCCCTTTG	GGGCTTGAAGCTGCTTACGA
MMP-3	GGAAGCTGGACTCCGACACTC	TGGTGTATAATTCACAATCCTGTATGTAA
MYC	GCCACGTCTCCACACATCAG	TGGTGCATTTTCGGTTGTTG
NOTCH1	CTGGTCAGGGAAATCGT	TGGGCAGTGGCAGAT
NOTCH2	ACAGTTGTGTCTGCTCAC	GCGGAAACCATTCACAC
NOTCH3	GAGCCAATGCCAACTGAA	GGGAGATCAGGTCGGA
NOTCH4	CCCAGGAATCTGAGATGGAA	CCACAGCAAACTGCTGACAT
PDGFRα	ATCAATCAGCCCAGATGGAC	TTCACGGGCAGAAAAGGTACT
PDGFRβ	AATGTCTCCAGCACCTTCGT	AGCGGATGTGGTAAGGCATA
SNAI1	ATGAGGAATCTGGCTGCTGT	CAGGAGAAAATGCCTTTGGA
Twist-1	TGCATGCATTCTCAAGAGGT	CTATGGTTTTGCAGGCCAGT
VEGF	GCACCCATGGCAGAAGG	CTCGATTGGATGGCAGTAGCT
VEGFR1	CAGGCCCAGTTTCTGCCATT	TTCCAGCTCAGCGTGGTCGTA
VEGFR2	CCAGCAAAAGCAGGGAGTCTGT	TGTCTGTGTCATCGGAGTGATATCC
VEGFR3	CCCGAGAGCATCTTTGATAAGGTGT	CCATCCCGCTGTCTGTCTGGTTATC
Vimentin	AGTCCACTGAGTACCGGAGAC	CATTTCACGCATCTGGCGTTC
TNF-α	CACCATGAGCACTGAAAGCATGATCC	GTTCGTCCTCCTCACAGGGCAATGAT

2.2 Cell lines and culture conditions

The cell lines pertaining to human breast cancer, such as MCF7, MDA-MB-231 and MDA-MB-468, and the human embryonic kidney cell line, HEK293 were purchased from National Centre for Cell Science, Pune, India. Following which, they were cultured in the Dulbecco's Modified Eagle's Medium–high glucose supplemented with L-glutamine, Sodium pyruvate (Sigma Aldrich, St. Louis, USA), 10% Fetal Bovine serum (Thermo Fisher Scientific, Waltham, USA), Sodium bicarbonate (Sigma-Aldrich), along with 100 U/ml Penicillin and 100 µg/ml Streptomycin (Thermo Fisher Scientific). The cells were maintained at 37 °C in humidified air comprising 5% Carbon-dioxide.

2.3 Methods (*In-silico* Analysis)

2.3.1 Expression analysis

The expression profile of the desired proteins was extracted from The Cancer Genome Atlas (TCGA) database, using the UALCAN portal (http://ualcan.path.uab.edu/). The protein expression among the major subtypes of breast carcinomas was obtained from the Clinical Proteomic Tumour Analysis Consortium (CPTAC) database. Also, the mRNA expression was retrieved from the TCGA database, which utilizes the 'Breast cancer gene- expression miner' (bc-GenExMiner) to analyze the mRNA expression difference between different tumours from the TCGA database. Moreover, the role of the proteins on the clinical outcome of TNBC patients was also evaluated using the Gene Expression Profiling Interactive Analysis 2 (GEPIA 2) portal.

2.3.2 Functional network construction

The interconnection between the functions of the two proteases was established via the Search Tool for the Retrieval of Interacting Genes, (STRING) v9.1 database (https://string-db.org) [79]. It endows the protein-protein interaction network derived from high throughput experimental data, followed by literature and database mining. In this study, the desired proteins for *Homo sapiens* were queried, keeping the confidence score of 0.9, along with the first shell of interacting proteins. Further Gene Ontology analysis was performed using the WEB-based Gene SeT Analysis Toolkit, the WebGestalt (http://bioinfo.vanderbilt.edu/webgestalt/).

2.3.3 Preparation of the proteins and ligands for docking

The 3D coordinates of the target proteins were downloaded in the PDB format from the RCSB PDB database (https://www.rcsb.org/). Following this, the water molecules, ions and small molecules were removed, using PyMol 2.3 (Schrodinger, LLC. 2010. The PyMOL Molecular Graphics System, Version 2.3.). DEPTH server (http://cospi.iiserpune.ac.in/depth/) was used to predict the active site residues of the respective proteins.

Subsequently, hydrogen atoms and charges were added to the respective PDB structures and the atom types werechanged to AD4, using Autodock4. The structures were then saved in pdbqt format and were further used for docking studies.

The potent binding partner for the target proteins was predicted using Autodock Vina 1.1.2, which considers the proteins as rigid and ligands as flexible during the screening process [80]. Here, the grid box was set to the desiredsize. Moreover, the interactions of the drug with target proteins were visualized and the images were obtained using PyMol 2.3 and Discovery studio Visualizer v20.1.0.19195.

2.3.4 Molecular dynamic (MD) simulation

The dynamic behaviours of biomolecules such as proteins, nucleic acids and lipids in solvent-rich environments have been successfully studied for over a decade by using several molecular dynamics simulation methods. In this study, dynamic simulation of the target protein and its selected drug complexes are studied in a water-rich and membrane environment.

2.3.4.1 MD simulation in water

MD simulation of protein and drug complexes in water was carried out using GROMACS 2019.6 and CHARMM27 force field [81]. The topology files of the docked drug molecules were obtained from the server PRODRG2 (http://davapc1.bioch.dundee.ac.uk/cgi-bin/prodrg/). The protein and drug complexes were prepared for the MD simulation by following Justin's GROMACS tutorial [82]. A dodecahedron box was generated and protein-drug complexes were positioned at a distance of 1.0 nm from the edge of the box. Then TACE-drug complex system was solvated with a TIP3P water model and neutralized with Na+ ions and Cl ions using the "genion" module of GROMACS. The energy of the system was minimized up to 10 kJ/mol using the steepest descent algorithm, and then, the canonical ensemble (NVT equilibration) was carried out for 100 ps with a velocity-rescale thermostat with the reference temperature of 300 K. Followed by the canonical ensemble, isobaric isothermal ensemble (NPT equilibration) was carried out with 1 atm reference pressure, using Berendsen pressure coupling over 100 ps. The final MD run was carried out for 100 ns and the root means square deviation (RMSD), root means square fluctuations (RMSF), H-bond, and pair distance of protein-drug complexes were calculated from each MD simulation trajectory.

2.3.4.2 MD simulation in membrane

Protein in membrane simulation was also carried out in GROMACS 2019.6 and CHARMM27 force field [81]. The input files for GROMACS were generated using CHARMM-GUI (https://www.charmm-gui.org/) server. The membrane composition used for simulation was 72 molecules of cholesterol, 74 molecules of POPE (1-palmitoyl-2-oleoyl-snglycero-3-phosphatidylethanolamine), 67 molecules of PSM (Palmitoyl sphingomyelin) in the upper leaflet and 73 molecules of cholesterol, 75 molecules of POPE, 68 molecules of PSM in the lower leaflet to mimic the mammalian cell membrane.

The membrane molecules were built around the γ-secretase protein-ligand complex using CHARMM-GUI. The system was added with water molecules and neutralized with K+ and Cl^- ions. The input files were downloaded from CHARMM-GUI in GROMACS format. Energy minimization, equilibration and MD runs were carried out as mentioned in the MD simulation in water protocol. The final MD runwas carried out up to 100 ns with 2 femtosecond time steps.

2.3.5 Binding free energy of the protein-ligand interaction

Molecular Mechanics Poisson-Boltzmann Surface Area (MM-PBSA) is a well-established method to predict thebinding free energies of the target protein-drug complexes from MD trajectories. Binding free energy simulationwas carried out using g_mmpbsa GROMACS function with 1 ns time interval for 100 ns MD trajectory [83]. ΔG_{bind} (Binding free energy) of drug molecules with target proteins were calculated using the following equation:

$$\Delta G_{bind} = \Delta EEMM + \Delta GPBSA - T\Delta SMM$$

Where, ΔG_{bind} is the average binding free energy of the protein-drug complex, ΔEMM denotes the average molecular mechanics' energy, ΔGPBSA represents the solvation-free energy, and TΔSMM represents the solute configuration entropy [84].

2.4 Methods (*In-vitro* Analysis)

2.4.1 Generation of spheroids

The spheroids of MDA-MB-231 and MDA-MB-468 were generated using a forced flotation method. The cells were cultured up to confluency in a 60 mm dish and harvested. Simultaneously, the 96-well plates were coated with agarose (1.5% w/v) containing serum-free DMEM. The cells were then seeded on it at a density of 20 x 10^4 cells/well, following which the plates were centrifuged at 750 rcf for 10 minutes. The plates were then incubated at 37 °C in humidified conditions with 5% CO2 for 96 hours. The resulting spheroids were visually monitored with a Nikon Eclipse Ti microscope and used for subsequent experiments.

2.4.2 Induction of EMT

For induction of EMT, the cells were trypsinized, counted and seeded in appropriate numbers in 6-well plates or 60 mm dishes. Cells were then allowed to attach for 24 hours in a complete media containing 10% FBS. After attachment, the cells were maintained in 0.5% serum media for 12 hours and subsequently treated with 20 ng/mlconcentration of EGF, 30 minutes prior to the desired drug treatments.

2.4.3 Cell viability assay

In order to assess the therapeutic potential of the drugs and/or inhibitors alone or in combination therapy, the percentage of viability was assessed following treatment, using either alamarBlue or MTT.

The cell viability for the monolayer culture was evaluated using [3-(4,5-dimethylthiazol-2-yl)-2,5-diphenyltetrazolium-bromide] MTT assay (HiMedia), whereby the tetrazolium salt is reduced to purple-coloured formazan by the respiring mitochondria of the living cells. A total of 7000 cells/well was seeded in a 96-well plate, following which the dose-dependent cell viability of the drugs in singlet as well as in combination was assessed. After 48 hours of treatment, 5µl of MTT was directly added to the wells and was incubated for 2 hours at 37 °C under humidified conditions with 5% CO2. The percentage cell viability was calculated upon taking the absorbance of the formazan crystals dissolved in DMSO at 570 nm, whereas the background measurement was normalized at 630 nm using a microplate reader (Thermo Fisher Scientific).

Similarly, the cell viability for the spheroids was assessed using the alamarBlue assay, wherein, the active ingredient in the alamarBlue, Resazurin is reduced to resorufin upon entering into the living cells. Following treatment for 96 hours in 96-well plates, 20 µl of alarm blue was directly added into the wells and incubated for 4 hours at 37 °C under humidified conditions with 5% CO2. After this, absorbance was measured at 570 nm, along with a reference of 600 nm using a microplate reader (Thermo Fisher Scientific).

Moreover, the data was normalized by taking the viability of the untreated cells as 100%. The cell viability was then determined using the formula:

$$Cell\ viability\ \% = \frac{[(Abs\ 570 - Abs\ 630)\ treated\ cells]}{[(Abs\ 570 - Abs\ 630)\ control\ cells]} * 100$$

The inhibitory concentration, IC50 values were determined from the sigmoidal dose-response curves, using the GraphPad Prism. (Version 6.0.0 for Windows, GraphPad Software, San Diego, California USA, www.graphpad.com).

2.4.4 Determination of drug synergism

The combined effect of the drugs was determined by analyzing the Chou-Talay combination index (CI) using Calcusyn software (Biosoft). It is a widely accepted tool in the field of combination therapy research, playing a crucial role in evaluating the effectiveness of mixed drug treatments in various diseases, including cancer and AIDS. It's automated calculations and analysis capabilities make it a valuable asset in the pursuit of improved treatment strategies and personalized medicine.

A CI value obtained post-analysis determines the synergistic, additive or antagonistic effects of the drugs in combination. For example, a value less than 1 indicates synergy, a value of 1 indicates additivity and a value greater than 1 indicates antagonism. CalcuSyn can also calculate the dose reduction index (DRI), which indicates the extent to which the dose of each drug can be reduced in a combination therapy while maintaining the same level of efficacy.

2.4.5 Cell cycle analysis

To analyze the effect of the drugs in mono therapy as well as in combination therapy on the cell cycle progression of the malignant cell lines, propidium iodide (PI) based flow cytometric analysis was performed. Cells were seeded at a density of 1 x 10^5 cells per wells in a 6-well plate and were allowed to attach for 12 hours. The cells were then synchronized prior to the drug treatment by serum starvation for a time period of 24 h. Subsequently, treatment was carried on for 48 h, following which the cells were trypsinized, and resuspended in 70% chilled ethanol dropwise. The fixed cells were stored at -20 °C until further analysis as per the protocol of Richardi *et al.* [85]. Briefly, cells were washed with chilled PBS and incubated with RNAse for 1 h at 55 °C. The cells were thenstained with PI and incubated on ice in the dark until further analysis. The samples were analyzed using the BD FacsCalibur, and the collected data were analyzed using the FCS Express software.

2.4.6 Detection of the reactive oxygen species (ROS)

The cellular ROS generation following treatments was analyzed using 2',7'-dichlorofluorescein diacetate (DCFDA) dye. DCFDA is a cell-permeant reagent, which is oxidized to DCF (2',7'-dichlorofluorescin) in the presence of hydroxyl, peroxyl and other ROS activities within the cells. The DCF exhibits a green fluorescence, which is analyzed using a flow cytometer.

Following 6 h treatment with the inhibitors alone and in combinations, cells were incubated with 5 µM of DCFDA for 30 minutes. The cells were then trypsinized, washed in PBS thrice and resuspended in 500 µl of PBS. The cells were then analyzed in the FITC channel using the CytoFLEX flow cytometer (Beckman Coulter).

2.4.7 Detection of the mitochondrial membrane potential

Mitochondrial membrane potential was determined using the JC-1 (5,5',6,6'-tetrachloro-1,1',3,3'-tetraethylbenzimi-diazolylcarbocyanine iodide) dye. JC-1, a cyanine dye, forms red aggregates in the polarized mitochondria, while it remains as a monomer in depolarized mitochondria [86]. After subsequent treatment for 48 h, the cells are stained with 10 µM of JC-1 dye and incubated for 20 minutes. For positive control, cells were incubated with 50 µM of CCCP (carbonyl cyanide 3-chlorophenylhydrazone) for 30 minutes along with the JC-1 dye. After incubation, the cells are trypsinized and washed with PBS extensively.

Finally, the cells were resuspended in 500 µl PBS and analyzed using a CytoFLEX flow cytometer (Beckman Coulter). The fluorescence intensities were collected in the red and green channels. However, the positive and negative controls were used to detect the depolarised population and for fluorescence compensation.

2.4.8 Determination of apoptotic and/or necrotic cells

The FITC Annexin-V apoptosis detection kit was used to detect and thereby differentiate among the early apoptotic, late apoptotic and necrotic cell populations. Subsequent to the treatment for 48 hours, cells were trypsinized, washed with chilled PBS and processed according to the manufacturer's protocol. The fluorescence data were collected in the green (FL1) and red (FL2) channels using a CytoFLEX flow cytometer (Beckman Coulter). Furthermore, the data analysis and fluorescence compensation were performed using CytExpert software.

2.4.9 Immunofluorescence flow cytometry

Following treatment, cells were washed with PBS, fixed with 4% formaldehyde and washed extensively with PBS. The cells are then resuspended in 1X PBS. Cells are then permeabilized by the addition of 100 % chilled methanol dropwise to the prechilled cells, while gently vertexing to a final concentration of 90 % methanol. Following fixation and permeabilization, cells were washed in PBS thrice to ensure the removal of methanol. Further, cells were resuspended in 100 µl of diluted primary antibody, prepared in antibody dilution buffer and incubated overnight at 4 °C. Cells are then washed thrice with antibody dilution buffer and resuspended in 100 µl of diluted fluorochrome-conjugated secondary antibody. After 2 h of incubation at room temperature, cells were washed thrice with antibody dilution buffer and resuspended in 500 µl of it. Following this, the cells were analyzed using a CytoFLEX flow cytometer (Beckman Coulter).

2.4.10 Live and dead cell analysis by Calcein-AM/Propidium Iodide (PI) staining

To estimate the live and dead cell populations following treatment, cells were stained with Calcein-AM and PI. Calcein-AM is a cell-permeant non-fluorescent dye, which upon entering the healthy cells is converted to Calcein,which has a characteristic green fluorescence. This is attributed to the acetoxymethyl ester hydrolysis by the intracellular esterase. On the other hand, PI is a non-permeant agent, which intercalates to the DNA of the dead cells thereby giving red fluorescence. For visualizing the live-dead cell populations, monolayer cultures were treated for 48 h, while the spheroids were treated for 72 hours. Cells were then trypsinized and carefully washed with PBS thrice. Furthermore, cells were treated with (2 µM) Calcein AM and (4 µM) PI solution and was incubated in dark for 30 minutes. Following incubation, cells were washed thrice with PBS and imaged using a Zeiss LSM 880 confocal microscope in conjunction with Z-stacking analysis.

2.4.11 Immunocytochemistry

Following treatment, the cells were washed thrice with PBS and were fixed with 4% formaldehyde at room temperature for 15 minutes. The cells were then immersed in a blocking buffer for 2 h and subsequently incubatedovernight at 4 °C with primary antibodies. The cells were washed with PBST, and incubated with a fluorochrome-conjugated secondary antibody for 2 h at room temperature in the dark. After three washes, Alexa Flour® 555 Phalloidin diluted in PBS was added and incubated with DAPI (1 µM) for 5 minutes. Moreover, the cells were rewashed thrice with PBST and imaging was performed using a Zeiss LSM 880 confocal microscope.

2.4.12 RNA isolation and Gene expression analysis

After treatment for 48 h, the total RNA from the cells was extracted using a Tri reagent. 1 µg of RNA was subjected to reverse transcription using an iScript cDNA synthesis kit (BioRad) according to the manufacturer's protocol. Amplification of the gene of interest was performed using a PowerUp™ SYBR™ Green Master mix (Applied Biosystems) and a Rotor-Gene Q (Qiagen) real-time PCR cycler. The data obtained were normalized to β-actin orGAPDH (glyceraldehyde-3-phosphate dehydrogenase). Furthermore, the normalized data were quantified using the delta-delta CT method [87]. The obtained quantitative RT-PCR (qRT-PCR) data were analyzed by the LinReg PCR software.

2.4.13 Immunoblotting

Following treatment, total proteins were extracted from the cells using RIPA lysis buffer, supplemented with a protease inhibitor cocktail, sodium orthovanadate, sodium fluoride, phenylmethylsulphonyl fluoride (PMSF) and0.5M EDTA. Proteins from each sample were quantified using the bicinchoninic acid (BCA) protein assay kit. An equal amount of each sample was subjected to SDS-PAGE, following which the proteins were transferred onto a PVDF-nitrocellulose membrane. The membranes were then blocked using a blocking buffer (4% BSA in TBST) and incubated overnight with primary antibodies at 4 °C. Following this, the blots were extensively washed using TBST. They were then incubated with HRP-conjugated secondary antibodies for a period of 2 h at room temperature. Further, blots were rewashed extensively with TBST. Signals were developed using a chemiluminescent reagent, and images were acquired using ChemiDoc (BioRad). The images were quantified using ImageJ software (Fiji). Finally, the data obtained were normalized to β-actin and protein expression data were analyzed.

2.4.14 Determination of migration potential

Migration potential was assessed using a scratch wound-healing assay, where the migration rate of the cells towards the wounded area (created a scratch using a microtip) was determined. The scratch wound healing assay was performed using a protocol described by Wu *et al.* [88]. Briefly, cells were grown to 70-80% confluence incomplete DMEM media, which was replaced with 0.5% serum media for 24 h.

A scratch or wound was created using a sterile pipette tip. The wounded monolayers were washed with PBS to remove cell debris. Further, the cells were treated with the respective drugs and their combination, and were incubated at 37 °C under humidified conditions and 5% CO_2 for a period of 18 h. the images of the scratch before and after treatment were captured using a Nikon Eclipse Ti microscope and analyzed using ImageJ software.

2.4.15 Matrigel invasion assay

Matrigel invasion assay was performed to detect the alterations of invasiveness of cells, following the methods described by Chen *et al.* [89]. Initially, the upper chamber of the trans well inserts was coated with diluted Matrigel (1mg/ml in serum-free medium) and incubated at 37 °C overnight for solidification. In the upper chamber, treated cells were seeded at a density of 2 x 10^5 in serum-free media, while the lower chambers were filled with 750 µl of 10% serum media. Following incubation of 24 h, the upper side of the chamber was then carefully wiped, using a wet swab to remove the non-migrated cells and washed thrice with PBS. To fix the migrated cells, the lower part of the chamber was incubated with 4% formaldehyde at 37 °C for 15 minutes. After fixation, the cells were washed thrice with PBS and subsequently stained with DAPI (1 µM). Finally, cells were rewashed thrice in PBS and visualized using Zeiss LSM 880 confocal microscope.

DAPI binds to the minor groove of the double-stranded DNA, hence preventing the non-specific staining of the membrane of the trans-well inserts. Thus, the fold change in the fluorescence intensity of DAPI represents the alteration of invasive potential.

2.4.16 Colony formation assay

The colony formation assay was performed using the protocol described by Crowley *et al.* [90]. Briefly, cells wereseeded in a 6-well plate at a density of 2 x 10^5 and were treated with the inhibitors and drugs singularly and in combination for a period of 48 h. Following treatment, cells were washed with PBS, trypsinized and resuspendedin serum media supplemented with 10% FBS. The cells were counted and plated at a density of 5 x 10^2 cells per well in a 6-well plate for a period of 14 days at 37 °C in humidified conditions with 5% CO_2. It is ensured that the media was replaced after every 3 days. After the subsequent formation of colonies comprising >50 cells, the colonies were washed with PBS, fixed with 100% methanol for 20 minutes and stained with 0.5% crystal violet solution for a period of 1 hour. The stained colonies were washed with excess water and dried overnight. The colonies were then visualized and counted.

2.4.17 Spheroid formation assay

Following treatment with the respective inhibitors alone and in combination, the spheroids of the desired cell lineswere generated. Briefly, cells were seeded at a density of 2.0 ×10^6 per well in a 6-well plate.

After 24 h, cells weretreated with the respective inhibitors for a time period of 48 h, following which cells were trypsinized, counted and seeded at a density of 10^4 cells/ well, in an agarose-coated 96-well plate. The cells were then centrifuged at 700 rcf for 15 minutes and incubated at 37 °C in a humidified atmosphere containing 5% CO2 for a period of 96 h. After 96 h, the cells were visually monitored and images were obtained with Zeiss LSM 880 confocal microscopy.

2.4.18 HDAC activity assay

The HDAC inhibition was estimated using the fluorometric HDAC activity assay kit (Sigma). Briefly, cells wereseeded at a density of $2x10^6$, following which they were subsequently treated with respective inhibitors alone or in combination. After treatment, cells were lysed with lysis buffer (50 mM HEPES, 150 mM NaCl and 0.1% Triton X-100 supplemented with a protease inhibitor cocktail). The obtained cell lysates were sonicated and further experiment was performed as per the manufacturer's protocol. For measuring the luminescence intensity, the Tecan plate reader (Infinite 200 PRO, Tecan, Switzerland) was used with λex = 350 nm and λem = 440 nm.

2.4.19 Statistical analysis

All the statistical analysis were carried out using the GraphPad Prism software. Based on three independent experiments, the data are expressed as mean ± SEM. Additionally, the one-way and two-way ANOVA test was used to access the correlations among the groups. A p-value < 0.05 (*) is considered to be statistically significant, where (*) $p < 0.05$,(**) $p < 0.01$, (***) $p < 0.001$ and (****) $p < 0.0001$ are considered to be highly significant.

Section 3

Results and Discussions

3.1. *In-silico* evidence of ADAM metalloproteinase pathology in cancer signalling networks.

- ***Journal of Biomolecular Structure and Dynamics,*** 2021, 1-16.
DOI: 10.1080/07391102.2021.1964602
[Taylor & Francis publishing group]

Results and Discussions

Abstract

Lack of effective targeted therapies often contributes to poor clinical outcomes of aggressive malignancies associated with drug resistance, angiogenesis and metastasis. Literature mining portrays the major role of ADAM17 in cancer and inflammatory diseases. However, it is quite challenging to design a candidate drug for targeting ADAM17 due to its structural similarity with the catalytic domain of the matrix metalloproteases (MMPs). The present study reports the protein-protein interaction analysis of ADAM17, along with the molecular docking and MD simulation studies for the screened compounds. The analysis confirms the association of ADAM17 with numerous oncogenes that facilitate cancer progression and inflammation, especially the members of the Notch, receptor tyrosine kinase (RTK) and TNFα pathways. The outcome provides evidence that the prevalent protease ADAM17 could attribute to cancer signalling regulation though the shedding of various inflammatory and oncogenic molecules. Moreover, the analogues of the existing inhibitors were further exploited, with the aim of discovering a potent molecule, which could be repurposed as a drug against ADAM17-inflicted cancer progression. Upon stringent screening, two specific compounds (I6 and I9; analogues of IK862, a type of y-lactam hydroxamates) were chosen, possessing the lowest binding energy (–9.1 Kcal/mol), stable MD-simulation studies and superior pharmacodynamic properties. The current information illustrates the avenue to persuade further research on targeting ADAM17 with small molecular compounds (I6 and I9) in cancer therapeutics.

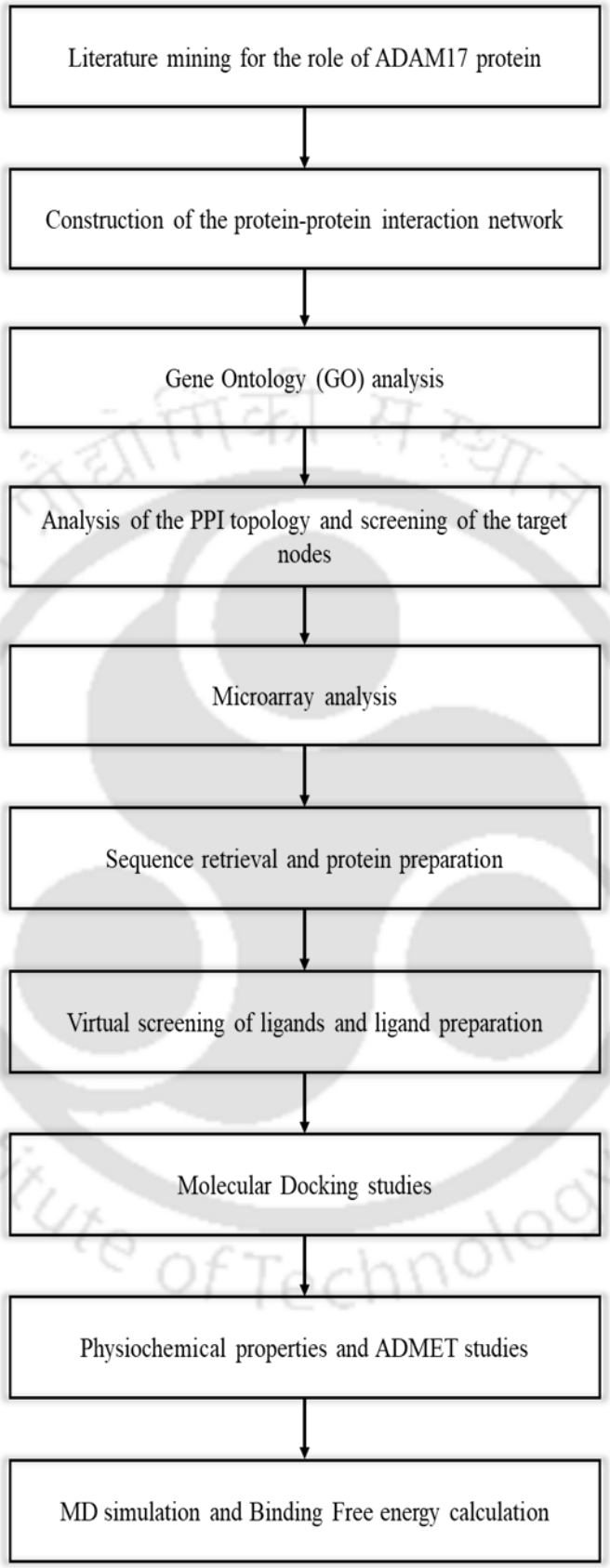

Figure 3.1.1: *Flow chart depicting the methodologies (in brief)*

3.1.1. Functional network of ADAM17 protein

The protein-protein interacting network derived using the STRING database provided a network comprising 58 nodes. The highly connected protein interactions were observed at the centre connecting the ADAM17 proteins **(Figure 3.1.1)**. To infer a better understanding of the interactions, the network was divided into 5 clusters using the k-means clustering algorithm **(Figure 3.1.2)**. It is observedthat the clusters are composed of densely connected protein interactors that mostly shared similar functions or occurrences in one or more pathways.

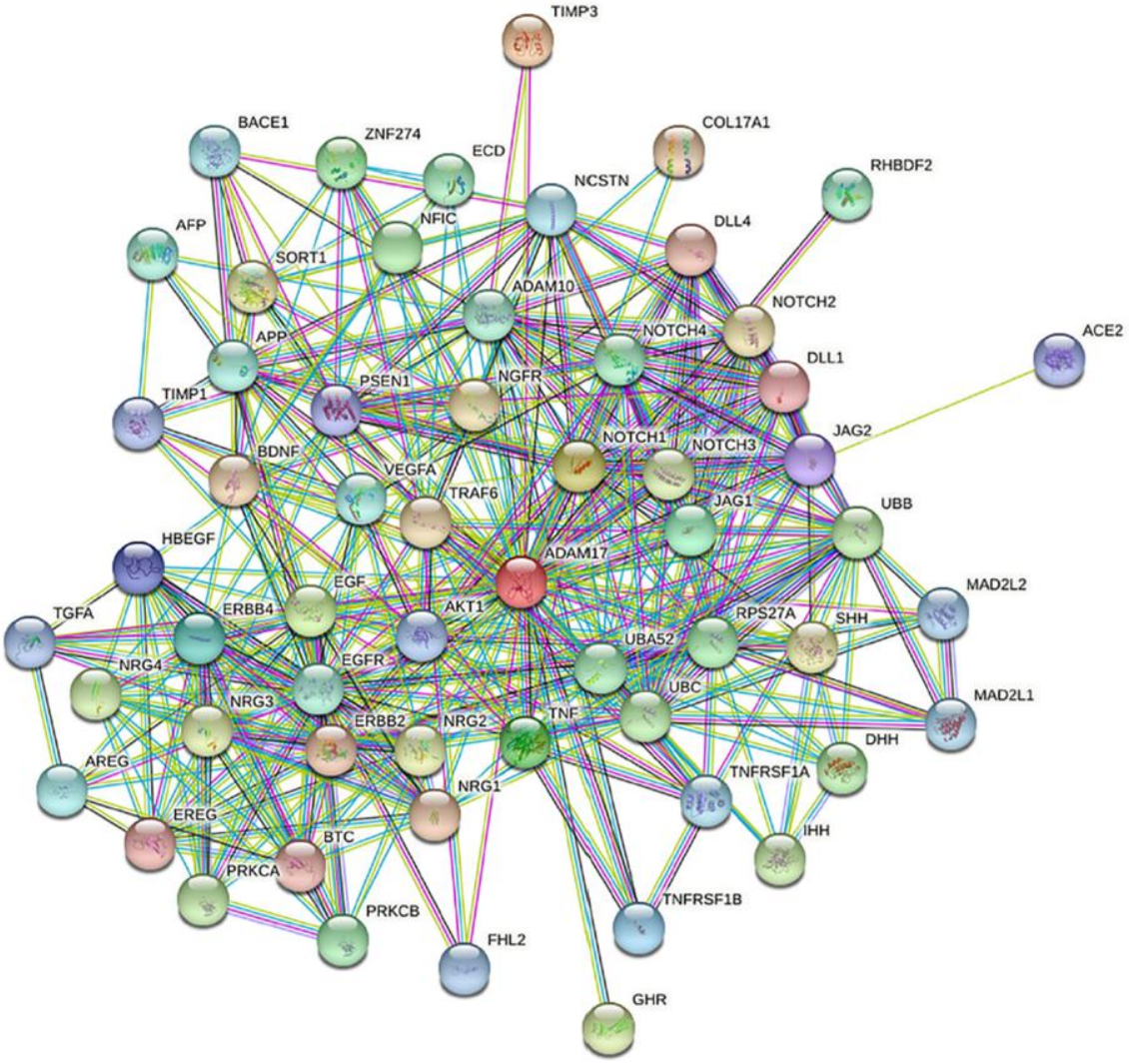

Figure 3.1.2: *STRINGS depicting the ADAM17 network. Briefly, ADAM17 for Homo Sapiens was fed as the query molecule. The interacting network was restricted to the first shell, with a confidence score of 0.7 that is indicated to be of significant reliability.*

The clusters represent the various sub-pathways associated with the ADAM17 protein, which are closely connected to each other and exhibit greater interactions. Moreover, some of the components ofa particular cluster have established functions in common pathways.

From amongst the 5 clusters, Cluster 1 mostly comprises the components of the γ-secretase enzyme NCSTN (Nicastrin) and PSEN1 (Presenilin); components of the TNF receptor superfamily such as NGFR (Tumours necrosis factor receptor superfamily member 16); a U3 Ubiquitin ligase TRAF6 (TNF receptor-associated factor 6), Ubiquitin such as UBB (Polyubiquitin B), RPS27A (Ubiquitin-40S ribosomal protein S27a), UBA52 (Ubiquitin-60S ribosomal protein L40), UBC (Polyubiquitin-C) and some other proteins like ZNF274 (Neurotrophin receptor-interacting factor homolog), a neurotrophic factor BDNF (Brain-derived neurotrophic factor), ECD (Protein ecdysoneless homolog), FHL2 (Four and a half LIM domains protein 2) and AKT1 (RAC-alpha serine/threonine-protein kinase).

Cluster 2 represents the components of the Notch pathway, a developmental pathway associated with various cellular processes such as proliferation, cell fate determination, regulation of metabolism, etc. This cluster comprises the Notch signalling molecules such as the ligands DLL1 (delta-like ligand1), DLL4 (delta-like ligand 4) and JAG2 (Jagged2), the extracellular Notch receptors NOTCH1, NOTCH2, NOTCH3 and NOTCH4 and the cleavage protease, ADAM10. Besides, some other molecules such as APP (amyloid precursor protein), BACE1 (beta-secretase 1) that is responsible for the proteolytic processing of the APP; AFP (α-fetoprotein) and COL17A1 (collagen-α-1(XVII) chain) are also found to be associated in close conjunction within the cluster 1.

Cluster 3 comprises the EGF signalling molecules such as the ligands [EGF (pro-epidermal growth factor), HBEGF (heparin-binding EGF-like growth factor), VEGFA (vascular endothelial growth factor A), AREG (amphiregulin), TGFA (transforming growth factor-alpha), BTC (betacellulin)], along with the receptor tyrosine kinases such as EGFR (epidermal growth factor receptor), and ERBB2 (Receptor tyrosine-protein kinase erbB-2). It also contains neuregulins such as NRG1, NRG2, NRG3 and NRG4, protein kinase C family proteins such as PRKCA (Protein kinase C alpha type) and PRKCB (Protein kinase C beta type), along with TIMP1 (metalloproteinase inhibitor 1).

Cluster 4 comprise ligand of the hedgehog pathway such as DHH (desert hedgehog protein), SHH (sonic hedgehog protein) and IHH (Indian hedgehog protein). They transduce the hedgehog signalling pathway upon binding to the PTC (patched) receptor proteins, thereby facilitating various patterning events during development. It also consists of the TNFR (tumour necrosis factor receptor), along with the adaptor proteins MAD2L1 (Mitotic spindle assembly checkpoint protein MAD2A) and MAD2L2 (Mitotic spindle assembly checkpoint protein MAD2B). Some other protein components include the Notch ligand JAG1 (Jagged1); RHBDF (Inactive rhomboid protein 2), a rhomboid protease-like protein that regulates the secretion of several ligands of the EGFR; receptor protein like the GHR (growth hormone receptor), ERBB4 (Receptor tyrosine-protein kinase erbB-4), along with EREG (Pro-

epiregulin) a ligand of EGFR and ERBB4, which stimulates tyrosine phosphorylation; SORT (Sortilin) that functions as a sorting receptor in the Golgi compartment and as a clearance receptor on the cell surface; followed by ACE2 (Angiotensin-converting enzyme 2); ADAM protease (ADAM 17) and TIMP3 (Metalloproteinase inhibitor 3).

Cluster 5 is composed of the proteins of the TNF signalling pathway such as the TNF (Tumour necrosis factor) ligand, TNFRSF1A (Tumour necrosis factor receptor superfamily member 1 A), TNFRSF1B (Tumour necrosis factor receptor superfamily member 1B), which plays a crucial role in various physiological and pathological processes.

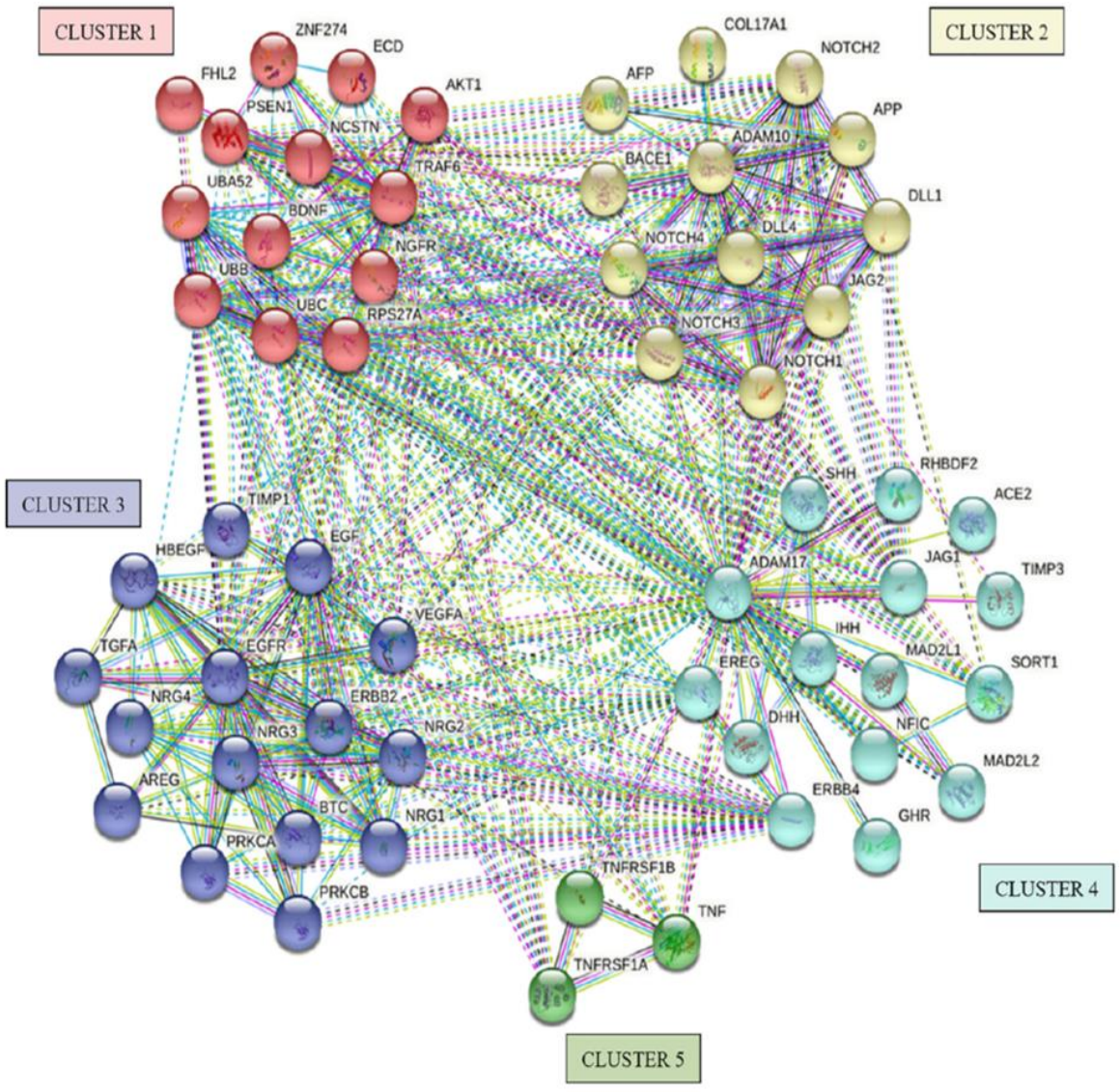

Figure 3.1.3: *Cluster of networks associated with ADAM17 protein, to obtain a better understanding of ADAM17 along with its interactors. Obtained using k-means clustering algorithm in STRINGS v9.1 database.*

Table 3.1.1: *The important pathways identified through the KEGG pathway enrichment analysis*

Pathways	Number of protein interactors	Enrichment ratio
Notch signalling pathway	11	30.296
ERBB signalling pathway	16	24.885
EGFR tyrosine kinase inhibitor resistance	10	16.734
Endocrine resistance	12	16.188
Non-small cell lung cancer	7	14.021
Breast cancer	12	10.792
Micro RNAs in cancer	10	8.8133
Proteoglycans in cancer	12	8.0121
MAPK signalling pathway	16	7.1702
Pathways in cancer	18	4.5412

3.1.2. Gene ontology analysis

The gene ontology analysis was performed to obtain a hierarchical classification of the ADAM17-associated genes and gene products. Some of the most important biological processes in which these proteins participate include the signalling pathways that assist in the progression of various malignancies such as the Notch, ERBB and TNFα pathways. Also, KEGG pathway enrichment analysis revealed the involvement of these proteins in numerous signalling pathways, the most important being the Notch signalling pathway with an enrichment ratio of 30.296 **(Table 3.1.1)**. Additionally, upon querying the implication of these genes into DisGenet, a repository of gene-disease association, provided by the Web Gestalt, it is observed that the genes facilitate many disorders **(Figure 3.1.4)** such as pancreatic ductal carcinoma, glioblastoma along with Alzheimer's and depression.

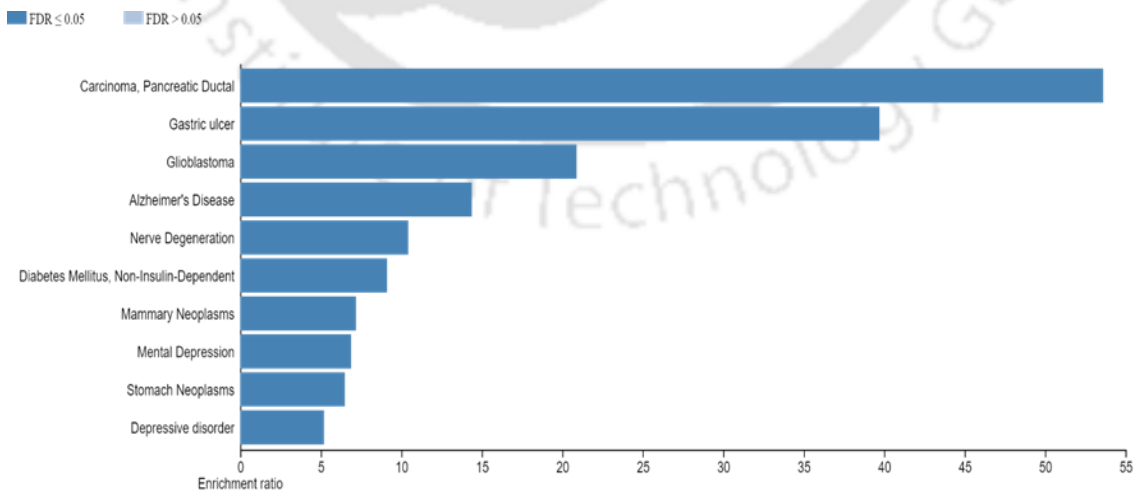

Figure 3.1.4: *Graph depicting the gene-disease association (using Web Gestalt)*

3.1.3. Screening of the target nodes

Analysis of the network revealed that the ADAM17 protein lies in the central hub of the pathway comprising 58 primary nodes. The number of edges is 402, which sums up the average number of neighbours to be around 13.862. The clustering coefficient, measuring the cluster-forming ability of a particular node, was found to be 0.693, indicating that the network is highly significant.

It is evident that some of the genes have greater and stronger interaction with each other, which might result in a significant outcome upon targeting ADAM17 in multiple malignancies. The top 21 genes obtained from centrality analysis were further analyzed for their expression profile in various cancer subtypes, using the Oncomine database **(Table 3.1.2)**.

The Oncomine database calculates the gene rank of an individual gene based on its p-value. To ensure a significant difference in the expression profiles of genes in malignant versus normal cells, only those genes were considered, which exhibited a cumulative gene ranking above 20%. Most of the overexpressed genes are known to facilitate cell cycle progression, proliferation, cell survival and transcriptional regulation. Furthermore, upon examining the role of these genes in breast cancer, we found out that some of them had previously been established in having a predominant role in the progression of breast cancer. For example, ADAM10 promotes invasion and cancer progression [91]. Notch along with its ligand Jagged facilitates poor prognosis in breast cancer patients [92], ERBB receptors positively correlate with breast cancer progression [93], etc. Therefore, it is expected that targeting ADAM17 in breast cancer samples (*in-vitro* and *in-vivo*) might provide some positive outcomes.

Table 3.1.2: *Microarray expression analysis of the genes in cancer versus normal cells*

Gene	Over-expression in various cancers					Over-expression in breast cancer				
	p-value	Fold change	Ranking %	Cancer Type	Groups	p-value	Fold change	Ranking %	Cancer Type	Group
ADAM17	8.80E-07	2.054	1	Gastric Cancer	Wang Gastric	1.94E-10	1.781	13	Invasive Breast Carcinoma Stroma	Finak Breast
EGF	1.98E-09	2.94	2	Colon Carcinoma	Skrzypczak Colorectal 2	0.199	1.097	14	Invasive Papillary Breast Carcinoma	TCGA Breast 2
EGFR	2.31E-10	4.438	1	Clear Cell Sarcoma Of The Kidney	Cutcliffe Renal	1.66E-06	2.921	4	Ductal Breast Carcinoma	Richardson Breast 2
UBA52	4.53E-08	2.608	1	Follicular Lymphoma	Brune Lymphoma	8.81E-17	1.288	9	Invasive Ductal And Invasive Lobular Breast Carcinoma	Curtis Breast

RPS27A	8.94E-10	2.48	1	Diffuse Large B-Cell Lymphoma	Brune Lymphoma	5.40E-02	3.859	10	Invasive Lobular Breast Carcinoma	Turashvili Breast
UBB	5.38E-08	2.725	1	Hodkin's Lymphoma	Brune Lymphoma	3.75E-14	1.284	12	Invasive Ductal And Invasive Lobular Breast Carcinoma	Curtis Breast
UBC	3.01E-12	2.834	2	Hairy Cell Leukemia	Basso Lymphoma	1.30E-16	1.265	9	Invasive Ductal And Invasive Lobular Breast Carcinoma	Curtis Breast
ADAM10	1.07E-12	35.428	1	Ovarian Serous Surface Papillary Carcinoma	Welsh Ovarian	0.003	1.511	6	Invasive Ductal Breast Carcinoma Stroma	Karnoub Breast
NOTCH1	1.53E-08	4.231	2	T-Cell Acute Lymphoblastic Leukemia (Childhood)	Coustan-Smith Leukemia	0.022	1.418	5	Invasive Lobular Breast Carcinoma	Turashvili Breast
ERBB2	8.89E-07	5.166	1	Meningioma	Watson Brain	8.00E-05	2.056	4	Invasive Breast Carcinoma	Gluck Breast
PSEN1	4.14E-10	19.673	2	Classic Medulloblastoma	Pomeroy Brain	4.68E-13	1.801	1	Invasive Ductal Breast Carcinoma	Zhao Breast
TRAF6	3.27E-11	4.003	3	Papillary Renal Cell Carcinoma	Jones Renal	0.293	1.117	37	Lobular Breast Carcinoma	Perou Breast
NRG2	2.37E-05	14.582	3	Esophageal Adenocarcinoma	Hao Esophagus	1.13E-08	1.063	9	Invasive Lobular Breast Carcinoma	TCGA Breast 2
ERBB4	1.27E-10	2.415	1	Rectosigmoid Adenocarcinoma	TCGA Colorectal	6.51E-19	3.973	1	Intraductal Cribriform Breast Adenocarcinoma	TCGA Breast 2
NOTCH4	4.60E-06	2.145	1	Pancreatic Ductal Adenocarcinoma	Buchholz Pancreas	0.18	1.044	9	Invasive Ductal And Invasive Lobular Breast Carcinoma	TCGA Breast 2
BDNF	1.86E-06	3.653	3	Rectosigmoid Adenocarcinoma	TCGA Colorectal	1.93E-04	2.029	8	Lobular Breast Carcinoma	Zhao Breast
NRG1	3.42E-07	3.378	1	Superficial Bladder Cancer	Modlich Bladder	5.95E-17	2.242	4	Invasive Breast Cancer Stroma	Finak Breast
NCSTN	2.56E-06	2.78	1	Prostatic Epithelial Neoplasia Epithelia	Tomlins Prostrate	4.92E-134	1.278	1	Invasive Ductal Breast Carcinoma	TCGA Breast 2
NGFR	2.04E-07	7.394	2	Lee Brain Glioblastoma	Lee Brain	0.077	1.981	4	Invasive Papillary Breast Carcinoma	TCGA Breast 2
VEGFA	6.05E-14	12.5828	1	Teratoma	Korkola Seminoma	2.80E-06	2.598	5	Invasive Ductal Breast Carcinoma	Zhao Breast
TNF	0.015	1.14	17	Multiple Myeloma	Agnelli Myeloma 3	0.181	1.044	9	Invasive Ductal and Invasive Lobular Breast Carcinoma	TCGA Breast 2

3.1.4. Screening of ligands

Upon the establishment of the role of ADAM17 and its associated genes in various malignancies, the screening of inhibitors was performed to obtain a potent compound, having inhibitory action against ADAM17.

- **Prinomastat** belongs to the sulfonamide class of MMP inhibitors, which are tested in a number of phase II clinical trials for evaluating its effects on esophageal adenocarcinoma, metastatic melanoma and progressive breast cancer [94].
- **INBC7839** was selected, which has dual inhibitory properties against ADAM10 and ADAM17. It is currently being used in combination with Rituximab for the treatment of diffusive large B-cell non-Hodgkin lymphoma (NCT02141451). INBC7839 has also been used in combination with Trastuzumab in metastatic HER2-positive breast cancer patients [95].
- In order to reduce the potency of the inhibitors towards MMPs, the P10 and P20 groups of some compounds (such as **SPO57**) were conjugated to form a cyclic moiety. In SPO57, the isopropyl group has been used as the P10 moiety in the construction of the macrocyclic carbamate compound [96].
- Thiomorpholine sulphonamide hydroxamates bearing novel propargylic P1' groups are also reported as potent TACE inhibitors, such as **TMI-1**, possessing butynyloxy moiety at the P10 site. It is under Phase II clinical trials and is one of the best dual-acting compounds (for ADAM17, MMP-1, MMP-2 and MMP-13), exhibiting high activity in various *in vivo* models [97].
- **IK682**, a y-lactam hydroxamate, developed by the Bristol-Myers-Squibb, which possesses a (2-methyl quinolin-4-yl) methoxy group is 1000 times more selective towards ADAM17 over MMPs. Its bioavailability (32% in dogs and 41% in rats) and free fraction (3.6%) in human serum are relatively higher in comparison to other compounds of this class [98].
- **ZLDI8** is a potent ADAM17 inhibitor, besides being a competitive and irreversible lymphoid tyrosine phosphatase inhibitor. Treatment with ZLDI8 has been shown to disrupt the Notch signalling pathway significantly in hepatocellular carcinomas, along with EMT inhibition *in vitro* [99]. Also, ZLDI8 are known to enhance the susceptibility of HCC cells towards chemotherapeutic drugs such as Sorafenib, Paclitaxel and Etoposide [100].

Altogether, these compounds were chosen because of their enhanced potency in comparison to the other inhibitors of their class. Furthermore, the analogues of these six compounds were generated using the PubChem database, among which 50 of them were chosen depending on their favourable properties (such as molecular weight <500 g/mol; H-bond acceptor ≤ 8; H-bond donor ≤ 5, etc.).

3.1.5. Molecular docking studies

The ligand files were subjected to docking with the available crystal structure of the catalytic site of ADAM17, obtained from the PDB database. The inhibitor (INN) obtained from the 2I47-complex was kept as a reference for our docking studies in order to validate our results. The molecular docking was performed using AutoDock Vina, which provided us with 11 compounds having binding energies lesser than -9 Kcal/mol that was chosen for further studies (details provided in **Table 3.1.3**). The binding energies for the following compounds are mentioned in **Table 3.1.4**.

From the molecular docking studies, we obtain the binding energies for the reference compounds such as Prinomastat, IK862, ZLDI8, SPO57, INBC7839 and TMI-1 to be -7.5 kcal/mol, -7.8 kcal/mol, -8 kcal/mol, -7.6 kcal/mol, -7.9 kcal/mol, -7.8 kcal/mol, respectively. The binding energy obtained from the compound library is depicted as a heat map **(Figure 3.1.5)**. From the 2 D interaction profile, it is evident that the compounds S10, and S13 have the maximum number of hydrogen bonds along with 18 non-covalent interactors, suggesting that they exhibit a strong affinity towards the catalytic site of the ADAM17 protein.

Table 3.1.3: *IUPAC names of the compounds*

Compounds	Formula	IUPAC
INN	$C_{19}H_{37}N_5O_5$	(2*R*)-*N*-[(2*S*)-1-[[(2*S*)-1-(2-aminoethylamino)-1-oxopropan-2-yl]amino]-3,3-dimethyl-1-oxobutan-2-yl]-*N*'-hydroxy-2-(2-methylpropyl)butanediamide
I37	$C_{25}H_{28}N_4O_4$	3-[3-amino-2-oxo-3-[4-(quinolin-4-ylmethoxy)phenyl]pyrrolidin-1-yl]-*N*-hydroxy-2,2-dimethylpropanamide
I6	$C_{26}H_{30}N_4O_4$	(2*S*)-2-[(3*S*)-3-amino-1-[4-[(2-methylquinolin-4-yl)methoxy]phenyl]-2-oxopyrrolidin-3-yl]-*N*-hydroxypentanamide
I9	$C_{28}H_{32}N_4O_4$	(1*S*,2*R*)-2-[3-amino-3-[4-[(2-methylquinolin-4-yl)methoxy]phenyl]-2-oxopyrrolidin-1-yl]-*N*-hydroxycyclohexane-1-carboxamide
S10	$C_{26}H_{46}N_6O_7$	(8*S*,11*R*,12*S*)-12-*N*-hydroxy-3-methyl-8-*N*-[2-(4-methylpiperazin-1-yl)-2-oxoethyl]-11-(2-methylpropyl)-2,10-dioxo-1-oxa-3,9-diazacyclopentadecane-8,12-dicarboxamide
S11	$C_{27}H_{46}N_6O_9$	ethyl 4-[2-[[(8*S*,11*R*,12*S*)-12-(hydroxycarbamoyl)-11-(2-methylpropyl)-2,10-dioxo-1-oxa-3,9-diazacyclopentadecane-8-carbonyl]amino]acetyl]piperazine-1-carboxylate
S12	$C_{26}H_{43}N_5O_9$	1-[2-[[(8*S*,11*R*,12*S*)-12-(hydroxycarbamoyl)-11-(2-methylpropyl)-2,10-dioxo-1-oxa-3,9-diazacyclopentadecane-8-carbonyl]amino]acetyl]piperidine-4-carboxylic acid
S13	$C_{25}H_{43}N_5O_8$	(8*S*,11*R*,12*S*)-12-*N*-hydroxy-3-methyl-11-(2-methylpropyl)-8-*N*-(2-morpholin-4-yl-2-oxoethyl)-2,10-dioxo-1-oxa-3,9-diazacyclopentadecane-8,12-dicarboxamide
I32	$C_{26}H_{28}N_4O_4$	2-[3-amino-2-oxo-3-[4-(quinolin-4-ylmethoxy)phenyl]pyrrolidin-1-yl]-*N*-hydroxycyclopentane-1-carboxamide
I33	$C_{24}H_{25}N_3O_4$	(1*R*,2*R*)-2-*N*-hydroxy-1-*N*,1-*N*-dimethyl-1-[4-[(2-methylquinolin-4-yl)methoxy]phenyl]cyclopropane-1,2-dicarboxamide
I43	$C_{27}H_{29}N_3O_4$	(2*S*,5*S*)-*N*-hydroxy-2-methyl-2-[4-[(2-methylquinolin-4-yl)methoxy]phenyl]-3-oxo-1,5,6,7,8,8*a*-hexahydroindolizine-5-carboxamide
Z38	$C_{25}H_{25}N_3O_3S$	5-[[1-[2-(2-butan-2-ylphenoxy)ethyl]indol-3-yl]methylidene]-2-sulfanylidene-1,3-diazinane-4,6-dione

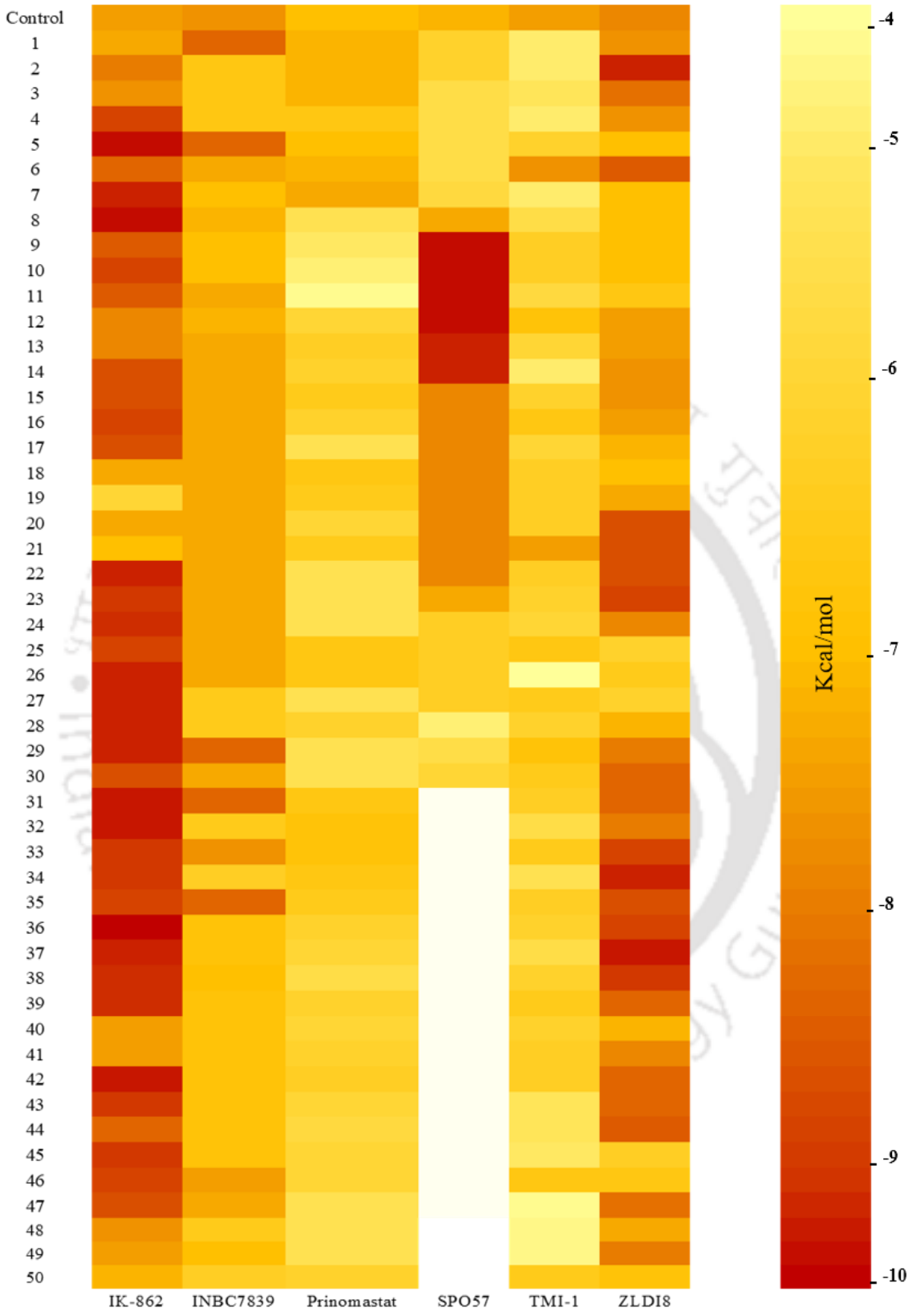

Figure 3.1.5: *The binding energy of the selected analogues against the catalytic site of ADAM17 by molecular docking study*

***Table 3.1.4**: Binding energies of the top 11 compounds and their 2D interaction profile s from molecular docking studies*

Parent compound	Probable Name	Compound Name/CIDs	Binding energies (Kcal/mol)	No. of Hydrogen bonds	Interacting amino acids (in H-bond)	No. of non-covalent interactions	Interacting amino acids
INN	INN	444587	-6.4	4	ASN389, LEU348, GLY349, HIS415	16	THR347, GLU398, GLY346, ALA439, ILE394, TYR390, VAL402, HIS405, ILE438, MET345, PRO437, HIS409, LEU350, GLU406, TYR436, VAL440
IK862	I37	10182273	-9.2	2	PRO437, GLY349	17	MET845, ASP344, ASP313, VAL 314, THR347, PHE343, TRP312, LEU348, HIS405, ALA439, TYR436, ILE438, GLU406, VAL402, HIS415, LEU350 and LYS315
	I6	9847191	-9.1	4	PRO437, HIS415, GLY349, LEU348	6	TYR352, LYS315, LEU350, VAL475, HIS405, ALA439
	I9	9875069	-9.1	5	GLY349, LEU348, PRO437, HIS415, HIS405	12	TYR352, GLU319, LEU318, LYS315, LEU350, ALA351, HIS409, GLU406, VAL402, ALA439, GLY346, THR347
SPO57	S10	11124523	-9.1	7	ASN389, GLY346, ALA439, LEU348, PRO437, GLY349, GLU406	11	TYR390, MET345, HIS415, LEU350, HIS409, HIS405, VAL402, TYR436, ILE438, THR347, GLU398
	S11	11103972	-9.1	6	ASN389, GLY346, ALA439, LEU348, PRO437, GLY349	13	TYR390, MET345, HIS415, LEU350, HIS409, HIS405, VAL402, TYR436, ILE438, THR347, GLU398, GLU406, ALA351
	S12	11103765	-9.1	6	ASN389, GLY346, ALA439, LEU348, PRO437, GLY349	12	TYR390, MET345, HIS415, LEU350, HIS409, HIS405, VAL402, TYR436, ILE438, THR347, GLU398, GLU406
	S13	11103515	-9.1	7	ASN389, GLY346, ALA439, LEU348, PRO437, GLY349, GLU406	11	TYR390, MET345, HIS415, LEU350, HIS409, HIS405, VAL402, TYR436, ILE438, THR347, GLU398
IK862	I32	10161675	-9.0	1	LEU395	15	LEU350, GLY349, PRO437, HIS405, LEU348, TYR390, LYS392, THR393, ILE394, GLU398, ASN389, ILE438, GLY346, ALA439, THR347
	I33	10173292	-9.0	1	LEU395	15	LEU350, GLY349, PRO437, HIS405, LEU348, TYR390, LYS392, THR 393, ILE394, GLU398, ASN389, ILE438, GLY346, ALA439, THR347
	I43	10238572	-9.0	1	LEU395	15	GLY349, PRO437, LEU348, TYR390, LYS392, THR 393, ILE394, GLU398, ASN389, ILE438, GLY346, ALA439, THR347, SER441, GLU406
ZLDI8	Z38	2888817	-9.0	1	ALA439	14	MET345, GLY346, PRO437, TYR347, GLY349, GLU406, HIS405, TYR390, ILR438, LEU348, VAL402, VAL434, VAL440, LEU401

3.1.6. Prediction of the physiochemical properties

From the pharmacokinetic and pharmacodynamic study, it is observed that compounds I6 and I9 follow Lipinski's rule with zero violations, indicating that the compounds possess a potential for drug-like activities. However, compounds such as S10, S11, S12 and S13 has some violations **(Table 3.1.5)**. Altogether, six compounds (I6, I9, S10, S11, S12 and S13) were further chosen based on their physiochemical profile and ADMET study (data not shown) for further molecular dynamic simulation studies.

Table 3.1.5: *The physiochemical properties of the compounds*

Properties	**Range**	**I6**	**I9**	**S10**	**S11**	**S12**	**S13**	**INN**
Molecular weight (g/mol)	< 500	462.54	488.58	554.68	598.69	569.65	541.64	415.53
LogP	≤ 5	2.81	3.37	3.27	2.72	1.59	2.69	0.67
PSA (Å^2)	< 150	117.78	117.78	160.62	195.71	203.47	166.61	162.65
Number of HBD	< 5	3	3	4	5	6	4	6
Number of HBA	< 10	6	6	8	9	9	8	6
Number of RB	≤ 10	9	7	9	12	10	9	16

** iLogP – octanol-water partition coefficient; PSA – polar surface area; HBD – hydrogen bond acceptors; HBA – hydrogen bond donors; RB – rotatable bonds*

3.1.7. MD simulation studies

The Molecular dynamics simulation was carried out up to 100 nanoseconds. The RMSD of the protein backbone was compared with and without the ligand (compound) binding **(Figure 3.1.6: A).** It was observed that the binding of the compounds, including control inhibitor (INN), caused deviations in the protein backbone; however, the deviation is comparably less and remains below 2.0 Å, suggesting the negligible effect on the stability of the protein upon ligand binding. The mean values of the deviation are mentioned in **Table 3.1.6**.

To investigate more about the protein backbone deviations upon ligand binding, we extracted RMSF data from the trajectory and plotted against ADAM17 only (without ligands). The RMSF graph **(Figure 3.1.6: B)** provided insight into the residues causing deviations in protein backbone upon ligand binding. It is observed that the residues from 351 to 375 fluctuated more than that of ADAM17 alone (without ligand). Upon analyzing the structure, it is found that these are the loop region residues present

nearby the binding pocket. Therefore, suggesting that the binding of the compounds did not cause any notable fluctuations in the secondary structure of the protein, such as α-helices and β-sheets.

Furthermore, the strength of the H-bond facilitating the binding of small molecular compounds with ADAM17 was analyzed. A total of 10,000 frames were extracted from the MD trajectory file with 10 picoseconds intervals and the number of H-bond formed in each frame was calculated using the *gmx_hbond* gromacs function **(Figure 3.1.6: C)**. The mean number of H-bonds formed between the compounds and ADAM17 was higher than the control inhibitor **(Table 3.1.6).** The strength of the H-bonds formed between the compounds and ADAM17 was analyzed by pair distance. It is stated that the donor-acceptor distance of strongest H-bonds should be 2.2 to 2.4 Å, modest H-bonds should be 2.5 to 3.2 Å, and weakest should be 3.2 to 4.0 Å [101]. In this case, I6, I9, S11 and S12 had less than 2.0 Å distance. However, compounds S10, S13 and the control inhibitor (INN) possess adistance greater than 4.0 Å. Additionally, it is seen that S10, S13 and INN are unable to form stable H-bonds throughout the simulation.

Subsequently, to check the instability upon the ligand binding, the binding poses of the compounds with ADAM17 was extracted for every 20 ns **(Figure 3.1.7)**. It is evident that S10, S13 and INN didn't form a stable complex after 60th ns and got detached from the protein backbone **(Figure 3.1.7: B).** However, the compounds I6, I9, S11 and S12 remained in the same binding pocket throughout the whole simulation **(Figure 3.1.7: A).** Therefore, suggesting that I6, I9, S11 and S12 can act as potent inhibitors for ADAM17.

Table 3.1.6: *Mean values of molecular dynamics simulations parameters*

	Protein	**I6**	**I9**	**S10**	**S11**	**S12**	**S13**	**INN**
RMSD (nm)	0.12057	0.149755	0.168426	0.177508	0.129186	0.146615	0.150651	0.130977
RMSF (nm)	0.106213	0.188166	0.120467	0.110487	0.10646	0.117632	0.114534	0.108486
H-bond	-	1.563	2.046	0.880	0.496	2.532	2.218	0.348
Paired Distance (nm)	-	0.183337	0.189509	0.565381	0.171963	0.184023	0.477671	0.477437

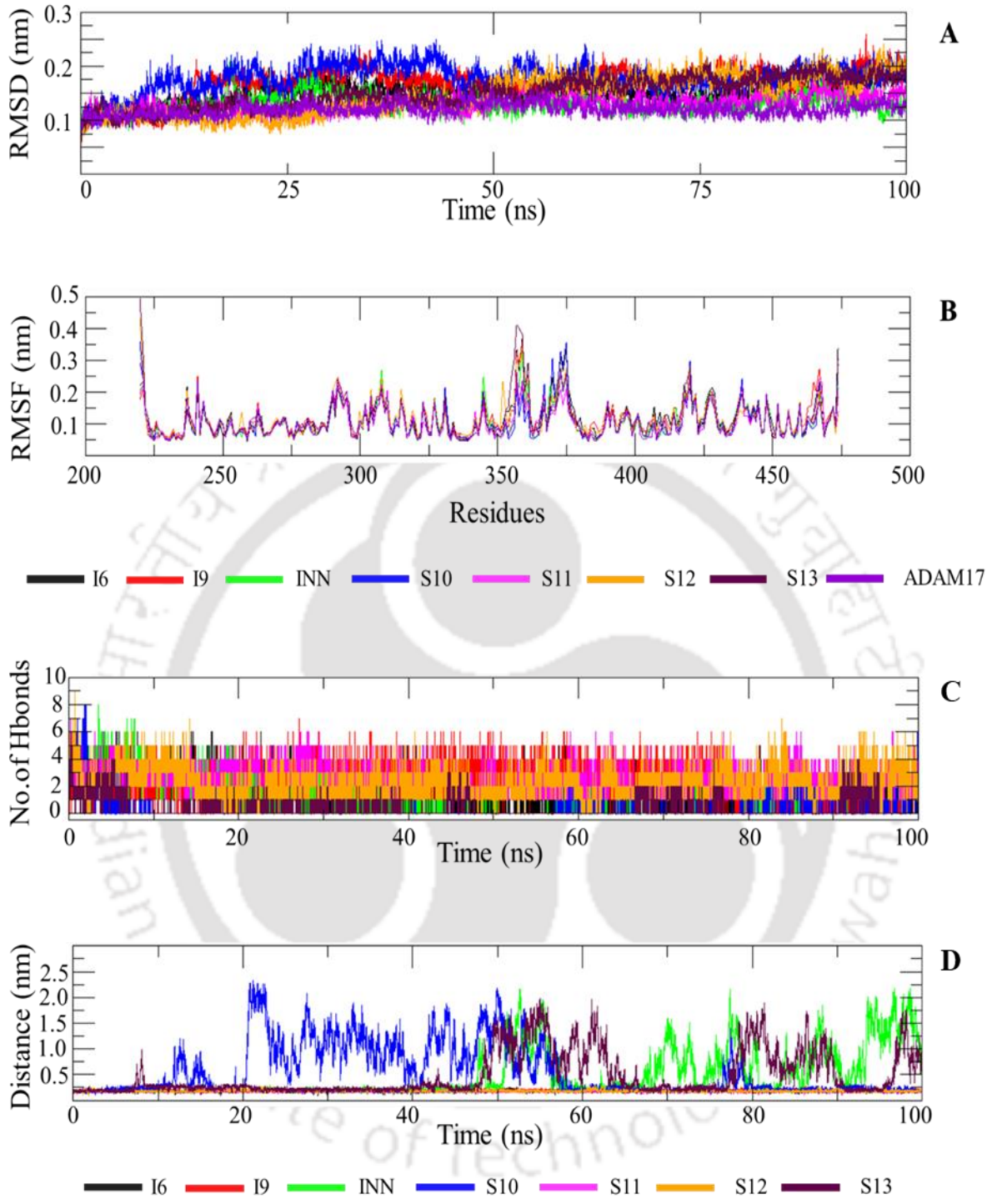

Figure 3.1.6: (A) *Root mean square deviation (RMSD) and* ***(B)*** *Root mean square fluctuation (RMSF) of ADAM17 with small molecular compounds; H-bond analysis graph of ADAM17 with small molecular compounds.* ***(C)*** *Number of H-bonds formed between ADAM17 and the compounds over 100 ns simulation.* ***(D)*** *The pair distance between ADAM17 and the compounds.*

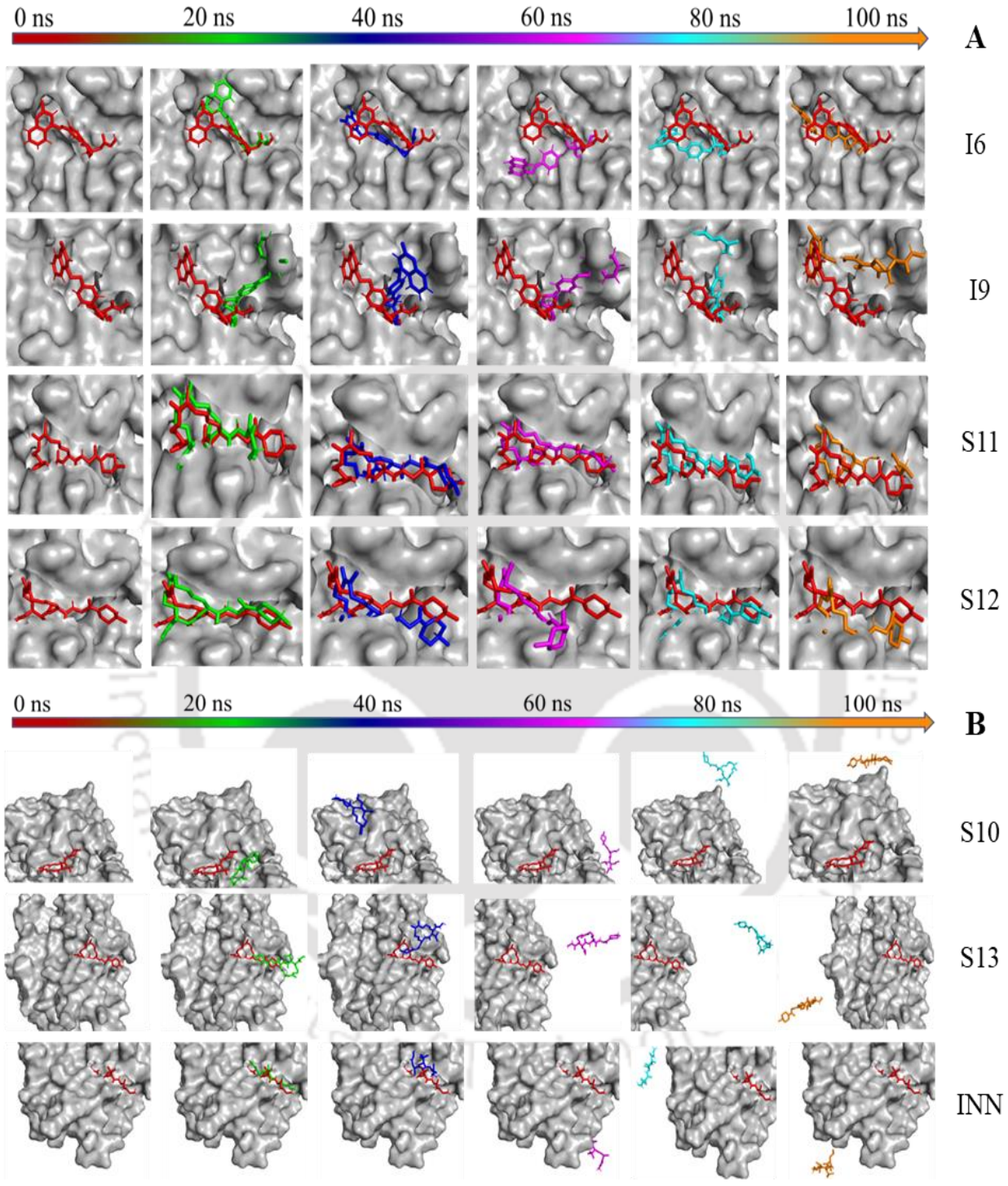

Figure 3.1.7: *Binding poses of the small molecular compounds with ADAM17.* ***(A)*** *I6, I9, S12 and S13 remained in the same binding pocket throughout the simulation in different postures.* ***(B)*** *S10, S13 and INN were detached and moved away from the binding pocket after 60 ns.*

3.1.8. Binding free energy calculation

The binding free energy of the protein-inhibitor complex was then calculated from the MD trajectory using MMPBSA (Molecular Mechanics Poisson-Boltzmann Surface Area) method. It was calculated based on the formula,

$$\triangle G = \triangle E_{MM} + \triangle G_{PBSA} - \mathrm{T}\triangle S_{MM}$$

where $\triangle G$ is the calculated average free energy, $\triangle E_{MM}$ is the average molecular mechanics' energy, $\triangle G_{PBSA}$ is the solvation-free energy, and $\mathrm{T}\triangle S_{MM}$ represents the solute configuration entropy.

The compounds S11 and S12 had the lowest binding free energy, followed by I9 and I6 **(Table 3.1.7)**. It was noted that the binding free energies of compounds S11, S12, I9 and I6 were better than the control inhibitor (INN). Since INN is a potent inhibitor of ADAM17, therefore these four selected compounds can also be considered as a potent inhibitor for ADAM17.

Table 3.1.7: *The predicted binding free energy for the protein-ligand complexes by the MMPBSA method*

	I6	**I9**	**S10**	**S11**	**S12**	**S13**	**INN**
Vander Waals energy (kJ/mol)	-127.792	-124.693	-41.672	-152.215	-124.367	-45.456	-61.762
Electrostatic energy (kJ/mol)	-492.847	-430.791	-243.942	-385.702	-358.301	-257.154	-254.191
Polar solvation energy (kJ/mol)	405.404	325.457	146.699	300.102	242.665	131.169	103.691
SASA energy (kJ/mol)	-16.767	-14.076	-6.013	-18.388	-15.989	-6.479	-8.588
Binding energy (kJ/mol)	-232.003	-244.102	-144.928	-256.203	-255.992	-177.921	-220.851

Conclusion

The implications of ADAM17 in various diseases are phenomenal. It is seen that ADAM17 is a druggable target, which can be utilized for the inhibition of pathogenic signalling in cancer. Many chemical compounds have been synthesized to date as selective ADAM17 inhibitors for curing rheumatoid arthritis (RA) and cancer, which has been validated in pre-clinical trials. However, the higher affinity of the inhibitor towards MMPs, on account of their similar catalytic site to that of ADAM17, has led to adverse clinical outcome.

Herein, the protein interaction studies through network biology provide an insight into the possible pathogenic pathways that are associated with the ADAM17 protein. These interactors are associated with numerous malignancies as well as other inflammatory diseases, which is essential towards understanding the disease etiology. Thus, these interactions signify the therapeutic approaches concentrating on the specific ADAM17 mediated target genes and proteins that help in controlling the progression of malignancy, which might prove as an effective target towards obliterating cancer. It is predicted that our study could serve as a repository for the selection of ADAM17 as the prognostic therapeutic marker for the selection of appropriate therapeutic moieties involved in various diseases where ADAM17 is the main regulator.

Molecular docking study of ADAM17 with the analogues of Prinomastat, IK862, ZLDI8, SPO57, INBC7839 and TMI-1 endows us with the knowledge of the compounds that exhibits the ability to bind to the catalytic site of the protein more efficiently. Herein, the compound IK862 possess the analogues with the lowest binding energies. The drug-likeness and ADME/T profile of the following compounds were performed to choose the best among the eleven. It is observed that the compounds S10, S11, S12 and S13 had some violations, while the rest of the compounds (I6, I9, I32, I33, I37, I43 and Z38) had zero violations. Moreover, the ADME/T profile reveals that I6 and I9 exhibit superior pharmacokinetic and pharmacodynamic properties in comparison to the other compounds.

MD-simulation study enlightened us with the knowledge of the stability and strength of the chosen small molecules, having an inhibitory role against ADAM17. Out of six molecules, four of them (I6, I9, S11 and S12) showed better results than the control inhibitor (INN). It is also observed that the INN, along with S10 and S13, showed greater fluctuations and instability in the binding pattern. Hence suggesting that the analogues of IK862 (I6 and I9) have the capability of being used as a potential drug in future.

The therapeutic targeting of ADAM17 signifies an attractive strategy to combat various types of cancer with aberrant and/or overexpression of ADAM17. The inhibition of ADAM17 may serve as a novel avenue in the treatment modality for numerous malignancies. Despite the promising therapeutic efficacy that could be achieved upon targeting the ADAM17, there is limited knowledge of the possible substrates and their role in the facilitation of malignancies. Conclusively, it can be stated that the therapeutic interception of the ADAM17 protein by the existing small molecules may pave the way for developing a potent and efficient inhibitor, thereby facilitating the therapeutic efficacy in cancer theranostic.

भारतीय प्रौद्योगिकी संस्थान गुवाहाटी
Indian Institute of Technology Guwahati

3.2 Multi-Targeting TACE/ADAM17 and γ-Secretase of Notch Signalling Pathway in TNBC via Drug Repurposing Approach using Lomitapide

- ***Cellular signalling,*** *102*, 110529.

Doi: 10.1016/j.cellsig.2022.110529

[Elsevier]

Results and Discussions

Abstract

The aberrant expression of the Notch signalling pathway genes aids in potentiating the belligerent characteristics of numerous malignancies. Besides imparting abnormal proliferation and metastasis, the Notch also aids in the metabolic reprogramming of tumour cells. Since the activation of the Notch pathway is mediated via TACE/ADAM protease and the γ-secretase complex, hence it is crucial in determining a multi-targeted therapeutic approach to target these major proteases to downregulate the aberrant Notch signalling pathway. In this study, Lomitapide was chosen based on its binding score (-305.108 kJ/mol and -173.174 kJ/mol) against the crucial proteases, TACE and γ-secretase, respectively. Further, the remarkable antitumour properties of Lomitapide were established on the TNBC cell lines (MDA-MB-231 and MDA-MB-468), along with the EMT induced MDA-MB-468 cells. Apart from inducing ~2 to 2.5-fold increase in the cellular ROS levels, Lomitapide treatment induced significant apoptosis, arrested cell cycle progression and reduced sphere and colony forming abilities of the TNBC cells. Additionally, differentiated epithelial phenotype with diminished CD44- stem cell marker was also observed upon treatment. Furthermore, reduction of migration potential, decrease in the gene expression profile of the EMT markers, along with downregulation of the Notch signalling genes were evident in the treated TNBC cells. Altogether, the present study attributes the repurposing of Lomitapide as an effective therapeutic agent against the major proteases of the Notch pathway to combat TNBC progression and dissemination.

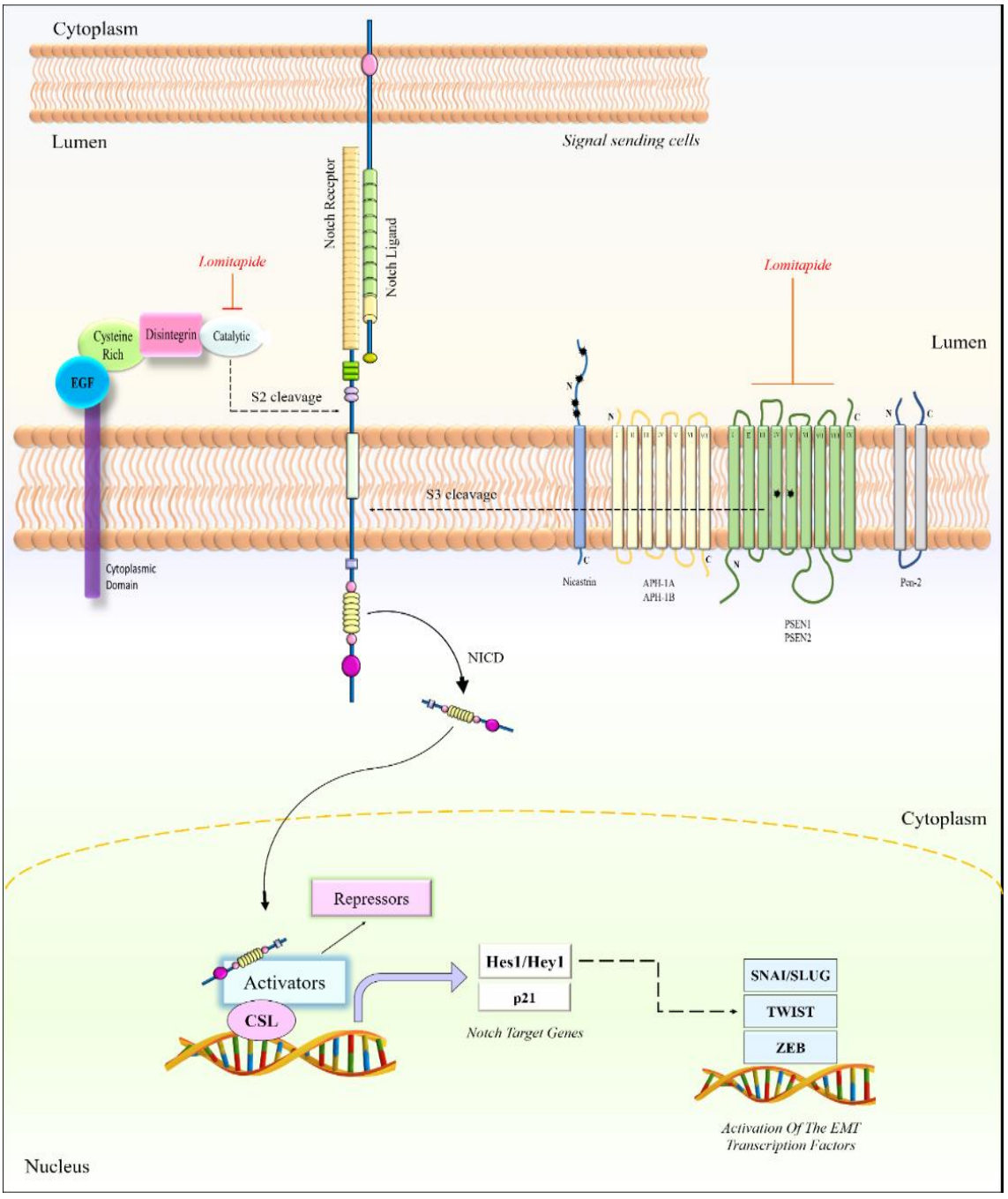

Schematic 3.2.1: *Schematic representation of the work. (Concept source: adapted and redrawn from https://doi.org/10.3390/cells8030209)*

3.2.1. Higher expression of the genes in the Notch pathway culminates poor prognosis of TNBC

Upon the establishment of the major proteases in the Notch pathway, the expression profile of the following proteases, namely, TACE and the components of the γ-secretase enzyme (NCSTN, PSENEN, PSEN1, PSEN2, APH1A, and APH1B) were subjected to their expression analysis in tumour samples, using the UALCAN portal. It was observed that besides the expression of the Notch ligands and receptors, the expression of TACE and the components of γ-secretase enzyme (especially, APH1A and NCSTN) were found to be elevated in TNBC **(Figure 3.2.1)**.

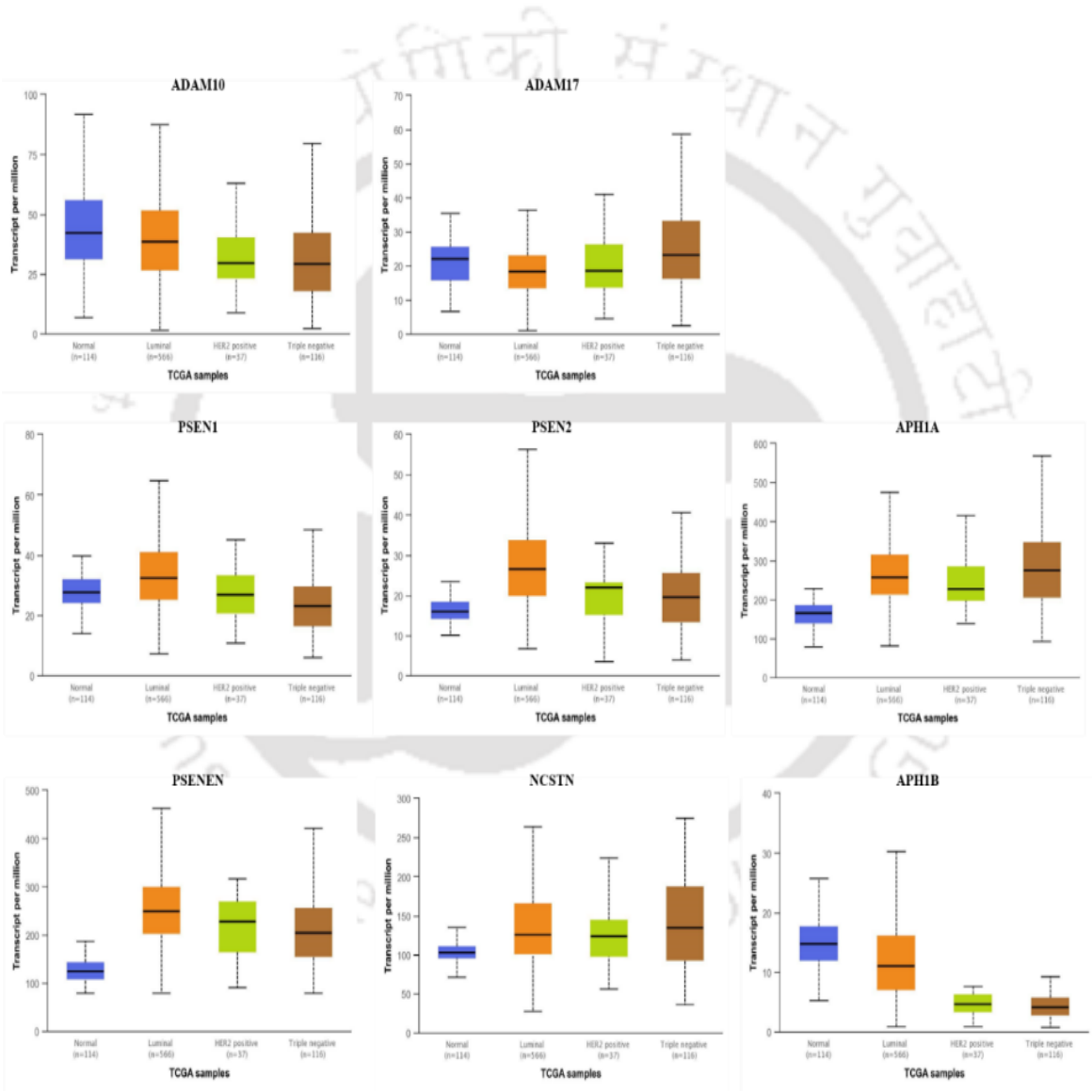

Figure 3.2.1: *Protein expression data of the Notch target genes in normal, luminal, HER-2 positive and TNBC breast cancer tissues obtained from the UALCAN database.*

3.2.2. Structural and functional analysis of TACE and γ-secretase

Furthermore, the structural analysis of the proteins (TACE and γ-secretase) was carried out. It was observed that the γ-secretase, a multiprotein intramembrane-cleaving protease, is a complex of four different proteins, exhibiting individualistic function. The tetrameric complex of the γ-secretase comprises Nicastrin (NCT), anterior pharynx defective (APH-1), Presenilin enhancer 2 (PEN2) and Presenilin (PSEN), as depicted in **Figure 3.2.2**. Nicastrin is a type-1 membrane glycoprotein, which potentiates complex maturation and stabilization [102]. Presenilin enhancers (PSENEN) are required for endoproteolytic processing of the inactive Presenilins to their active heterodimeric conformation. APH1 acts as a substrate receptor for the protease complex [103]; while the Presenilins act as the catalytic core of the γ-secretase complex, which facilitates the cleavage of various type-I transmembrane proteins via regulated intramembrane proteolysis [104], [105]. Besides Notch, there are numerous pro-oncogenic genes, which are known to be activated by the proteolytic activity of the γ-secretase enzyme, such as CD44, ErBB4, etc.

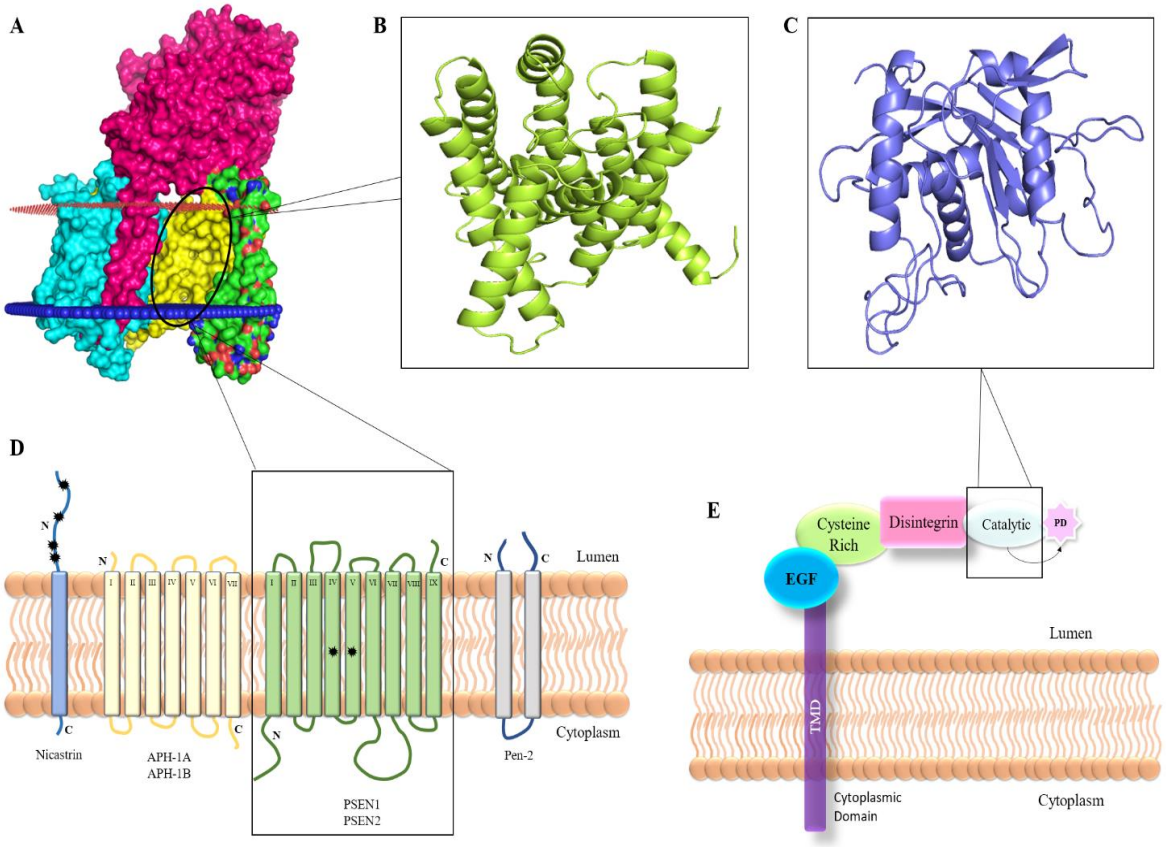

Figure 3.2.2: *Structural and functional analysis of TACE and γ-secretase.* ***(A)*** *3D structure of γ-secretase (PDB_ID: 5FN2).* ***(B)*** *Catalytic domain (Presenilin) of γ-secretase.* ***(C)*** *Catalytic domain of ADAM.* ***(D)*** *Schematic interpretation of the γ-secretase enzyme.* ***(E)*** *Schematic interpretation of ADAM protease.*

Similarly, the TACE (also known as ADAM17) is also a type-I transmembrane protease, comprising extracellular multidomain regions **Figure 3.2.2**. The ectodomain of TACE consists of an N-terminal signal sequence adjacent to a prodomain, which is attached to the catalytic domain, followed by a disintegrin and a cysteine-rich domain. Removal of the prodomain activates the catalytic subunit of the protease [105]. It is evident that TACE/ADAM17 is not only responsible for mediating the S2 cleavage of the Notch receptor, but also activates other pathways by cleaving the various oncogenic proteins such as TNFα, EGF, etc. [106].

Therefore, in this study the γ-secretase/presenilin complex inhibitor, LY411575 is selected as the control inhibitor for γ-secretase, while TMI-1 is selected as the control inhibitor for TACE/ADAM17. LY411575 is a derivative of Azepine class of compounds that belongs to the transition-state analogues, which mimics the transition state of a substrate cleavage by γ-secretase and binds competitively to the catalytic active site of presenilins [107]; while TMI-1 is a derivative of the thiomorpholine sulphonamide hydroxamate class, bearing butynyloxy moiety at the P10 site. This compound is under Phase II clinical trials and is one of the best dual-acting compounds against TACE17, MMP-1, MMP-2 and MMP-13 [108].

Moreover, to establish the complex interconnection of these two major proteases the functional network analysis was performed, using the STRING v9.1 database. From **Figure 3.2.3** it is evident that both the proteases play a major part in the activation of various type-I transmembrane proteases, including the Notch pathway.

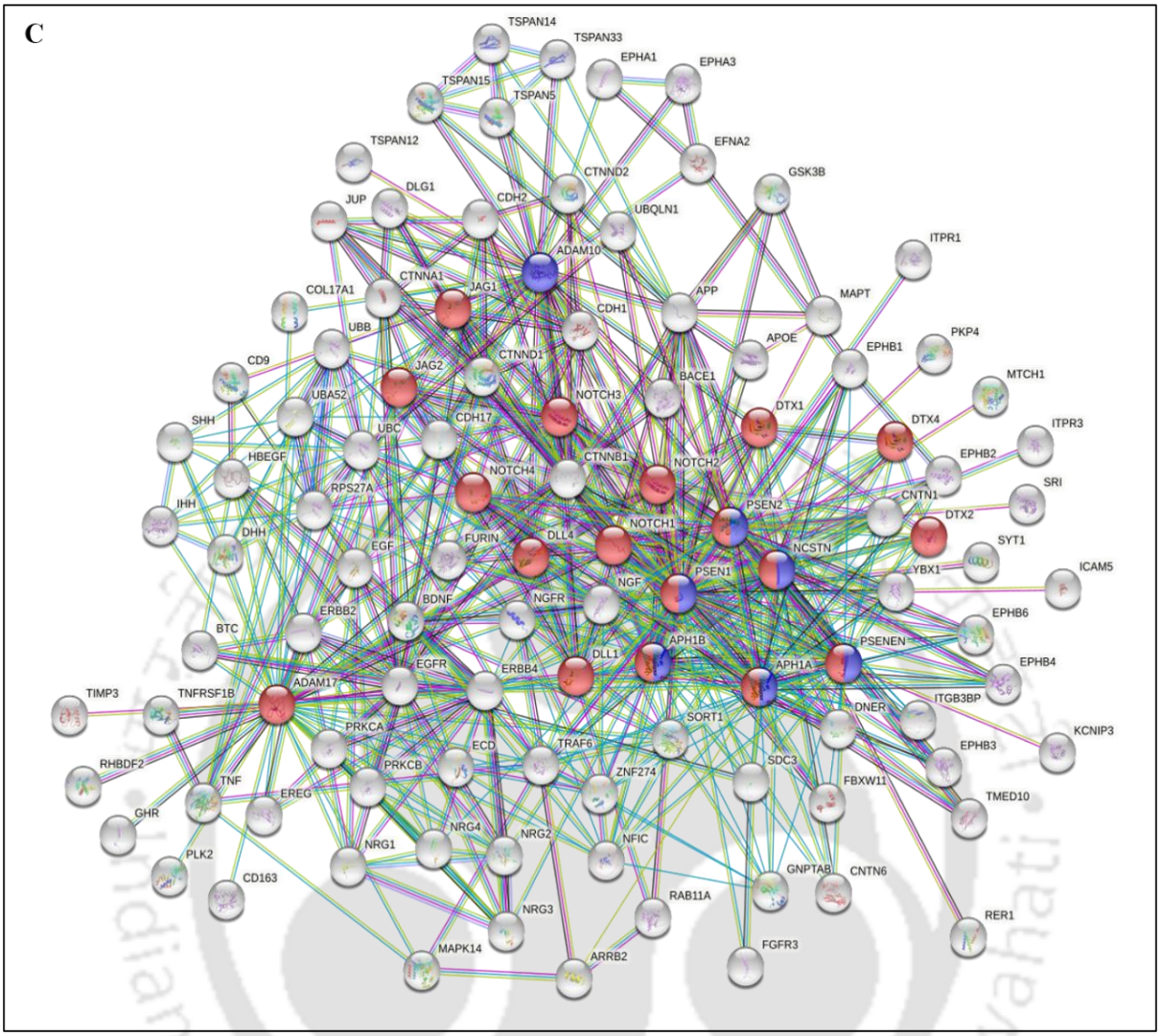

Figure 3.2.3: *STRINGS network depicting the network of ADAM and γ-secretase enzyme. Briefly, ADAM and the components of γ-secretase (NCSTN, APH-1A, APH1B, PSENEN, PSEN1 and PSEN2) for Homo Sapiens was fed as the query molecule. The interacting network was restricted to the first shell, with a confidence score of 0.7 that is indicated to be of significant reliability.*

3.2.3. Molecular docking studies identified seven drugs having an affinity towards the target proteases

The virtual screening was performed using AutoDock Vina, which endowed us with more than 802 and 70 drugs with greater binding energy than the control inhibitors for TACE and γ-secretase, respectively. The predicted binding energy for TMI-1 and LY411575 was found to be -6.8 Kcal/mol and -8.9 Kcal/mol, respectively. Following this, the top 7 drugs having interactions with both the proteins were selected, which exhibited the least binding score than the control inhibitors. The binding energies and the interactors of the complexes are mentioned in **Table 3.2.1.** Among these seven drugs **(Table 3.2.2)**, Lomitapide was chosen for further studies to ascertain its efficacy in inhibiting the aggressive properties of TNBC.

Table 3.2.2: *Binding scores and interacting residues of TACE and γ-secretase protease*

Drug	Binding score kcal/mol	Interacting residues
TACE/ADAM17		
Conivaptan	-9.5	GLU319, VAL373, PHE323, LYS296, GLN320, LEU380, TYR369, TYR352, LYS315, ILE378, SER371, PRO372
Dutasteride	-9.6	TYR352, GLU319, LYS315, ILE328, PHE323, VAL373, LYS296, GLN320, TYR369, LEU380
Irinotecan	-9.7	VAL353, ALA439, GLU406, GLY349, THR347, LEU350, LYS315, GLU319, LEU380, TYR352, ALA351, HIS409, HIS415, PRO348, HIS405, VAL402
Lomitapide	-11.2	VAL440, LEU348, PRO437, GLU406, HIS415, LEU350, VAL402, HIS405, GLY349, ALA439, GLU398, LYS392, ILE394, ASN389, TYR390, ILE438, GLY346, THR347, LEU401, TYR436, VAL434
Nilotinib	-9.9	PRO437, ALA439, ASN389, SER441, ILE438, VAL440, TYR436, VAL434, HIS405, LEU402, GLU406, VAL402, LEU348, THR347, ILE394, GLY349, TYR390, GLY346, GLU398
Radotinib	-9.7	TYR390, PRO437, VAL402, HIS415, GLU406, LEU350, HIS405, LEU348, ALA351, GLU398, ASN389, ILE394, ILE438, GLY346, THR347, LEU401
Umbralisib	-10	GLU406, VAL440, VAL434, HIS409, LEU350, GLY349, HIS415, THR347, MET345, TYR390, GLY346, ILE438, PRO437, LEU348, ALA439, HIS405, VAL402, LEU401, GLU398
Control	-6.8	MET345, VAL440, ILE438, GLY346, LEU401, PRO437, ALA439, VAL402, GLU406, HIS405, LEU348, GLY349, HIS415, THR347, LEU350, LYS315, ASP344
γ-secretase		
Conivaptan	-10.8	GLU339, GLU323, PHE336, ASN316, SER313, SER357, PRO355, GLU356, VAL328, SER346, HSD347, HSD351, GLN343, THR320, SER324, TRP340
Dutasteride	-10.8	ARG377, HSD214, LYS216, THR281, LYS160, GLU277, LEU219, THR291, GLY378, GLU376, LYS380, ILE287, ARG278
Irinotecan	-10	LYS265, LEU150, PHE283, THR47, PHE388, MET146, PHE237, LEU241, VAL236, MET139, ILE114, LEU113, TYR115, TYR240, PHE177, LEU172, TRP165, ILE143, MET233, GLY384, ASP257, LEU268
Lomitapide	-10.1	LEU219, ILE287, GLU376, LYS380, GLU375, LYS16, ARG278, PRO303, GLY300, HSD214, TRP215, ALA305, LEU364, GLU277, ILE213, THR281, GLN222
Nilotinib	-10.3	THR291, ASN279, HSD163, LEU219, GLN232, ILE287, THR281, GLU277, GLU280, ILE167, ALA164, HSD214, LYS160, LYS216, ARG278, LYS380, GLU375, GLY378, GLU376, ARG377
Radotinib	-9.9	GLU376, GLU372, GLY371, GLN276, ARG377, ILE287, GLY378, TYR288, LEU219, THR291, GLU275, LYS380, ARG278, ASP373, GLU277, SER367, LEU364, ILE368, ALA225
Umbralisib	-10.8	HSD214, GLN222, GLU376, ILE287, GLU375, LYS216, TRP215, LYS160, HSD163, GLU280, ILE213, THR281, GLU277, SER212, LEU219, THR291
Control	-8.9	ALA434, ILE287, VAL272, GLY382, LEU383, PHE283, LEU272, LEU282, LEU286, THR147, ILE143, TYR256, ILE253, GLY384, PHE388, ASP257, ALA385, LEU435, PRO433, LEU381, VAL261

Table 3.2.2: *The top seven interactors of TACE and γ-secretase protease*

Drugs	Uses
Conivaptan	*a non-peptide inhibitor of the Vasopressin receptor is used for the treatment of hyponatremia.*
Dutasteride	*used to treat men who have symptoms of an enlarged prostate gland, which is also known as benign prostatic hyperplasia (BPH).*
Irinotecan	*a topoisomerase inhibitor, is used in the treatment of metastatic colon cancer.*
Lomitapide	*an inhibitor of the microsomal triglyceride transfer protein (MTP), is used in the treatment of familial hypercholesterolemia.*
Nilotinib	*inhibitor of the Bcl-Abl kinase, c-kit and Platelet-Derived Growth Factor (PDGF), which is used for the treatment of Chronic Myeloid Leukaemia (CML), whereby it binds to and stabilizes the inactive conformations of the kinase domain of the Abl protein.*
Radotinib	
Umbralisib	*a PI3K inhibitor, is used in the treatment of Marginal Zone Lymphoma and Follicular Lymphoma.*

3.2.4. Molecular dynamics simulation (MDS) to identify the binding affinity of Lomitapide

In this study, the molecular dynamics simulation of protein-drug complexes for both target proteins were carried out in two different environments. On one hand, the TACE–drug complexes were simulated in a water-rich environment, while the γ-secretase drug complexes were simulated in a membrane-water-rich environment. The dynamic behaviour of target protein and drug complexes was analyzed using GROMACS parameters such as RMSD (root means square deviation), RMSF (root means square fluctuations), Number of H-bonds and pair distance.

3.2.4.1. MDS of TACE–drug complexes

TACE plays a predominant role in the Notch signalling pathway by cleaving the Notch receptors into a membrane-tethered intermediate domain called the Notch extracellular truncated domain (NEXT) domain, which is further identified and cleaved by the γ-secretase to generate the intracellular domain (also known as NICD). Hence, the strength and stability of TACE–drug complexes were analyzed after a 100 ns MD run, using GROMACS commands. The root means square deviation of the protein backboneindicates the stability of protein during MD simulation. In this study, the average root means square deviation of TACE-drug complexes **(Table 3.2.3)** was lesser than the TACE alone (0.2372 nm). The RMSDs of TACE and TACE - drug complexes were in the range of 0.1 nm to 0.3 nm over 100 ns **(Figure 3.2.4: A)**. The deviation of each residue over 100 ns was also analyzed upon drug binding,

which is depicted as RMSF in **Figure 3.2.4: B**. The residual fluctuation was observed to be higher in the region of residue number 350 to 375 on account of the binding of the drugs in that region.

However, the average RMSF of complexes was lesser than the TACE alone. Altogether, these observations indicate that the binding of drug molecules to TACE causes the deviation in the binding pocket to accommodate itself within the binding pocket and forms stable complexes without deviating from the whole structure of the protease. The strength of drug binding to TACE was analyzed through a number of H bonds and pair distances over 100 ns. The number of H-bond formed between TACE and drug molecules was between 0 and 5 **(Figure 3.2.4: C)** and the average number of H-bonds formed by drug molecules was higher than the control inhibitor **(Table 3.2.3).** Out of seven selected drugs, Conivaptan shows higher average H-bonds and Dutasteride shows the lowest average H-bonds. The distance between protein and drug complexes was also measured from MD trajectory with a 100 ps time interval and it was observed that all the drug molecules maintained a distance of lesser than 0.3 nm, except Irinotecan **(Figure 3.2.4: D).** The average pair distance maintained by the drug molecules with TACE was lesser than 0.24 nm (24 Å), which signifies the strongest binding. Pair distance analysis shows that drug molecules were present inside the binding pocket throughout the simulation. However, Irinotecan and Dutasteride got detached and moved to another binding pocket after 60 ns and 90 ns, respectively. The snapshot of drug molecules with binding pockets was extracted from the MD trajectory with a 20 ns time interval **(Figure 3.2.4: I)** to support the pair distance data. Additionally, the rest of the drugs were found to retain their positions within the same binding pocket over 100 ns. Thus, all the drug molecules have the potential to form a stable and strong interaction with TACE, except Irinotecan and Dutasteride.

3.2.4.2. MDS of γ-secretase–drug complexes

γ-secretase is a membrane protein, which cleaves the transmembrane proteins at the residues within the membrane, thereby resulting in the generation of the Notch intracellular domain (commonly known as NICD). Unlike TACE, the interaction of drug molecules with γ-secretase depends on the membrane molecules also. In this study, molecular dynamic simulation of γ-secretase with selected drug molecules was carried out in a membrane-rich environment. The membrane composition was kept as standard mammalian cell membrane composition provided by the CHARMM-GUI tutorial. The simulation was carried out using GROMACS for 100 ns, and the stability and strength of the drug-binding were analyzed using GROMACS parameters such as RMSD, RMSF, H bonds and pair distance. The root means square deviation of the γ-secretase backbone was observed to be 0.2827 nm over 100 ns (Figure 1E). Similarly, the drug complexes were also lesser than the γ-secretase, except for Dutasteride (0.2938 nm) and Irinotecan (0.31662 nm) complex **(Table 3.2.3)**. However, the difference in the RMSDs of Dutasteride, Irinotecan and γ-secretase is at a negligible level. The residual fluctuation over 100 ns was analyzed to check the involvement of the residues in the structural stability **(Figure 3.2.4: F)**. There

was no significant difference observed between complexes and γ-secretase at a residual level. It indicates the stable interaction of drug molecules with γ-secretase in a membrane-rich environment also. The number of H-bonds formed between drugs and γ-secretase was plotted in **Figure 3.2.4: G**. The maximum number of H-bonds formed varied between 0 and 3, which was lesser than the TACE-drug complex. In the case of Nilotinib and Radotinib complexes, the maximum number of H-bonds formed with the γ-secretase was 5 to 6 for a time period of 30 ns, which also got reduced to 0 to 3. This can be attributed to the hydrophobic environment of the membrane, which might have caused the reduction in the H-bonds. The analysis of the distance between the drugs and γ-secretase shed some light on the strength of binding. Even though a smaller number of H-bonds were formed between the protein and drugs, the pair distance was maintained between 0.17 nm to 0.25 nm throughout the simulation **(Figure 3.2.4: H)**, which indicates the strongest binding of the drugs with γ-secretase. The pictorial representation of drugs binding with γ-secretase is also portrayed in **Figure 3.2.4: J** to support the pair distance analysis. The snapshots were extracted every 20 ns from the MD trajectory and it was noted that all the drugs were bound to remain in the same binding pocket for the whole 100 ns simulation. It was also observed that all the drugs were bound in the same binding pocket as the control inhibitor, except Dutasteride **(Figure 3.2.4: J).**

Table 3.2.3: *Mean values of the MD simulation parameters over 100 ns*

	TACE	**Conivaptan**	**Dutasteride**	**Irinotecan**	**Lomitapide**	**Nilotinib**	**Radotinib**	**Umbralisib**	**Control**
RMSD (nm)	0.2372	0.1616	0.1822	0.1265	0.21	0.1874	0.1538	0.1731	0.2153
RMSF (nm)	0.1237	0.1088	0.116	0.1181	0.1163	0.1195	0.1044	0.1210	0.1172
H-bond	--	0.8884	0.1792	0.5345	0.5838	0.6286	0.2727	0.5318	0.1953
Paired Distance (nm)	--	0.1731	0.2027	0.2382	0.184	0.1783	0.2084	0.1977	0.2042
	Gamma secretase	**Conivaptan**	**Dutasteride**	**Irinotecan**	**Lomitapide**	**Nilotinib**	**Radotinib**	**Umbralisib**	**Control**
RMSD (nm)	0.2827	0.2664	0.2938	0.31662	0.2744	0.2790	0.2515	0.2653	0.2369
RMSF (nm)	0.2712	0.1310	0.1390	0.1474	0.1262	0.1438	0.1330	0.1249	0.1225
H-bond	--	0.0379	0	0.9760	0.2877	1.3566	1.3756	1.3886	0.2297
Paired Distance (nm)	--	0.2113	0.2205	0.1873	0.2012	0.1927	0.1973	0.1764	0.2018

3.2.5. Binding free energy analysis

Binding free energy analysis provides the details of drug interaction with target proteins in the form of interacting forces. Two main forces are involved in drug binding, which sheds the light on the strength of the interaction. One is the Van der Waal's force of interaction, which is important to hold the drugs inside the binding pocket; the other is the electrostatic force of interaction, which helps to attract the drugs to the binding pocket and is the strongest force of interaction [109]. In this study, the binding free energy of target proteins and drug molecules was analyzed using the MM-PBSA method. g_mmpbsa module of GROMACS was used to simulate the binding free energy of complexes from MD trajectory with one ns time interval. The predicted binding free energy of selected drugs with both target proteins was tabulated in **Table 3.2.4**. Out of seven, four drugs namely Conivaptan, Irinotecan, Lomitapide and Umbralisib were shown better binding energy than the control inhibitors of both target proteins. Since the detachment of Irinotecan from TACE was observed after 90^{th} ns, it was excluded from the potential dual-target drugs, whereas the rest three drugs were proposed as the dual-target drugs for TACE and γ-secretase. Among the three dual-target drugs, Lomitapide has better binding energy against both target proteins, followed by Conivaptan and Umbralisib. Hence, Lomitapide was chosen for further *in vitro* validations.

Table 3.2.4: *MMPBSA binding free energy of protein – drug complexes from MD-trajectory*

TACE	**Conivaptan**	**Dutasteride**	**Irinotecan**	**Lomitapide**	**Nilotinib**	**Radotinib**	**Umbralisib**	**Control**
Vander Waals energy(kJ/mol)	-171.826	-96.937	-88.039	-169.030	-166.918	-118.255	-136.404	-147.096
Electrostatic energy(kJ/mol)	-10.925	-30.449	-339.224	-333.476	-51.528	-22.079	-150.499	-22.879
Polar solvation energy(kJ/mol)	96.828	94.601	177.871	215.166	129.408	86.607	205.024	110.949
SASA energy (kJ/mol)	-18.011	-11.282	-9.855	-17.768	-16.905	-12.437	-15.078	-15.287
Binding energy(kJ/mol)	-103.934	-44.067	-259.247	-305.108	-105.943	-66.165	-96.958	-74.314
Gamma secretase	**Conivaptan**	**Dutasteride**	**Irinotecan**	**Lomitapide**	**Nilotinib**	**Radotinib**	**Umbralisib**	**Control**
Vander Waals energy(kJ/mol)	-206.139	-109.745	-292.024	-287.114	-232.5	-231.058	-220.710	-196.571
Electrostatic energy(kJ/mol)	-22.615	-17.408	-23.890	-22.756	-30.691	-29.455	-30.997	-11.781
Polar solvation energy(kJ/mol)	97.546	96.208	187.404	171.246	193.487	190.161	137.842	104.178
SASA energy (kJ/mol)	-25.262	-13.513	-31.260	-34.549	-28.219	-28.483	-27.980	-23.618
Binding energy(kJ/mol)	-156.470	-44.458	-159.770	-173.174	-97.923	-98.835	-141.846	-127.792

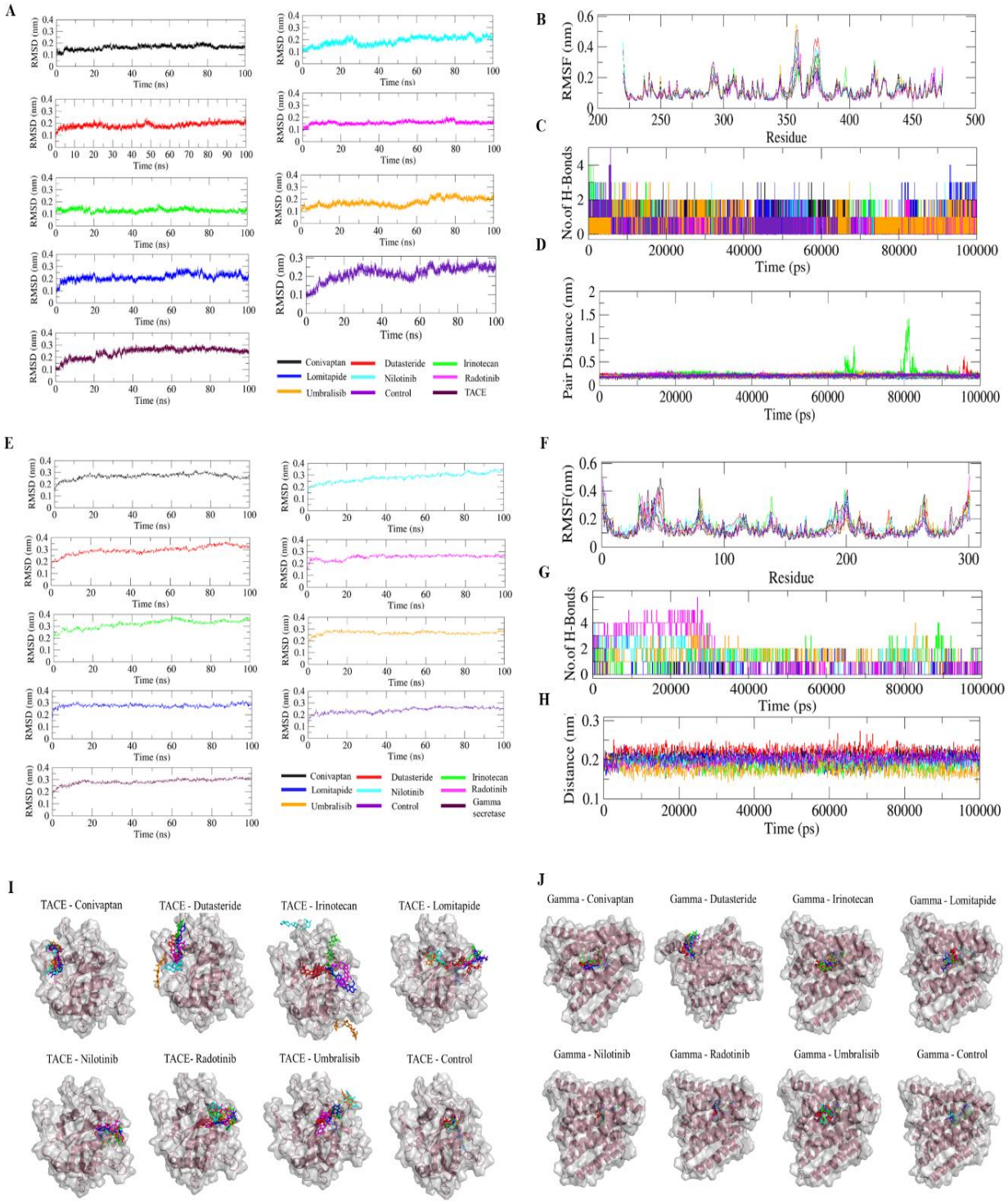

Figure 3.2.4: *Root means square deviation of protein backbone upon binding of drugs over 100 ns simulation for* ***(A)*** *TACE and* ***(E)*** *γ-secretase. Root means square fluctuation of each residues of target proteins upon drug binding over 100ns in* ***(B)*** *TACE and* ***(F)*** *γ-secretase. Number of H-bonds formed between target protein and drug over 10 ns simulationfor* ***(C)*** *TACE and* ***(G)*** *γ-secretase. Pair distance between the target protein and drugs for 100 ns for* ***(D)*** *TACE and* ***(H)*** *γ-secretase. Binding conformation of FDA approved drugs in the binding pocket of the target proteins with 20 ns time interval for* ***(I)*** *TACE and* ***(J)*** *γ-secretase. Each colour represents different time period of the simulation. Red- 0th ns, green-20th ns, blue- 40th ns, magenta- 60th ns, cyan- 80th ns, orange- 100th ns.*

3.2.5. Anti-cell proliferative activity

In the present study, Lomitapide has been chosen on account of its high binding affinity toward both the target genes (TACE and γ-secretase). Hence, for further validation and to prove its cytotoxic effects against the TNBC cells (MDA-MB-231 and MDA-MB-468), an MTT assay was performed. A dose-dependent decrease in cell viability was observed in both cell lines, upon treatment with Lomitapide. Additionally, the control inhibitors against TACE (TMI-1) and γ-secretase (LY411575) also bestowed us with a dose-dependent decrease in cell viability. However, the IC_{50} obtained for Lomitapide was much lower for the TNBC cells in comparison to the small molecule inhibitor, as depicted in **Figure 3.2.5**.

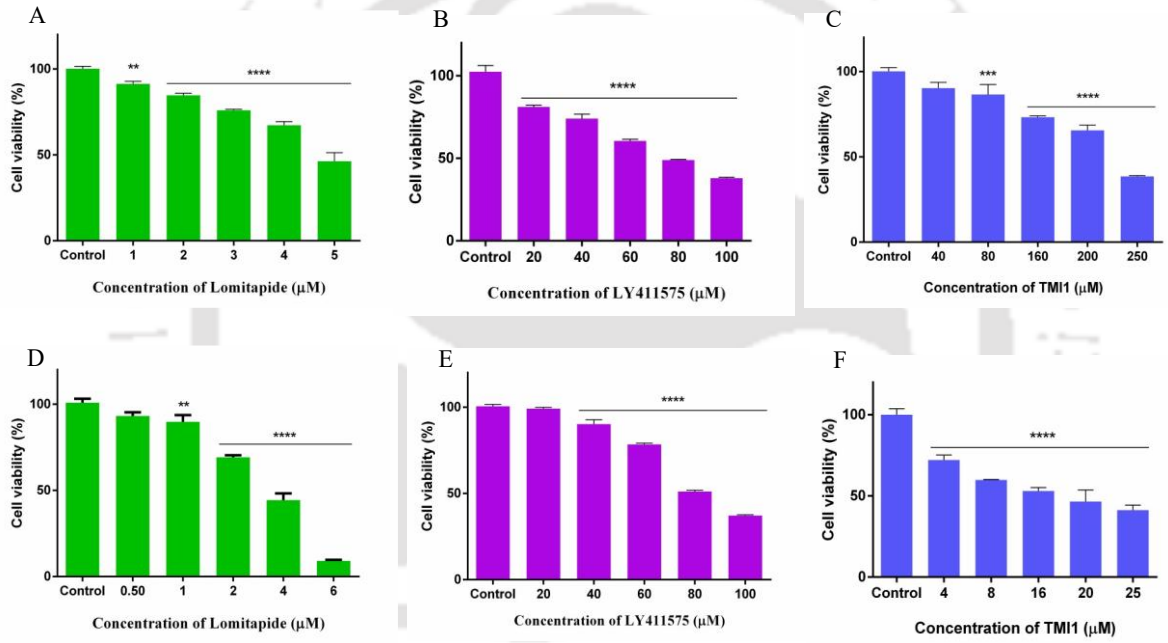

Figure 3.2.5: *Determination of cell viability by MTT assay following treatment with* ***(A)*** *Lomitapide,* ***(B)*** *LY411575,* ***(C)*** *TMI-1 for a time period of 48 h in MDA-MB-231. Determination of cell viability by MTT assay following treatment with* ***(D)*** *Lomitapide,* ***(E)*** *LY411575,* ***(F)*** *TMI-1 for a time period of 48 h in MDA-MB-468. The results are expressed as the mean ± SEM for three independent experiments. The statistical significance was assessed in comparison to the untreated cells. The significance level was set at $p < 0.05$ (*), $p < 0.01$ (**), $p < 0.001$ (***), $p < 0.0001$ (****).*

3.2.6. Lomitapide triggers ROS and apoptosis in TNBC

Following treatment with Lomitapide, TMI-1 and LY411575 for a time period of 6 h, it was observed that there was a 5.0-fold change and 2.8-fold change of ROS generation in the LY411575 and Lomitapide treated MDA-MB-231 cells, respectively **(Figure 3.2.6: A)**. Similarly, the ROS generation was found to be 2-fold and 1.85-fold in the case of Lomitapide and LY411575 treated MDA-MB-468 cells, respectively **(Figure 3.2.6: B).** However, in both the TNBC cells, there were no significant changes in the generation of ROS after treatment with TMI-1 **(Figure 3.2.6: C)**. Therefore, suggesting a plausible role of Lomitapide and LY411575 in affecting the metabolic pathways of the TNBC cells.

Furthermore, the increase in intracellular ROS is indicative of various cellular damages that ultimately leads to cell death. Hence, an apoptosis assay was carried out to confirm the population of apoptotic and/or necrotic cells after subsequent treatment for 48 h. It was observed that the Lomitapide induces apoptosis in TNBC cells. However, when compared to LY411575 and TMI-1 treated cells, it was observed that TMI-1 induces apoptosis more prominently in the TNBC cell lines in comparison to Lomitapide, as depicted in **Figure 3.2.6: D and E**.

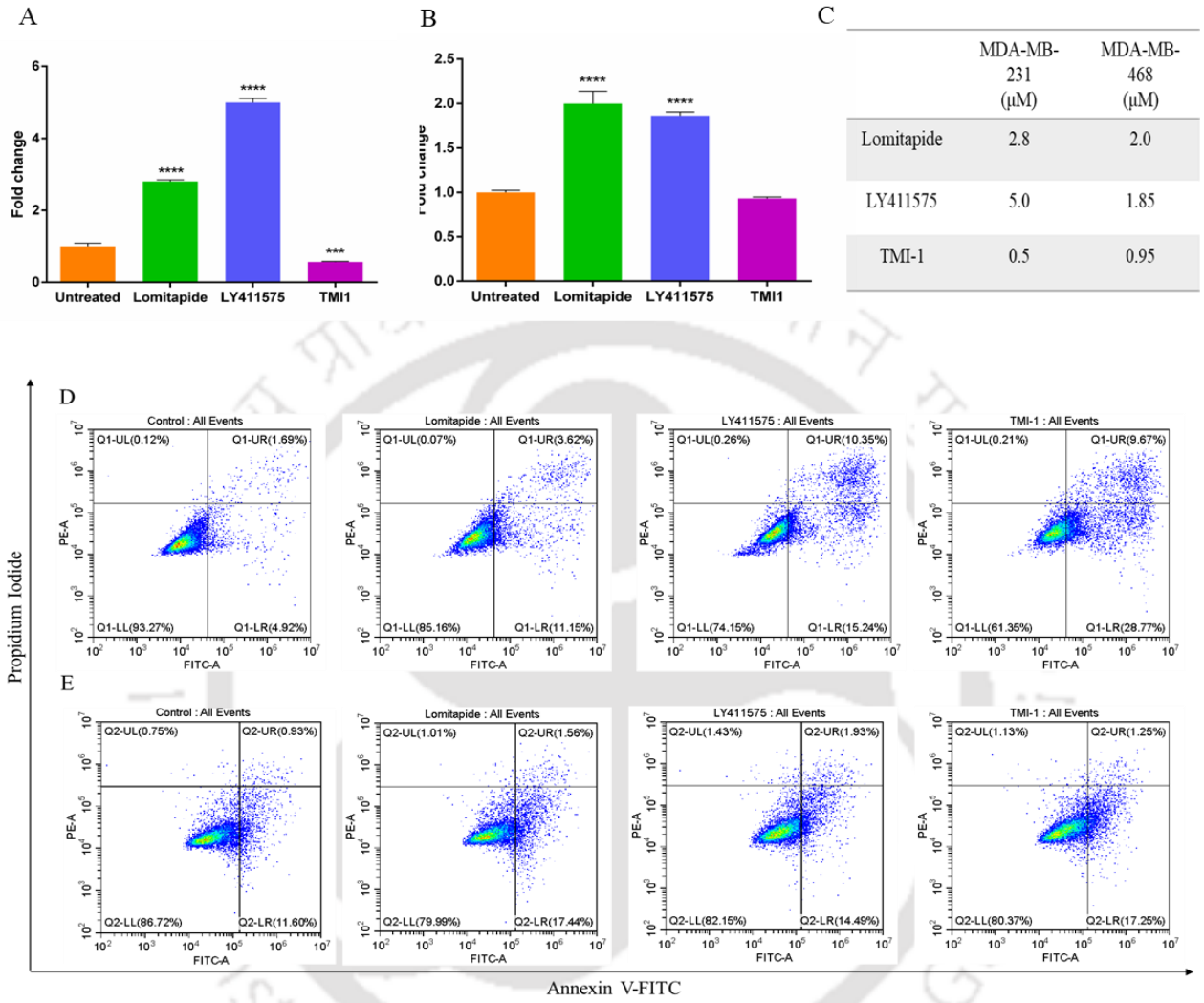

Figure 3.2.6: *Graphical representation of the cellular ROS detection using DCFDA based flow cytometryin* ***(A)*** *MDA-MB-231,* ***(B)*** *MDA-MB-468.* ***(C)*** *Fold-change generation of ROS in TNBC cells. Flow cytometric analysis of apoptotic population by annexin-V_FITC PI assay, following 48 h of treatment in* ***(D)*** *MDA-MB-231,* ***(E)*** *MDA-MB-468. The results are expressed as the mean ± SEM on the basis of three independent experiments. The statistical significance was obtained in comparison to the untreated control cells. The significance level was set at $p < 0.05$ (*), $p < 0.01$ (**), $p < 0.001$ (***) and $p < 0.0001$ (****).*

3.2.7. Effect of Lomitapide on sphere-forming capabilities of TNBC Cells

Following treatment for 48 h, the sphere-forming capability of the TNBC cells reduced significantly after treatment with Lomitapide **(Figure 3.2.7)**, subsequently followed by LY411575, while not many changes were observed after treatment with TMI-1. Similar results were also observed in MDA-MB-468 cells, whereby following treatment with Lomitapide and LY411575 there was a disruption in the spheroid forming capability of the cells, while no such disruptive effect was observed in TMI-1 treated cells **(Figure 3.2.7: B)**.

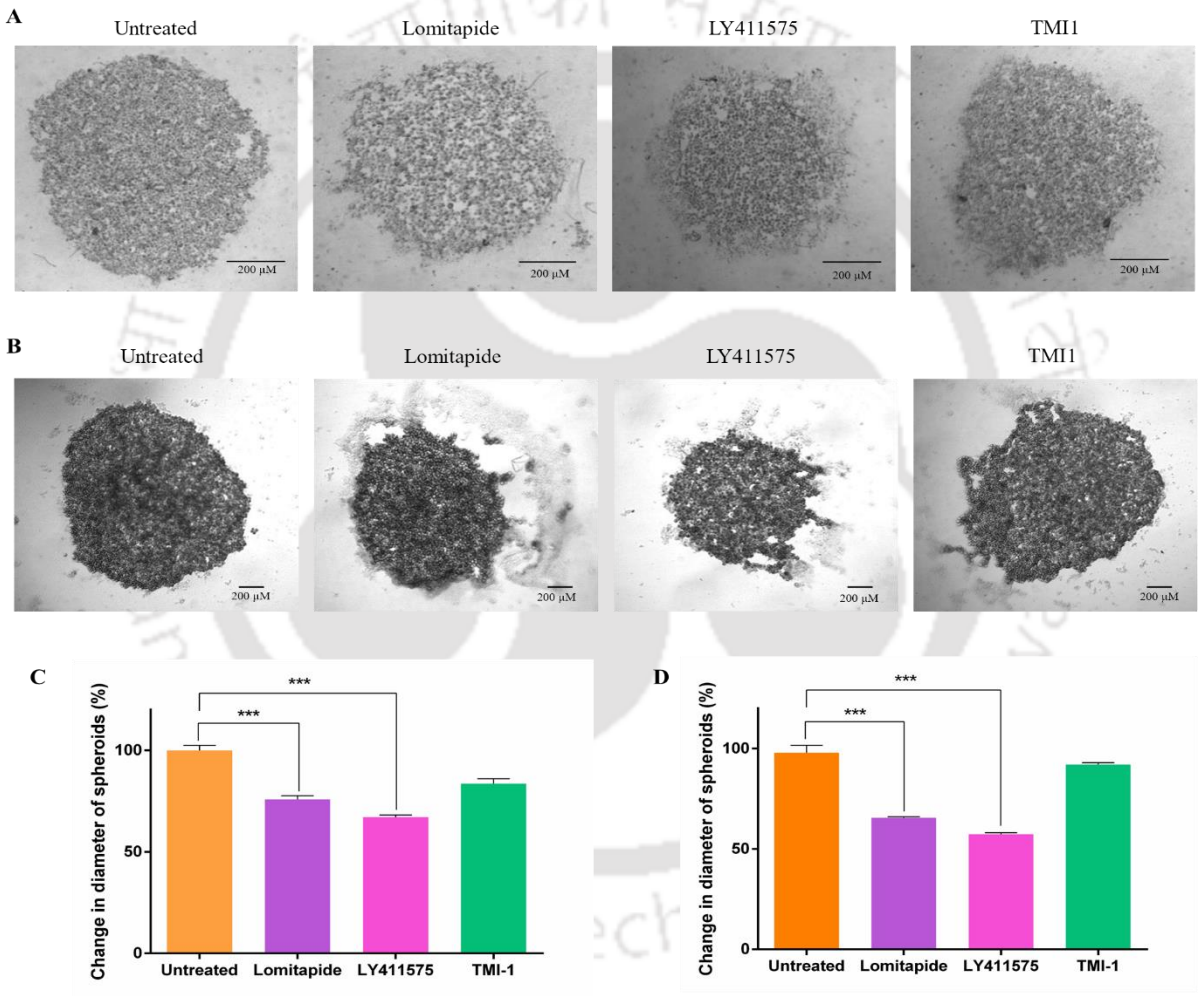

Figure 3.2.7: *Assessment of the spheroid formation ability following treatment with the respective inhibitors in* ***(A)*** *MDA-MB-231 and* ***(B)*** *MDA-MB-468 cells. Graphical representation of changes in the diameter of the spheroids, following treatment with the respective inhibitors in comparison to the untreated samples in* ***(C)*** *MDA-MB-231 and* ***(D)*** *MDA-MB-468 cells. The results are expressed as the mean ± SEM on the basis of three independent experiments. The statistical significance was obtained in comparison to the untreated control cells. The significance level was set at $p < 0.05$ (*), $p < 0.01$ (**), $p < 0.001$ (***) and $p < 0.0001$ (****).*

3.2.8 Lomitapide reduces the migration potential of TNBC cells

The migration or wound healing properties of the TNBC cells were observed via the scratch assay. It was observed that in MDA-MB-231 cells, following treatment with Lomitapide, the wound healing capacity was found to decrease by 3.46-fold in comparison to the untreated cells **(Figure 3.2.8)**. Similarly, the wound healing capacity was the lowest subsequent to the treatment with TMI-1 (2.22-fold) in MDA-MB-468 cells, followed by LY411575 (1.76-fold) and Lomitapide (1.73-fold). Conclusively, it can be stated that besides LY411575 and TMI-1, Lomitapide has the potential to decrease the migratory potential of the TNBC cells.

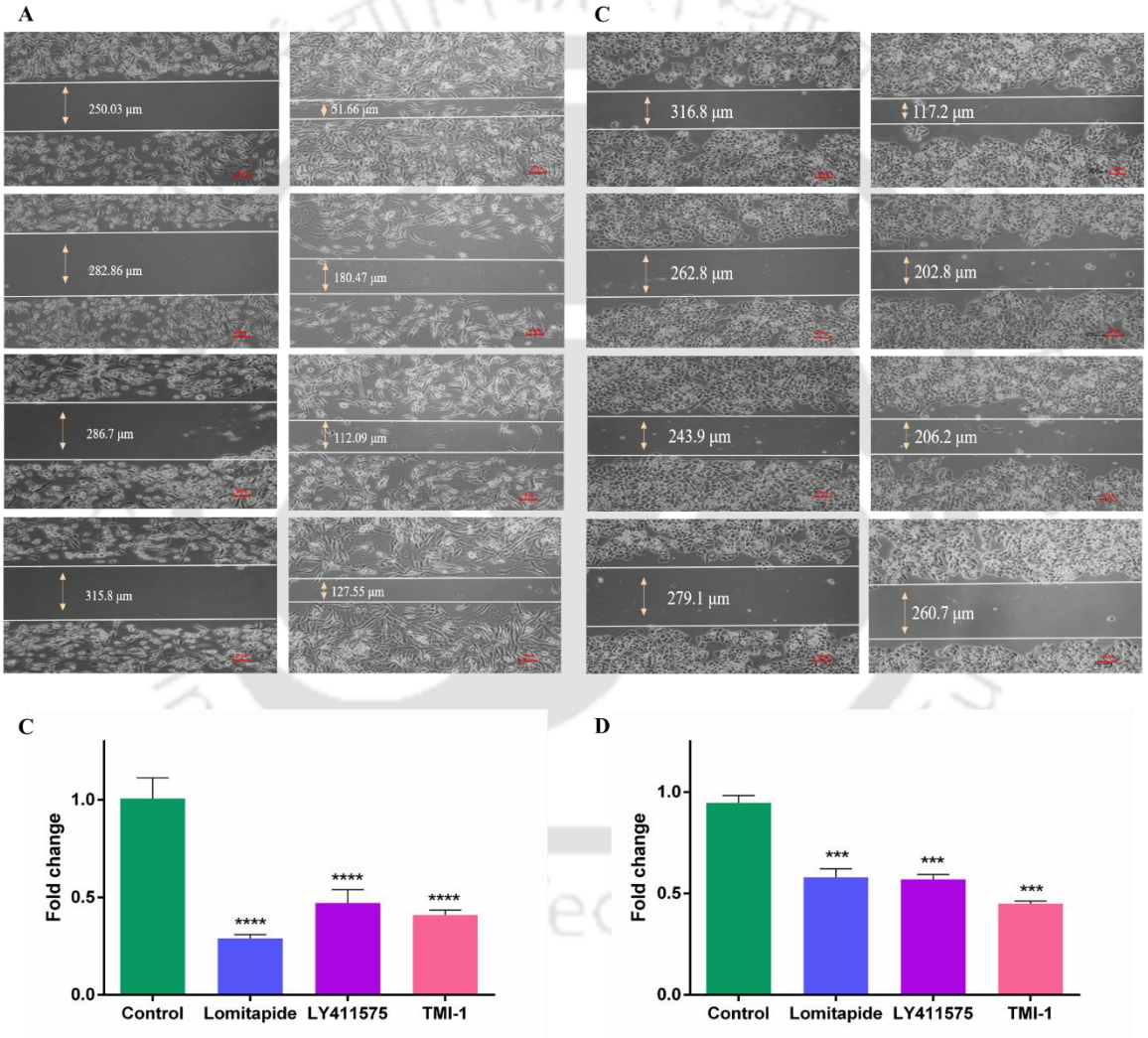

Figure 3.2.8: *Scratch wound-healing assays of* ***(A)*** *MDA-MB-231 and* ***(B)*** *MDA-MB-468 cells. Graphical representation of changes in the wound healing capacity following treatment with the respective inhibitors in comparison to the untreated samples in* ***(C)*** *MDA-MB-231 and* ***(D)*** *MDA-MB-468 cells. The results are expressed as the mean ± SEM on the basis of three independent experiments. The statistical significance was obtained in comparison to the untreated control cells. The significance level was set at $p < 0.05$ (*), $p < 0.01$ (**), $p < 0.001$ (***) and $p < 0.0001$ (****).*

3.2.9. Effect of Lomitapide on the stemness properties, cell cycle and mitochondrial membrane potential

After treatment with the respective inhibitors, the cancer stem cell population was identified, using cell surface markers such as CD24 and CD44. Immuno-flow cytometry assay revealed a differentiated epithelial phenotype, following treatment in the TNBC cell lines **(Figure 3.2.9)**. Especially after treatment with TMI1, the cells acquired prominent epithelial phenotype. However, after treatment with Lomitapide, there was a significant increase in the population of cells expressing CD24, along with differentiated epithelial phenotype in MDA-MB-468 cells, which is indicative of its efficacy in reducing the stemness of TNBC cells.

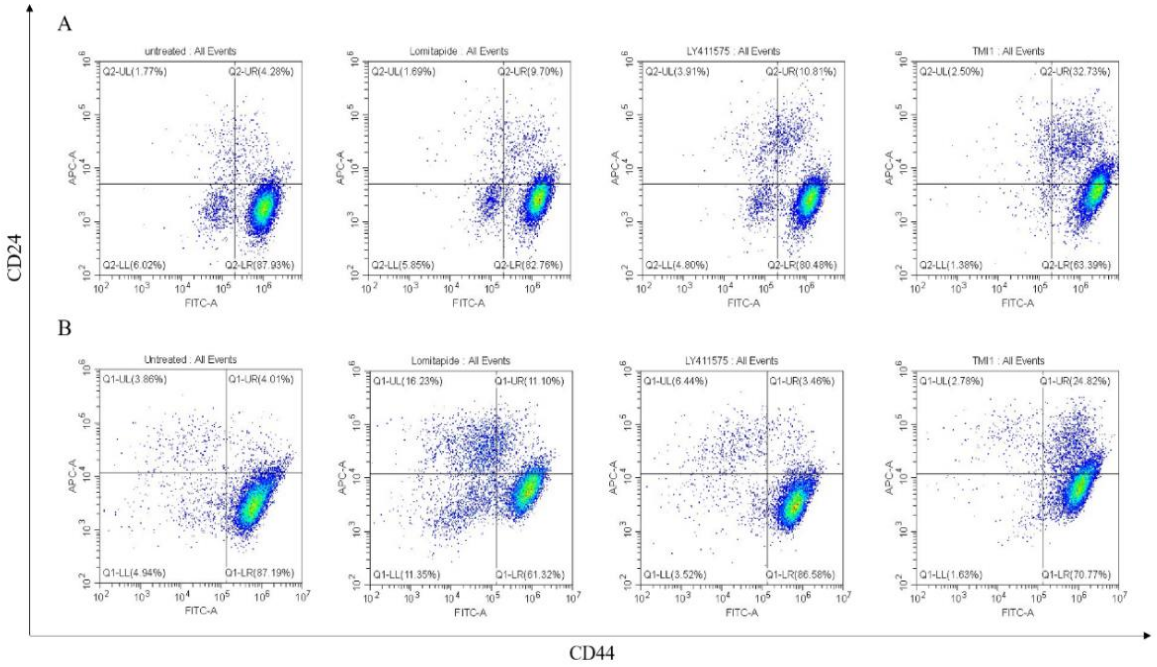

Figure 3.2.9: *The pseudo-plot representation of CD44/CD24 population in* ***(A)*** *MDA-MB-231 and* ***(B)*** *MDA-MB-468 cells.*

To document the effects of Lomitapide and other inhibitors on the cell growth and survival, cell cycle progression was monitored, following 48 h of treatment. A G0/G1 phase cell cycle arrest was observed in MDA-MB-468 cells **(Figure 3.2.10: A and B),** which is indicative of apoptosis and has been ascertained in the previous experiment. However, an S-phase arrest was observed in MDA-MB-231 cells, following treatment with Lomitapide.

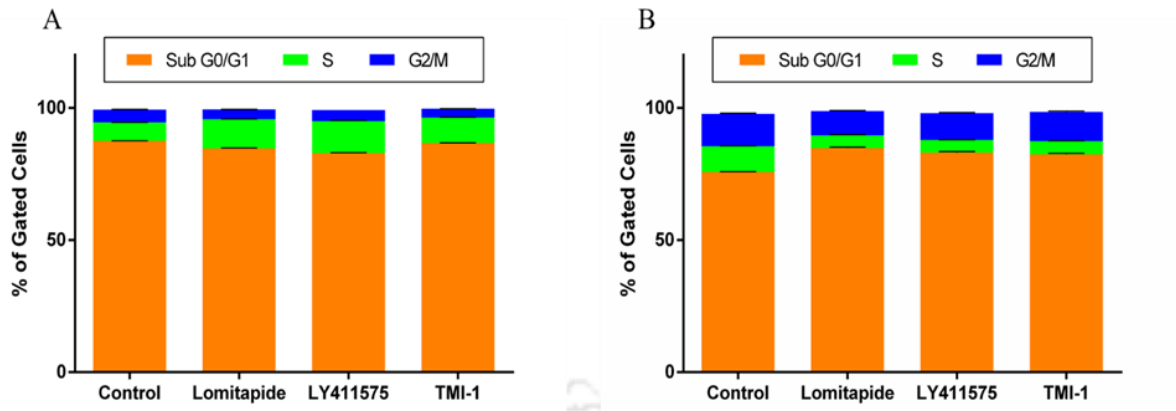

Figure 3.2.10: *Evaluation of cell cycle profile of* ***(A)*** *MDA-MB-231 and* ***(B)*** *MDA-MB-468 cells.*

Further to assess the action of Lomitapide on the mitochondrial membrane potential, JC-1 based flow cytometry was carried out. In both TNBC cells, the LY411575 treated cells exhibited maximum green fluorescence as compared to the other treatments suggesting the depolarization of the mitochondrial membrane. However, not much changes were observed following treatment with Lomitapide in MDA-MB-231 cells **(Figure 3.2.11).**

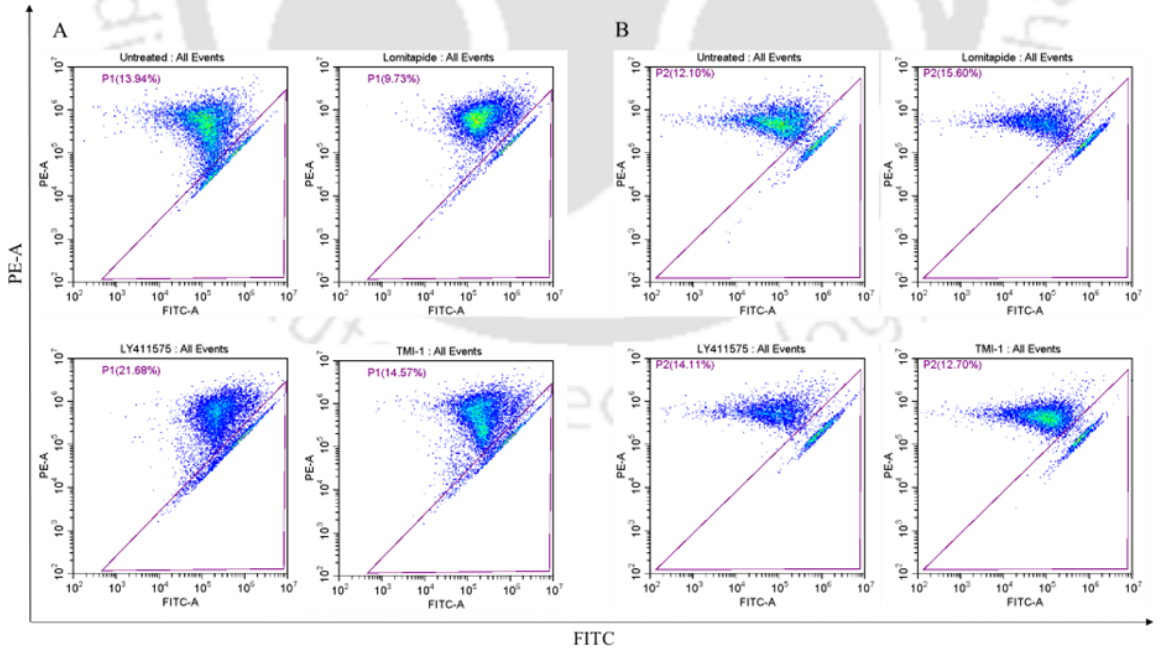

Figure 3.2.11: *Mitochondrial membrane potential detection of* ***(A)*** *MDA-MB-231 and* ***(B)*** *MDA-MB-468 cells, using JC-1 staining.*

3.2.10. Effect of Lomitapide on protein expression profile of the Notch downstream genes.

Following treatment, the expression profile of the Notch downstream protein, such as NICD (notch intracellular domain), HES-1 (Hairy enhancer of Split) and p21 was observed **(Figure 3.2.12)**. It was found that after treatment with Lomitapide, the protein expression profile of HES-1 remained almost unaltered in both the TNBC cell lines. Subsequently, the expression profile of NICD was found to be upregulated by 1.08-fold and 1.73-fold in MDA-MB-231 and MDA-MB-468 cell lines, respectively. However, when treated with LY411575, the expression level of NICD was downregulated by 1.31-fold and 2.44-fold in MDA-MB-231 **(Figure 3.2.12: A and C)** and MDA-MB-468 **(Figure 3.2.12: F and H)** cell lines, respectively. Thus, indicating the prominent effect of γ-secretase enzyme in the activation of the Notch pathway. Similarly, p21, a downstream target gene of the Notch signalling pathway was found to be downregulated by 1.4-fold in MDA-MB-231 cells **(Figure 3.2.12: A and E)**, while it was marginally upregulated in the MDA-MB-468 cells **(Figure 3.2.12: B and J)**, following Lomitapide treatment.

Table 3.2.5: *Fold change in the protein expression level of TNBC cells*

Genes	MDA-MB-231			MDA-MB-468		
	Lomitapide	LY411575	TMI-1	Lomitapide	LY411575	TMI-1
NICD	- 1.12	** 1.31	** 1.02	* 1.75	** 2.44	- 1.39
HES-1	- 1.02	-- 1.18	- 1.33	- 1.02	- 1.11	- 1.18
p21	- 1.44	* 4.07	** 1.74	- 1.13	** 2.41	* 1.09
Beclin-1	- 1.14	- 1.134	- 1.11	- 1.04	- 1.04	- 1.02

 # Red depicts upregulation in the expression level, while green depicts downregulation in expression level.

The significance level was set at $p < 0.05$ (*), $p < 0.01$ (**), $p < 0.001$ (***) and $p < 0.0001$ (****)

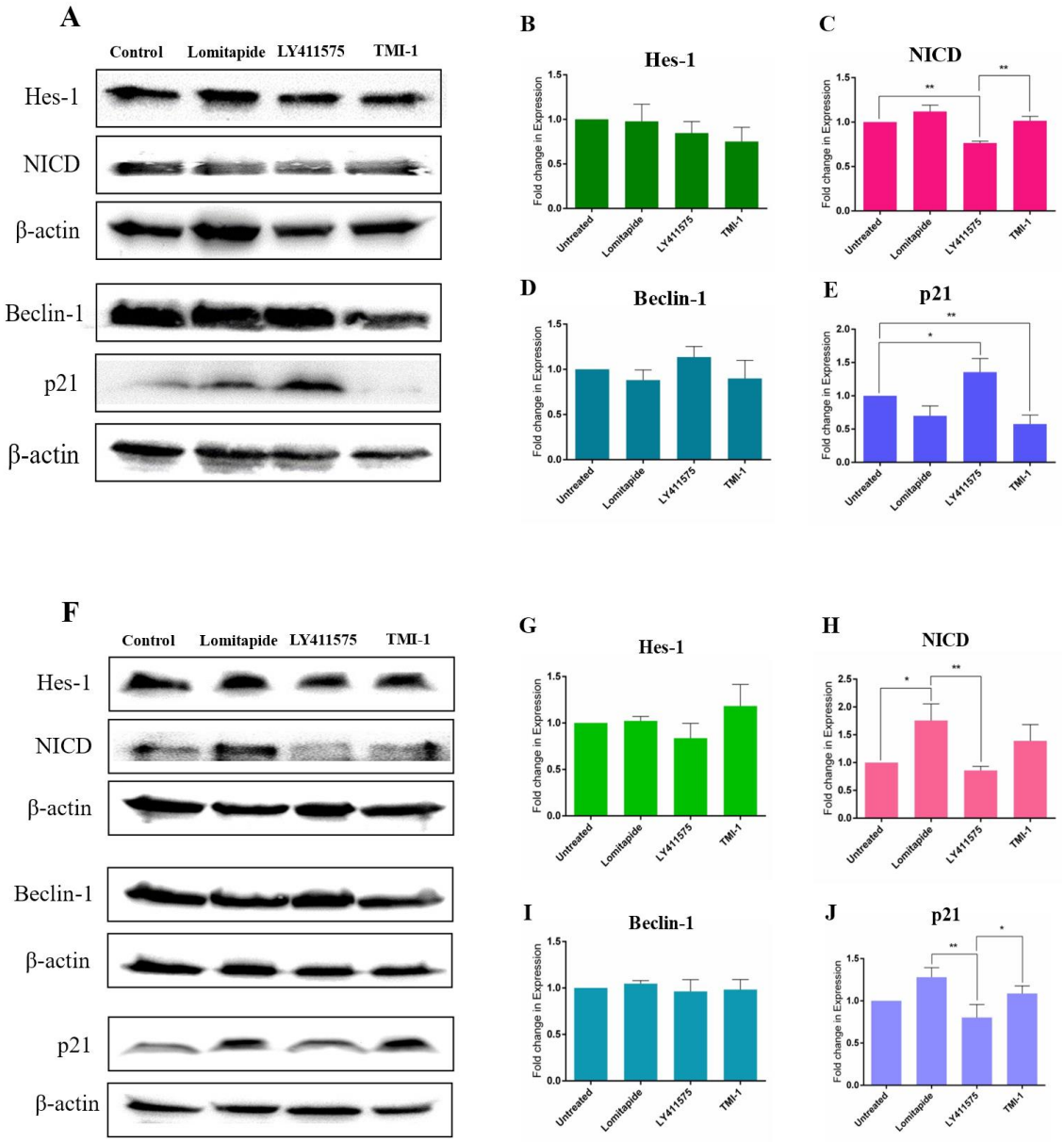

Figure 3.2.12: *Representative western blot showing HES-1, NICD, Beclin-1 and p21 levels in* ***(A)*** *MDA-MB-231and* ***(F)*** *MDA-MB-468 cells. β-actin serves as the loading control. The graphs are representation of the changes in the expression level of the proteins* ***(B)*** *HES-1,* ***(C)*** *NICD,* ***(D)*** *Beclin-1 and* ***(E)*** *p21 in MDA-MB-231 cells, and* ***(G)*** *HES-1,* ***(H)*** *NICD,* ***(I)*** *Beclin-1 and* ***(J)*** *p21 in MDA-MB-468 cells with respect to the untreated samples. The changes in the level of protein expression were deduced using the ImageJ software. The results are expressed as the mean ± SEM on the basis of three independent experiments. The statistical significance was obtained in comparison to the untreated control cells. The significance level was set at $p < 0.05$ (*), $p < 0.01$ (**), $p < 0.001$ (***) and $p < 0.0001$ (****).*

3.2.11. Effect of Lomitapide on autophagy

In order to observe the effect of Lomitapide on autophagy, following treatment, immunoblot analysis of the gene, Beclin1 and immunocytochemistry analysis of the autophagy marker LC3 was performed. The expression of Beclin-1 was found to be downregulated, after treatment with Lomitapide in MDA-MB-231 **(Figure 3.2.12: A and C).** However, not much changes were observed in MDA-MB-468 cells **(Figure 3.2.12: F and I)**. To ascertain the effect of treatment on LC3, an immunocytochemistry assay was performed **(Figure 3.2.13** and **Figure 3.2.23: A and B).** It is observed that following treatment with Lomitapide and LY411575, there was a significant downregulation in the formation of LC3 puncta in comparison to the untreated MDA-MB-231 cells. Similarly, the formation of LC3 puncta was downregulated after treatment with LY411575 in MDA-MB-468, followed by Lomitapide and TMI-1. Taken together, these results indicate that Lomitapide inhibits autophagy in TNBC cell lines.

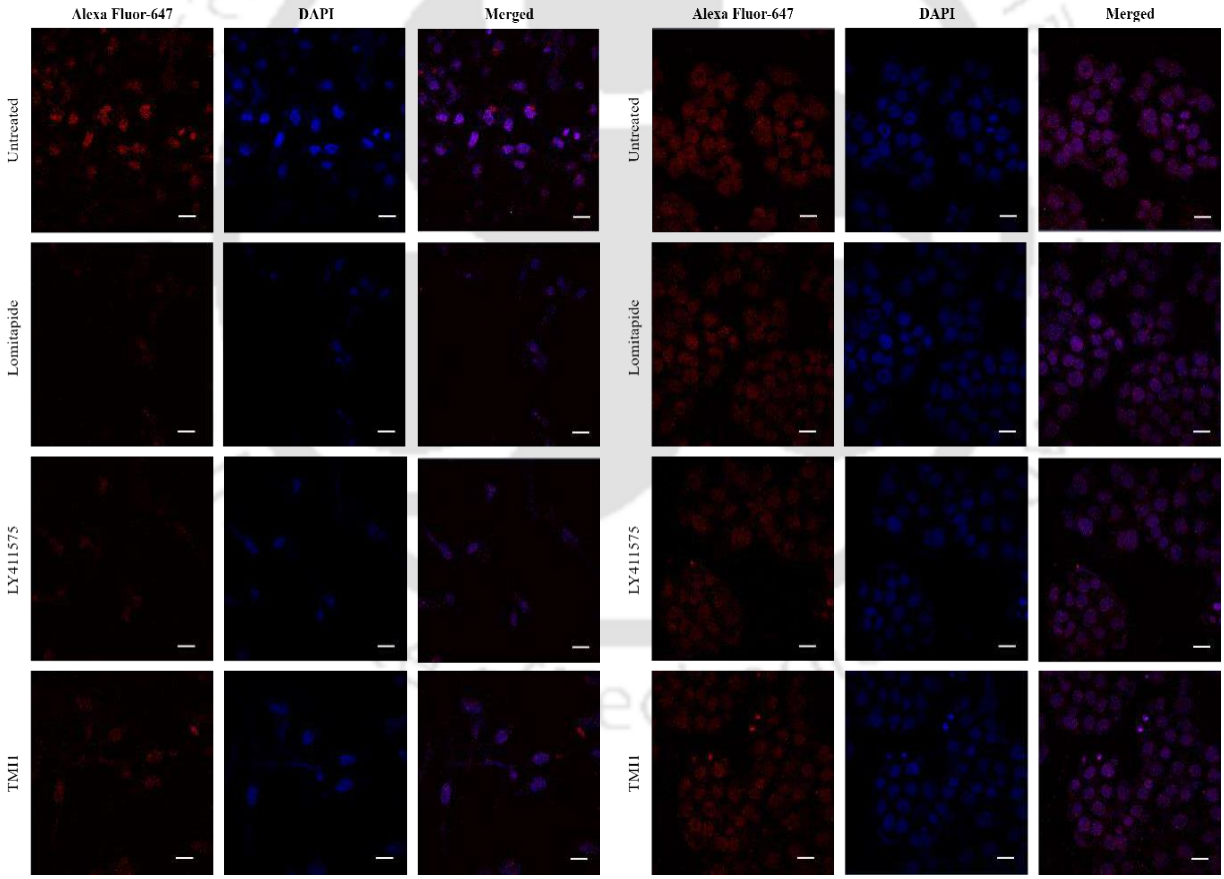

Figure 3.2.13: *Immunocytochemistry of LC3 (left) MDA-MB-231 cells and (right) MDA-MB-468 cells. The formation of the LC3B puncta (red) in cells were observed under confocal microscopy. The nuclei are counterstained with DAPI (blue). The scale bar represents 20 µm.*

3.2.12. Mechanism of action of Lomitapide

Lomitapide exerts its effect by inhibiting the microsomal triglyceride transfer protein (MTTP), which is involved in the loading of triglycerides onto the apolipoprotein B100 that further aids in the assemblage of the VLDLs (very low-density lipoproteins). Hence, by blocking the assembly of VLDLs, Lomitapide reduces VLDL release and VLDL-mediated triglyceride secretion. Altogether, resulting in the inhibition of the production of free fatty acids [110, 111]. However, it is observed that upon inhibition of the MTTP protease, there is a concomitant accumulation of lipid droplets in the cells, which is attributed to the loss in uptake and synthesis of the free fatty acids in the cancer cells. Thus, to observethe effect of Lomitapide on the accumulation of lipid droplets in TNBC cells, Nile Red staining was done [112]. It was observed that following treatment with Lomitapide, there was a significant increase inthe accumulation of lipid droplets. Similarly, LY411575 exhibit a maximum amount of accumulation oflipid droplets inside cells. Therefore, besides Lomitapide, the accumulation of lipid droplets upon treatment with the γ-secretase inhibitor, LY411575 also signifies the prominent role of the Notch pathway in lipid metabolism **(Figure 3.2.14)**.

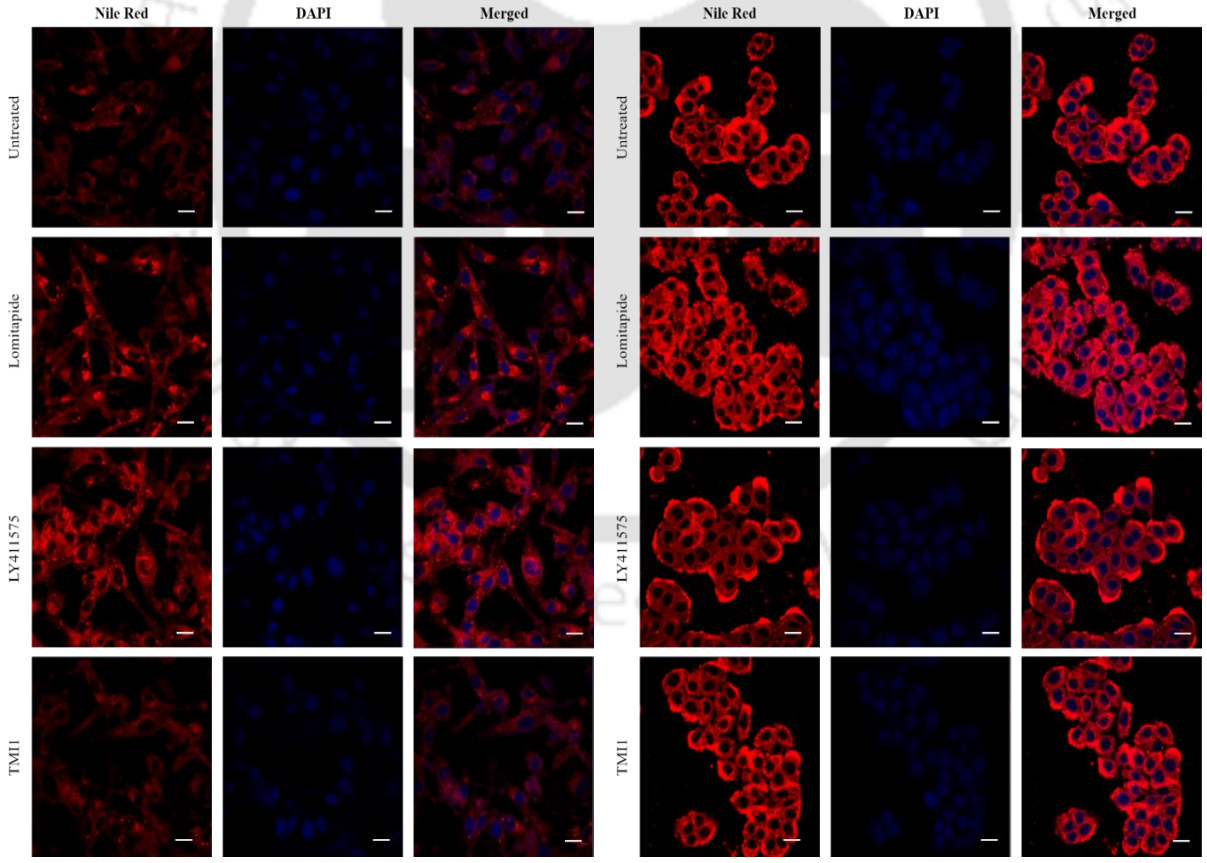

Figure 3.2.14: *Nile Red staining of MDAMDA-MB-231 (left) and MDAMDA-MB-468 (Right). The scale bar represents 20 µm.*

3.2.13. Role of Lomitapide on EMT-induced TNBC cells

The cytotoxic potential of Lomitapide, LY411575 and TMI-1 was also ascertained in the EMT-induced MDA-MB-468 cell model, which provided us with a dose-dependent decrease in cell-viability **(Figure 3.2.15)**. The IC_{50} was observed to be 3.16 µM, 48.2 µM and 15.13 µM for Lomitapide, LY411575 and TMI-1, respectively.

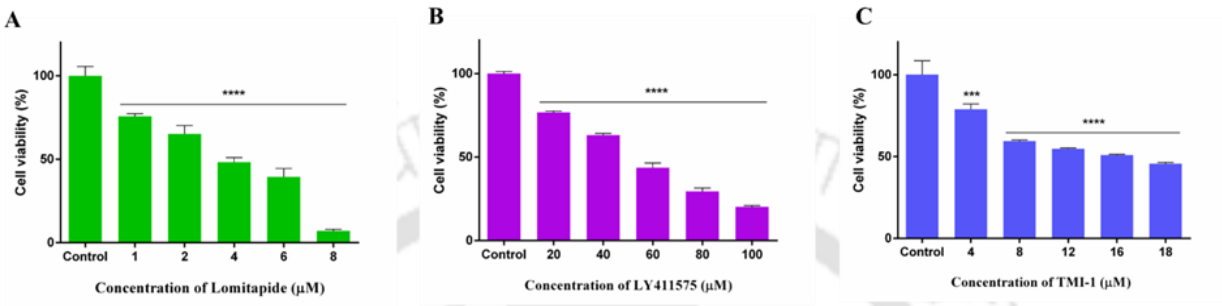

Figure 3.2.15: *Determination of cell viability by MTT assay following treatment with* ***(A)*** *Lomitapide,* ***(B)*** *LY411575,* ***(C)*** *TMI-1 for a time period of 48 h in EMT-induced MDA-MB-468 cells. The results are expressed as the mean ± SEM on the basis of three independent experiments. The statistical significance was obtained in comparison to the untreated control cells. The significance level was set at $p < 0.05$ (*), $p < 0.01$ (**), $p < 0.001$ (***) and $p < 0.0001$ (****).*

Following treatment for a time period of 6 h, a 3.7-fold and a 2.25-fold change increase in the generation of ROS was observed in the Lomitapide and LY411575 treated cells, respectively as compared to the untreated cells. However, the generation of ROS was found to be lessened (~1.25-fold) in the case of TMI-1 treated cells **(Figure 3.2.16)**.

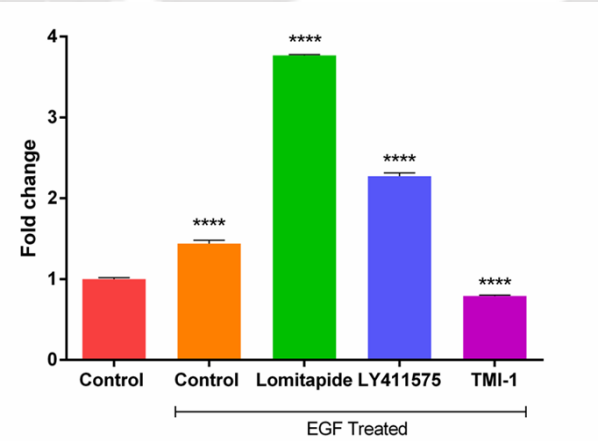

Figure 3.2.16: *Fold-change generation of ROS in the EMT induced MDA-MB-468 cells. The results are expressed as the mean ± SEM on the basis of three independent experiments. The statistical significance was obtained in comparison to the untreated control cells. The significance level was set at $p < 0.05$ (*), $p < 0.01$ (**), $p < 0.001$ (***) and $p < 0.0001$ (****).*

Further, an apoptosis assay was carried out, which also confirms the increase in the number of apoptotic cell populations following treatment. It was observed that Lomitapide increased the apoptotic cell population to 24.54%, while it was found to be 20.14% and 21.18% in the case of LY411575 and TMI-1, as depicted in **(Figure 3.2.17)**.

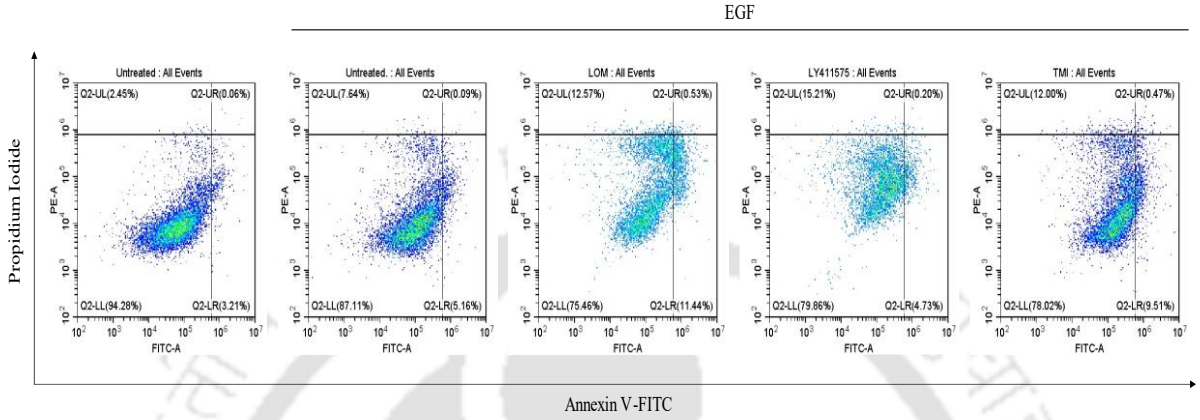

Figure 3.2.17: *Flow cytometric analysis of apoptotic population by annexin-V_FITC/PI assay, following 48 hof treatment in EMT-induced MDA-MB-468 cells.*

Similarly, the stem cell population was assessed using Immuno-flow cytometry. It was observed that following treatment with Lomitapide, there was a significant increase in the population of cells expressing CD24, in comparison to the untreated and EMT-induced cells. Altogether, the data is indicative of the efficacy of Lomitapide in reducing the stemness of EMT-induced MDA-MB-468 cells **(Figure 3.2.18)**.

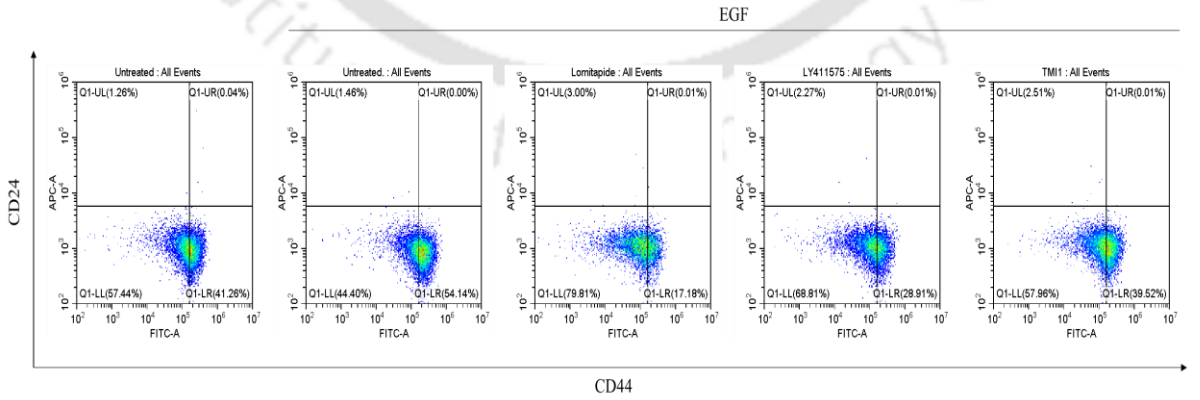

Figure 3.2.18: *The pseudo-plot representation of CD44/CD24 population in EMT induced MDA-MB-468 cells.*

The sphere-forming capability of the EMT-induced MDA-MB-468 was assessed after treatment with the respective compounds. It was found that there was a subsequent degradation and distortion in the formation of spheroids after treatment with Lomitapide and LY411575, thereby depicting the efficacy of the drugs in the EMT-induced cells. Additionally, the colony formation assay also confirmed the prominent role of TMI-1 and Lomitapide in inhibiting the ability of the single cells to survive and reproduce to form colonies in the EMT-induced MDA-MB-468 cells **(Figure 3.2.19).**

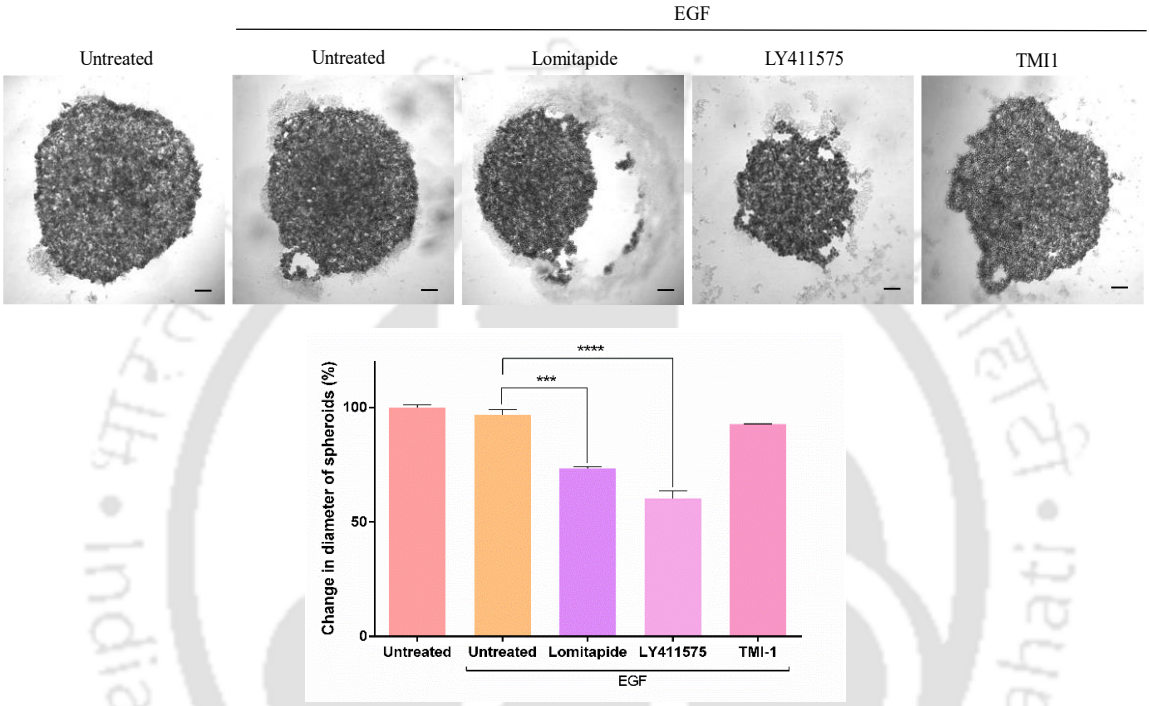

Figure 3.2.19: *Assessment of the spheroid formation ability following treatment in EMT-induced MDA-MB-468 cells. Graphical representation of changes in the* diameter of the spheroids, *following treatment with the respective inhibitors in comparison to the untreated samples in EMT-induced MDA-MB-468. The results are expressed as the mean ± SEM on the basis of three independent experiments. The statistical significance was obtained in comparison to the untreated control cells. The significance level was set at p < 0.05 (*), p < 0.01 (**), p < 0.001 (***) and p < 0.0001 (****).*

Moreover, scratch assay confirms the action of Lomitapide in the migration potential of the EMT-induced MDA-MB-468 cells. It was observed that the wound healing capacity was the lowest subsequent to the treatment with Lomitapide and LY411575, followed by TMI-1 **(Figure 3.2.20)**.

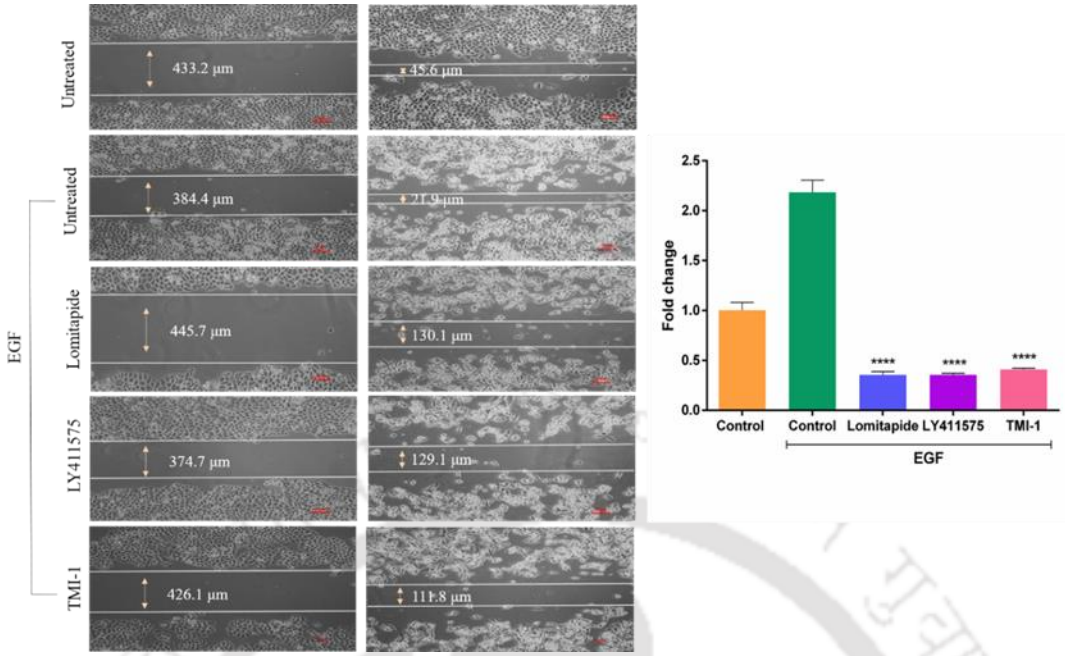

Figure 3.2.20: *Scratch wound-healing assays of EMT-induced MDA-MB-468 cells. Graphical representation of changes in the wound healing capacity following treatment with the respective inhibitors in comparison to the untreated samples in EMT-induced MDA-MB-468 cells. The results are expressed as the mean ± SEM on the basis of three independent experiments. The statistical significance was obtained in comparison to the untreated control cells. The significance level was set at $p < 0.05$ (*), $p < 0.01$ (**), $p < 0.001$ (***) and $p < 0.0001$ (****).*

Furthermore, to understand the effects of Lomitapide on the gene expression profile of the EMT markers, qRT-PCR was performed, following treatment for 24 h and 48 h **(Figure 3.2.21)**. It is observed that there was no significant change observed in the expression profile of E-cadherin after 24 h of treatment. However, a marginal increment of the epithelial marker, E-cadherin by 1.28-fold was observed, following 48 h treatment. Similarly, the mesenchymal genes such as fibronectin and vimentin were found to be downregulated by 1.39-fold and 2.86-fold, respectively, following 48 h of treatment with Lomitapide. Moreover, the expression profile of N-cadherin was found to decrease after 48 h of treatment in comparison to the 24 h treated cells, which was found to decrease from 13.3-fold to 8.76-fold. Similarly, the gene expression profile of the EMT transcription factors, SNAI1 and Twist-1 was found to be downregulated after 48 h of treatment in comparison to the 24 h treated cells. However, in comparison to Lomitapide, both LY411575 and TMI-1 prominently downregulated the gene expression profile of the EMT markers as well as the EMT transcription factors. The fold change in expression of the respective genes subsequent to the treatment is provided in **Table 3.2.6**.

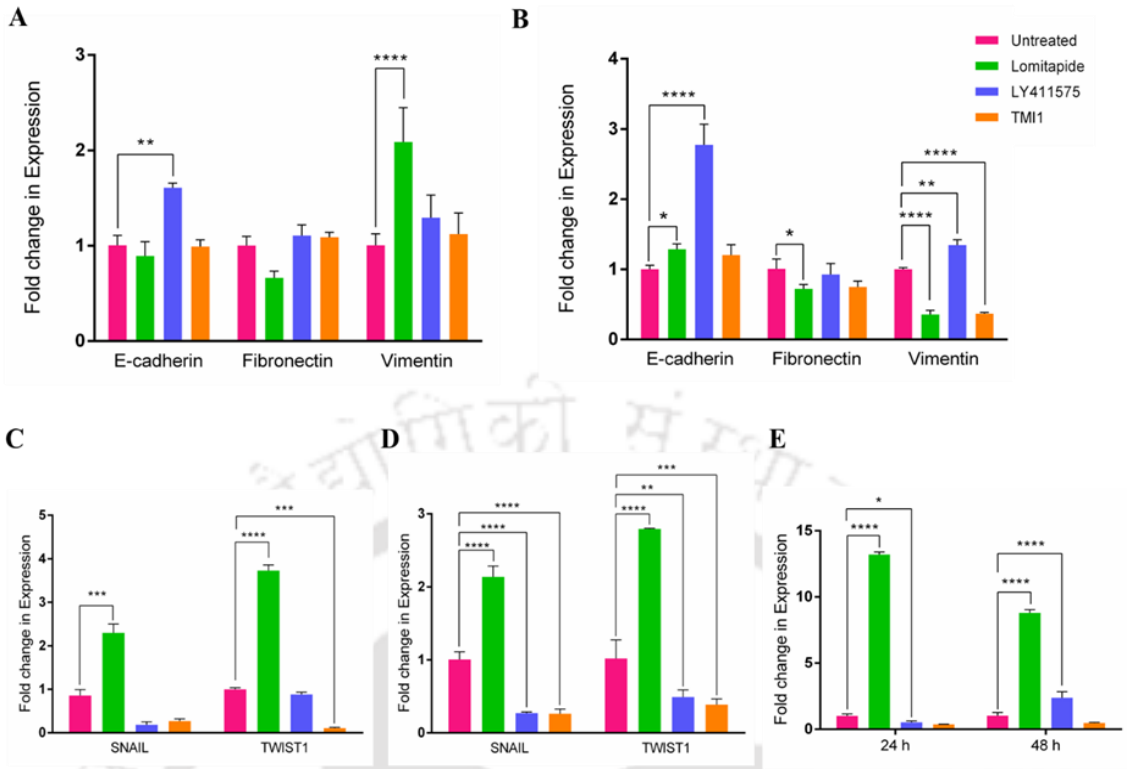

Figure 3.2.21: *Graphical representation of the changes in the expression level of the EMT markers: E- cadherin, Fibronectin and Vimentin, following treatment for a time period of 24 h* ***(A)*** *and 48 h* ***(B)****; Graphical representation of the changes in the expression level of the EMT transcription factors: Snai1 and Twist1, following treatment for a time period of 24 h* ***(C)*** *and 48 h* ***(D)****.* ***(E)*** *Graphical representation of the changes inthe expression level of the EMT marker: N-cadherin, following treatment for a period of 24 h and 48 h. The results are expressed as the mean ± SEM on the basis of three independent experiments. The statistical significance was obtained in comparison to the untreated control cells. The significance level was set at $p < 0.05$ (*), $p < 0.01$ (**), $p < 0.001$ (***) and $p < 0.0001$ (****).*

Table 3.2.6: *Fold change in the gene expression level in EMT induced MDA-MB-468 cells*

Genes	24 h			48 h		
	Lomitapide	LY411575	TMI-1	Lomitapide	LY411575	TMI-1
E-cadherin	- 1.15	** 1.60	- 1.01	* 1.28	- 2.77	**** 1.21
Fibronectin	- 1.52	- 1.11	- 1.08	* 1.39	- 1.08	- 1.34
N-cadherin	- 13.63	- 1.92	- 2.74	-- 8.78	- 2.38	- 2.15
Vimentin	**** 2.08	- 1.29	- 1.11	**** 2.86	** 1.34	**** 2.70
Snai1	*** 2.28	- 5.43	- 3.81	**** 2.13	**** 3.70	**** 3.73
Twist-1	**** 3.72	- 1.13	*** 9.8	**** 2.79	** 2.04	*** 2.63

 # Red depicts upregulation in the expression level, while green depicts downregulation in expression level
The significance level was set at $p < 0.05$ (*), $p < 0.01$ (**), $p < 0.001$ (***) and $p < 0.0001$ (****)

Furthermore, to determine the effects of Lomitapide on the Notch downstream genes in the EMT-induced cell line, an immunoblot assay was performed to determine the protein expression profile following 48 h of treatment **(Figure 3.2.22).** It was observed that the protein expression level of NICD (Notch intracellular domain) was found to be unaltered, whereas the protein expression level of HES-1 was found to be downregulated by 1.87-fold. The fold-change in the expression profile of the respective proteins subsequent to the treatment is provided in **Table 3.2.7**.

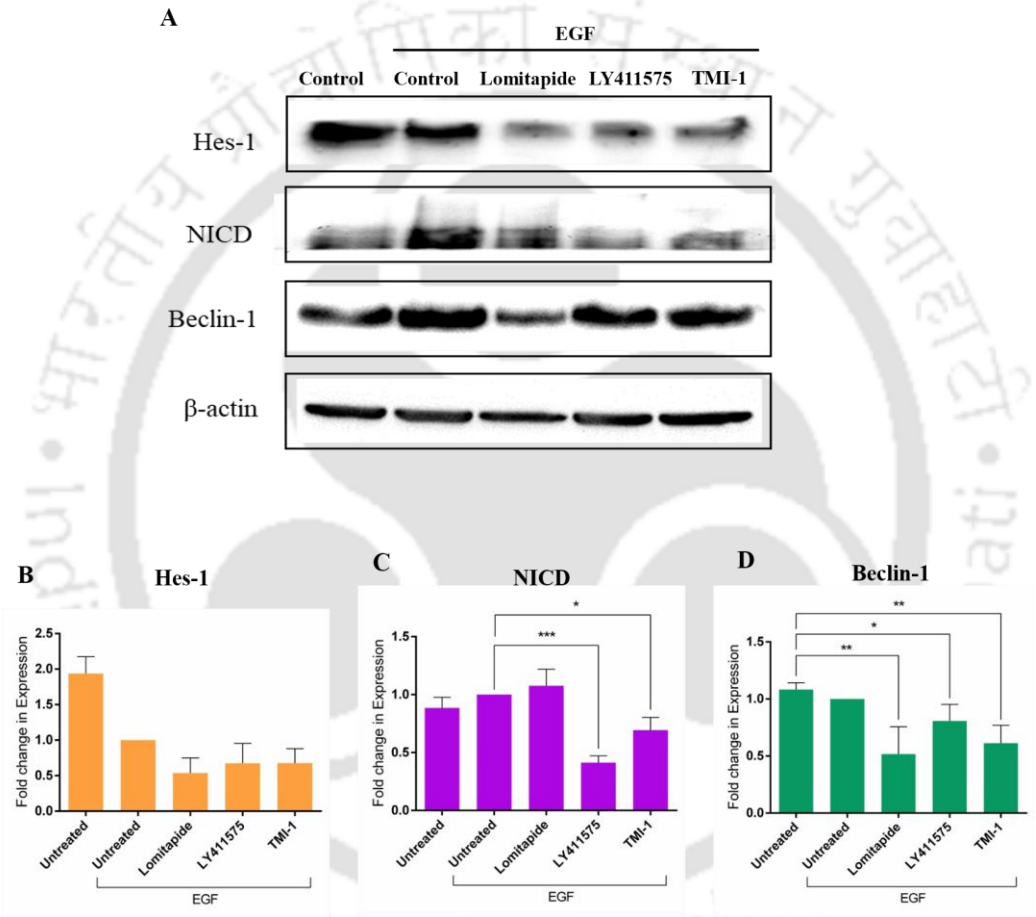

Figure 3.2.22: (A) *Representative western blot showing HES-1, NICD and Beclin-1 in EMT-induced MDA-MB-468 cells. β-actin serves as the loading control. Graphical representation of the changes in the expression level of the proteins* ***(B)*** *HES-1,* ***(C)*** *NICD and* ***(D)*** *Beclin-1 in EMT-induced MDA-MB-468 cells. The results are expressed as the mean ± SEM on the basis of three independent experiments. The statistical significance was obtained in comparison to the untreated control cells. The significance level was set at $p < 0.05$ (*), $p < 0.01$ (**), $p < 0.001$ (***) and $p < 0.0001$ (****).*

Table 3.2.7: *Fold change in the protein expression level in EMT induced MDA-MB-468 cells*

Genes	MDA-MB-468		
	Lomitapide	LY411575	TMI-1
NICD	- 1.08	*** 2.44	* 1.45
HES-1	** 1.87	- 1.35	* 1.48
Beclin-1	** 1.92	* 1.23	** 1.64

 # Red depicts upregulation in the expression level, while green depicts downregulation in expression level
The significance level was set at $p < 0.05$ (*), $p < 0.01$ (**), $p < 0.001$ (***) and $p < 0.0001$ (****)

Autophagy is a double-edged sword in cancer progression and metastasis, but there exists a strong correlation between EMT and autophagy in TNBC. Autophagy enhances the metastatic process by supporting cell survival upon Anoikis, nutrient depletion and metabolic stress [113]. Hence, the necessity to confirm the role of Lomitapide on autophagy in the EMT-induced cell was determined by immunoblot of Beclin-1 **(Figure 3.2.22: A and D)** and immunocytochemistry of LC3 **(Figure 3.2.23: C and Figure 3.2.24)**. It was foundthat Lomitapide decreased the protein expression profile of Beclin-1 by 1.94-fold; whereas there was aconcomitant downregulation in the formation of LC3 puncta, which is suggestive of the fact that Lomitapide inhibits autophagy in the EMT-induced MDA-MB-468 cells. A similar result was also observed following treatment with TMI-1, while a slight decrease in the formation of LC3 puncta was observed following treatment with LY411575 in comparison to the untreated cells (EGF treated). Altogether, these data correlate with the protein expression profile of Beclin-1, indicating the downregulation of autophagy after treatment with the respective Notch inhibitors in MDA-MB-468, thereby suggesting a strong correlation between the Notch signalling pathway, autophagy and EMT.

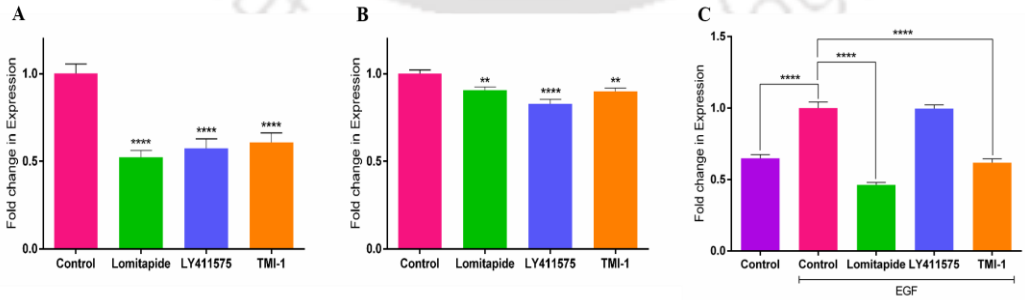

Figure 3.2.23: *Graphical depiction in the fold change alteration in the expression profile (following ICC) of autophagy marker, LC3 in* ***(A)*** *MDA-MB-231,* ***(B)*** *MDA-MB-468 and* ***(C)*** *EMT induced MDA-MB-468. Based on three independent experiments, the results are represented as mean ± SEM, along with a statistical significance denoting $p < 0.5$ (*), $p < 0.1$ (**), $p < 0.01$ (***) and $p < 0.001$ (****).*

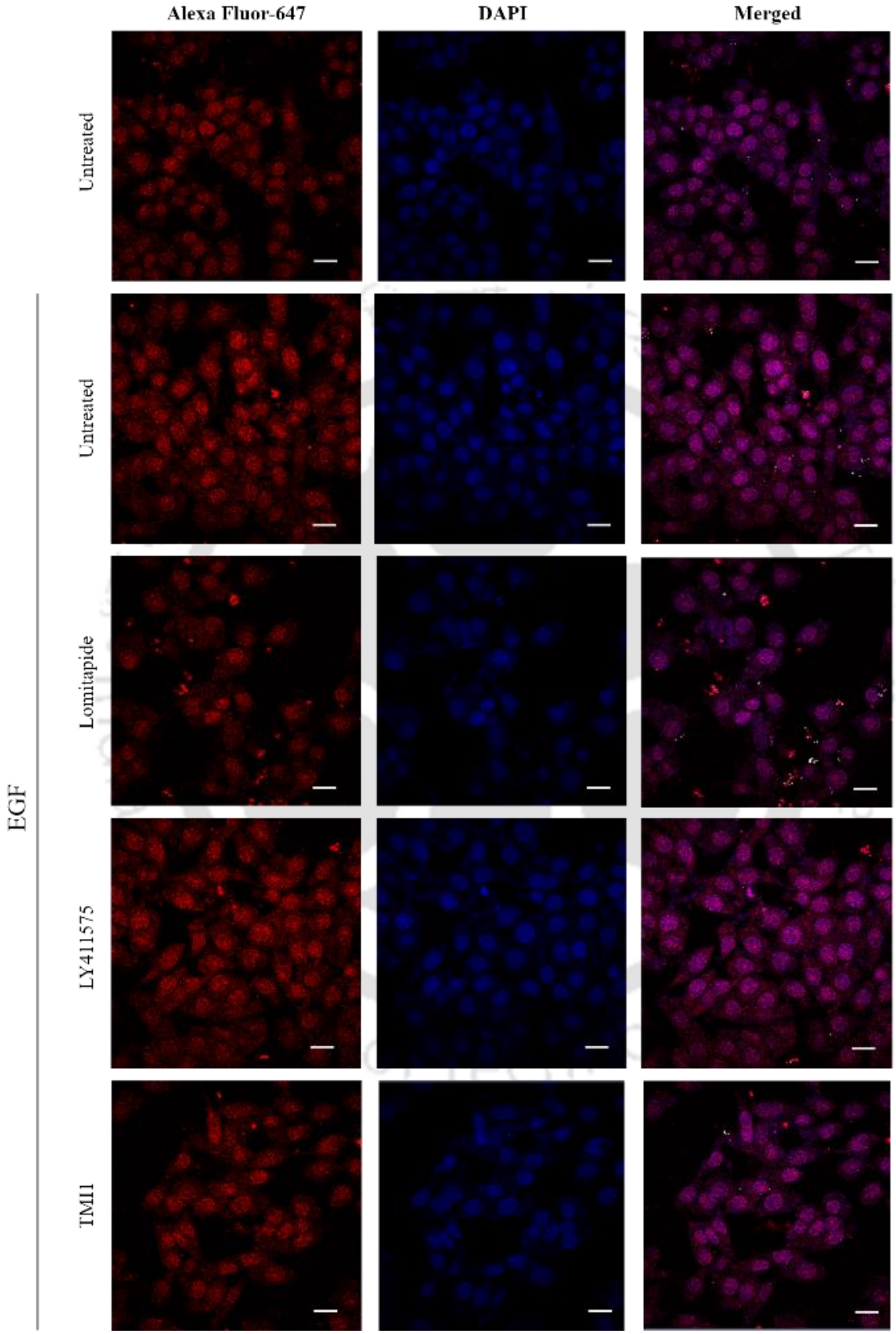

Figure 3.2.24: *Immunocytochemistry of LC3 in EMT induced MDA-MB-468 cells (left). The formation of the LC3B puncta (red) in cells were observed under confocal microscopy. The nuclei are counterstained with DAPI (blue). The scale bar represents 20 µm.*

Additionally, the role of Lomitapide on the EMT-induced MDA-MB-468 cells was determined by Nile red staining. Interestingly, it is observed that following induction of EMT, there is a concomitant reduction of the accumulation of lipid droplets as compared to the untreated cells **(Figure 3.2.25)**. However, there was a significant amount of accumulation of lipid droplets after treatment with Lomitapide, TMI-1 followed by LY411575. Altogether, these data suggest that Lomitapide downregulates the EMT markers, while it effectively downregulates the Notch downstream protein, HES-1 and the autophagy marker, Beclin-1 in the EMT-induced MDA-MB-468 cells. Therefore, providing some basic insights into the role of Lomitapide in successfully inhibiting the EMT in MDA-MB-468 cells.

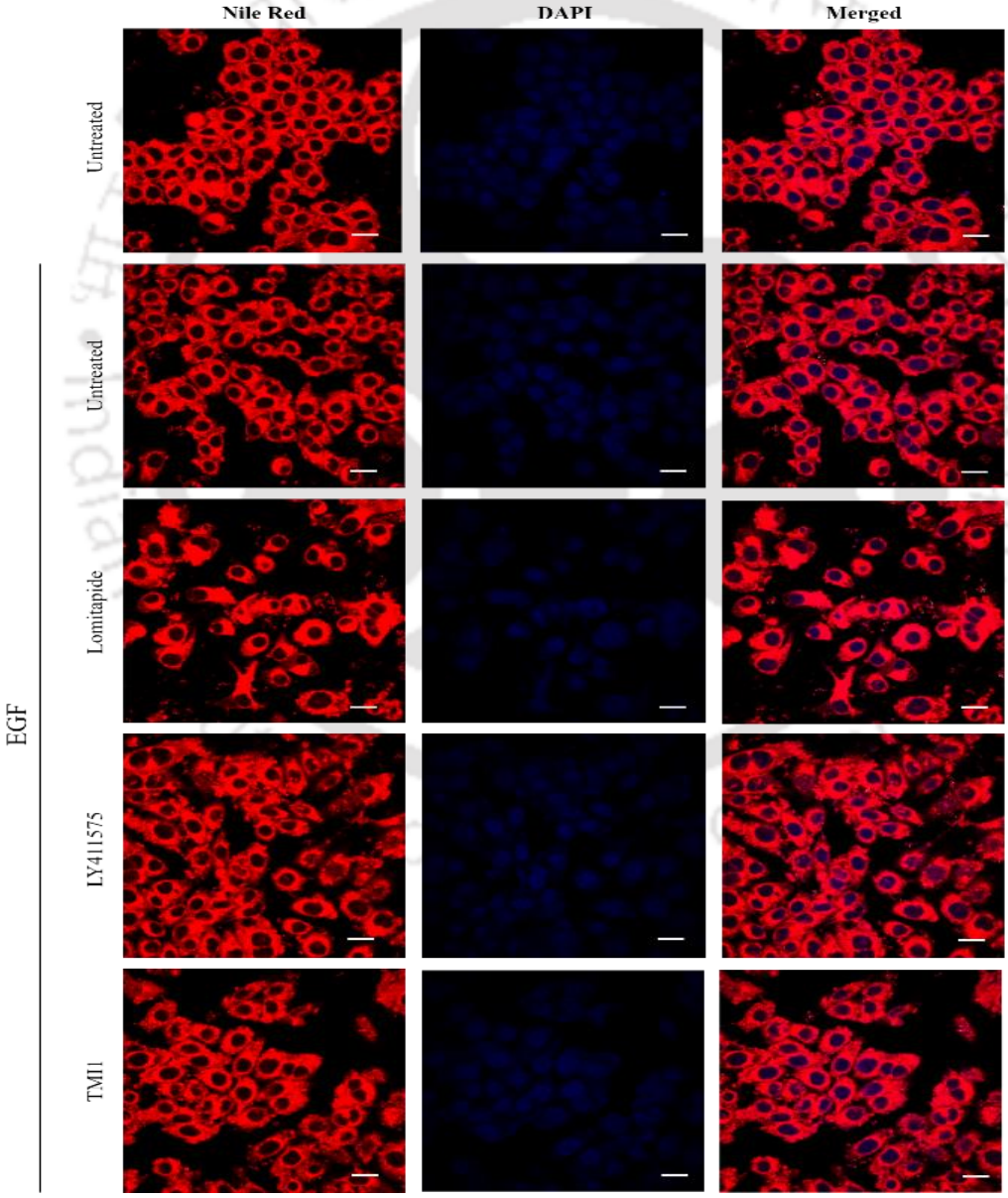

Figure 3.2.25: *Nile Red staining of EMT induced MDA-MB-468. The scale bar represents 20 µm.*

Conclusion

The Notch has been the cynosure signalling pathway that is responsible for imparting numerous aggressive characteristics to cancer cells. It is evident that not only the Notch pathway aids in tumour progression and dissemination but also in the maintenance and metabolic reprograming of cancer cells. Inthis study, *the in-silico* analysis identified potential drugs to target the major proteases of the Notch pathway, which was further substantiated by *in-vitro* studies. From *in-silico* analysis, Lomitapide, an FDA-approved drug, which is used for the treatment of hypercholesterolemia, was chosen from among the library of 1293 drugs, with an aim to repurpose it in the treatment of TNBC. However, i*n vitro,* validations ascertained the efficacy of Lomitapide with outstanding anti-cancer properties, which is attributed to its inherent nature of metabolic rewiring. Lomitapide is responsible for inhibiting the MTTP (microsomal triglyceride transfer protease), thereby resulting in the downregulation of VLDL and triglycerides. Further, the higher amount of lipid droplets observed in the cells treated with Lomitapide accounts for the inhibition of MTTP protease that had impaired lipid metabolism of the TNBC cells. The relationship between autophagy and lipid metabolism is quite intriguing, while in a stressful environment, lipid metabolism is involved in the formation of autophagosomes, in other instances autophagy promotes lipid catabolism [114]. Research evidence suggests that Lomitapide induces autophagy via the AMPK/Beclin1-mediated pathway in colorectal cancer [115]. Herein, it is observed that Lomitapide slightly downregulates the expression of Beclin-1 in MDA-MB-231 cells, while its expression remainsalmost unaltered in MDA-MB-468 cells. However, there is a concomitant reduction in the formation of LC3 puncta in both the TNBC cells treated with Lomitapide. Altogether it suggests the role of Lomitapide in inhibiting autophagy in the TNBC cells.

It is widely known that EMT, CSCs (cancer stem cells) and autophagy are the three prime contributing factors of cancer metastasis [116]. In this study, it is observed that there was a significant upregulation in the formation of LC3 puncta in the EMT-induced cells as compared to the untreated MDA-MB-468 cells, signifying the activation of autophagy in the EMT-induced cells. Besides autophagy, Lomitapide exhibits remarkable properties in the inhibition of EMT. Not only does Lomitapide downregulate the expression of EMT markers, but it also induces ROS by 3.7-fold. Moreover, it also aids in apoptosis and diminishes the migration potential by ~3.12-fold. Additionally, it also reduces the stemness properties and the ability to form colonies and spheres in the EMT-induced MDA-MB-468 cells. Hence, it provides insights into the role of Lomitapide in inhibiting proliferative, metastatic and invasive properties of the TNBC cells.

Moreover, the action of Lomitapide was also ascertained on the human embryonic kidney cell line, HEK293, which exhibited IC50 at a higher concentration (15.33 μM) in comparison to that of the TNBC cells. Additionally, the western blot analysis reveals negligible fluctuations in the protein expression profile of the Notch downstream proteins (NICD and HES-1), thereby ruling out the inimical

impact of the drug on normal cells. Altogether, the present work suggests that in comparison to the inhibitors for TACE (TMI-1) and γ-secretase enzyme (LY411575), Lomitapide effectively exhibits anti-cell proliferative activity. While γ-secretase was very prominent in the inhibition of the Notch pathway, the TMI1 was found to be effective in reducing the migration properties of TNBC in comparison to the Lomitapide-treated cells. Further, these Notch signalling-targeted compounds predominantly inhibited the phenomenon of EMT, thereby suggesting the strong correlation between the Notch pathway and EMT. Conclusively, Lomitapide has been evaluated as an effective repurposed drug to inhibit TNBC progression and dissemination in comparison to the Notch inhibitors. Hence, the study provides a preclinical rationale for manoeuvring Lomitapide in the future treatment of TNBC.

3.3. The γ-secretase inhibitor, LY411575 potentiates the activity of Suberoylanilide hydroxamic acid (SAHA) by inhibiting its ability to induce EMT via the activation of the Notch signalling pathway in TNBC cells

- (Manuscript communicated)

Results and Discussions

Abstract

HDACIs, such as SAHA possess great therapeutic value for TNBC patients. However, their inherent ability to induce EMT in various malignancies has been of greater concern. Herein, it was hypothesized that SAHA facilitates EMT via activation of the Notch pathway. In the present study, it is evident that HDAC mediates the formation of the co-repressor complex upon interacting with the CSL (CBF1, Suppressor of Hairless, Lag-1), thereby inhibiting the transcription of the Notch target genes. Hence, the use of HDACIs (such as SAHA) facilitates the transcriptional activation of the Notch target genes, by disrupting the corepressor complex and recruiting the coactivator complex, thereby facilitating EMT. SAHA also upregulates the protein expression profile of the Notch ligands (such as JAG1, and JAG2), thereby aberrantly activating the signalling pathway. Therefore, the main focus was on combination therapy using a γ-secretase inhibitor, LY411575 that would enhance the efficacy of SAHA by blocking the canonical Notch pathway mediated via NICD. It was observed that co-treatment synergistically mediates apoptosis, generates ROS, depolarizes mitochondria, and diminishes the stemness properties. Besides, it also mediates autophagy-independent cell death, and diminishes the expression of inflammatory cytokines, along with the downregulation in the expression of the Notch downstream genes, EMT markers and EMT-TFs. Altogether, the current study provides a mechanistic basis for combating EMT potentiated by SAHA, which could be utilized as a rational strategy for the treatment of solid tumours, especially TNBC.

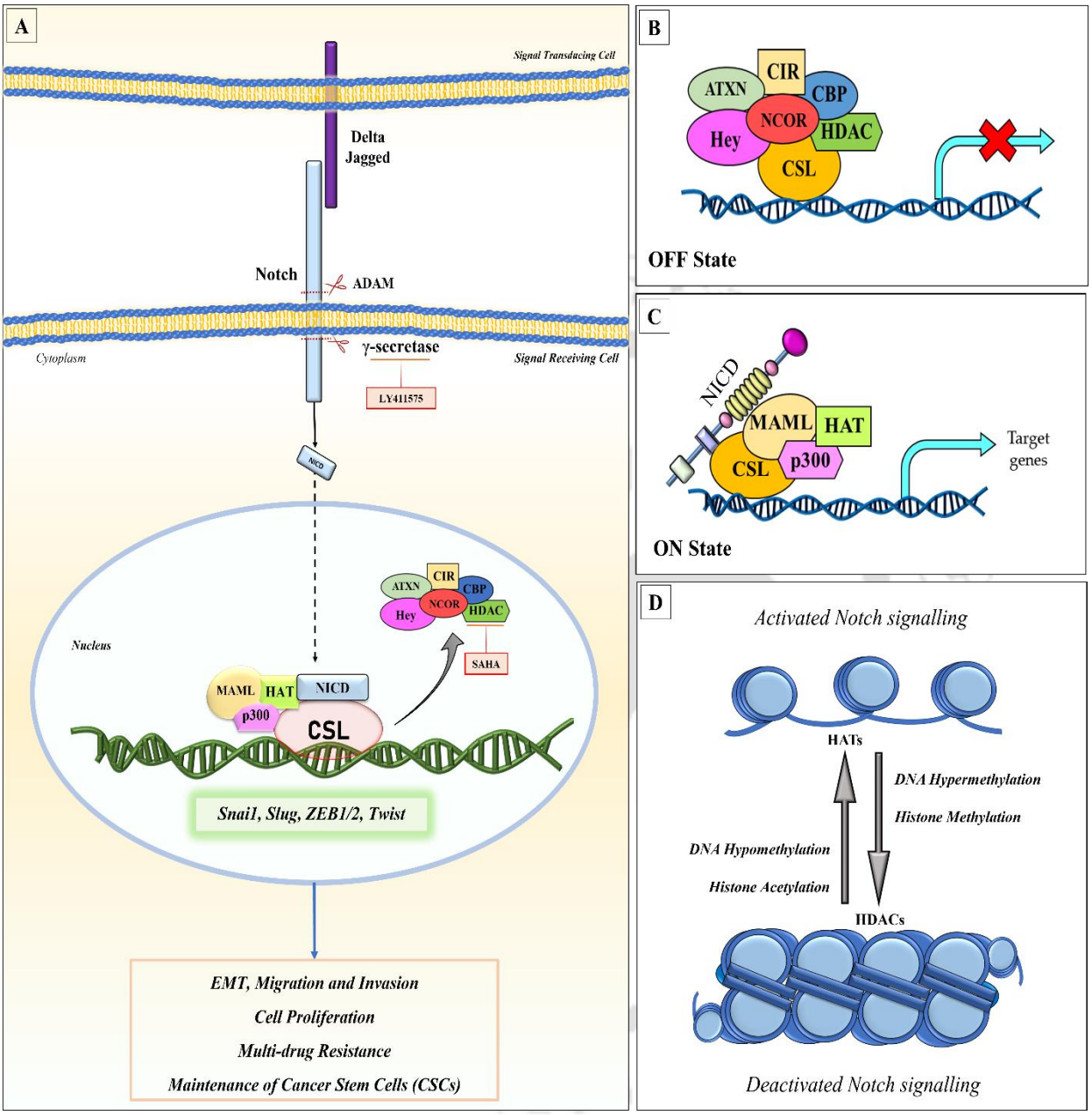

Schematic 3.3.1: *Schematic illustration of the work.* ***(A)****. The Notch pathway gets activated when the DSL ligands (Delta, Serrate and Jagged) comes in contact with the Notch receptor thereby activating a series of proteolytic cleavage facilitated by ADAM and γ-secretase. This result in the generation of NICD, which has the capability of traversing through the nucleus and binds to the CSL (a DNA binding domain), thereby activating the Notch downstream genes and EMT transcription factors. Alternatively, SAHA also blocks the HDAC, a component of the co-repressor complex, which further activates the Notch signalling pathway.* ***(B)*** *Components of the co-repressor complex when Notch pathway is not activated (i.e, in OFF state).* ***(C)*** *Components of the co-activator complex when Notch pathway gets activated (i.e., in ON state).* ***(D)*** *Epigenetic modifications in activated and deactivated Notch pathway. (Concept source: https://doi.org/10.1021/acsptsci.2c00239)*

3.3.1. Role of HDACs in the Notch signalling pathway

Besides the various proteins in the inhibitory complex, HDAC1 and HDAC2 also downregulate the Notch signalling pathway. The functional network analysis, using the Strings v9.1 database endowed us with the list of 47 protein interactors of CSL, with a PPI (Protein-Protein Interaction) enrichment value of <1.0e-16 **(Figure 3.3.1)**.

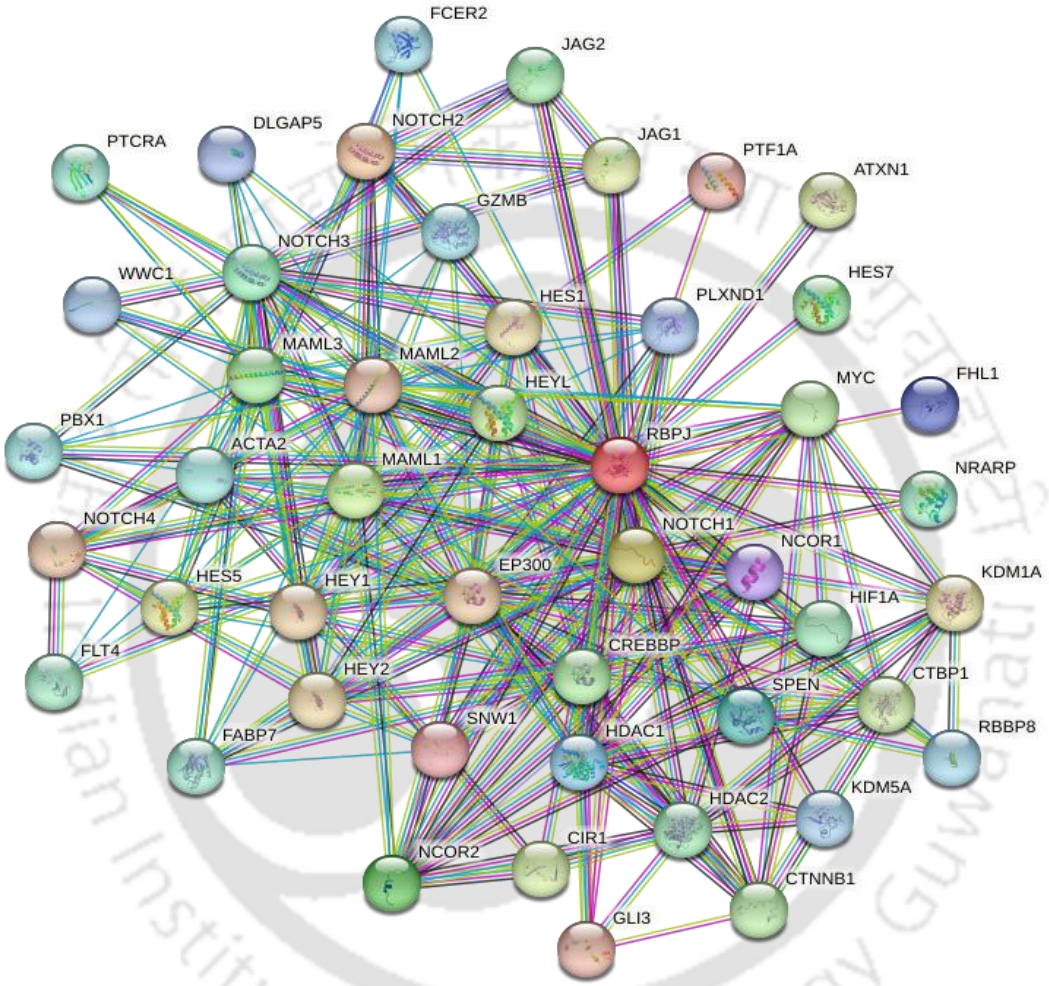

Figure 3.3.1: *STRINGs image of the interacting proteins with the query protein RBPJ (CSL). Briefly, RBPJ for Homo Sapiens was fed as the query molecule. The interacting network was restricted to the first shell, with a confidence score of 0.7 that is indicated to be of significant reliability.*

Gene ontology analysis was performed to obtain a hierarchical classification of the following genes, which showed their significant biological processes **(Figure 3.3.2), the** KEGG pathway enrichment graph illustrating the association of these genes in a particular signalling pathway **(Figure 3.3.2)** and the commonly used drug against them, obtained from the Drug Bank, using the Web Gestalt database **(Figure 3.3.2)**. Moreover, Vorinostat (SAHA) was selected for proving our hypothesis in the TNBC cells.

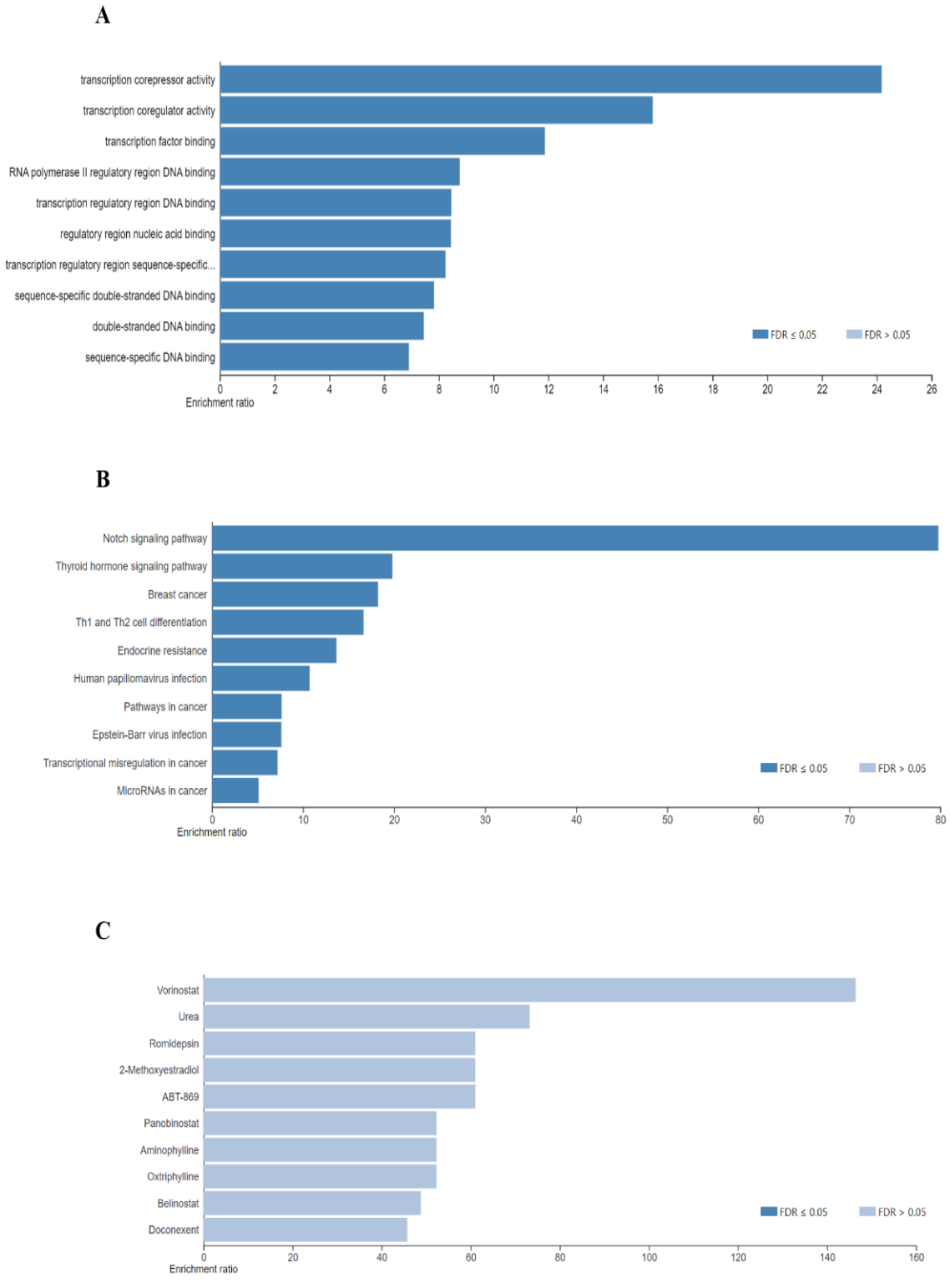

Figure 3.2.2: *Graph depicting the* ***(A)*** *biological processes;* ***(B)*** *KEGG pathway enrichment graph illustrating the association of these genes in a particular signalling pathway;* ***(C)*** *drug used against them obtained from the Drug Bank, using Web Gestalt database*

3.3.2. SAHA effectively downregulates the HDAC activity

The HDAC activity was measured following treatment with the respective inhibitors alone and in combination. It was observed that following combination therapy, the HDAC activity was found to be downregulated by 1.58-fold and 5.77-fold in MDA-MB-231 and MDA-MB-468, respectively. The HDAC activity remained almost unchanged following treatment with LY411575 in both the cell lines; whereas, after treatment with SAHA, there was 1.1-fold and 1.71-fold downregulation in the HDAC activity in MDA-MB-231 and MDA-MB-468 cells, respectively (as depicted in **Figure 3.3.3**). However, the underlying molecular mechanisms for the synergistic effect of the combination therapy on HDAC activity remain obscure.

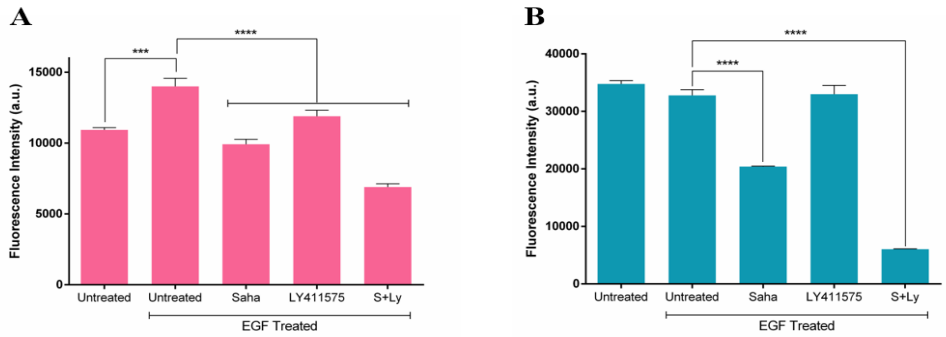

Figure 3.3.3: *HDAC activity assay in* ***(A)*** *MDA-MB-231 and* ***(B)*** *MDA-MB-468 cells. The results are expressed as the mean ± SEM based on three independent experiments. The statistical significance was assessed in comparison to the untreated cells. The significance level was set at $p < 0.05$ (*), $p < 0.01$ (**), $p < 0.001$ (***) and $p < 0.0001$ (****).*

3.3.3. Combination therapy with SAHA and LY411575 synergistically inhibits the overall survival of the TNBC cells *in vitro*

In order to examine the effects of SAHA and the γ-secretase inhibitor, LY411575 on TNBC cell survival, an MTT assay was performed. Upon treatment with the respective inhibitors in monotherapy and combination, a dose-dependent decrease in cell viability was observed in the EMT-induced TNBC cells (MDA-MB-231 and MDA-MB-468). In comparison to SAHA, a higher dose of the LY411575 was required to obtain the IC_{50} in both cell lines. Moreover, it was observed that the combination of SAHA with LY411575, decreased the cell viability in a dose-dependent manner **(Figure 3.3.4)**.

The combination index calculated using the Chou-Talay method revealed a synergistic effect of the two drugs at higher concentrations. However, at lower concentrations of both SAHA and LY411575 in MDA-MB-468 cells, the CI was found to be >1, which indicates the antagonistic effects of the two drugs at lower concentrations. Hence, it was concluded that the administration of the two drugs in combination yields higher anti-proliferative effects in comparison to their respective monotherapy *in vitro*.

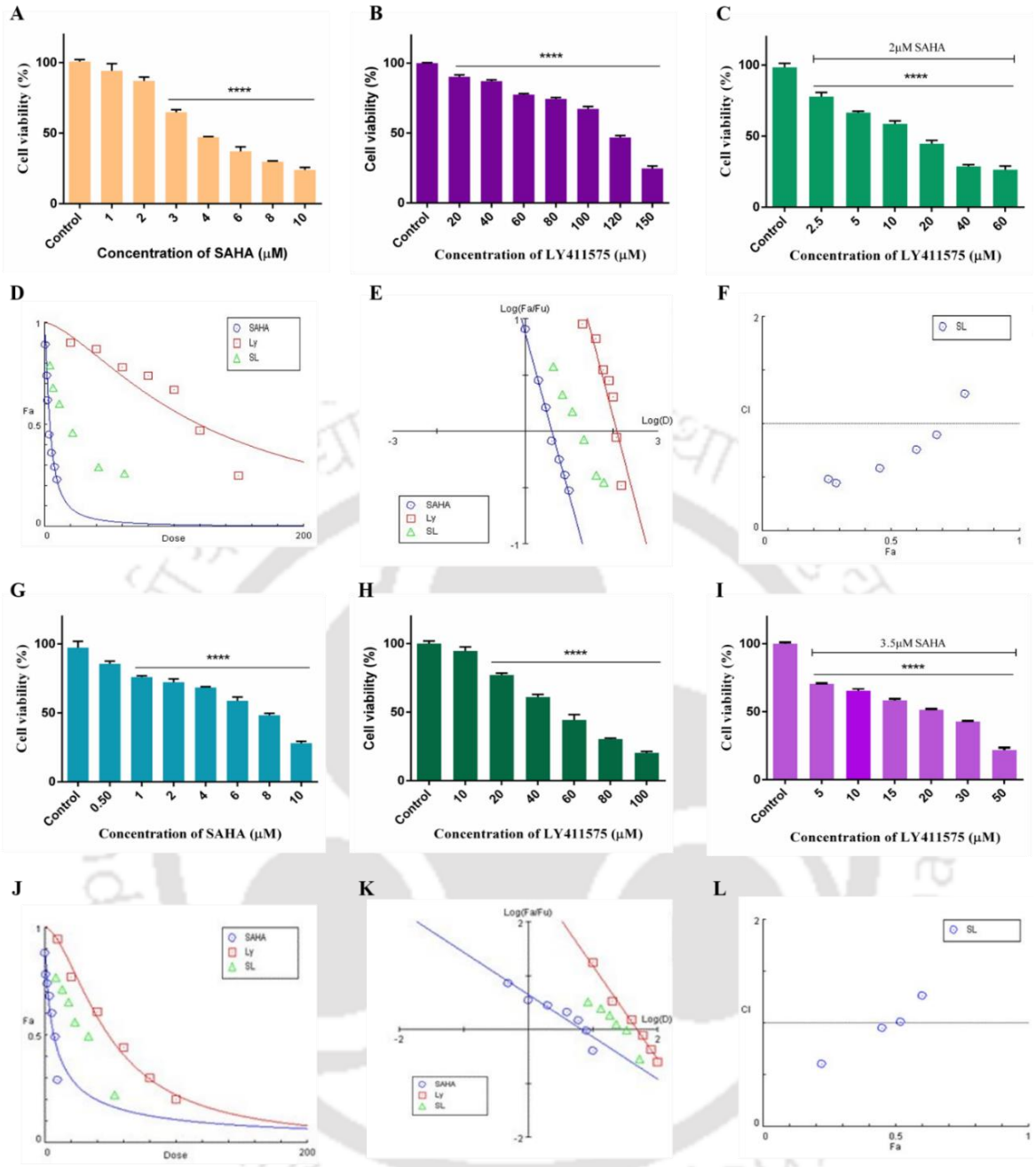

Figure 3.3.4: *Determination of viability of EMT-induced TNBC cell lines (MDA-MB-231 and MDA-MB-468) monolayer cultures by MTT assay, upon treatment with inhibitors for a period of 48 h.* ***(A)****,* ***(B)****, and* ***(C)*** *refer to thetreatment with SAHA, LY411575 and SAHA+LY411575, respectively in MDA-MB-231.* ***D*** *depicts the dose-effect curve,* ***(E)*** *depicts Median-Effect Plot, and* ***(F)*** *depicts Combination Index Plot for MDA-MB-231 following combination treatment. Similarly,* ***(G)****,* ***(H)****, and* ***(I)*** *refer to the treatment with SAHA, LY411575 and SAHA+LY411575, respectively in MDA-MB-468.* ***(J)*** *depicts the dose-effect curve,* ***(K)*** *depicts Median-Effect Plot, and* ***(L)*** *depicts Combination Index Plot for MDA-MB-468 following combination treatment. Drug combinationswith CI<1 are considered synergistic, while CI=1 is considered additive, while CI>1 is considered synergistic. The results are expressed as the mean ± SEM based on three independent experiments. The statistical significance was assessed in comparison to the untreated cells. The significance level was set at $p < 0.05$ (*), $p < 0.01$ (**), $p < 0.001$ (***) and $p < 0.0001$ (****).*

Moreover, similar results were obtained in the case of MCF7 and HEK293 cells. However, the IC_{50} obtained for SAHA in HEK293 was much higher in comparison to the breast cancer cells **(Figure 3.3.5)**. Further, the combination index calculated revealed a synergistic effect of the two drugs at higher concentrations in MCF7. However, no such synergism was observed in the case of HEK293 cells **(Figure 3.3.6).**

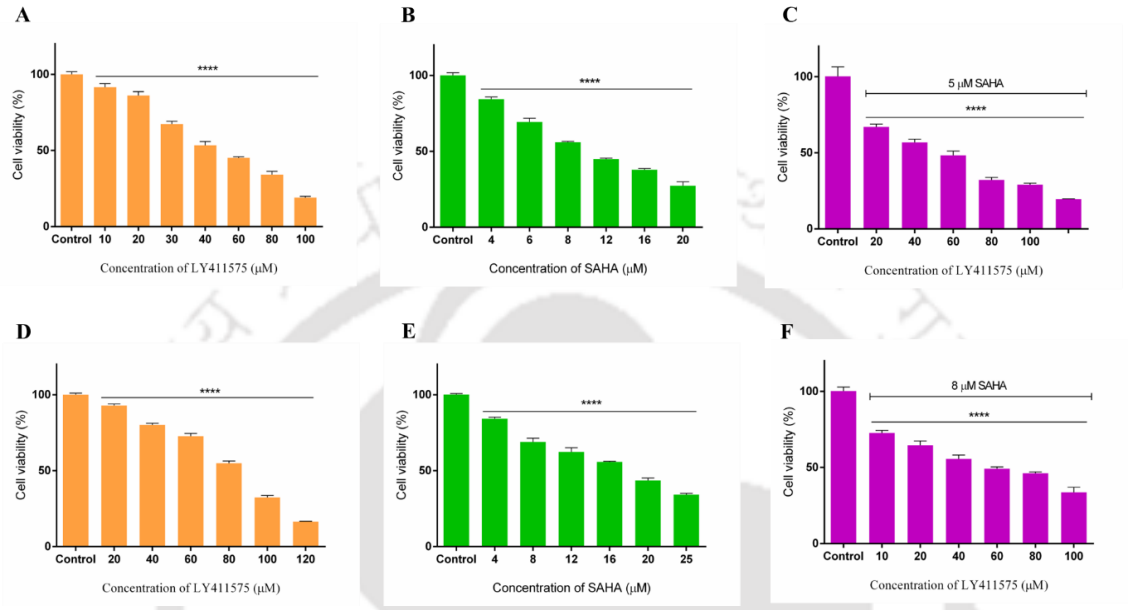

Figure 3.3.5: *Determination of viability by MTT assay, upon treatment with inhibitors for a period of 48 h.* ***(A)****,* ***(B)****, and* ***(C)*** *refers to the treatment with LY411575, SAHA and SAHA+LY411575, respectively in MCF7.* ***(D)****,* ***(E)****, and* ***(F)*** *refers to the treatment with LY411575, SAHA and SAHA+LY411575, respectively in HEK293 cells. The results are expressed as the mean ± SEM based on three independent experiments. The statistical significance was assessed in comparison to the untreated cells. The significance level was set at p < 0.05 (*), p< 0.01 (**), p < 0.001 (***) and p < 0.0001 (****).*

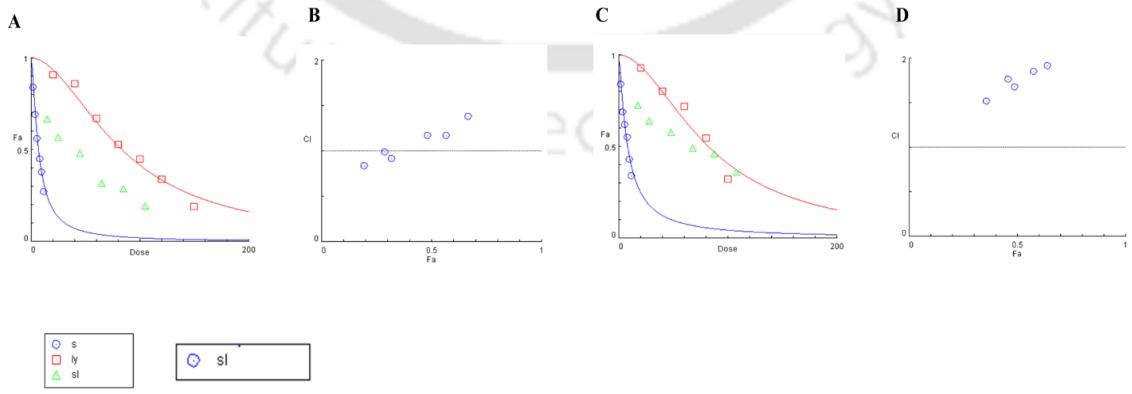

Figure 3.3.6: *Dose effect curve of the breast cancer cells* ***(A)*** *MCF7 and* ***(C)*** *human embryonic kidney cells (HEK293) treated with SAHA (s), LY411575 (ly), and their combination (sl) respectively. Combination Index plot for* ***(B)*** *MCF7 and* ***(D)*** *HEK293 cells.*

3.3.4. The combination therapy generates ROS, induces apoptosis, depolarizes the mitochondrial membrane potential along with inducing G0/G1 arrest.

To demonstrate the cytotoxic effects of the drugs on the respective cell lines, the generation of ROS was examined. From the flow cytometry data, it is observed that LY411575, induced the generation of ROS by 2.7-fold in comparison to the MDA-MB-231 untreated cells. However, there was an increase in the generation of ROS by 2-fold in SAHA-treated cells and by 1.32-fold in combination (LY411575 and SAHA) treatment in the MDA-MB-231 cells **(Figure 3.3.7)**. Similarly, the generation of ROS was found to be 1.16-fold, 1.8-fold and 1.5-fold in LY411575, SAHA and combination treatment, respectively, as compared to the untreated MDA-MB-468 cells.

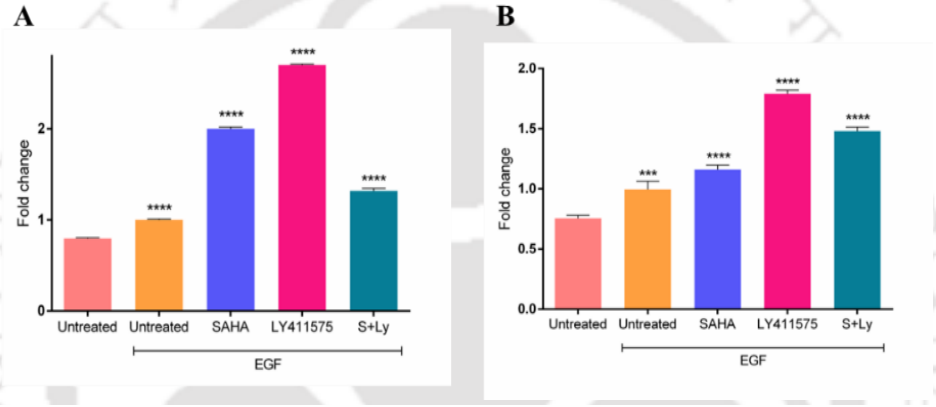

Figure 3.3.7: *Graphical representation of the generation of ROS following respective treatments in* ***(A)*** *MDA-MB-231 and* ***(B)*** *MDA-MB-468. The results are expressed as the mean ± SEM based on three independent experiments. The statistical significance was assessed in comparison to the untreated cells. The significance level was set at $p < 0.05$ (*), $p < 0.01$ (**), $p < 0.001$ (***) and $p < 0.0001$ (****).*

The elevated levels of ROS usually manifest their pernicious effect on the integrity of the mitochondrial membrane potential, which is assessed using JC-1-based flow cytometry. Hence, the present observation concluded a prominent red fluorescence from the healthy mitochondria and a 29.84% and 23.82% increase in the intensity of green fluorescence from the treated MDA-MB-231 and MDA-MB-468 cells, respectively, suggesting the loss of mitochondrial membrane integrity post-combination treatment **(Figure 3.3.8)**.

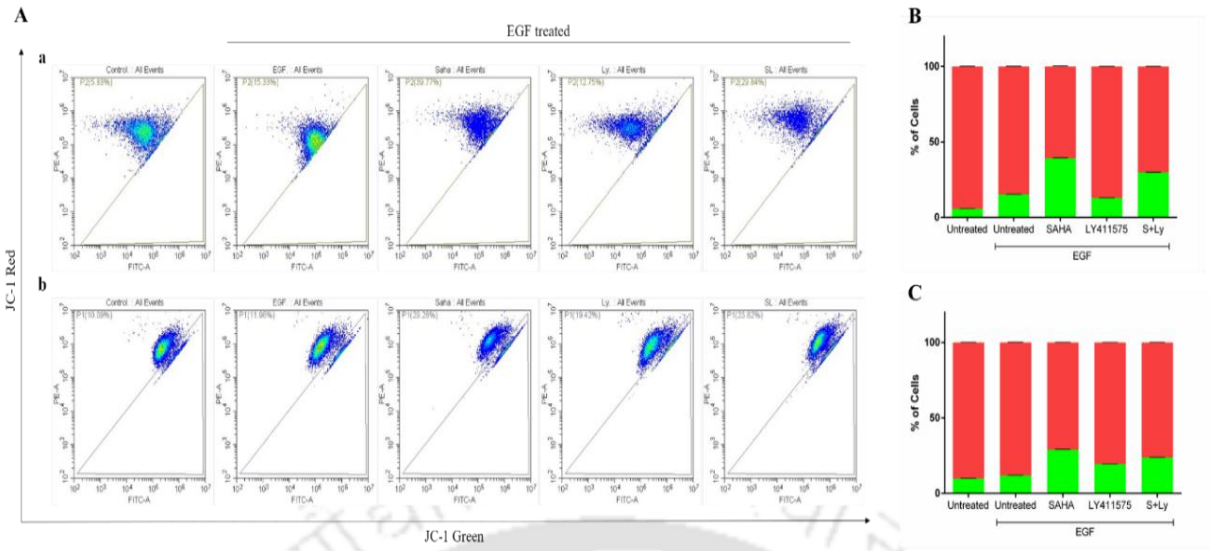

Figure 3.3.8: (A) *Assessment of Mitochondrial membrane potential using JC-1 based flow cytometry in* ***(a)*** *MDA-MB-231 and* ***(b)*** *MDA-MB-468 cells. Graphical representation of the green vs red fluorescence following mitochondrial depolarization in* ***(B)*** *MDA-MB-231 and* ***(C)*** *MDA-MB-468. The results are expressed as the mean ± SEM based on three independent experiments. The statistical significance was assessed in comparison to the untreated cells. The significance level was set at $p < 0.05$ (*), $p < 0.01$ (**), $p < 0.001$ (***) and $p < 0.0001$ (****).*

The generation of reactive oxygen species and the dysfunction of the mitochondrial membrane potential is an indication of the initiation of apoptosis via receptor-mediated activation of apoptotic pathway genes (such as caspases and the Bcl-2 family of proteins). The percentage of apoptotic and necrotic cell populations was evaluated post-treatment using flow cytometry. It was observed that co-therapy increased apoptotic cell populations by approximately 41.69% and 34.91% in MDA-MB-231 and MDA-MB-468 cells, respectively **(Figure 3.3.9)**.

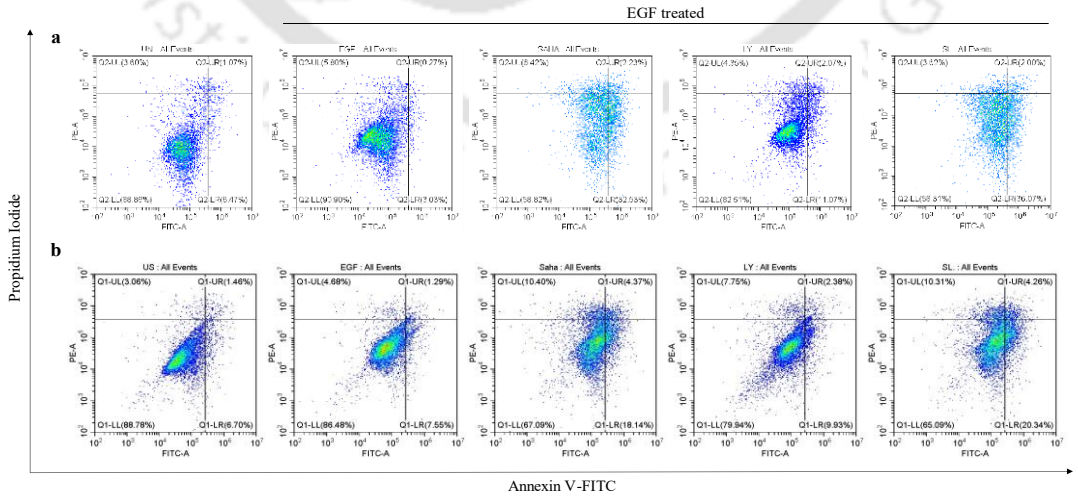

Figure 3.3.9: *Flow cytometric analysis of the apoptotic and necrotic populations probed by Annexin V-FITC/PI based assay following treatment with the respective inhibitors in* ***(a)*** *MDA-MB-231 and* ***(b)*** *MDA-MB-468 cells.*

Further, the effect of SAHA on the cell cycle progression was assessed by PI-based Flow cytometric analysis **(Figure 2: C and D)**. It was observed that SAHA in monotherapy as well as in combination treatment increased the sub-G0 population of the cells, which is in coherence with the increase in apoptotic cell populations. It is also observed from previous studies that SAHA is responsible for the upregulation of the Sub-G0/G1 population in colon cancer cells [117], breast cancer cells [118], etc.

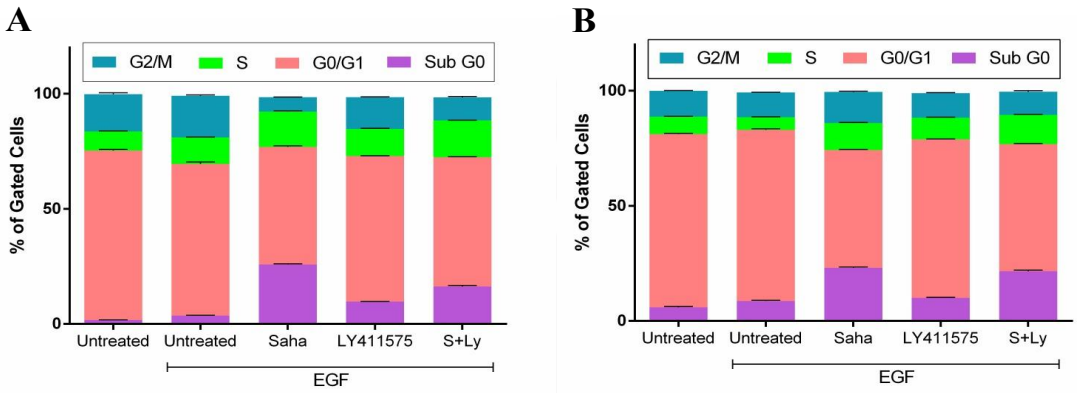

Figure 3.3.10: *Evaluation of the cell cycle profile of* ***(A)*** *MDA-MB-231 and* ***(B)*** *MDA-MB-468.*

3.3.5. SAHA activates the Notch signalling pathway, thereby upregulating the expression of the Notch downstream genes

Owing to the correlation of the HDACs and the Notch pathway, initially, the effect of SAHA on the Notch downstream genes, such as NICD, p21, HES-1, and HEY-1 was ascertained by qRT-PCR analysis. It was observed that there was a significant downregulation in the gene expression profile following combination therapy in both cell lines **(Figure 3.3.11)**. It is interesting to note that the expression profile of the Notch downstream genes was upregulated after treatment with SAHA. For example, there was a 1.66-fold and 2.56-fold increase in the expression of HES-1 in MDA-MB-231 and MDA-MB-468 cells, respectively. Also, there was a 2.44-fold increase in the expression of HEY-1 in MDA-MB-468 cells. However, not much changes were observed in the gene expression profile of HEY-1 in MDA-MB-231 cells.

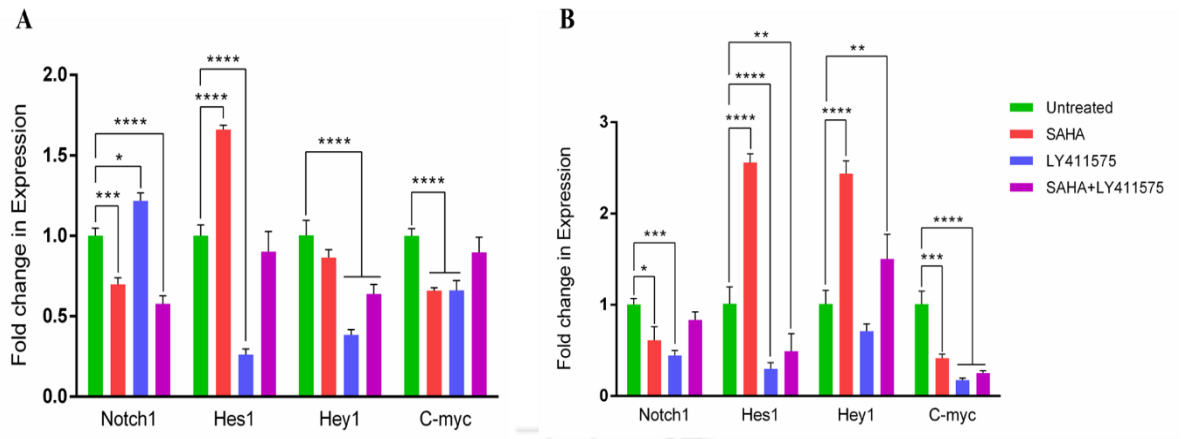

Figure 3.3.11: *Graphical representation of changes in gene expression levels following treatment with the inhibitors in monotherapy as well as in combination therapy as quantified by qRT-PCR analysis.* ***(A)*** *and* ***(B)*** *show gene expression levels obtained from MDA-MB-231 and MDA-MB-468 monolayer cultures, respectively. The results are expressed as the mean ± SEM based on three independent experiments. The statistical significance was assessed in comparison to the untreated cells. The significance level was set at $p < 0.05$ (*), $p < 0.01$ (**), $p < 0.001$ (***) and $p < 0.0001$ (****).*

Further, the protein expression profile of the Notch downstream genes was assessed using immunoblot analysis. Similar to the gene expression profile, SAHA induced the expression of the Notch downstream proteins. For example, there was a 5.03-fold upregulation in the expression of Cyclin D3 **(Figure 3.3.12: A)**, 1.73-fold in HES-1 **(Figure 3.3.12: C)**, 1.95-fold in NICD **(Figure 3.3.12: D)** and 1.26-fold upregulation in p21 **(Figure 3.3.12: G)** protein in case of MDA-MB-231 cells. Similarly, in MDA-MB-468 cells, there was a 2.26-fold upregulation in the expression profile of Cyclin D3 **(Figure 3.3.13: A)**, 1.24-fold in HES-1 **(Figure 3.3.13: C)**, 1.59-fold in NICD **(Figure 3.3.13: D)** and 1.28-fold upregulation in the protein expression profile of p21 **(Figure 3.3.13: G)**, following treatment with SAHA alone.

Besides being a downstream target gene of the Notch pathway, c-Myc is also reported to be positively correlated with self-renewal, stemness and chemoresistance of the TNBC. It was observed that the gene, as well as the protein expression profile of c-Myc, was found to be downregulated significantly upon treatment with the inhibitors alone, as well as in combination **(Figure 3.3.12: C and 3.3.13: C)**.

The JAG1/Notch signalling cascades activate numerous oncogenic factors, thereby regulating proliferation, metastasis, drug-resistance, etc. [119]. Similarly, Jagged-2 (JAG2) is also associated with imparting metastasis, stemness properties, drug-resistance and tumorigenesis in numerous tumours, especially in breast cancer cells via regulating miR-200 [120]. Hence, the protein expression profile of the Notch ligands was also assessed.

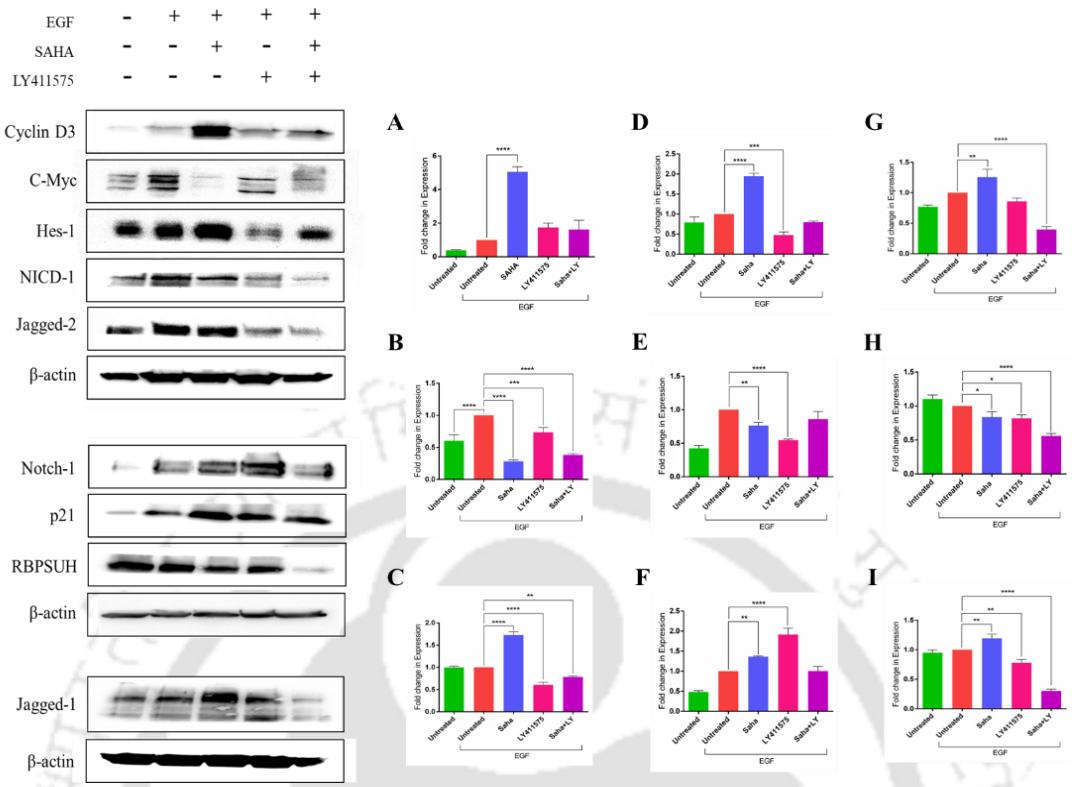

Figure 3.3.12: *Representative immunoblots showing the expression of the Notch downstream genes in MDA-MB-231 cells, Graphical representation of the fold change in* ***(A)*** *Cyclin-D3,* ***(B)*** *c-Myc,* ***(C)*** *HES-1,* ***(D)*** *NICD-1,* ***(E)*** *Jagged-2,* ***(F)****Notch1,* ***(G)*** *p21,* ***(H)*** *RBPSUH and* ***(I)*** *Jagged-1 in MDA-MB-231 cells. The results are expressed as the mean ± SEM based on three independent experiments. The statistical significance was assessed in comparison to the untreated cells. The significance level was set at $p < 0.05$ (*), $p < 0.01$ (**), $p < 0.001$ (***) and $p < 0.0001$ (****).*

It was found that following combination therapy there was a 3.3- fold and 1.68-fold downregulation in the protein expression profile of Jagged-1 in MDA-MB-231 **(Figure 3.3.12: I)** and MDA-MB-468 cell **(Figure 3.3.13: I)**, respectively. Similarly, there was a 1.16-fold and 2.53-fold downregulation in the protein expression profile of Jagged-2, after combination therapy in MDA-MB-231 **(Figure 3.3.12: E)** and MDA-MB-468 **(Figure 3.3.13: E)** cells, respectively.Moreover, it was also observed that the protein expression profile of the Notch1 receptor is similar to its gene expression profile. In both cases, the expression of the Notch proteins, as well as the Notch1 genes were upregulated after treatment with LY411575 in MDA-MB-231 cells. However, the Notch1 gene exhibits significant downregulation following combination therapy by a 1.73-fold and 1.2-fold change in MDA-MB-231 **(Figure 3.3.12: F)** and MDA-MB-468 **(Figure 3.3.13: F)** cells, respectively.Also, there was a significant downregulation of the Notch1 protein by 1.52-fold in MDA-MB-468 cells,while there was no such change in the protein expression profile in MDA-MB-231 cells. Altogether, these data suggest the plausible role of SAHA in the upregulation of the Notch pathway.

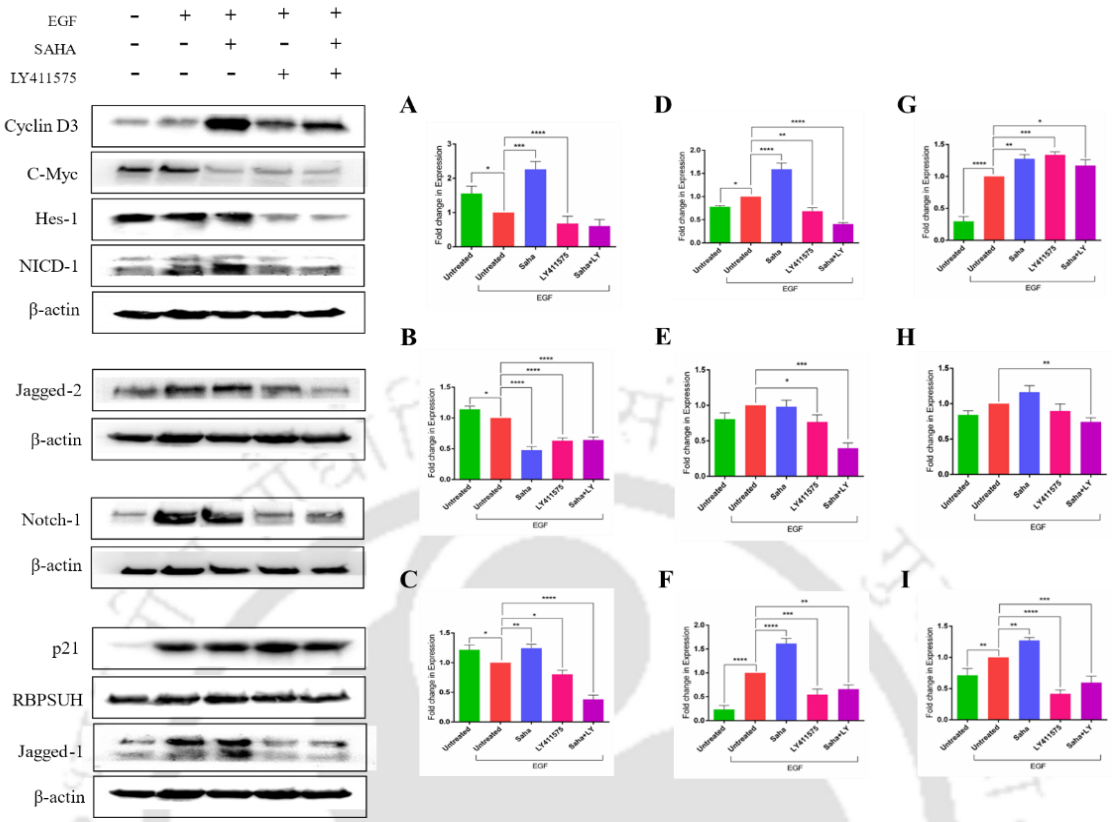

Figure 3.3.13: *Representative immunoblots showing the expression of the Notch downstream genes in MDA-MB-468 cells, Graphical representation of the fold change in* ***(A)*** *Cyclin-D3,* ***(B)*** *c-Myc,* ***(C)*** *HES-1,* ***(D)*** *NICD-1,* ***(E)*** *Jagged-2,* ***(F)*** *Notch1,* ***(G)*** *p21,* ***(H)*** *RBPSUH and* ***(I)*** *Jagged-1 in MDA-MB-468 cells. The results are expressed as the mean ± SEM based on three independent experiments. The statistical significance was assessed in comparison to the untreated cells. The significance level was set at $p < 0.05$ (*), $p < 0.01$ (**), $p < 0.001$ (***) and $p < 0.0001$ (****).*

Further, the protein expression profile of the DNA binding domain, CSL (or Recombining Binding Protein, SUppressor of Hairless, also known as RBPSUH) was assessed. It was found that following combination therapy there was a significant downregulation in the protein expression profile by 1.78-fold and 2.35-fold in MDA-MB-231 **(Figure 3.3.12: H)** and MDA-MB-468 **(Figure 3.3.13: H)**, respectively. The fold change in the protein expression profile of the Notch downstream genes are depicted in **Table 3.3.1**.

Table 3.3.1: Protein expression profile of the Notch downstream genes

Genes	MDAMDA-MB-231				MDAMDA-MB-468			
	Control	**SAHA**	**LY411575**	**S + Ly**	**Control**	**SAHA**	**LY411575**	**S + Ly**
Cyclin D3	- 2.72	**** 5.03	- 1.74	- 1.62	* 1.56	*** 2.26	**** 1.47	* 1.65
c-Myc	* 1.66	**** 3.53	**** 1.36	**** 2.61	* 1.14	**** 2.1	**** 1.59	* 1.56
HES-1	- 1.04	**** 1.73	**** 1.65	** 1.28	* 1.21	** 1.24	* 1.25	* 2.63
NICD	- 1.26	**** 1.95	*** 2.1	- 1.25	* 1.28	**** 1.59	** 1.46	* 2.46
p21	- 1.30	** 1.26	- 1.16	**** 2.52	*** 3.38	** 1.28	*** 1.34	** 1.16
RBPSUH	- 1.10	* 1.19	* 1.22	**** 1.78	- 1.19	- 1.16	- 1.12	** 2.35
Jagged-1	- 1.05	** 1.19	** 1.28	**** 3.3	** 1.40	** 1.27	**** 2.40	*** 1.68
Jagged-2	- 2.36	** 1.32	**** 1.83	- 1.16	- 1.24	- 1.02	* 1.31	*** 2.53
Notch-1	- 2.08	** 1.36	**** 1.91	- 1.03	**** 4.24	- 1.61	- 1.84	- 1.52

 # Red depicts upregulation in the expression level, while green depicts downregulation in expression level
The significance level was set at $p < 0.05$ (*), $p < 0.01$ (**), $p < 0.001$ (***) and $p < 0.0001$ (****).

3.3.6. SAHA in combination with the γ-secretase inhibitor, LY411575, reduces its ability to promote EMT.

HDAC inhibitors are crucial for the treatment of various cancer. However, it has been observed that HDAC promotes EMT in numerous cancers, including TNBC [121]. Hence, owing to the fact that SAHA activates the Notch pathway, thereby activating the Notch downstream genes (such as Snail, Twist, Zeb, etc.); it is hypothesized that a combination therapy (SAHA with LY411575) would effectively and synergistically inhibit the molecular mechanisms potentiating EMT. Therefore, to ascertain the effects of HDAC inhibitor (SAHA) and γ-secretase inhibitor (LY411575) on the molecular mechanisms of EMT, qRT-PCR, along with immunoblot analysis was performed following treatment in monotherapy as well as in combination therapy.

Loss of E-cadherin is one of the major characteristics to determine the onset of EMT. Following combination therapy, the gene expression profile of E-cadherin was found to be upregulated by 1.39 and 2.04-fold in MDA-MB-231 **(Figure 3.3.14: A)** and MDA-MB-468 **(Figure 3.3.14: B)** cell lines, respectively. Vimentin, N-cadherin and Fibronectin are sought to be the prominent markers of EMT. Following co-therapy, the expression of vimentin and fibronectin was downregulated by 2.04-fold and 1.37-fold, respectively in MDA-MB-231 cells, while in MDA-MB-468 cells the expression of vimentin and N-cadherin was downregulated by 1.13-fold and 1.26-fold respectively, in comparison to the control sample. However, upon treatment with SAHA, the expression of all three genes was found to be upregulated in the MDA-MB-468 cells (vimentin 1.4-fold, fibronectin 2.76-fold, and N-cadherin 1.67-fold); which in co-therapy was found to be downregulated by 1.13-fold for vimentin and 1.26-foldfor N-cadherin in comparison to the SAHA treated samples. Similarly, in MDA-MB-231, SAHA upregulated the expression of N-cadherin by 2.08-fold in comparison to the untreated samples, while the combination treatment reduced its expression by 1.77-fold, less in comparison to the SAHA- treated cells.

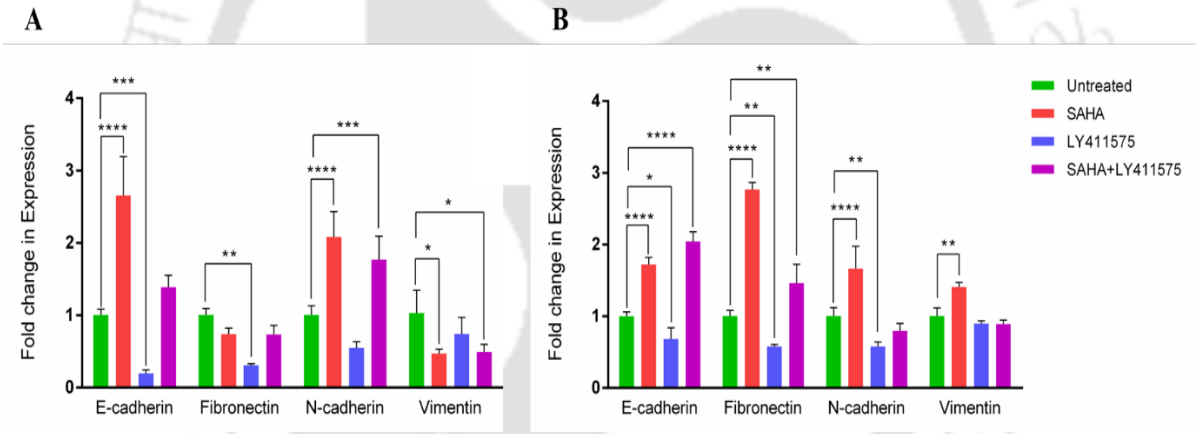

Figure 3.3.14: *Graphical representation of changes in gene expression levels following treatment with the inhibitors in monotherapy as well as in combination therapy as quantified by qRT-PCR analysis.* ***(A)*** *and* ***(B)*** *shows the gene expression levels obtained from MDA-MB-231 and MDA-MB-468 monolayer cultures, respectively. The results are expressed as the mean ± SEM based on three independent experiments. The statistical significance was assessed in comparison to the untreated cells. The significance level was set at p < 0.05 (*), p < 0.01 (**), p < 0.001 (***) and p < 0.0001 (****).*

Besides, EMT is orchestrated by a restricted number of transcription factors mainly the Snail, Twist, and Zeb families (EMT-TFs) [122]. In both the TNBC cells, the expression of Snail and Twist-1 was found to be downregulated following co-therapy **(Figure 3.3.15)**. However, SAHA upregulated the expression of Twist-1 by 1.15-fold and 1.28-fold in MDA-MB-231 and MDA-MB-468, respectively. Thefold change in the gene expression profile of the EMT markers and TFs is depicted in **Table 3.3.2**.

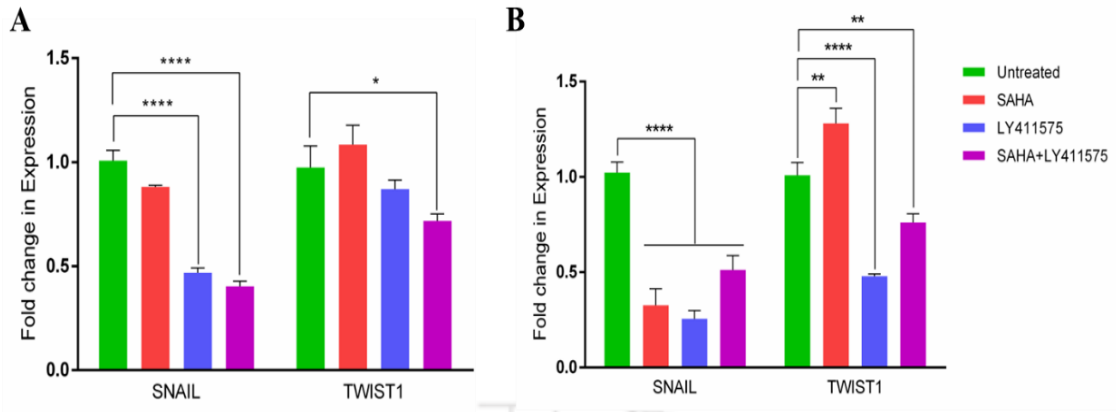

Figure 3.3.15: *Graphical representation of changes in gene expression levels following treatment with the inhibitors in monotherapy as well as in combination therapy as quantified by qRT-PCR analysis.* ***(A)*** *and* ***(B)*** *shows the gene expression levels obtained from MDA-MB-231 and MDA-MB-468 monolayer cultures, respectively. The results are expressed as the mean ± SEM based on three independent experiments. The statistical significance was assessed in comparison to the untreated cells. The significance level was set at p < 0.05 (*), p < 0.01 (**), p < 0.001 (***) and p < 0.0001 (****).*

Table 3.3.2: Gene expression profile of the EMT markers and TFs

Genes	MDAMDA-MB-231			MDAMDA-MB-468		
	SAHA	**LY411575**	**S + Ly**	**SAHA**	**LY411575**	**S + Ly**
E-cadherin	**** 2.65	*** 5.26	- 1.39	**** 1.72	* 1.1	**** 2.04
N-cadherin	**** 2.08	- 1.83	*** 1.77	**** 1.67	** 1.73	- 1.26
Fibronectin	- 1.36	** 3.26	- 1.37	**** 2.76	** 1.73	** 1.46
Vimentin	* 2.13	- 1.36	* 2.04	** 1.41	- 1.12	- 1.13
Snai1	- 1.14	**** 2.14	**** 2.48	**** 3.06	**** 3.9	**** 1.96
Twist	- 1.15	- 1.19	* 1.39	** 1.28	**** 2.09	** 1.32

#Red depicts upregulation in the expression level, while green depicts downregulation in expression level The significance level was set at p < 0.05 (*), p< 0.01 (**), p < 0.001 (***) and p < 0.0001 (****).

Moreover, the protein expression of the EMT markers was also evaluated using western blot. E-cadherin was found to be upregulated following combination therapy by 1.20-fold in MDA-MB-231 cells **(Figure 3.3.16: A(ii) and G)** and 1.92-fold in MDA-MB-468 cells **(Figure 3.3.16: D(i) and H)**. In the present study, it was also observed that there was a significant upregulation of claudins after monotherapy and combination therapy in MDA-MB-468 cells **(Figure 3.3.16: D(iii) and N)**. However, not much changes were observed in MDA-MB-231 cells, which might be attributed to its inherent high metastatic propensity and low claudin content [123].

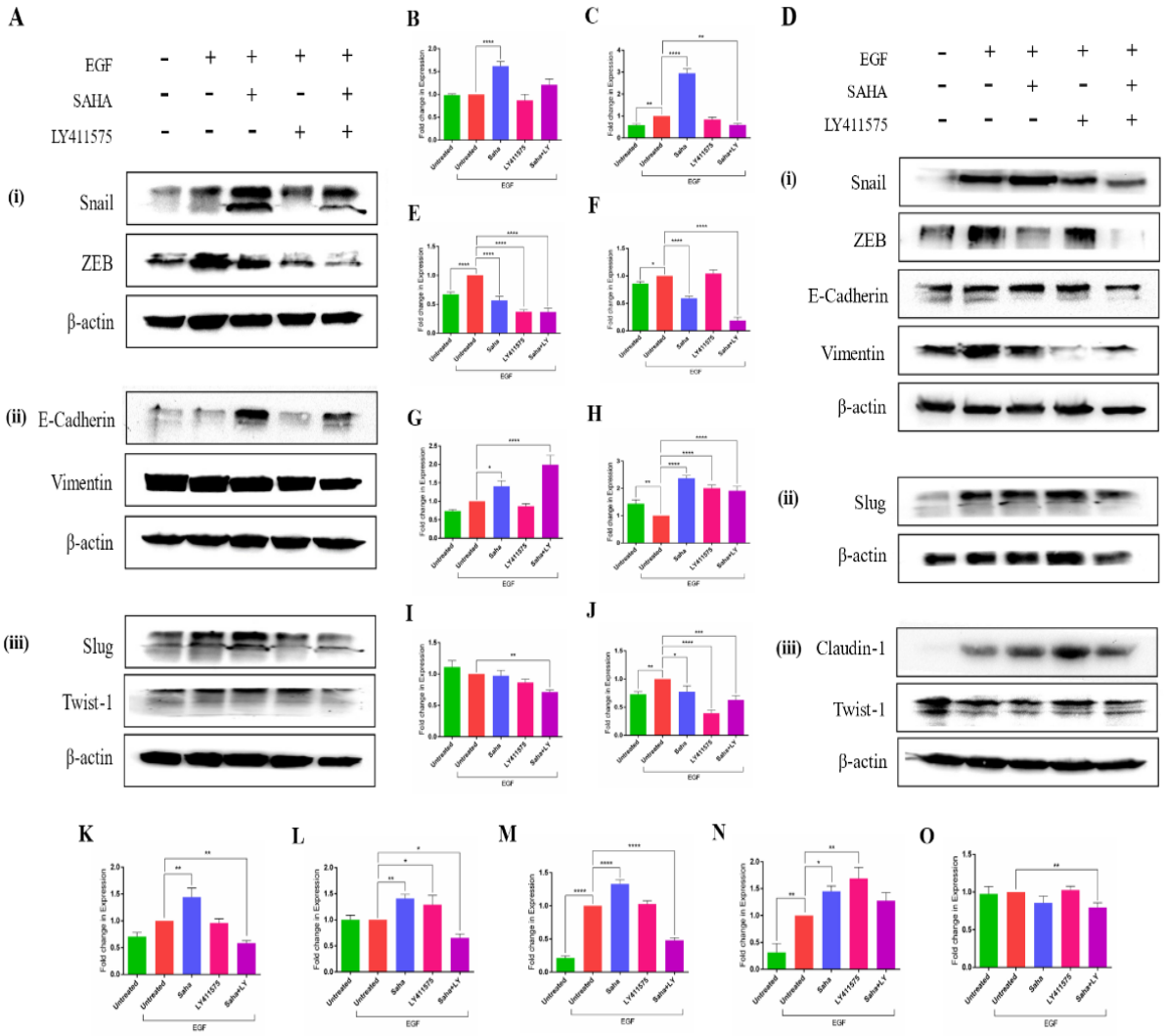

Figure 3.3.16: *Representative immunoblots showing the expression of the EMT markers and EMT-TFs in* ***(A)*** *MDA-MB-231 cells, and* ***(D)*** *MDA-MB-468 cells. Graphical representation of the fold change in* ***(B)*** *Snail,* ***(E)****Zeb,* ***(G)*** *E-cadherin,* ***(I)*** *Vimentin,* ***(K)*** *Slug, and* ***(L)*** *Twist-1 in MDA-MB-231 cells; while* ***(C)*** *Snail,* ***(F)*** *Zeb,* ***(H)*** *E-cadherin,* ***(J)*** *Vimentin,* ***(M)*** *Slug,* ***(N)*** *Claudin-1, and* ***(O)*** *Twist-1 in MDA-MB-468 cells. β-actin serves as a loading control. The results are expressed as the mean ± SEM based on three independent experiments. The statistical significance was assessed in comparison to the untreated cells. The significance level was set at $p < 0.05$ (*), $p < 0.01$ (**), $p < 0.001$ (***) and $p < 0.0001$ (****).*

Also, the protein expression profile of the mesenchymal markers shows a significant upregulation following treatment with SAHA alone. For example, after treatment with SAHA, Snail was found to be upregulated by 1.62-fold and 2.95-fold in MDA-MB-231 **(Figure 3.3.16: A(i) and B)** and MDA-MB-468 **(Figure 3.3.16: D(i) and C)**, respectively. Similarly, Slug was found to be upregulated by 1.44-fold and 1.33-fold in MDA-MB-231 **(Figure 3.3.16: A(iii) and K)** and MDA-MB-468 **(Figure 3.3.16: D(ii) and M)**, respectively. However, combination treatment tends to downregulate the protein expression pattern of the mesenchymal genes significantly in both TNBC cells, as shown in **Table 3.3.3.**

Table 3.3.3: Protein expression profile of the EMT markers and TFs

Genes	MDAMDA-MB-231				MDAMDA-MB-468			
	Control	**SAHA**	**LY411575**	**S + Ly**	**Control**	**SAHA**	**LY411575**	**S + Ly**
E-cadherin	**** 1.36	**** 1.41	**** 1.15	**** 1.2	- 1.44	** 2.37	- 2.01	** 1.92
Claudin-1					** 3.17	* 1.45	** 1.72	- 1.28
Vimentin	* 1.11	**** 1.03	- 1.15	**** 1.41	- 1.38	** 1.29	* 2.54	* 1.60
Slug	- 1.42	* 1.44	- 1.04	**** 1.71	**** 4.69	**** 1.33	- 1.03	**** 2.08
Snai1	- 1.08	*** 1.62	- 1.15	- 1.21	- 1.71	* 2.95	- 1.19	** 1.68
Twist-1	** 1.01	**** 1.41	**** 1.29	**** 1.54	- 1.02	- 1.17	- 1.03	** 1.26
Zeb-1	** 1.49	**** 1.75	- 2.70	** 2.72	** 1.16	* 1.69	**** 1.04	*** 5.38

 # Red depicts upregulation in the expression level, while green depicts downregulation in expression level
The significance level was set at $p < 0.05$ (*), $p < 0.01$ (**), $p < 0.001$ (***) and $p < 0.0001$ (****).

Further, immunocytochemical analysis of the aforementioned proteins such as Vimentin **(Figure 3.3.17)**, Snail-Zeb dual staining **(Figure 3.3.18)** and E-cadherin-Phalloidin **(Figure 3.3.19 and Figure 3.3.20)** was carried out. The result depicts the downregulation of the mesenchymal markers (Vimentin, Snail, Slug), and upregulation of the epithelial marker (E-cadherin), after combination treatment. The protein expression profile in ICCs was as consistent with the immunoblot analysis and the gene expression profile of the EMT markers and EMT-TFs. Altogether, these finding suggests that the γ-secretase inhibitor, LY411575 abrogates the metastatic propensity of the HDAC inhibitor, SAHA at the molecular level, thereby suggesting that the combination treatment inhibits EMT and reduces the metastatic potential ofTNBC cells.

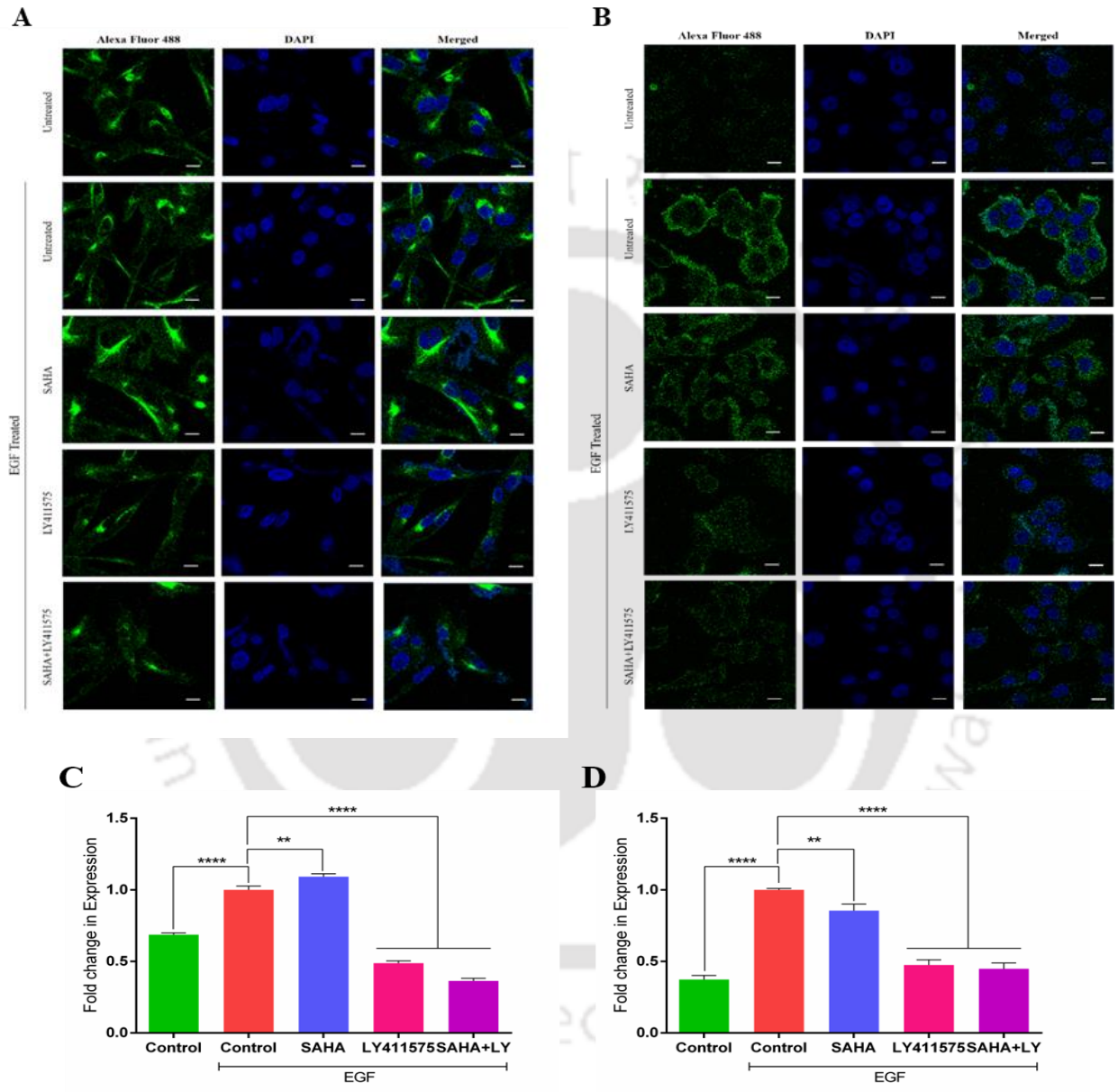

Figure 3.3.17: *Confocal images of* ***(A)*** *MDA-MB-231 and* ***(B)*** *MDA-MB-468 monolayer cultures immune-stained with anti-ZEB and anti-SNAI1 antibody visualized by Alexa Fluor-488 and Alexa Fluor-647. Nuclei were stained with DAPI. Cells were treated with individual inhibitors and drugs as well as in combination therapy for 48 h. The scale bar represents 20 µm. Graphical depiction in the fold change alteration in the expression profile (following ICC) of mesenchymal marker, Vimentin in* ***(C)*** *MDA-MB-231 and* ***(D)*** *MDA-MB-468, respectively. Based on three independent experiments, the results are represented as mean ± SEM, along with a statistical significance denoting p < 0.5 (*), p < 0.1 (**), p < 0.01 (***) and p < 0.001 (****).*

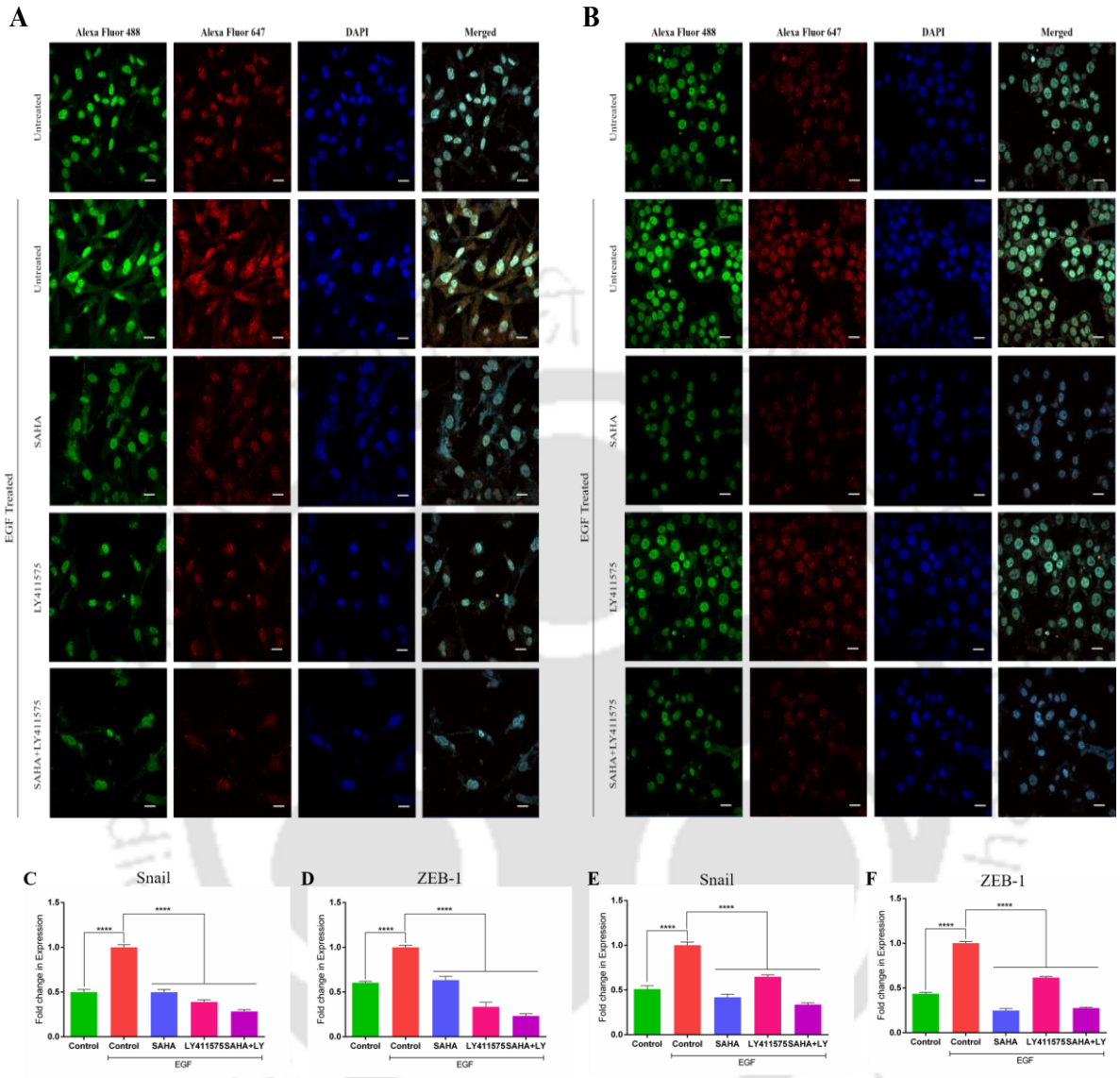

Figure 3.3.18: *Confocal images of* ***(A)*** *MDA-MB-231 and* ***(B)*** *MDA-MB-468 monolayer cultures immune-stained with anti-ZEB and anti-SNAI1 antibody visualized by Alexa Fluor-488 and Alexa Fluor-647. Nuclei were stained with DAPI. Cells were treated with individual inhibitors and drugs as well as in combination therapy for 48 h. The scale bar represents 20 µm. Graphical depiction in the fold change alteration in the expression profile (following ICC) of mesenchymal marker (such as Snail* ***(C)*** *and* ***(E)****, and Zeb-1* ***(D)*** *and* ***(F)****) in MDA-MB-231 and MDA-MB-468, respectively. Based on three independent experiments, the results are represented as mean ± SEM, along with a statistical significance denoting $p < 0.5$ (*), $p < 0.1$ (**), $p < 0.01$ (***) and $p < 0.001$ (****).*

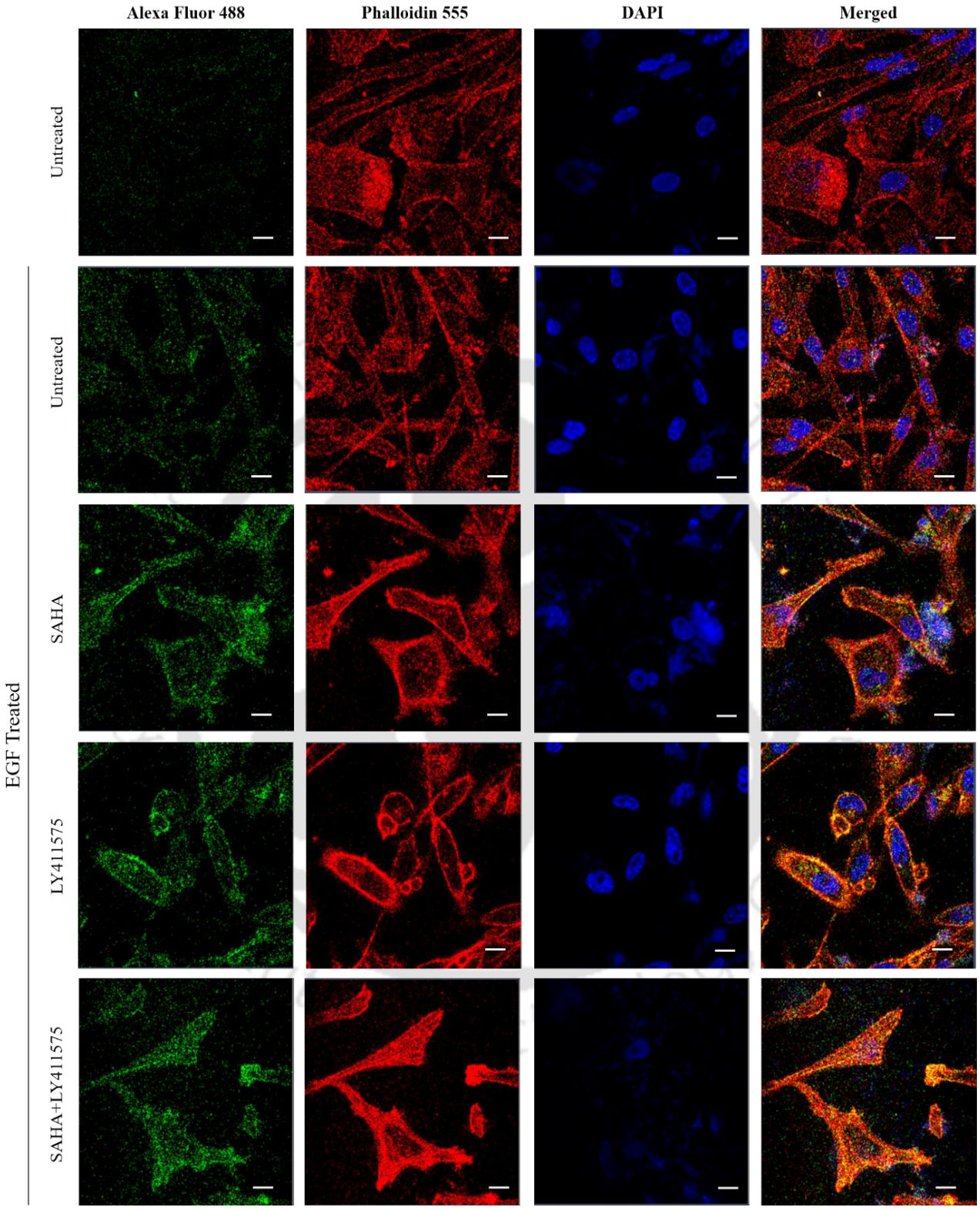

Figure 3.3.19: *Confocal images of MDA-MB-231 monolayer cultures immune-stained with anti-E-cadherin antibody visualized by Alexa Fluor-488. The Actin cytoskeleton was stained with Phalloidin-555. Nuclei were stainedwith DAPI. Cells were treated with individual inhibitors and drugs as well as in combination therapy for 48 h. The scale bar represents 20 µm.*

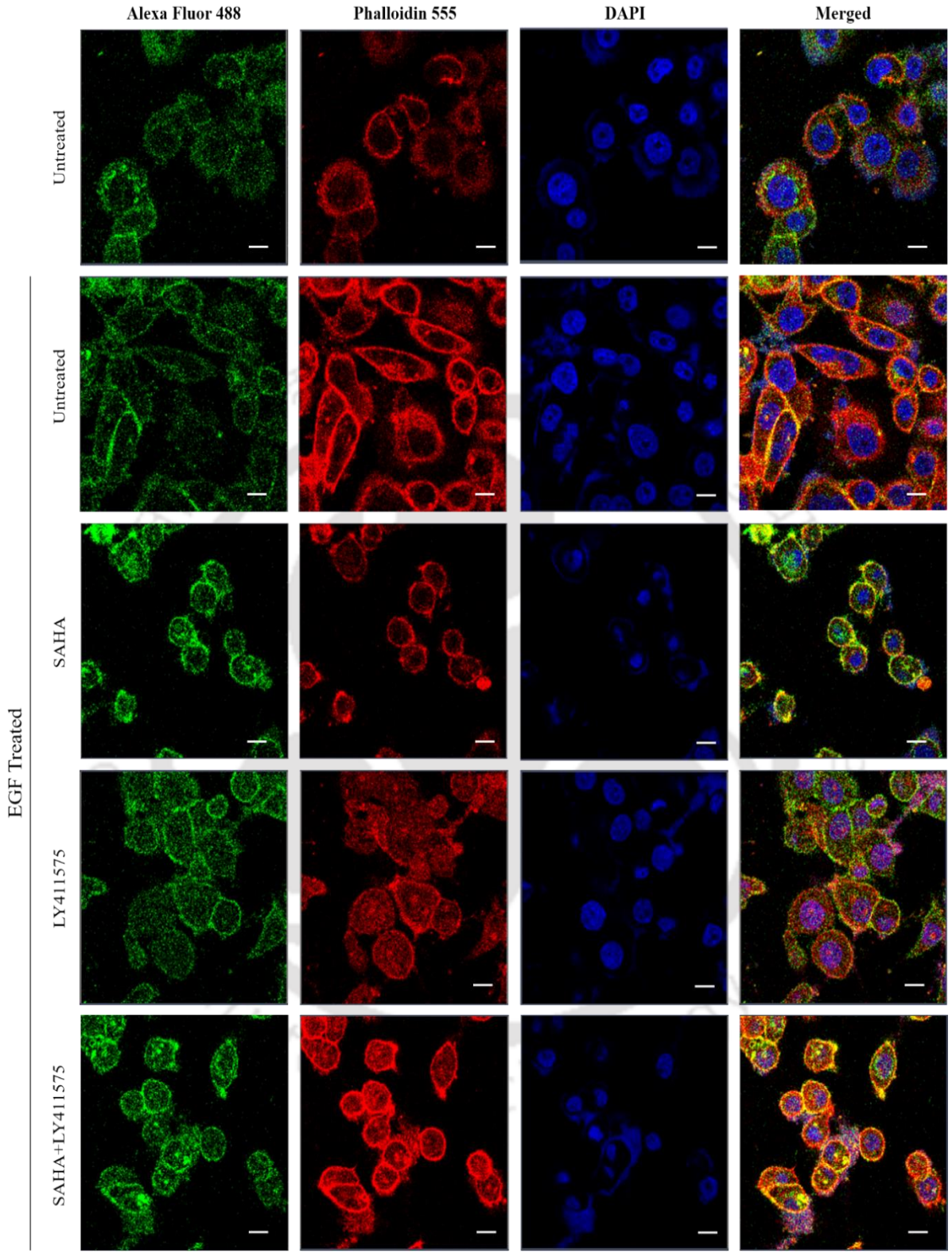

Figure 3.3.20: *Confocal images of MDA-MB-468 monolayer cultures immune-stained with anti-E-cadherin antibody visualized by Alexa Fluor-488. The Actin cytoskeleton was stained with Phalloidin-555. Nuclei were stainedwith DAPI. Cells were treated with individual inhibitors and drugs as well as in combination therapy for 48 h. The scale bar represents 20 µm.*

3.3.7. LY411575 in combination with SAHA reduces the *in vitro* motility of TNBC cells

Since treatment with SAHA is implicated in the facilitation of EMT at the molecular level, hence we further investigated the role of SAHA on the migratory and invasive properties of the TNBC cells. Initially, a Boyden chamber-based assay was utilized to monitor the invasive properties of the TNBC cells, whereby, cells on account of their invasive properties occupy the layer of Matrigel on top of a membrane. Herein, the *in vitro* trans-well migration assay reveals that SAHA in combination with LY411575 significantly reduced the invasive properties of both MDA-MB-231 **(Figure 3.3.21: A and C)** and MDA-MB-468 **(Figure 3.3.21: B and D)** cells by 3.27-fold and 1.67-fold, respectively.

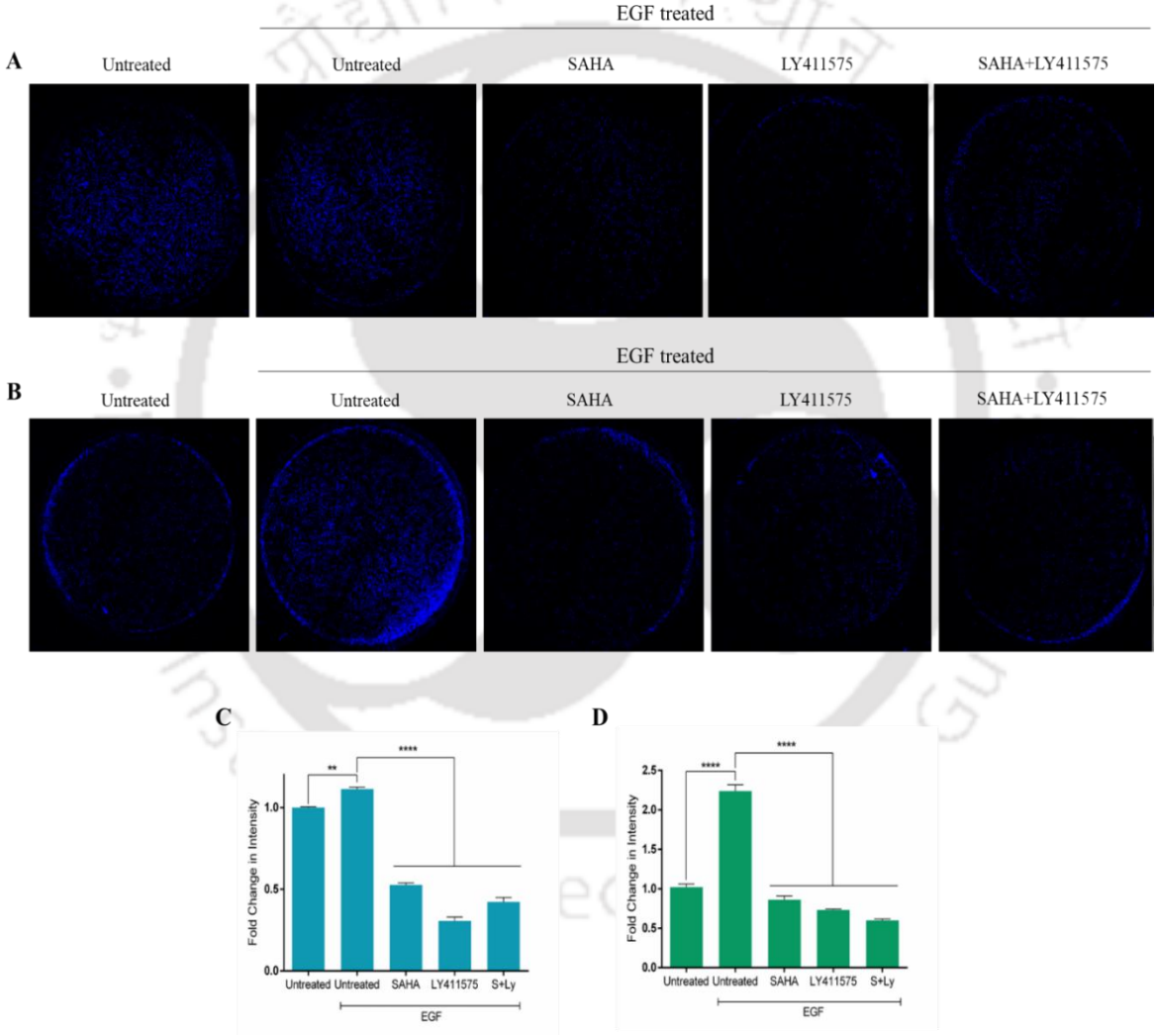

Figure 3.3.21: *Determination of Boyden-chamber invasion assay of* ***(A)*** *MDA-MB-231 and* ***(B)*** *MDA-MB-468 cells. Graphical representation of changes in invasiveness following treatment with respect to untreated samples in* ***(C)*** *MDA-MB-231 and* ***(D)*** *MDA-MB-468 cells. The results are expressed as the mean ± SEM based on three independent experiments. The statistical significance was assessed in comparison to the untreated cells. The significance level was set at $p < 0.05$ (*), $p < 0.01$ (**), $p < 0.001$ (***) and $p < 0.0001$ (****).*

Furthermore, the effects of SAHA in monotherapy and as well as in combination therapy on the *in vitro* migration of the EMT-induced MDA-MB-231 **(Figure 3.3.22: A and C)** and MDA-MB-468 **(Figure 3.3.22: B and D)** were assessed using the scratch wound healing assay, whereby the migration rate of the cells towards the wounded area was determined. Following treatment, it is observed that SAHA promotes the migration of MDA-MB-468 cell lines in comparison to the control cells. However, when in combination with the γ-secretase inhibitor, LY411575, the rate of cell migration was found to be lowest in both cells. Altogether, it is observed that SAHA in combination with the γ-secretase inhibitor, LY411575 reduces the migratory properties of the TNBC cell lines more profoundly.

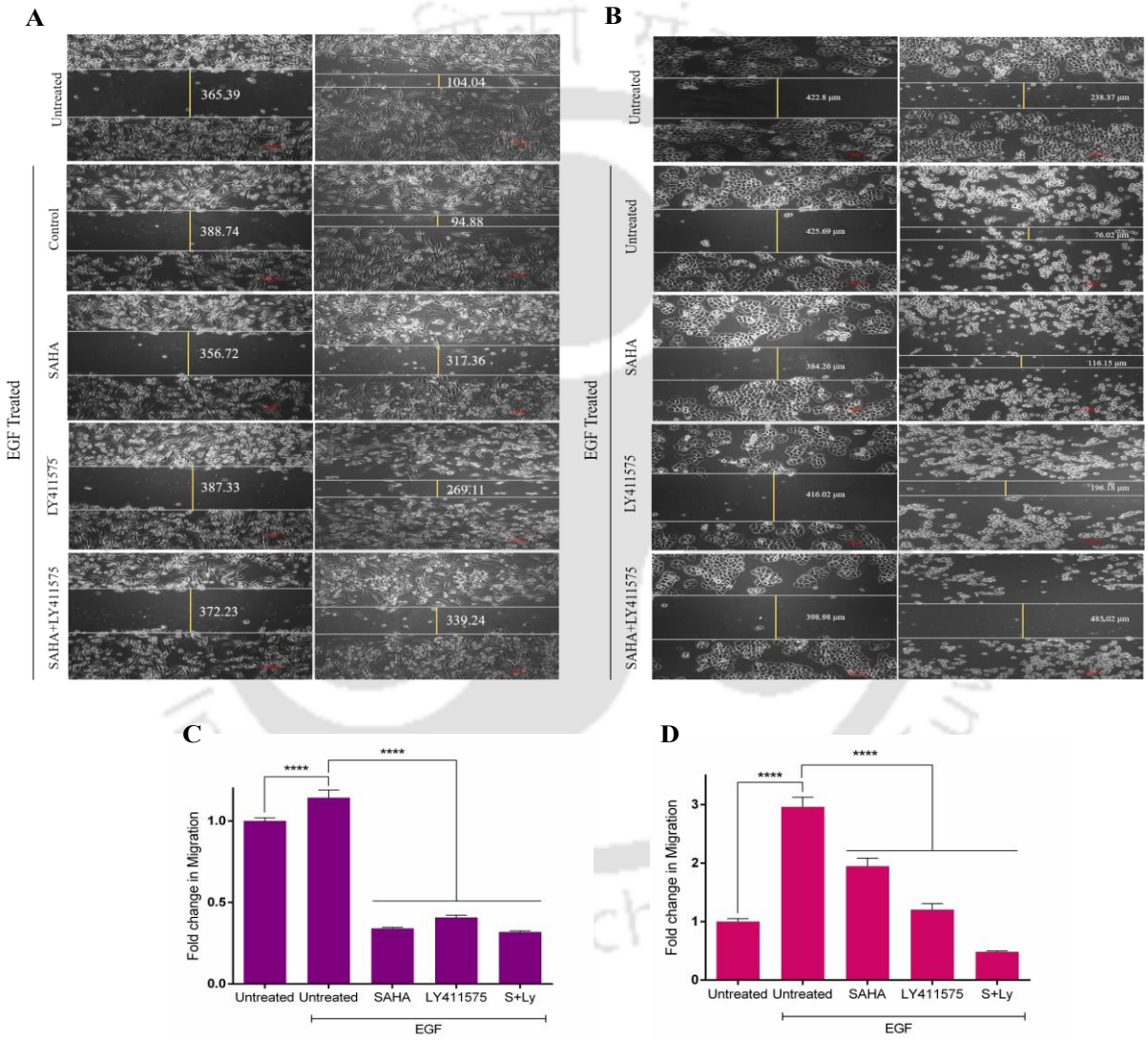

Figure 3.3.22: *Scratch wound-healing assays of* ***(A)*** *MDA-MB-231 and* ***(B)*** *MDA-MB-468 monolayer cultures. Graphical representation of changes in wound healing capacity following treatment with respect to untreated samples in* ***(C)*** *MDA-MB-231 and* ***(D)*** *MDA-MB-468 cells. The results are expressed as the mean ± SEM based on three independent experiments. The statistical significance was assessed in comparison to the untreated cells. The significance level was set at $p < 0.05$ (*), $p < 0.01$ (**), $p < 0.001$ (***) and $p < 0.0001$ (****).*

3.3.8. SAHA in combination with LY411575 inhibits the stem-cell-like properties of the TNBC cells

Among the several biomarkers for the determination of stemness, the role of CD44 remains implicit. The associations of $CD44^{high}/CD24^{low}$ with stemness are directly related to the cells exhibiting EMT characteristics in various tumour subtypes, such as oral squamous cell carcinoma [124], breast cancer [125], etc. Hence, to assess the contributions of SAHA in promoting the TNBC stem-cell-like properties, a flow cytometry-based immunofluorescence assay was carried out, utilizing the cell surface protein markers, such as CD24 and CD44.

It was observed that there was a significant decrease in the CD44 population and an increase in the CD24 population following co-treatment in both TNBC cells in comparison to the EMT-induced control cells **(Figure 3.3.23)**. Additionally, it was also observed that in comparison to the untreated cells, there was a significant increase in the CD44 population in both MDA-MB-231 and MDA-MB-468, which supports the fact that stemness is related to the phenomenon of EMT. However, the increase in the population of CD44 in EMT-induced MDA-MB-468 was found to be much higher in comparison to that of the MDA-MB-231, which is attributed to the mesenchymal and aggressive characteristics of the MDA-MB-231 cell lines.

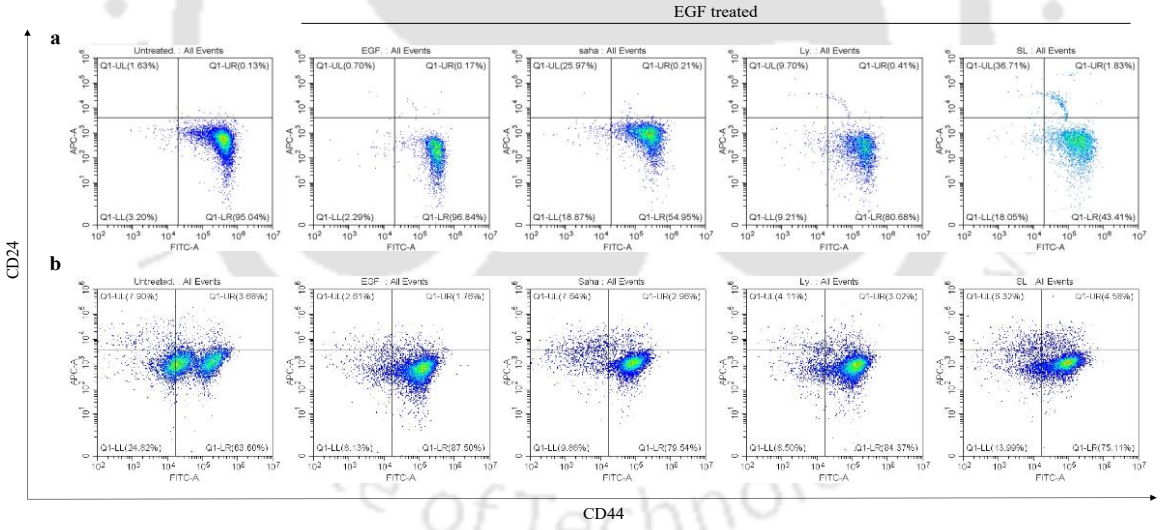

Figure 3.3.23: *A pseudo-plot representation of CD44/CD24 population in* ***(a)*** *MDA-MB-231 and* ***(b)*** *MDA-MB-468, respectively.*

Similarly, colony formation and sphere formation assays were performed to ascertain the effects of combination treatment in the TNBC cells. On one hand, sphere formation assay determines the proliferative potential of the CSCs to form tumours in the non-adherent serum-free gel matrix; while on the other hand, colony formation assay determines the ability of a single cell to grow into a colony. It was observed that combination treatment dramatically reduced the sphere-forming ability of the TNBC cells **(Figure 3.3.24: A and B)**.

The graphical representation of the change in the diameter of spheroidsis provided in **Figure 3.3.24: C and D** for MDA-MB-231 and MDA-MB-468 cells, respectively. Moreover, the effect of co-treatment was profound in the case of the colony-forming ability of the TNBC cells *in vitro* **(Figure 3.3.25)**. Graphical representations of the fold change in the colony formation assay are depicted in **Figure 3.3.25: B and C** for MDA-MB-231 and MDA-MB-468 cells, respectively.

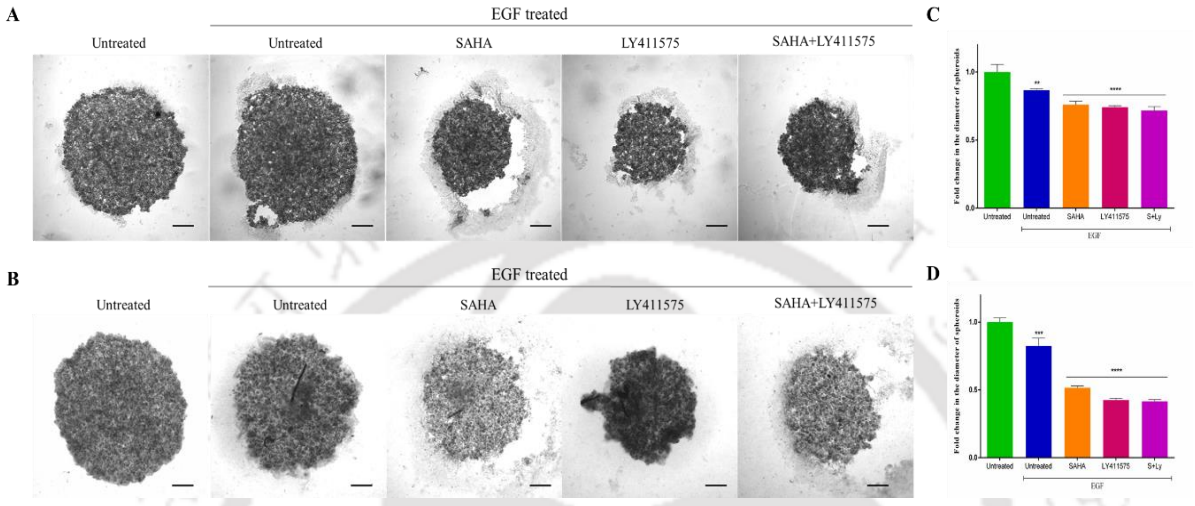

Figure 3.3.24: *Evaluation of sphere formation ability following respective treatments for 48 h in* ***(A)*** *MDA-MB-231 cells, and* ***(B)*** *MDA-MB-468 cells. Graphical representation of the sphere-forming ability of* ***(C)*** *MDA-MB-231 cells, and* ***(D)*** *MDA-MB-468 cells. The results are expressed as the mean ± SEM based on three independent experiments. The statistical significance was assessed in comparison to the untreated cells. The significance level was set at p < 0.05 (*), p < 0.01 (**), p < 0.001 (***) and p < 0.0001 (****).*

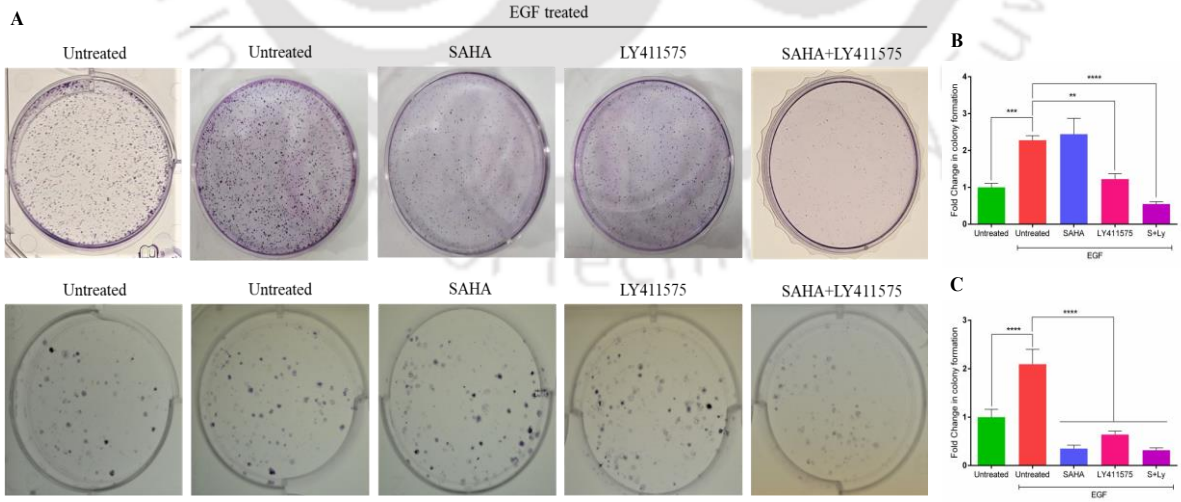

Figure 3.3.25: (A) *Assessment of colony formation assay in (a) MDA-MB-231 and (b) MDA-Mb-468 cells.Graphical representation of the fold change in colony forming ability of the cells of* ***(B)*** *MDA-MB-231 and* ***(C)*** *MDA-MB-468 cells, respectively. The results are expressed as the mean ± SEM based on three independent experiments. The statistical significance was assessed in comparison to the untreated cells. The significance level was set at p < 0.05 (*), p < 0.01 (**), p < 0.001 (***) and p < 0.0001 (****).*

Further, the epithelial cell adhesion molecule (EpCAM/CD326) is a prominent marker of stemness [126]; the gene expression profile was assessed using qRT-PCR. It was observed that SAHA increased the expression of EpCAM by 2.02-fold in MDA-MB-468 cells. However, after the administration of co-therapy, the gene expression profile was found to be downregulated by 2-fold in MDA-MB-231 **(Figure 3.3.26: A and B)**. Additionally, Ki-67 is associated with the maintenance of the cancer stem cell niche, along with maintaining the proliferative potential of both cancer and normal cells. Hence,the gene expression profile of Ki-67 was also assessed using qRT-PCR, which depicted a concomitant downregulation in the expression of Ki-67 following co-therapy. However, in both the TNBC cells, treatment with SAHA resulted in an upregulation in the gene expression of Ki-67 **(Figure 3.3.26).**

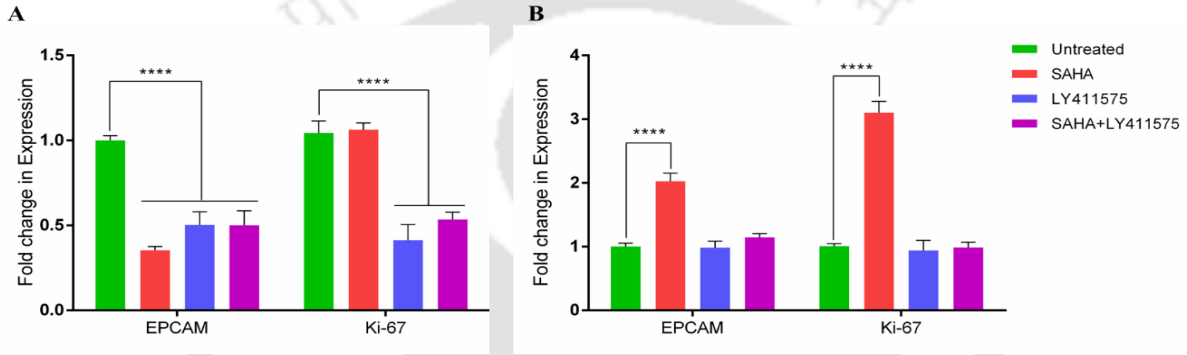

Figure 3.3.26: *Graphical representation of changes in gene expression levels following treatment with the inhibitors in monotherapy as well as in combination therapy as quantified by qRT-PCR analysis.* ***(A)*** *and* ***(B)*** *shows the gene expression levels obtained from MDA-MB-231 and MDA-MB-468 monolayer cultures, respectively. The results are expressed as the mean ± SEM based on three independent experiments. The statistical significance was assessed in comparison to the untreated cells. The significance level was set at $p < 0.05$ (*), $p < 0.01$ (**), $p < 0.001$ (***) and $p < 0.0001$ (****).*

3.3.9. Alteration in the expression of the autophagic markers and ABC transporters in TNBC cells

Autophagy is associated with the enhanced metastatic propensity of some cancers, such as the TNBC cells [127]. However, research evidence suggests that SAHA mediates cell death via enhanced autophagy [128]. Hence, the protein expression profile of Beclin-1, and LC3 **(Figure 3.3.27)** was ascertained using immunoblot assay. It was observed that SAHA induced the expression of Beclin1 by 1.23-fold in MDA-MB-231 cells **(Figure 9C)**, while it downregulates the expression of Beclin1 in MDA-MB-468 cells by 1.21-fold **(Figure 9E).** Moreover, the expression of Beclin1 and LC3 followed the different trends in the two TNBC cells, suggesting the varied cell-dependent mechanisms of autophagy-mediated cell death and autophagy-independent cell death in both cell lines.

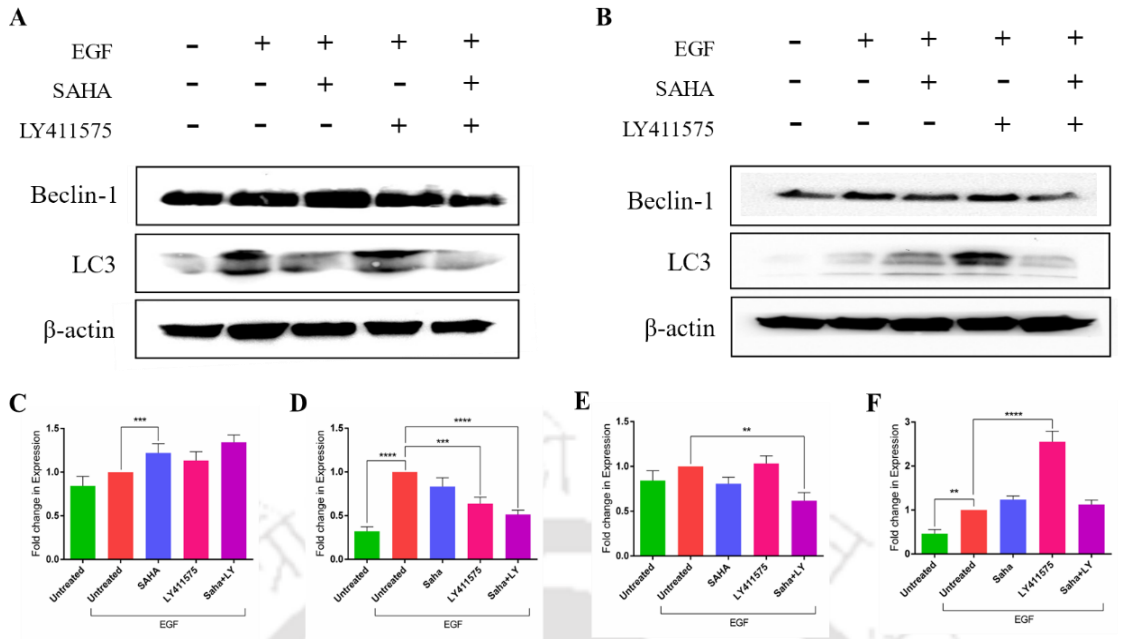

Figure 3.3.27: *Representative immunoblots showing the expression of autophagic markers: Beclin-1 and LC3 in* ***(A)*** *MDA-MB-231 cells, and* ***(B)*** *MDA-MB-468 cells. β-actin serves as a loading control. Graphical representation of the fold change in Beclin-1 in* ***(C)*** *MDA-MB-231 and* ***(D)*** *MDA-MB-468; and LC3 in* ***(E)*** *MDA-MB-231 and* ***(F)*** *MDA-MB-468. The results are expressed as the mean ± SEM based on three independent experiments. The statistical significance was assessed in comparison to the untreated cells. The significance level was set at $p < 0.05$ (*), $p < 0.01$ (**), $p < 0.001$ (***) and $p < 0.0001$ (****).*

Drug efflux transport systems have extensively been studied owing to the phenomenon of multi-drug resistance, whereby cancer cells acquire resistance to multiple cytotoxic anticancer drugs. Multi-drug resistance often results from the overexpression of the ABC transporters. Therefore, the expression levels of the ABC transporter, MDR1 in MDA-MB-231 and MDA-MB-468 were also observed, which was found to be downregulated following combination treatment **(Figure 3.3.28)**.

Furthermore, the expression of PD-L1 has been associated with enhanced tumorigenesis, and proliferation and inversely correlated with survival in breast cancer patients. It affects the potential for immune invasion in breast cancer [129]. HDAC inhibition induces PD-L1 expression in various cancer subtypes [130]. Additionally, the Notch signalling pathway is also responsible for activating the expression of PD-L1 [131]. Herein, it is observed that SAHA mediates the expression of PD-L1 by 1.43-fold and 1.26-fold in MDA-MB-231 and MDA-MB-468, respectively. However, combination therapy enhanced the expression of PD-L1 in both TNBC cells **(Figure 3.3.28)**, the underlying mechanism of which needs to be ascertained further.

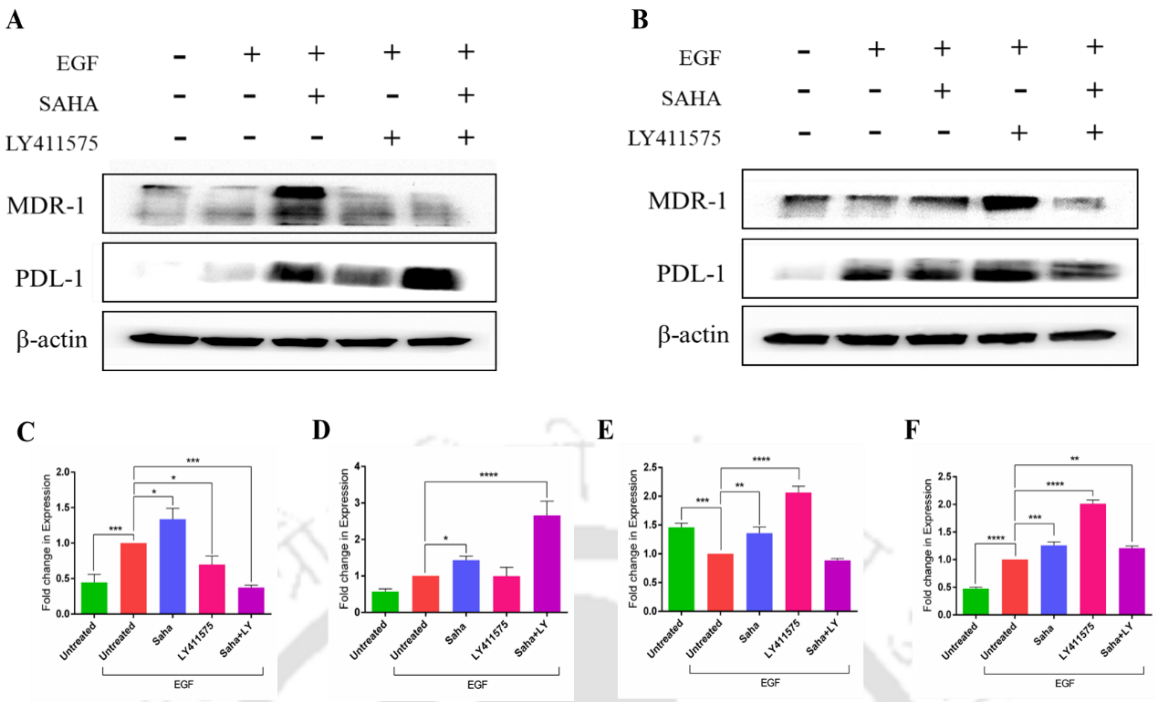

Figure 3.3.28: *Representative immunoblots showing the expression of MDR-1 and PDL-1 in* ***(A)*** *MDA-MB-231 cells, and* ***(B)*** *MDA-MB-468 cells. β-actin serves as a loading control. Graphical representation of the fold change in MDR-1 in* ***(C)*** *MDA-MB-231 and* ***(D)*** *MDA-MB-468; and PDL-1 in* ***(E)*** *MDA-MB-231 and* ***(F)*** *MDA-MB-468. The results are expressed as the mean ± SEM based on three independent experiments. The statistical significance was assessed in comparison to the untreated cells. The significance level was set at $p < 0.05$ (*), $p < 0.01$ (**), $p < 0.001$ (***) and $p < 0.0001$ (****).*

3.3.9. SAHA results in the epigenetic alterations of the TNBC cells

Epigenetic alterations such as DNA methylation and histone modifications such as histone acetylation plays a dominant role in the gene expression profiles, thereby promoting various cancer. Among various epigenetic alterations in cancer, hyperacetylation correlates to the activations of the proto-oncogenes, while hypoacetylation correlates to the suppression or silencing of the tumour suppressor genes [132]. Moreover, Histone 3 acetylation in lysine 9 (H3K9ac) and lysine 14 (H3K14ac) is generally related to the activation of the gene expression.

Hence, given the association of CREBBP and p300 with the CSL, and to obtain a deeper insight intothe histone acetylation status, immunoblot analysis was performed for H3K9ac, H3K14ac and H3K27ac proteins. It was found that the expression of the acetylated histones was upregulated following treatment with SAHA in both the TNBC cells **(Figure 3.3.29).** Moreover, combination treatment also resulted in the upregulation of the acetylated proteins in comparison to the untreated cells. Besides, the co-treatment reduced the expression of acetylated histones in comparison to that of the SAHA-treated cells. However, the detailed acetylation status of the concerned genes following treatment with SAHA is yet to be elucidated.

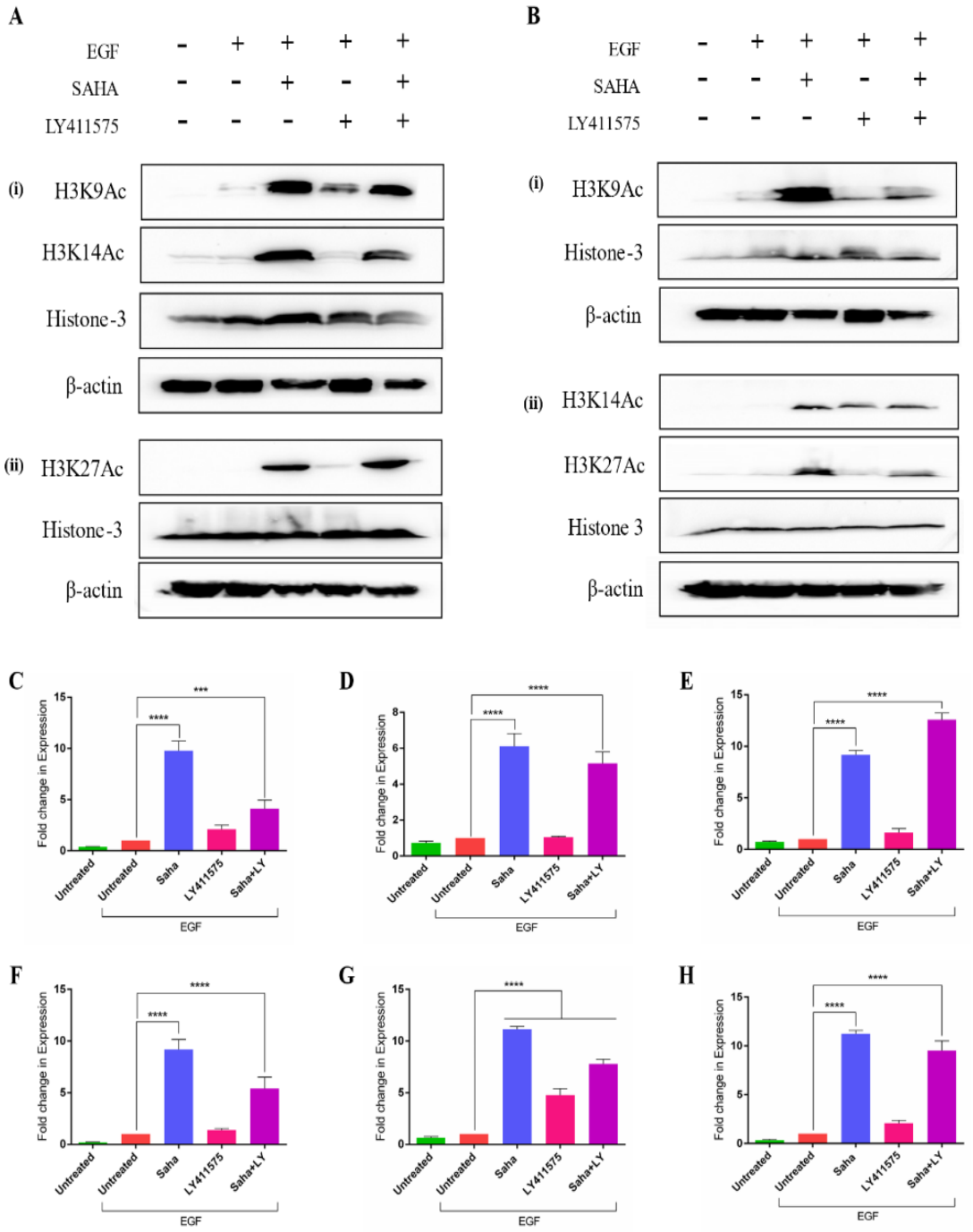

Figure 3.3.29: *Representative immunoblots showing the expression of the acetylated histones in* ***(A)*** *MDA-MB-231 cells, and* ***(B)*** *MDA-MB-468 cells. β-actin serves as a loading control. Graphical representation of the fold change in H3K9ac in* ***(C)*** *MDA-MB-231 and* ***(F)*** *MDA-MB-468; H3K14ac in* ***(D)*** *MDA-MB-231 and* ***(G)*** *MDA-MB-468; while H3K27ac in* ***(E)*** *MDA-MB-231 and* ***(H)*** *MDA-MB-468. Results are expressedas mean ± SEM based on at least 3 independent experiments. The statistical significance was assessed vs. that of the untreated cells. The significance level was set at $p < 0.05$ (*), $p < 0.01$ (**), $p < 0.001$ (***), or $p < 0.0001$ (****).*

It is interesting to note that aberrant histone acetylation contributes to enhanced IL-6 expression in rheumatoid arthritis [133]. Additionally, H3K9ac also results in increased expression in MMPs (such as MMP1, MMP3, MMP10, MMP12, and MMP13), IL6 and TNFα in various metabolic disorders (such as obesity) [134]. Therefore, to ascertain the effect of histone acetylation on the expression of the inflammatory cytokines, qRT-PCR studies were carried out. It was observed that co-treatment resulted in significant downregulation of the cytokines in both the TNBC cells **(Figure 3.3.30).** Following treatment, the MMPs were found to be significantly downregulated in MDA-MB-231 cells; while it was upregulated in MDA-MB-468 cells**.** Altogether, these data suggest that the abrogation of the Notch pathway also results in the inhibition of the inflammatory cytokines as well in the TNBC cells.

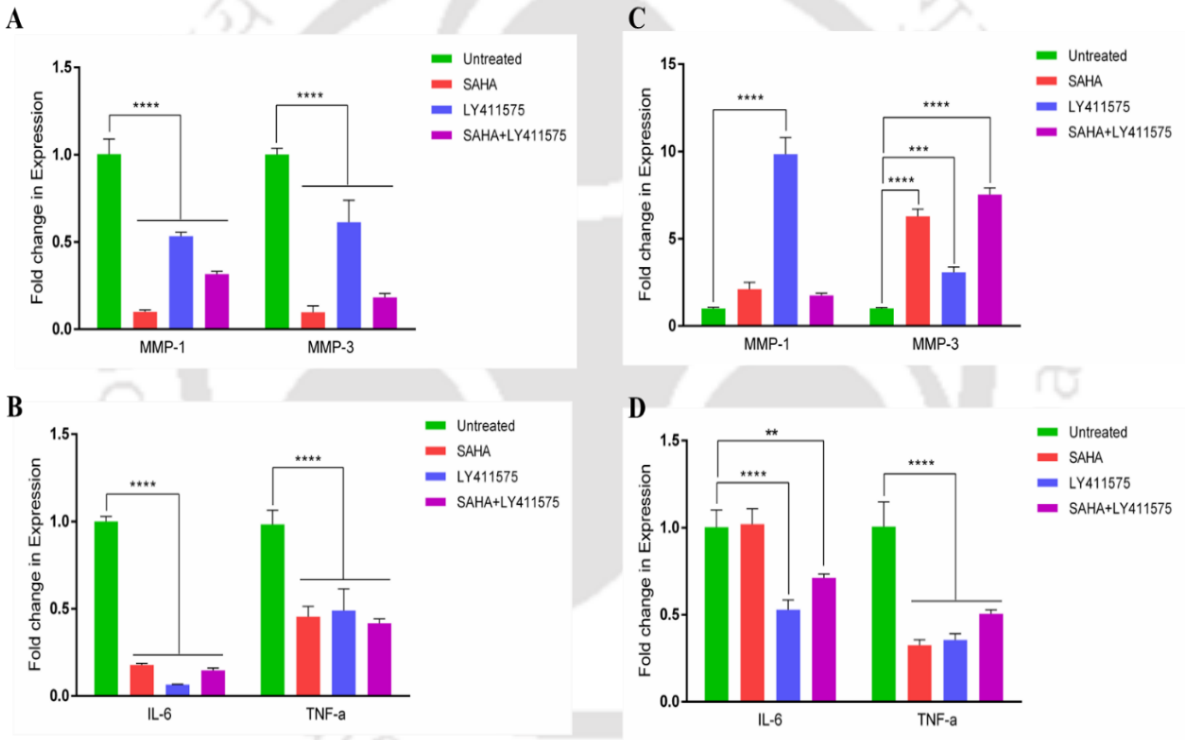

Figure 3.3.30*: Graphical representation of changes in gene expression levels following treatment with the inhibitors in monotherapy as well as in combination therapy as quantified by qRT-PCR analysis.* ***(A)*** *and* ***(B)*** *show gene expression levels obtained from MDA-MB-231 monolayer cultures, while* ***(C)*** *and* ***(D)*** *show gene expression levels obtained from MDA-MB-468 monolayer cultures. Results are expressed as mean ± SEM based on at least 3 independent experiments. The statistical significance was assessed vs. that of the untreated cells. The significance level was set at $p < 0.05$ (*), $p < 0.01$ (**), $p < 0.001$ (***), or $p < 0.0001$ (****).*

Conclusion

Besides a wide variety of genetic and genomic alterations, epigenetic modifications of histones and non-histone proteins play a major role in cancer progression and dissemination. Among them, acetylation and deacetylation of the histones play an important part in the transcriptional regulation of numerous genes in eukaryotic cells. However, cancer cells exhibit increased expression and activity of HDACs, which has led to the rational design and use of HDAC inhibitors for their therapy. Among the several HDACIs, SAHA is one of the most advanced pan-HDAC inhibitors that was approved by the FDA in 2006 for the treatment of cutaneous T-cell lymphoma. Surprisingly, some studies revealed the attritions of SAHA, on account of its ability to promote metastasis. Considering the limited data about the effects on the progression of TNBC, the role of SAHA was investigated in the EMT of TNBC cells.

Research evidence suggests that the Notch pathway facilitates EMT in TNBC cells, which in turn results in the facilitation of metastasis and invasions, drug resistance, maintenance of cancer stem cells (CSCs), etc. The Notch pathway is responsible for the transcriptional activation of the EMT-TFs such as Snail, Twist, Zeb, etc. that potentiate EMT. Interestingly, a study conducted by Jiang et al. has concluded that SAHA upregulates EMT by upregulating the expression of Snail [135]. Therefore, the detailed signalling mechanism was carried out to obtain a deeper insight into the role of HDAC on the Notch pathway. Interestingly, it was found that HDAC is a major component of the co-repressor complex, which might get dissociated upon the action of HDACIs, thereby resulting in the indirect activation of the Notch pathway.

The complex cross talks, feedback loops and their essential roles in maintaining normal homeostasis make it almost impossible to effectively and efficiently abrogate cancer progression. However, combination treatments have proved to be quite effective to avert the severe side effects of chemotherapeutic drugs at high doses. Therefore, the current study focuses on targeting the major protease of the Notch signalling axis, the γ-secretase enzyme, to perceive and prove that SAHA upregulates EMT via the Notch signalling axis. Additionally, the upregulation of the EMT transcription factors at the molecular level after treatment with SAHA, along with the upregulation of the Notch pathway justifies the hypothesis. Indeed, numerous established signalling axis and networks are activated upon treatment with SAHA. However, this study provides a glimpse of an aberrant conserved signalling pathway, being the major regulator of EMT, thereby responsible for the attrition of this drug in aggressive tumour subtypes.

Besides, the effects of HDACIs on the motility of the cancer cells are quite contradictory to the molecular profile. In this study, it was observed that SAHA significantly promotes the protein expression profile of Snail and Slug, which was further downregulated upon the administration of co-treatment. However, SAHA also confers the activation of E-cadherin in both the EMT-induced TNBC cells, while it has no such impact on the MDA-MB-468 cell line.

Additionally, the Notch downstream genes as well as the Notch ligands were found to be upregulated following treatment with SAHA; while co-treatment successfully downregulated the protein expression profile of the aforementioned genes. Besides, the expression of ABC-transporter genes was also found to be downregulated following combination therapy. Moreover, co-treatment mediates autophagy-independent cell death, diminishes the expressionof inflammatory cytokines and inhibits the stemness properties of TNBC cells. Additionally, SAHA also mediates the upregulation of global acetylation of histones, which might be due to the activation of EP300, a histone acetyltransferase p300; a component of the co-activator complex.

Conclusively, this study provides insight into the involvement of the Notch pathway in aggressive tumour subtypes, which can be therapeutically targeted in combination with SAHA to abrogate the undesirable impact of HDACIs.

3.4. Targeting Cross-talks of Notch and VEGF in the Realm of EMT and EPT Dynamics in Triple Negative Breast Cancer Cells

- Manuscript Communicated

Results and Discussions

Abstract

The associations of the Notch pathway with the major oncogenic pathways are primarily responsible for inducing EMT, angiogenesis, and chemoresistance. In this study, Axitinib was chosen to establish the connections between the oncogenic RTKs such as VEGFs, EGFR and Notch in TNBC progression and dissemination. Moreover, Axitinib was used in combination with LY411575 (a potent Notch pathway inhibitor) and it was observed that the co-treatment synergistically induced apoptosis (by 35.73% in MB-231 and 27.7% in MB-468), arrests cells at the G2/M phase, decreases the stemness properties of the TNBC cells. Also, it diminishes the capability of cells to form spheroids, enhances the expression of epithelial markers, such as E-cadherin (by 2.2-fold in MDA-MB-231 and 2.51-fold in MDA-MB-468) and downregulated the expression of mesenchymal genes and proteins. Additionally, the protein expression profile of the pro-oncogenic and pro-survival genes also reduced significantly after the administration of co-therapy, which was highlighted by a reduction in the levels of pEGFR, pFAK, pMAPK, NF-κB, etc. Moreover, the expression of pericyte markers (such as PDGFRs, α-SMA, c-kit and NG2) was also found to be downregulated following combination therapy. Especially, the protein expression levels of NG2 (a potent pericyte marker) were found to be diminished significantly by 1.69-fold in MDA-MB-231and 2.1-fold in MDA-MB-468 cells, thereby hinting towards the inhibition of epithelial-to-pericyte transition (EPT). The current work establishes the effectiveness of the co-therapy on the EMT andEPT dynamics of TNBC upon inhibition of the major cross-talk between the VEGF and Notch pathway.

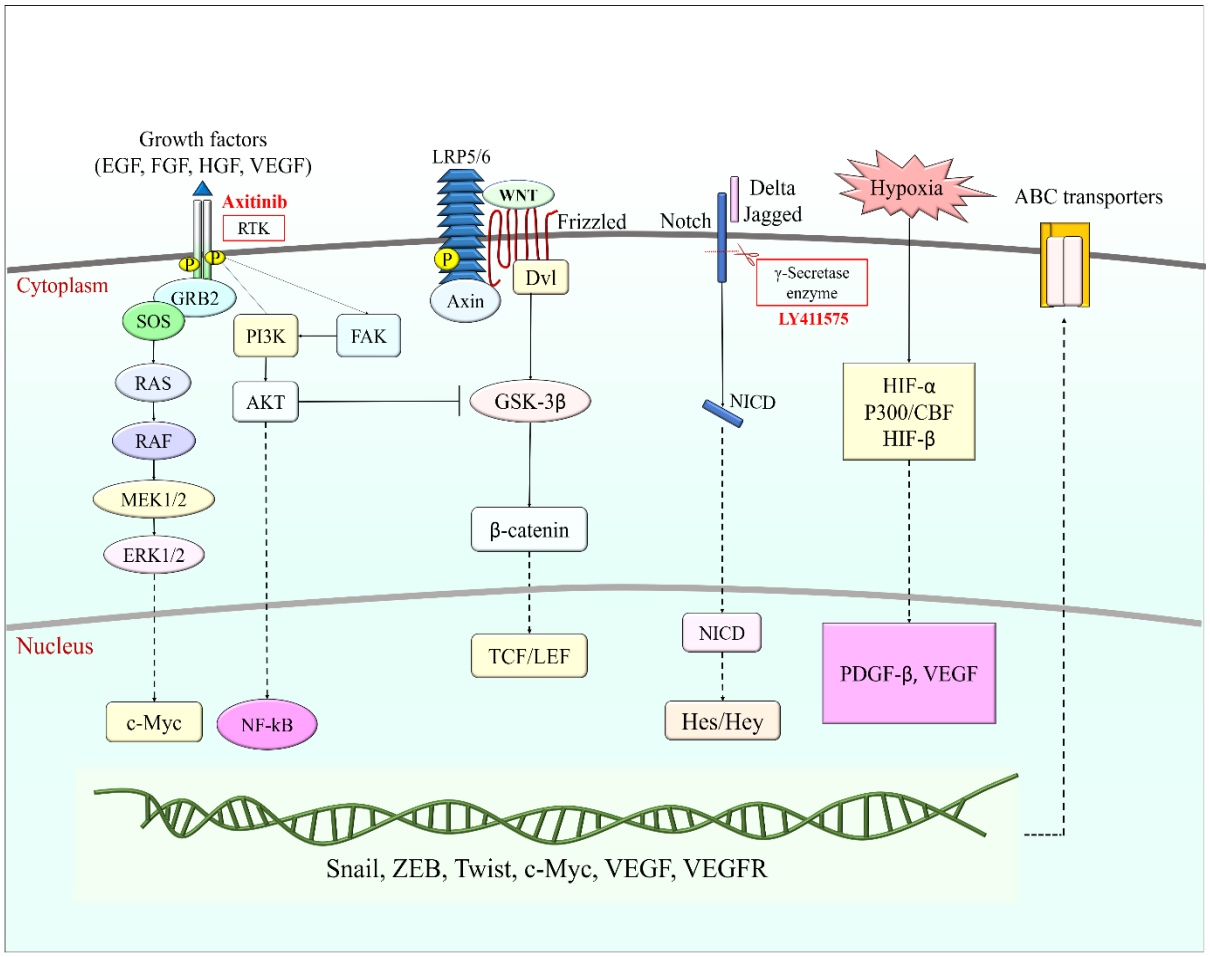

Downregulation of epithelial markers	*Proliferation and Survival*	*Angiogenesis*
Upregulation of mesenchymal markers	*Upregulation of pericyte markers*	*Drug resistance*

Schematic 3.4.1: *An overview of the crosstalk among the major oncogenic signals with the Notch pathway, which promotes the aggressiveness of TNBC. (Adapted and redrawn from: 10.1039/D0MA00455C)*

3.4.1 The functional network connections between the Notch and the VEGF pathway

Initially, cell signalling pathways have been treated as linear, and hence were always studied in isolation. However, the emerging fields of system biology emphasize the importance of intertwined networks and their close associations and cross-talks. Herein, the interconnection among the functional network was established upon combining the major regulatory pathways such as the VEGF pathway (KEGG ID: hsa04370), Notch pathway (KEGG ID: hsa04330), Wnt pathway (KEGG ID: hsa04310), Akt pathway (KEGG ID: hsa04151), MAPK (KEGG ID: hsa04010), JAK/STAT pathway (KEGG ID: hsa04630), FAK pathway (KEGG ID: hsa04510), and HIF signalling pathway (KEGG ID: hsa04066). Initially, the details of these pathways were obtained using the KEGG pathway database, following which the associations were established from a literature survey. However, the main aim was to establish the prominent crosstalk between the Notch and VEGF pathways, and their outcome on the aggressiveness of TNBC.

It is observed that the VEGF has direct associations with the Notch signalling pathway. It induces the expression of both ligands and receptors of the Notch. It was first demonstrated in human arterial endothelial cells (ECs), where Notch1 and DLL4 were found to be overexpressed [136]. Further studies confirmed that DLL4-mediated Notch signalling represses the transcription of VEGFR2 via upregulation of HEY1, thereby establishing a negative feedback loop. This, however, is an essential mechanism in developing the retina, where the genes are regulated in an oscillatory manner. In other words, an increase in the expression is correlated to tip cell phenotype that migrates towards the source of VEGF, while a subsequent decrease in its expression is essential for angiogenesis, along with the establishment of tube formation and vessel maturation [137], [138]. Altogether, the complex interactions of the functional associations between the various pathways, which facilitate the hallmarks of cancer (especially EMT, EPT and angiogenesis) are depicted in **Figure 3.4.1**.

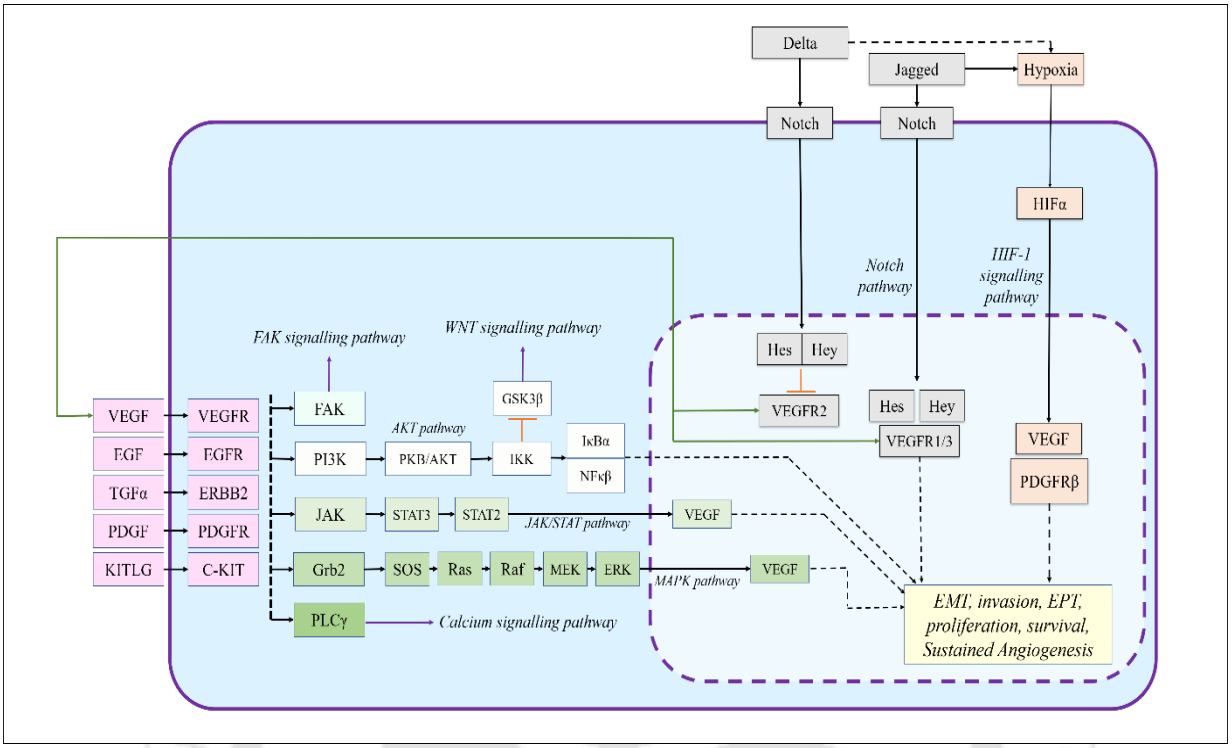

Figure 3.4.1: *Pictorial representation of the cohort of multiple pathways that facilitates the major hallmarks of cancer (Adapted and redrawn from https://doi.org/10.1039/D0MA00455C and KEGG pathway database)*

3.4.2 Axitinib in combination with LY411575 synergistically inhibits the overall survival of the TNBC monolayer cells and 3D spheroids *in vitro*

Keeping in mind the associations of Notch with VEGF and other RTK pathways, Axitinib was chosen to target the RTKs (such as VEGFRs, PDGFRs, α-SMA, c-Kit, etc.), whereas LY411575 was chosen to target the Notch pathway.

Moreover, to examine the effects of co-therapy on TNBC monolayer cells, an MTT assay was performed in monolayer cells. It was found that treatment with corresponding inhibitors alone and in combination decreases the viability of the cells in a dose-dependent manner **(Figure 3.4.2)**. However, in comparison to Axitinib, a higher dose of LY411575 was required to attain the IC_{50} in the TNBC cells. It was also observed that higher concentrations of inhibitors were required to obtain the IC_{50} in MDA-MB-231 cells, as compared to that of MDA-MB-468. Additionally, co-treatment resulted in a decrease in the IC_{50} concentrations effectively, thereby reducing the total drug load. The IC_{50} values for the respective drugs and their combinations are depicted in **Table 3.4.1**. Furthermore, the combination index (CI) values calculated utilizing the Chou-Talalay method revealed a CI <1, thereby depicting synergistic interactions of the two inhibitors when used in combination, as represented in **(Figure 3.4.2: C and F).**

Table 3.4.1: *The IC_{50} concentration of drugs on the TNBC cell lines*

Cell line	Axitinib	LY411575	Axitinib + LY411575
Monolayer culture (EMT induced) (µM)			
MDA-MB-231	40.96	113.60	20 + 64.24
MDA-MB-468	16.06	49.83	8 + 18.51
Monolayer culture (µM)			
MCF7	9.6	46.16	-
3D-spheroid (µM)			
MDA-MB-231	168.2	224	80 + 95.10
MDA-MB-468	89.23	108.2	40 + 49.18

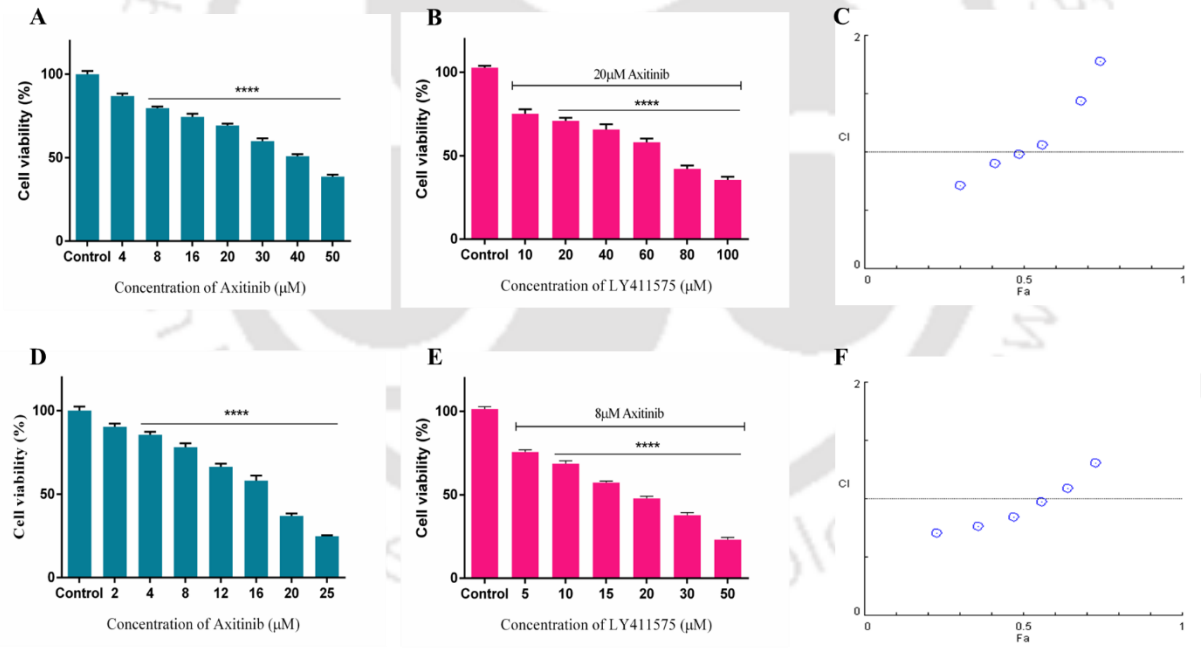

Figure 3.4.2: *Determination of cell viability of monolayer cells, using MTT-based cytotoxic assay. The viability of the TNBC cells was observed after 48 h of treatment with* ***(A)*** *Axitinib, and its combination with LY411575* ***(B)*** *in MDA-MB-231; while the viability obtained after treatment with* ***(C)*** *Axitinib, and its combination with LY411575* ***(D)*** *in MDA-MB-468 cells.* ***(E)*** *and* ***(F)*** *represents the combination index of the treatment MDA-MB-231 and MDA-MB-468 cells, respectively. Based on three independent experiments, the results are represented as mean ± SEM, along with a statistical significance denoting $p < 0.5$ (*), $p < 0.1$ (**), $p < 0.01$ (***) and $p < 0.001$ (****).*

Similarly, the viability of the 3D-Tumour spheroids was obtained after the respective treatments of the TNBC (MDA-MB-231 and MDA-MB-468) cells, using an alamarBlue assay **(Figure 3.4.3)**. It also revealed a dose-dependent cell death, especially in the case of co-therapy. The IC_{50} value was found to be approximately four-fold higher in comparison to the monolayer culture. Moreover, to ascertain the effects of the drugs in 3D Tumours spheroids, Calcein/AM-PI-based live-dead cell imaging was carried out. It is found that the co-treatment effectively reduces the cell viability, as ascertained by the increase in the PI intensity in comparison to that of the untreated cells. Furthermore, after the administration of co-treatment, the percentage of live cells reduced significantly in comparison to that of the untreated cells, which is visible in the Z-stack projection of the 3D tumour spheroids of MDA-MB-231 **(Figure 3.4.4)** and MDA-MB-468 **(Figure 3.4.4).** Altogether, these data suggest that tweaking the VEGF and the Notch pathway signalling synergistically inhibits the proliferation and survival of TNBC monolayer as well as of 3D spheroids.

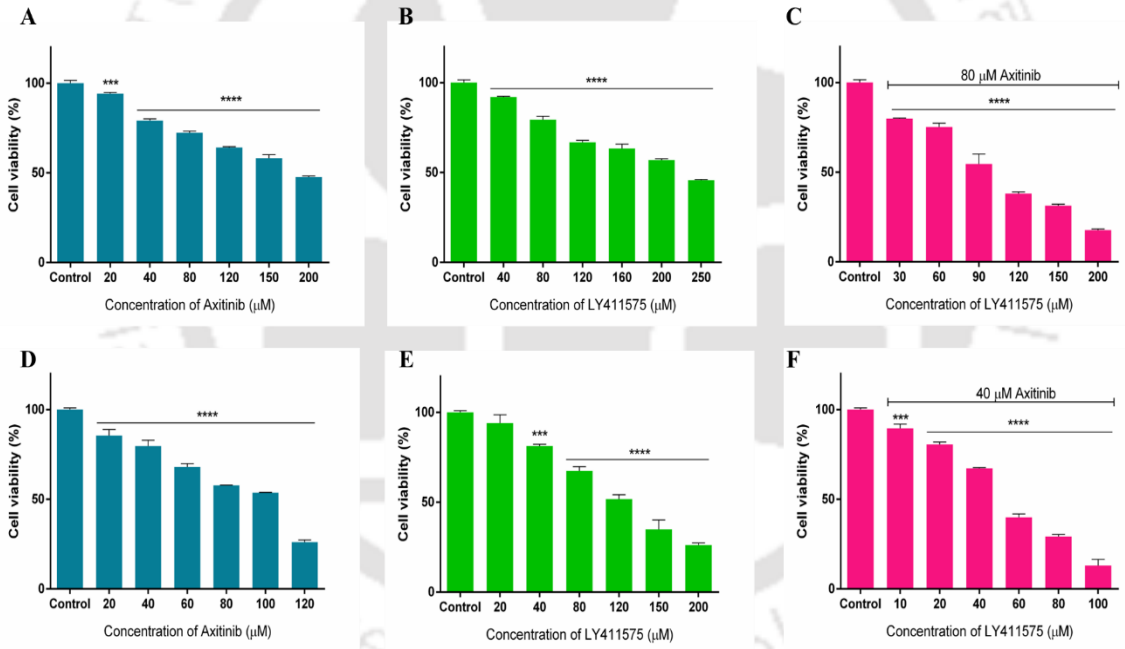

Figure 3.4.3: *Determination of cell viability of 3D-Tumours spheroids, using the alamarBlue-based cytotoxic assay. The viability of the TNBC cells was observed after 48 h of treatment with* ***(A)*** *Axitinib,* ***(B)*** *LY411575 and* ***(C)*** ***a*** *combination of Axitinib and LY411575 in MDA-MB-231 3D Tumours spheroids; while* ***(D), (E)*** *and* ***(F)*** *denotes treatment with Axitinib, LY411575 and combination of Axitinib and LY411575 in MDA-MB-468 3D Tumours spheroids, respectively. Based on three independent experiments, the results are represented as mean ± SEM, along with a statistical significance denoting p < 0.5 (*), p < 0.1 (**), p < 0.01 (***) and p < 0.001 (****).*

3.4.3 Co-treatment synergistically generates ROS, induces apoptosis and arrests cells in the G2/M phase

Next, the outcome of combination treatment was assessed by measuring cellular ROS in TNBC cells. It was noticed that there was a significant surge in cellular ROS after treatment with respective inhibitors. However, the fold-change generation of cellular ROS was found to be maximum after combination treatment in TNBC cells. For example, cellular ROS increased by 7.5-fold in MDA-MB-231 **(Figure 3.4.5: A)** and 1.93-fold in MDA-MB-468 **(Figure 3.4.5: B)** cells after co-treatment. The tabular representation regarding the fold change in cellular ROS generation after the respective treatments are presented in **Figure 3.4.5: C**.

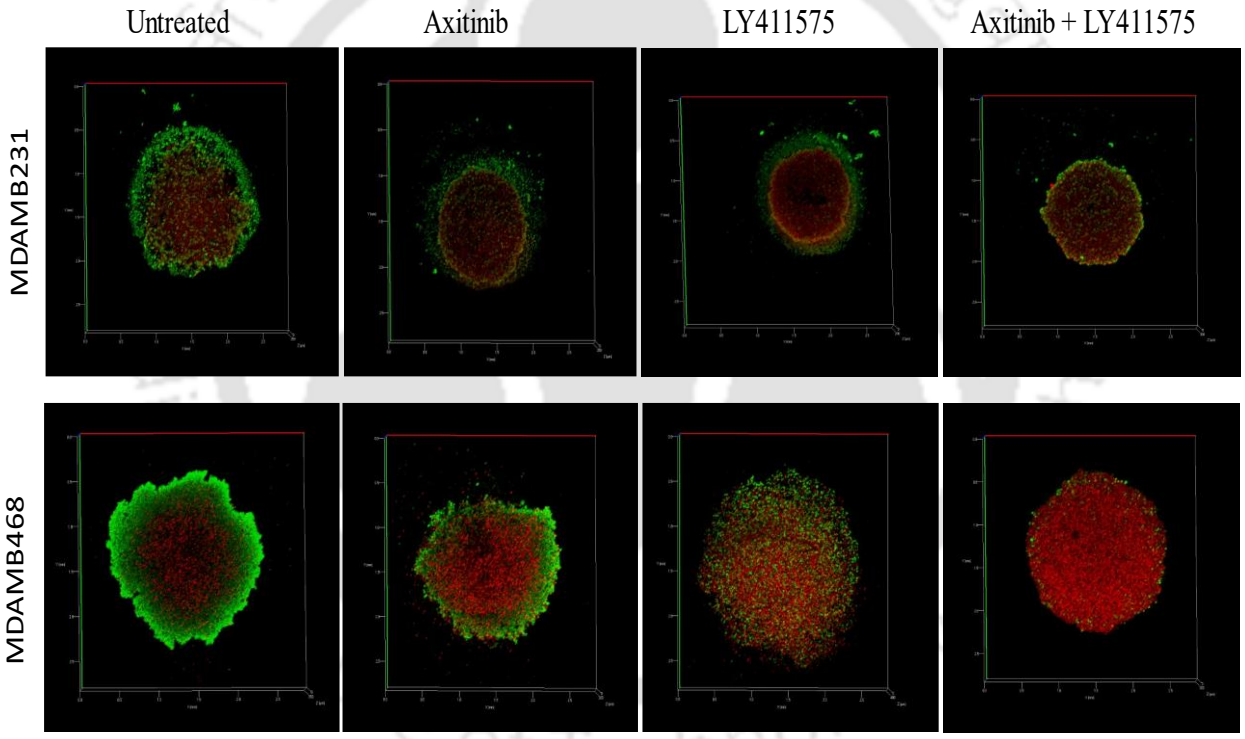

Figure 3.4.4: *Visualization of the z-stack projections of Live-dead cells of MDAMDA-MB-468 3D Tumours spheroids, after staining with Calcein-AM/Propidium Iodide (PI). The green fluorescence obtained from the Calcein-stained cellsrepresents the live cells, while the red fluorescence obtained from PI-stained cells represents dead cells. The scale barrepresents 200 μm.*

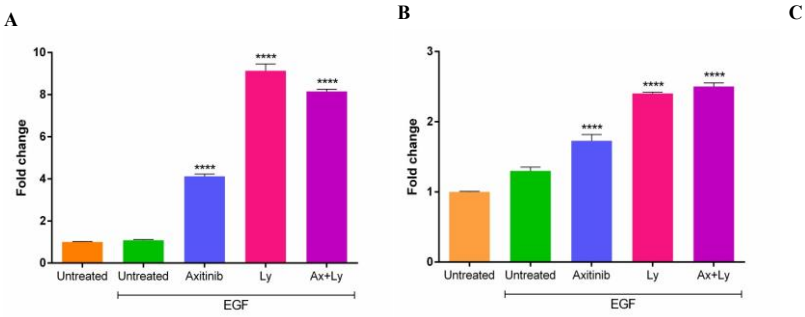

C

Inhibitors	MDA-MB-231	MDA-MB-468
Axitinib	3.67	1.33
LY411575	8.41	1.85
Axitinib + LY411575	7.5	1.93

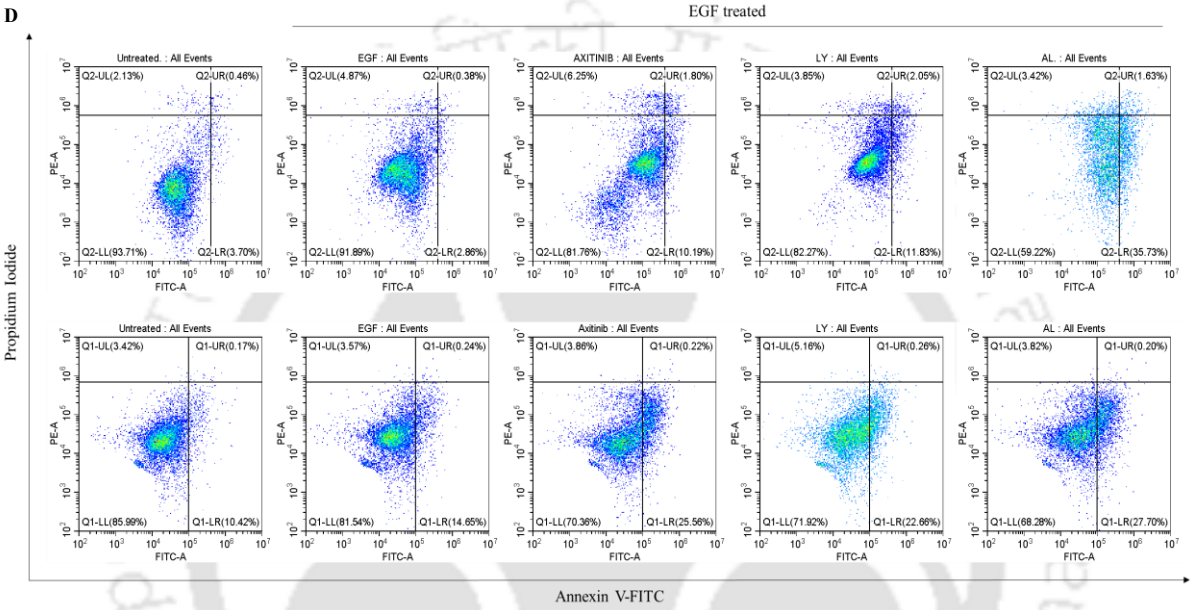

Figure 3.4.5: *Graphical representation of the fold-change generation of Reactive oxygen species (ROS) in* ***(A)*** *MDA-MB-231 and* ***(B)*** *MDA-MB-468 cells.* ***(C)*** *Tabular representation of the fold-change in the generation of cellular ROS.* ***(D)*** *Determination of apoptotic cell populations after subsequent treatments in comparison tothe control (untreated) in* ***(i)*** *MDA-MB-231 and* ***(ii)*** *MDA-MB-468 cells. The results are expressed as the mean ± SEM based on three independent experiments. The statistical significance was assessed in comparison to the untreated cells. The significance level was set at $p < 0.05$ (*), $p < 0.01$ (**), $p < 0.001$ (***) and $p < 0.0001$ (****).*

Moreover, ROS mediates apoptosis in cancer cells. Thus, we ventured into the effect of co-treatment on the apoptosis and/or necrotic cell populations. It was observed that combination treatment synergistically induced apoptosis in both the TNBC cells by approximately 35.73 % (in MDA-MB-231) and 27.7 % (in MDA-MB-468) in comparison to the control cells **(Figure 3.4.5: D)**. Further, to assess the role of Axitinib, LY411575 and their co-treatment on the membrane integrity of mitochondria, JC-1 based flow cytometric assay was performed. It was observed that Axitinib did not affect the integrity of mitochondrial membrane potential. Similar was the case for LY411575 and their co-treatment **(Figure 3.4.6)** in both TNBC cell lines.

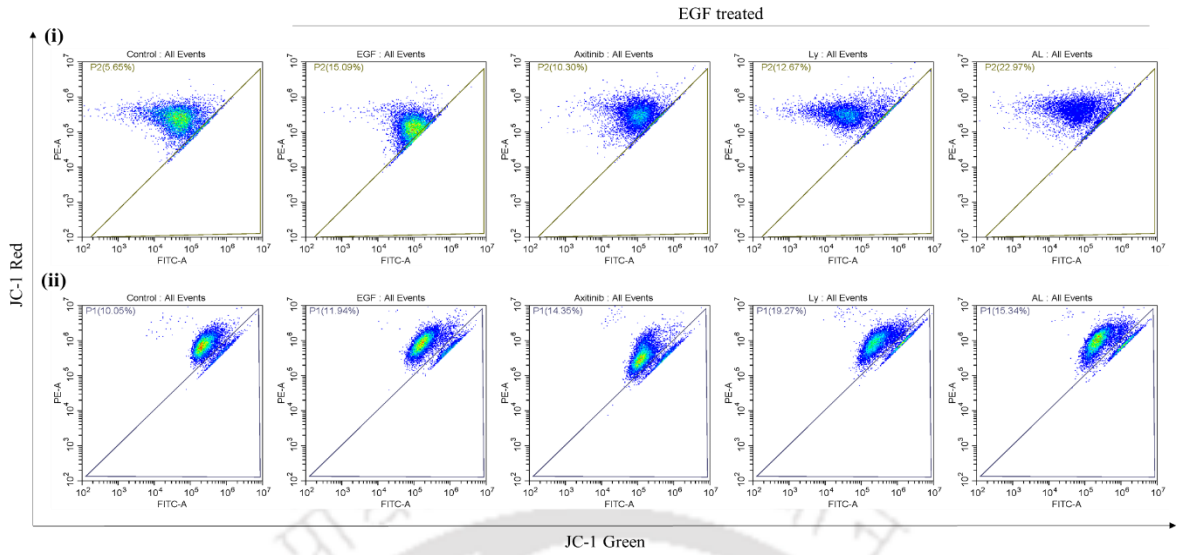

Figure 3.4.6: *Assessment of mitochondrial membrane integrity using JC-1 based flow cytometry in* ***(i)*** *MDA-MB-231 and* ***(ii)*** *MDA-MB-468 cells.*

Since ROS successfully induced apoptosis in TNBC cells, hence the effect of the drugs on the cell cycle profile was further assessed. Here, cell cycle analysis of the treated cells revealed that Axitinib induces G2/M cell cycle phase arrest in both MDA-MB-231 **(Figure 3.4.7: A)** and MDA-MB-468 cells **(Figure 3.4.7: B)**. This is in correlation with the studies performed by Stehle *et al.*, where they discovered that Axitinib resulted in the induction of the Mcl-1 protein, thereby leading to G2/M phase arrest and delayed apoptosisin T-cells [139].

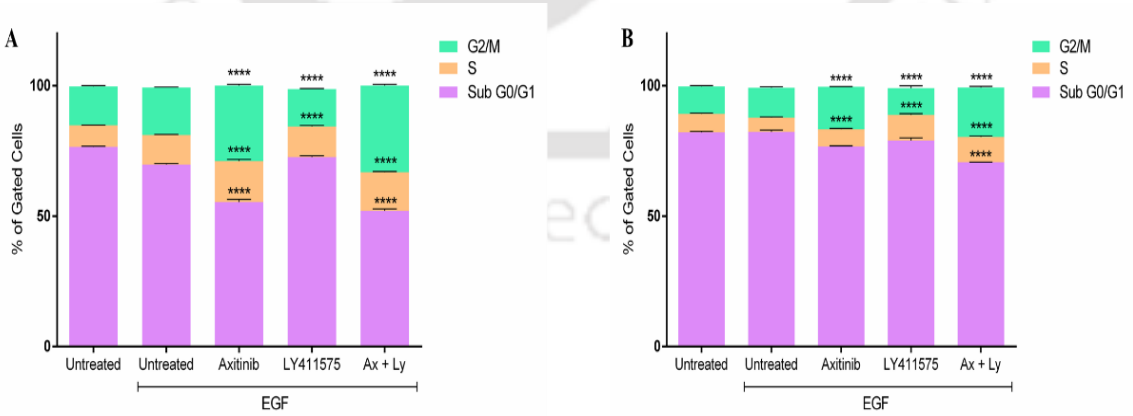

Figure 3.4.7: *Cell cycle profile following treatment in* ***(A)*** *MDA-MB-231 and* ***(B)*** *MDA-MB-468 cells. The results are expressed as the mean ± SEM based on three independent experiments. The statistical significance was assessed in comparison to the untreated cells. The significance level was set at $p < 0.05$ (*), $p < 0.01$ (**), $p < 0.001$ (***) and $p < 0.0001$ (****).*

3.4.4 Co-treatment reduces the stemness properties of the TNBC cells

Almost all malignant cells comprise stem-like characteristics, which exhibit an exclusive property of differentiation and self-renewal. The stemness of any cancer cells is determined by the presence of surface markers, such as $CD44^{high}/CD24^{low}$. The immune flow cytometry analysis revealed a concomitant upregulation in CD24 markers and a decrease in CD44 markers, after administration of combination treatment **(Figure 3.4.8).**

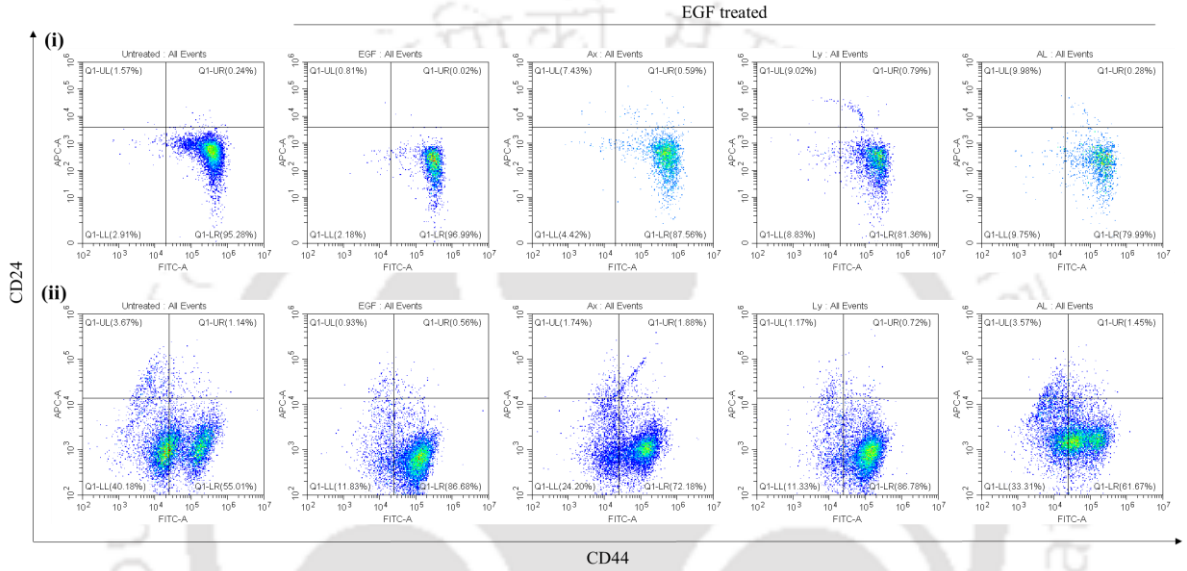

Figure 3.4.8: *A pseudo-plot presentation of alteration of stemness maerkers (CD44/CD24) in* ***(i)*** *MDA-MB-231 and* ***(ii)*** *MDA-MB-468 cells*

Given the significant associations of EpCAM and Ki-67 in enhancing the metastatic propensity of the TNBCs, along with their correspondence to the generation and maintenance of CSCs [140]. We ventured into the gene expression analysis of EpCAM and Ki-67, following respective treatments. It was observed that combination therapy, along with monotherapy reduces the gene expression level of EpCAM by 1.43-fold in MDA-MB-231 **(Figure 3.4.9: A)** and 1.35-fold in MDA-MB-468 cells **(Figure 3.4.9: B)**. Similarly, after treatment with respective inhibitors alone and their combinations, there was a significant downregulation in the expression of Ki-67 genes. Especially after co-treatment, there was a 2.64-fold change decrease in the expression of Ki-67 in MDA-MB-468 cells **(Figure 3.4.9: B)**.

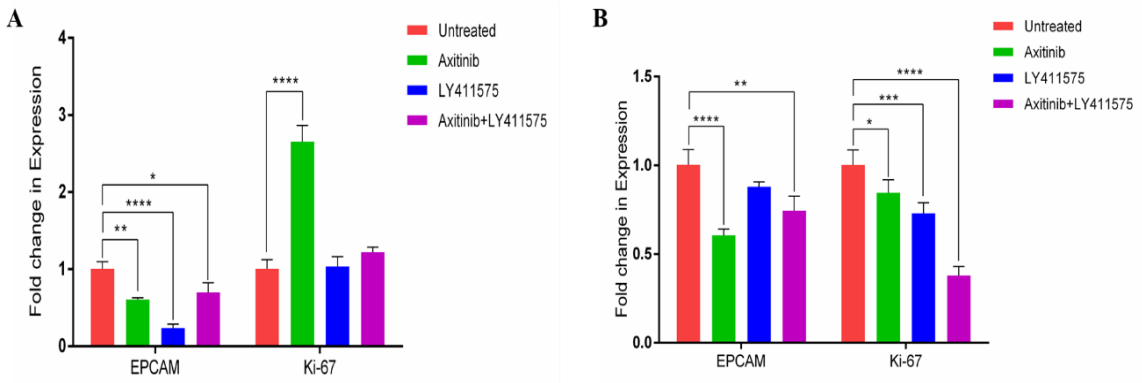

Figure 3.4.9: *Graphical depiction of the alteration in the gene expression profile of stemness markers EpCAM and Ki-67 in* ***(A)*** *MDA-MB-231 and* ***(B)*** *MDA-MB-468 cells, obtained by qRT-PCR analysis. The results are expressed as the mean ± SEM based on three independent experiments. The statistical significance was assessed in comparison to the untreated cells. The significance level was set at p < 0.05 (*), p < 0.01 (**), p < 0.001 (***) and p < 0.0001 (****).*

The stemness properties of the TNBC cells are not restricted to the gene expression profile of stemness markers, rather it also governs the spheroid-forming ability of a cohort of cells. Therefore, to evaluate the effect of treatment on the spheroid-forming ability of the TNBC cells, a spheroid formation assay was carried out. It was noted that combination treatment reduced the sphere-forming ability of MDA-MB-231 cells **(Figure 3.4.10: A and B).** A similar result was also obtained in the case of MDA-MB-468, along with the disintegration in the formation of spheroids **(Figure 3.4.10: A and C).** Moreover, there was also a significant reduction in the sphere-forming ability of the TNBC cells following treatment with LY411575, followed by Axitinib.

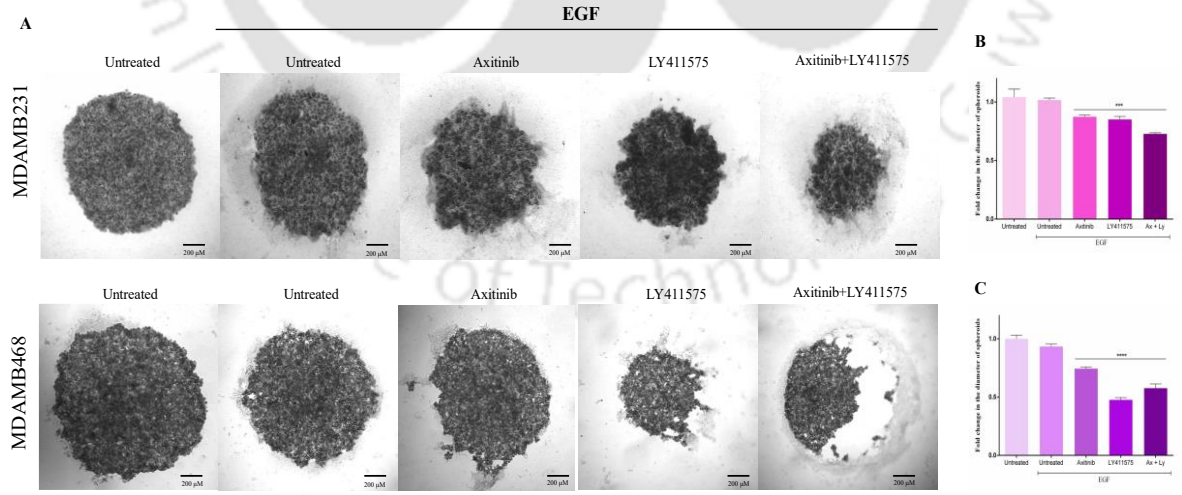

Figure 3.4.10: ***(A)*** *Evaluation of the spheroid forming ability of TNBC cells. Graphical illustration of the changesin the diameter of 3D tumour spheroids after administration of respective treatments in* ***(B)*** *MDA-MB-231 and* ***(C)*** *MDA-MB-468 cells. The results are expressed as the mean ± SEM based on three independent experiments. The statistical significance was assessed in comparison to the untreated cells. The significance level was set at p < 0.05 (*), p < 0.01 (**), p < 0.001 (***) and p < 0.0001 (****).*

3.4.5 Co-treatment synergistically reduces the metastatic and invasive potential of the TNBC cells

Besides, inducing apoptosis and cell cycle arrest, the effects of Axitinib on the migratory and invasive potential of TNBC cells were determined. Initially, a scratch (or wound) healing assay was executed to assess the two-dimensional migration of cells. For this, an artificial gap was generated on a confluent monolayer TNBC culture with the help of a 10 µl sterile pipette, to mimic a wound. Further, the movement of the migratory cells was tracked via the Nikon Eclipse Ti-U microscope. It is noticed that the wound healing capacity of the cells reduced significantly upon administration of the combination treatment in MDA-MB-231 **(Figure 3.4.11: A and C)**, as well as in MDA-MB-468 cells **(Figure 3.4.11: B and D).**

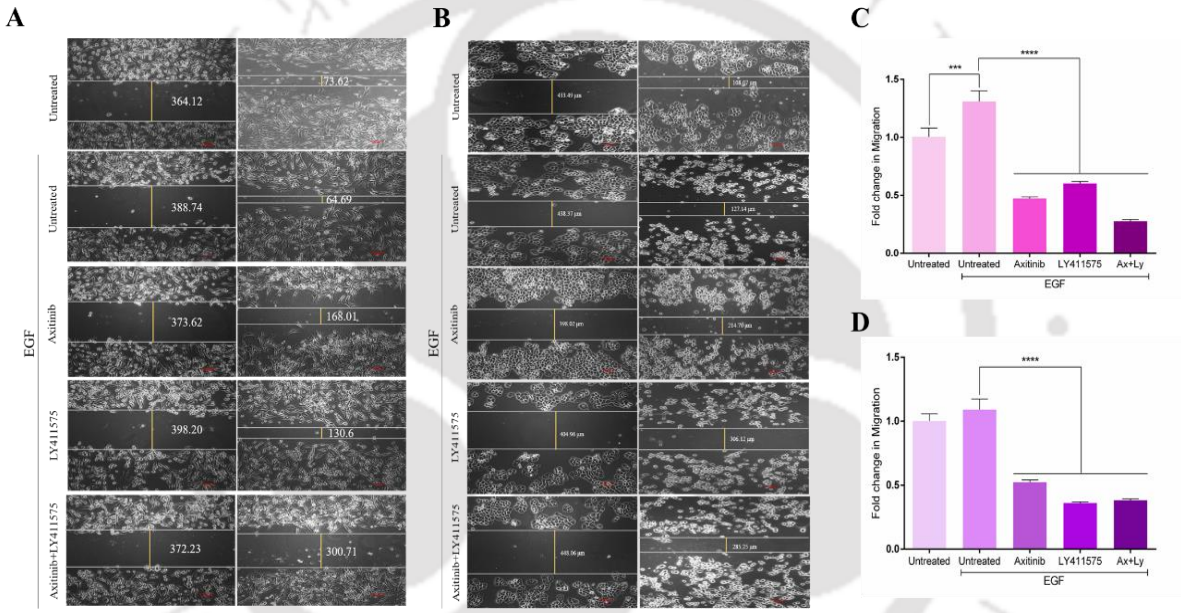

Figure 3.4.11: *Assessment of Scratch (or wound healing) assay after subsequent treatment with respective inhibitors in monotherapy and their combination in* ***(A)*** *MDA-MB-231 and* ***(B)*** *MDA-MB-468 cells. Graphical illustration of fold-change in migration and/or wound healing assay in* ***(C)*** *MDA-MB-231 and* ***(D)*** *MDA-MB-468 cells. The results are expressed as the mean ± SEM based on three independent experiments. The statistical significance was assessed in comparison to the untreated cells. The significance level was set at $p < 0.05$ (*), $p < 0.01$ (**), $p < 0.001$ (***) and $p < 0.0001$ (****).*

Furthermore, Boyden chamber-based Matrigel invasion assay was performed to assess the migratory properties of the TNBC cells. Herein, a significant increase in the number of migratory cells was observed, following the induction of EMT. This justifies the migratory and invasive characteristics of the EMT-induced cells. However, a notable decrease in the number of migrating cells after co-treatment was observed, which signifies the efficacy of the combination treatment in the inhibition of the invasiveness and migratory characteristics of the TNBC cells **(Figure 3.4.12: A).** The graphical presentation of the fold-change in the fluorescence intensity is provided in **Figure 3.4.12: B** and **C**.

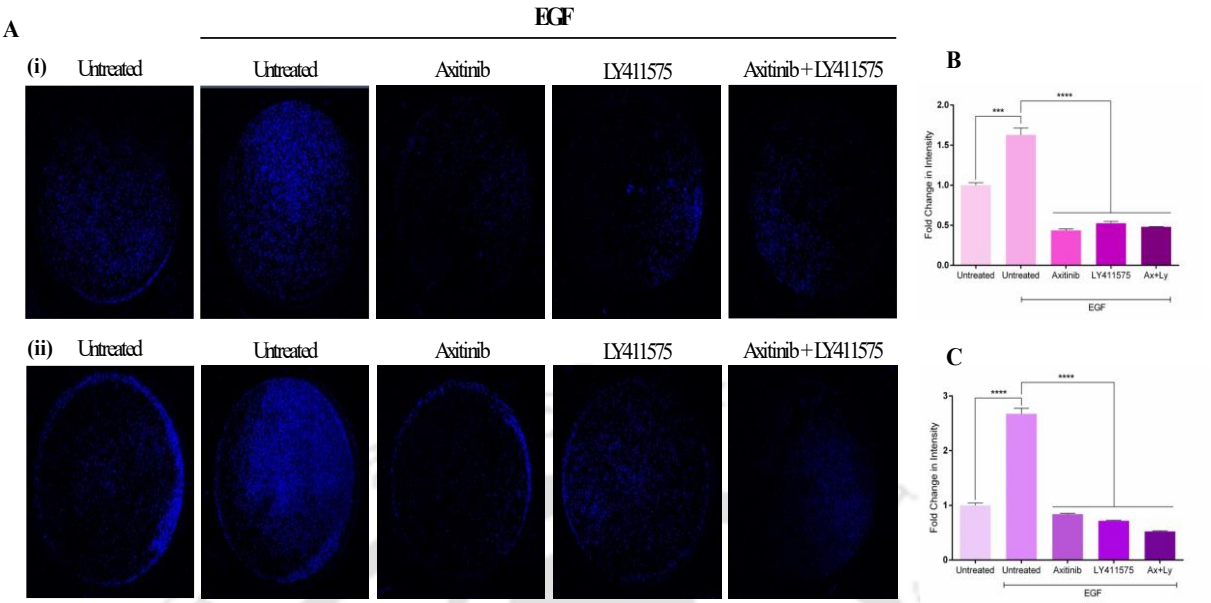

Figure 3.4.12: (A) *Boyden-chamber-based Matrigel invasion assay to obtain the migratory and/or invasive properties of* ***(i)*** *MDA-MB-231 and* ***(ii)*** *MDA-MB-468 cells.* ***(B)*** *and* ***(C)*** *are the graphical presentation ofthe fold-change in intensity to determine the number of migratory cells in MDA-MB-231 and MDA-MB-468, respectively. The results are expressed as the mean ± SEM based on three independent experiments. The statistical significance was assessed in comparison to the untreated cells. The significance level was set at p < 0.05 (*), p < 0.01 (**), p < 0.001 (***) and p < 0.0001 (****).*

3.4.6 Co-treatment synergistically inhibits the EMT markers, EMT-TFs and the Notch pathway genes

From the noteworthy reduction in migratory and invasive properties, along with the reduction in stemness markers of the TNBC cells after co-treatment, we ventured into the molecular profiling of the genes and proteins involved in the upregulation of EMT. Initially, the effect of Axitinib, LY411575 and their respective combination on the gene expression profile of EMT markers and TFs was determined using qRT-PCR analysis. It is found that there was a significant reduction in the expression of the mesenchymal markers. For example, the gene expression level of N-cadherin, Vimentin and Fibronectin decreased by 2.63-fold, 1.72-fold and 1.57-fold in MDA-MB-231, respectively **(Figure 3.4.13: A)**. Similarly, the reduction in N-cadherin, Vimentin and Fibronectin was found to be 3.44-fold, 1.49-fold and 1.37-fold in MDA-MB-468 cells **(Figure 3.4.13: B)**. Additionally, co-treatment also reduced the expression of EMT-TFs such as Snail and Twist by 25-fold and 3.45-fold in MDA-MB-468 **(Figure 3.4.14: D).** However, there was no substantial alteration in the expression of Snail and Twist genes in MDA-MB-231 **(Figure 3.4.13: C).** Moreover, the tabular representation of fold-change in the gene expression profile is represented in **Table 3.4.2**.

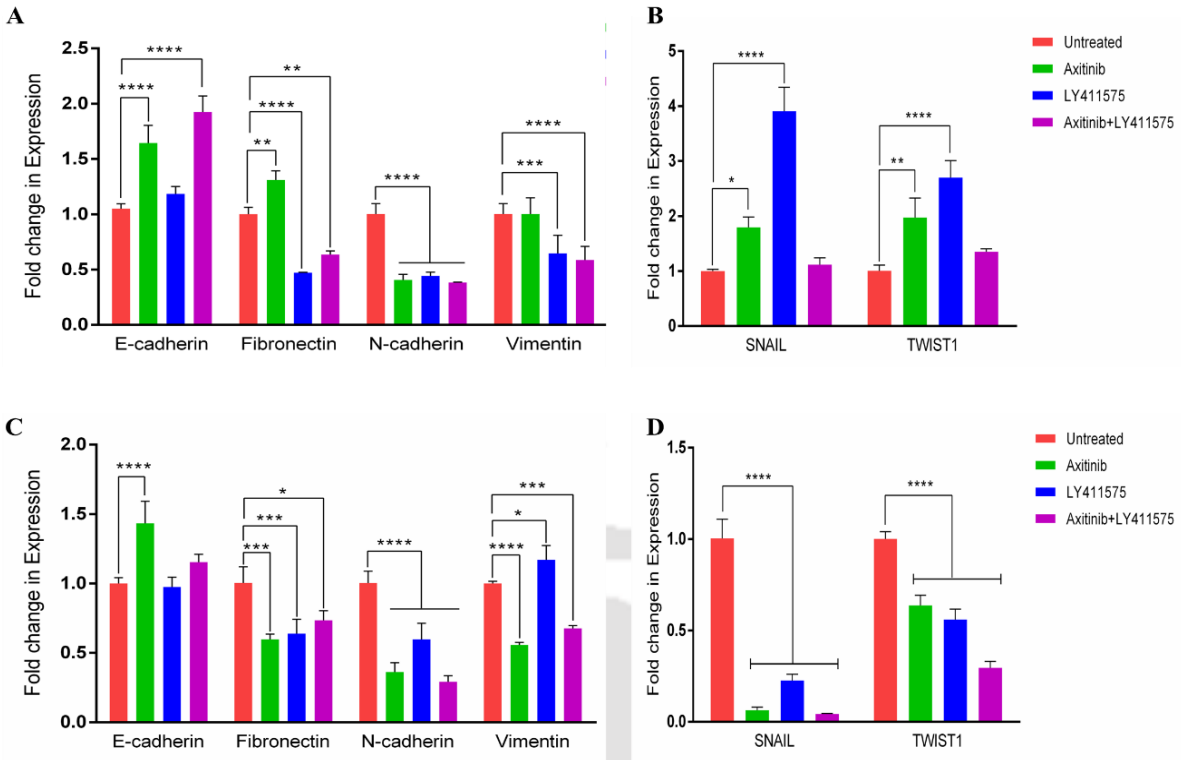

Figure 3.4.13: *Graphical depiction of the alteration in the gene expression profile of epithelial marker: E-cadherin, and mesenchymal markers: Fibronectin, N-cadherin, Vimentin, Snail, and Twist in MDA-MB-231* ***(A)*** *and* ***(B);*** *and MDA-MB-468 cells* ***(C)*** *and* ***(D)****, obtained by qRT-PCR analysis. Based on three independent experiments, the results are represented as mean ± SEM, along with a statistical significance denoting p < 0.5 (*), p < 0.1 (**), p < 0.01 (***) and p < 0.001 (****).*

Table 3.4.2: *Gene expression profile of the EMT markers and EMT-TFs*

Genes	MDA-MB-231			MDA-MB-468		
	Axitinib	LY411575	Ax + Ly	Axitinib	LY411575	Ax + Ly
EMT markers and EMT-TFs						
E-cadherin	**** 1.64	- 1.18	**** 1.92	**** 1.4	- 1.03	- 1.15
Fibronectin	** 1.31	**** 2.13	** 1.57	*** 1.67	*** 1.58	* 1.37
N-cadherin	**** 2.46	**** 2.27	**** 2.63	**** 2.77	**** 1.67	**** 3.44
Vimentin	- 1.07	*** 1.56	**** 1.72	**** 1.82	* 1.17	*** 1.49
Snail	* 1.79	**** 3.9	- 1.11	**** 16.66	**** 4.54	**** 25.00
Twist	** 1.97	**** 2.69	- 1.35	**** 1.58	**** 1.78	**** 3.45

 # Red depicts upregulation in the expression level, while green depicts downregulation in expression level
The significance level was set at p < 0.05 (*), p < 0.01 (**), p < 0.001 (***) and p < 0.0001 (****)

Further, the protein expression profile of the EMT-TFs (such as Twist and Snail) and mesenchymal markers (such as Vimentin) also revealed a significant decrease in the protein expression levels after co-treatment **(Figure 3.4.14 and Figure 3.4.15).** It was observed that co-treatment reduced the expression of Snail by 5.26 in MDA-MB-231 and 4.66 in MDA-MB-468, while the expression of Twist was degraded by 2.22-fold and 1.34-fold in MDA-MB-468 cell lines. **Table 3.4.6** depicts the fold-change difference inthe protein expression level after the administration of respective treatments with respect to the untreated cells. However, Immunocytochemistry analysis of cells stained with an anti-Vimentin antibody (conjugated to a secondary antibody bound with Alexa Fluor 488) was also assessed, which depicted the efficacy of the co-treatment in both the TNBC cells *(data not shown).* Altogether, these data suggest the role of co-treatment in effectively inhibiting the mesenchymal properties of the TNBC cells.

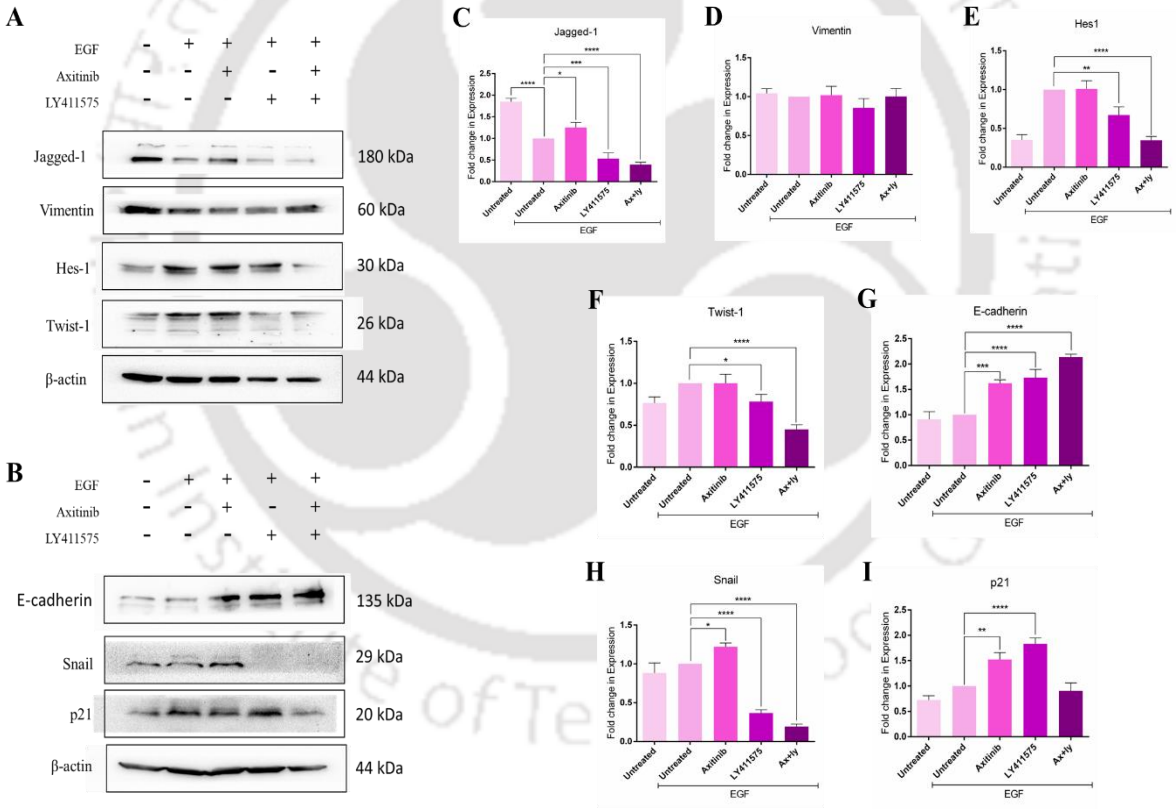

Figure 3.4.14: ***(A)*** *and* ***(B)*** *represents the western blots showing Notch ligand (Jagged-1), Notch target gene (HES-1 and p21), along with the epithelial marker (E-cadherin) and mesenchymal marker (Vimentin, Snail, andTwist-1) obtained from the treated MDA-MB-231 cells. Graphs depicting the alterations in the protein expression profile of* ***(C)*** *Jagged-1,* ***(D)*** *Vimentin,* ***(E)*** *HES-1,* ***(F)*** *Twist-1,* ***(G)*** *E-cadherin,* ***(H)*** *Snail and* ***(I)*** *p21. β-actin was used as a loading control. Based on three independent experiments, the results are represented as mean ± SEM, along with a statistical significance denoting p < 0.5 (*), p < 0.1 (**), p < 0.01 (***) and p < 0.001 (****).*

In addition, both the gene as well as the protein expression profile of E-cadherin (a potent epithelial marker) also endowed us with the rise in its expression profile following combination therapy. Altogether, the gene expression profile increased by 1.92-fold in MDA-MB-231 **(Figure 3.4.13: A)** and 1.15-fold in MDA-MB-468 **(Figure 3.4.13: C)** after co-treatment. Similar was observed in the case of the protein expression, which was upregulated by 2.2-fold in MDA-MB-231 **(Figure 3.4.14: B and G)** and 2.51-fold in MDA-MB-468 **(Figure 3.4.15: B and G)** cells. The immunocytochemistry analysis of the cells stained with anti-E-cadherin antibody (conjugated to a secondary antibody bound with Alexa Fluor488) also reveals a concomitant increase in the expression level of E-cadherin as compared to the untreated cells of MDA-MB-468 **(Figure 3.4.16; Figure 3.4.23: A and F),** along with that of MDA-MB-231 *(data not shown)***.** Additionally, Immunocytochemical analysis also depicts a concomitant decrease in the expression of mesenchymal markers as depicted in **Figure 3.4.23**. Altogether signifying the synergistic role of combination therapy in reversing EMT upon acquisition ofthe epithelial marker.

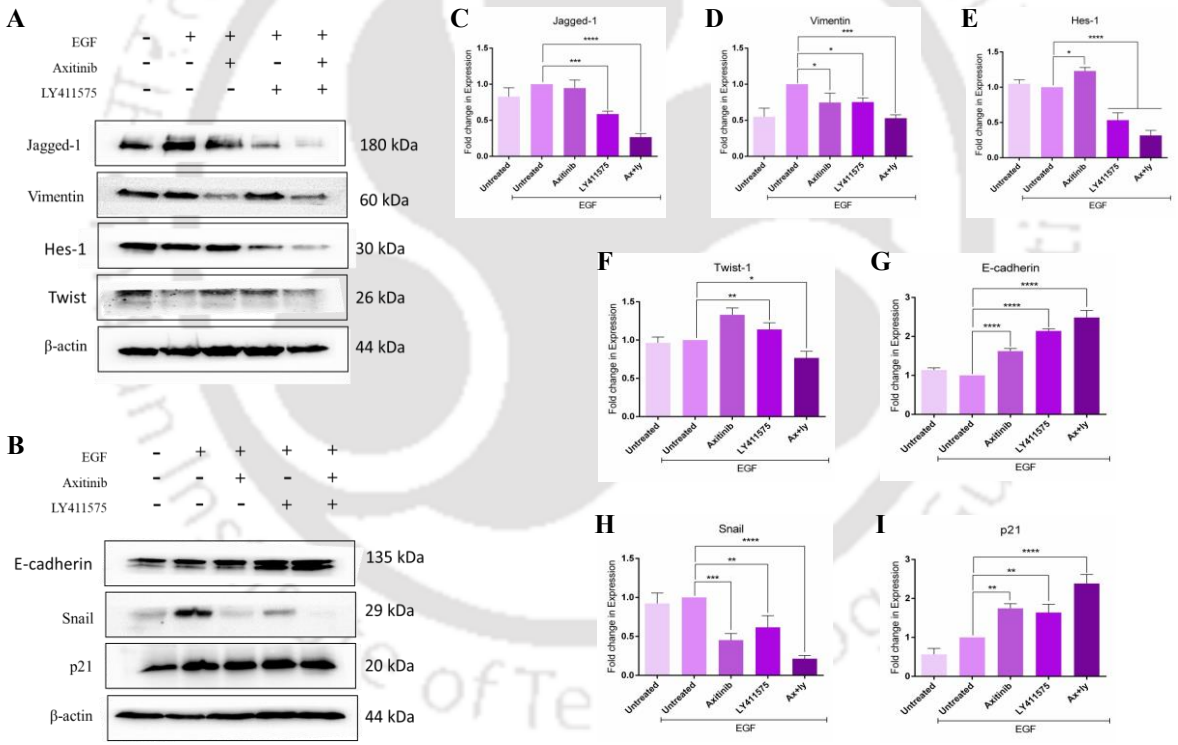

Figure 3.4.15: (A) *and* ***(B)*** *represents the western blots showing Notch ligand (Jagged-1), Notch target gene (HES-1 and p21), along with the epithelial marker (E-cadherin) and mesenchymal marker (Vimentin, Snail, andTwist-1) obtained from the treated MDA-MB-468 cells. Graphs depicting the alterations in the protein expression profile of* ***(C)*** *Jagged-1,* ***(D)*** *Vimentin,* ***(E)*** *HES-1,* ***(F)*** *Twist-1,* ***(G)*** *E-cadherin,* ***(H)*** *Snail and* ***(I)*** *p21. β-actin was used as a loading control. Based on three independent experiments, the results are represented as mean ± SEM, along with a statistical significance denoting p < 0.5 (*), p < 0.1 (**), p < 0.01 (***) and p < 0.001 (****).*

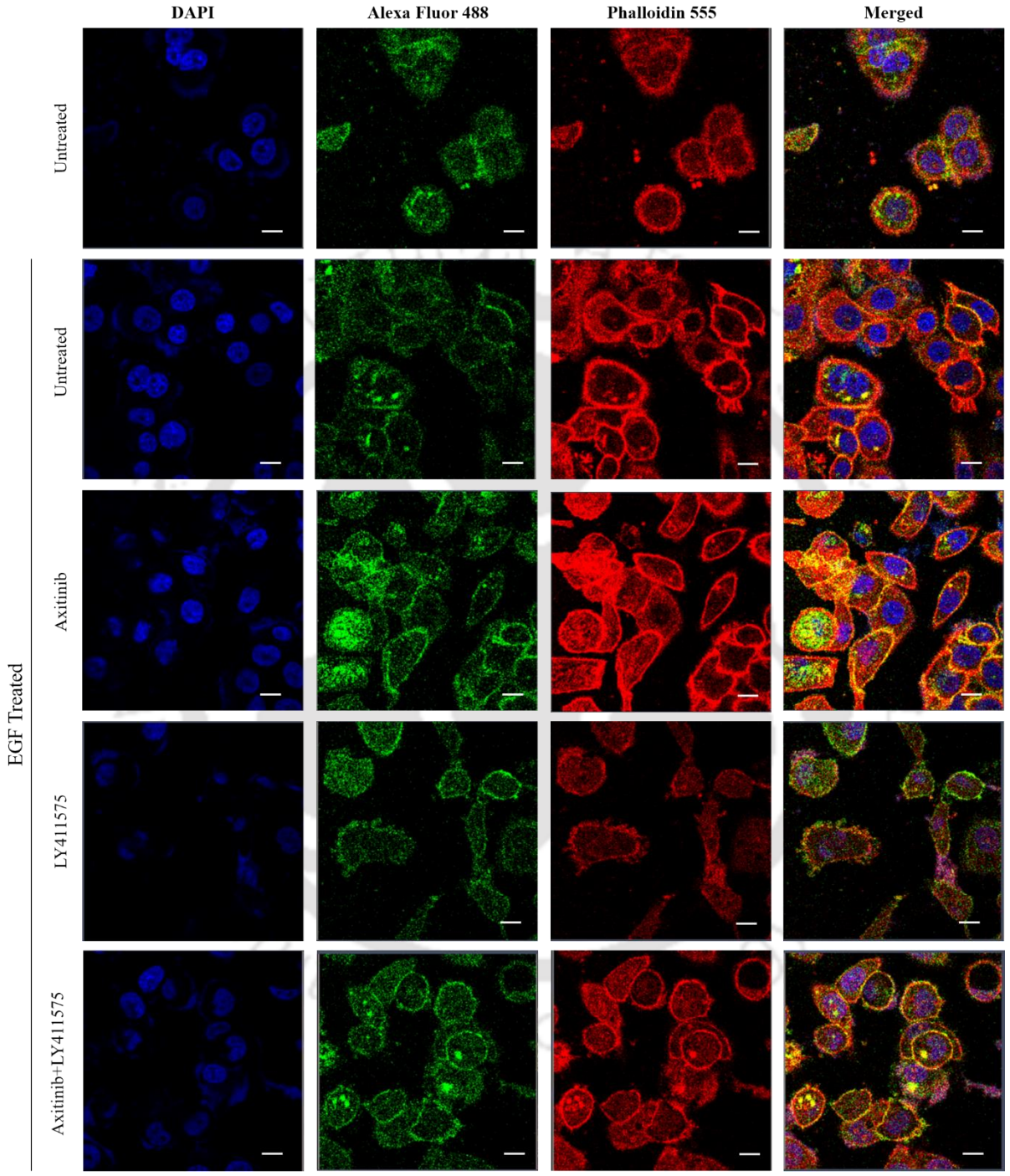

Figure 3.4.16: *Immune staining of MDA-MB-468 cells with anti-E-cadherin antibody as visualized by Alexa Fluor 488. The actin cytoskeletons were counterstained with Phalloidin-555, while the nuclei were stained with DAPI. Cells were treated with the aforementioned inhibitors and their combinations for 48 h. The scale bar represents 20 μm.*

The role of the Notch pathway in inducing EMT has already been extensively elucidated in previous studies [141]. Therefore, the role of combination therapy on the protein and gene expression profile of the Notch pathway genes was also determined. As hypothesized, there was a significant reduction in the protein levels of Jagged-1 (a potent Notch ligand that induces angiogenesis) and HES-1(the downstream target gene of the Notch pathway) following the administration of combination therapy in MDA-MB-231 (by 2.56-fold and 2.89-fold, respectively) as well as in MDA-MB-468 (by 3.75-fold and3.16-fold, respectively), as depicted in **Figure 3.4.14: A, C and E & Figure 3.4.15: A, C and E**, respectively. However, the protein expression levels of p21, another downstream effector of the Notch pathway were found to be highly upregulated 2.38-fold in MDA-MB-468 cells **(Figure 3.4.15: B and I),** while no such changes were observed in the case of MDA-MB-231 **(Figure 3.4.14: B and I).** This could be attributed to the enhanced expression of other pathways that mediates the upregulation of the p21 protein.

On the other hand, gene expression analysis of the Notch1 receptor, and its target genes such as HES-1, HEY-1 and c-Myc also illustrates the synergistic action of the two inhibitors in combination **(Figure 3.4.17)**. The fold change in the expression pattern of the Notch pathway genes is tabulated in **Table 3.4.3.**

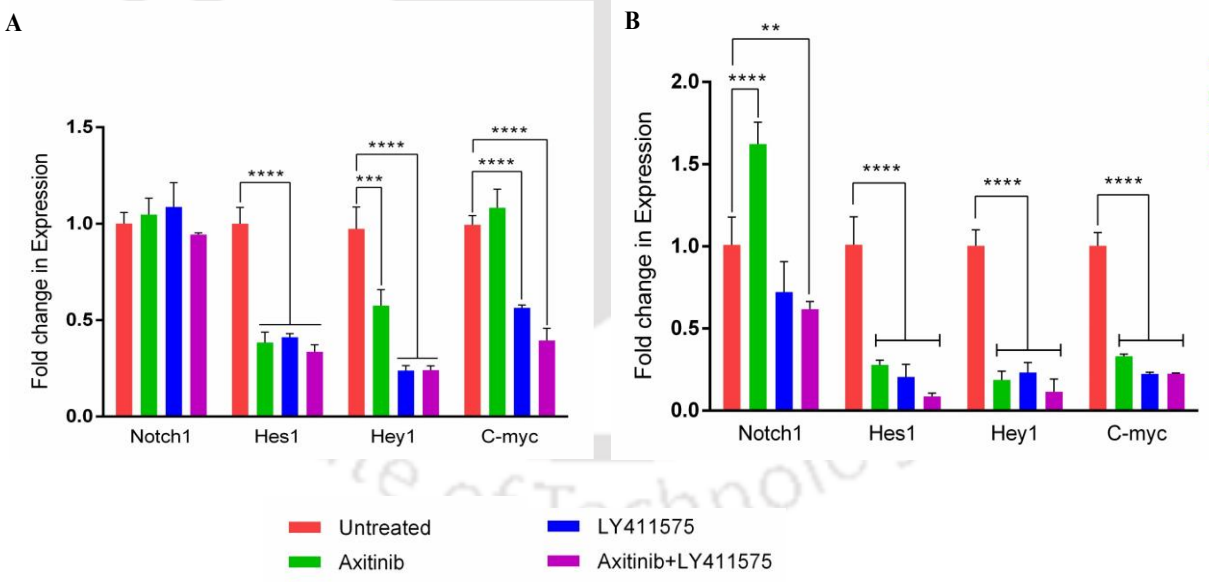

Figure 3.4.17: *Graphical depiction of the alteration in the gene expression profile Notch pathway genes in* ***(A)*** *MDA-MB-231 and* ***(B)*** *MDA-MB-468 cells, obtained by qRT-PCR analysis. Based on three independent experiments, the results are represented as mean ± SEM, along with a statistical significance denoting p < 0.5 (*), p < 0.1 (**), p < 0.01 (***) and p < 0.001 (****).*

Table 3.4.3: *Gene expression profile of the Notch pathway genes*

Genes	MDA-MB-231			MDA-MB-468		
	Axitinib	LY411575	Ax + Ly	Axitinib	LY411575	Ax + Ly
Notch pathway genes						
Notch1	- 1.05	- 1.09	- 1.06	**** 1.62	- 1.38	*** 1.61
Hes1	**** 2.63	**** 2.44	**** 3.03	**** 3.57	**** 5.02	**** 12.5
Hey1	*** 1.75	**** 4.2	**** 4.16	**** 5.55	**** 4.35	**** 9.1
c-Myc	- 1.08	**** 1.78	**** 2.56	**** 3.03	**** 4.54	**** 4.6

 # Red depicts upregulation in the expression level, while green depicts downregulation in expression level
The significance level was set at $p < 0.05$ (*), $p < 0.01$ (**), $p < 0.001$ (***) and $p < 0.0001$ (****)

3.4.7 Co-treatment synergistically reduces the expression of the pivotal nodes of the established interconnected networks

Given the complex cross-talks among the various pro-oncogenic pathways in the induction of tumorigenesis, as depicted in **Figure 3.4.1**, we ventured into the protein expression levels of the nodal genes (such as FAK, AKT, NF-κB, MAPK and EGFR), along with the gene expression levels of Wnt markers (such as TCF, LEF) after subsequent treatments. Initially, the effect of treatments on the expression of pro-survival proteins was assessed by Immunoblot analysis. Interestingly, it was found that the combination treatment resulted in the noteworthy downregulation of the active forms (i.e., the phosphorylated) proteins in both MDA-MB-231 **(Figure 3.4.18: A and B)** and MDA-MB-468 **(Figure 3.4.18: I and J)** cells. The fold change in the expression levels of the aforementioned proteins is tabulated in **Table 3.4.6.**

Precisely, after treatment with the combination of Axitinib and LY411575, the expression of p-EGFR, p-FAK and p-MAPK was found to be reduced by 1.82-fold **(Figure 3.4.18: A and C)**, 1.12- fold **(Figure 3.4.18: B and G)** and 1.3-fold **(Figure 3.4.18: B and H)** in MDA-MB-231, while it was downregulated by 1.65-fold **(Figure 3.4.18: I and K),** 1.85-fold **(Figure 3.4.18: I and L)** and 1.72-fold **(Figure 3.4.18: J and P)** in MDA-MB-468, respectively. However, the expression of p-AKT increased by 1.41-fold in MDA-MB-231**(Figure 3.4.18: A and D)** and 1.46-fold in MDA-MB-468 **(Figure 3.4.18: I and M),** following a combination treatment as compared to the untreated control cells.

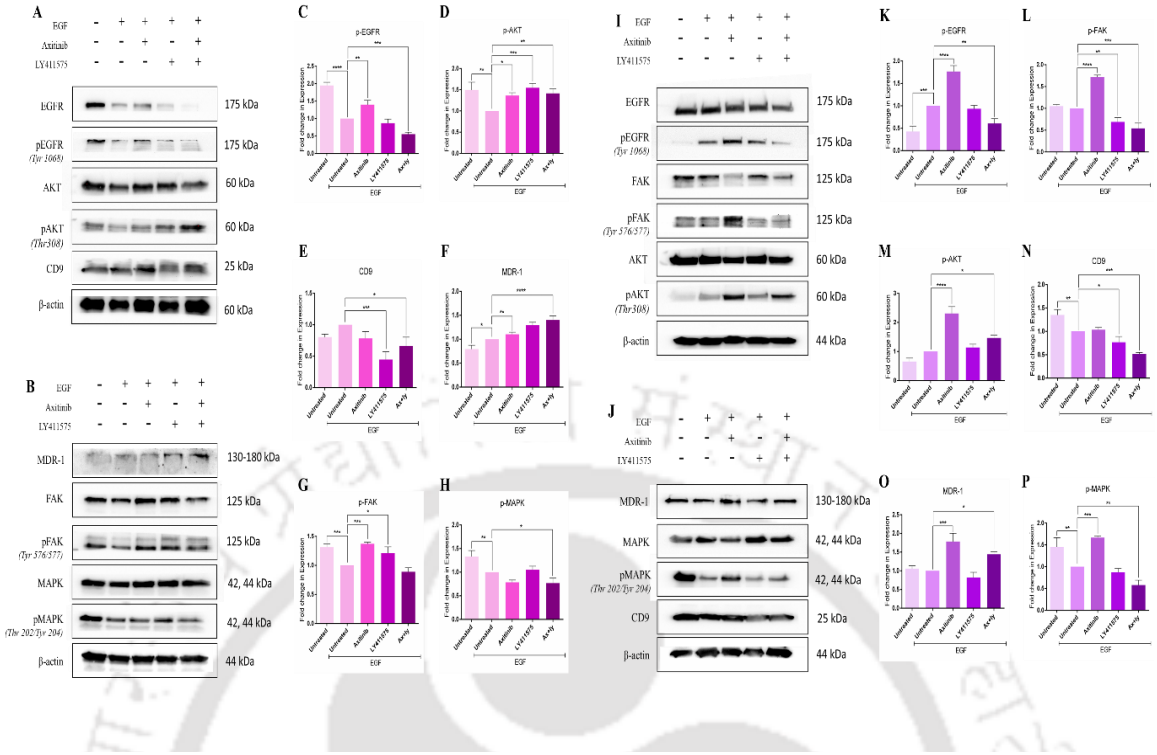

Figure 3.4.18: ***(A)*** *and* ***(B)*** *represents the western blots showing the protein expression profile of the nodal essential genes of the angiogenic pathway, obtained from the treated MDA-MB-231 cells. Graphs depicting the alterations in the protein expression profile of* ***(C)*** *p-EGFR,* ***(D)*** *p-AKT,* ***(E)*** *CD9,* ***(F)*** *MDR-1,* ***(G)*** *p-FAK and* ***(H)*** *p-MAPK.* ***(I)*** *and* ***(J)*** *represents the western blots showing the protein expression profile of the nodal essential genes of the angiogenic pathway, obtained from the treated MDA-MB-468 cells. Graphs depicting the alterations in the protein expression profile of* ***(K)*** *p-EGFR,* ***(L)*** *p-FAK,* ***(M)*** *p-AKT,* ***(N)*** *CD9,* ***(O)*** *MDR-1, and* ***(P)*** *p-MAPK.β-actin was used as a loading control. Based on three independent experiments, the results are represented as mean ± SEM, along with a statistical significance denoting $p < 0.5$ (*), $p < 0.1$ (**), $p < 0.01$ (***) and $p < 0.001$ (****).*

CD9 (also known as motility-related protein, MRP-1) facilitates numerous cellular events such as adhesion, migration, survival and proliferation of multiple cancer. It has been detected as a potent biomarker for exosomes, on account of its ubiquitous expression. Moreover, numerous studies demonstrate the associations of CD9 with enhanced oncogenic properties in many cancers, such as gastric cancer [142], breast cancer [143], etc. Therefore, owing to the effects of CD9 as a potential biomarker, we explored the protein expression profile using immunoblot analysis. It was observed that besides the combination treatment, Notch pathway inhibition alone significantly reduced the expression of CD9 proteins by 2.2-fold in MDA-MB-231 **(Figure 3.4.18: A and E)** and 1.3-fold in MDA-MB-468 **(Figure 3.4.18: J and N)** cells.

Further, the TCF/LEF (T-cell factor/lymphoid enhancer factor) transcription factors lie downstream of the Wnt signalling pathway and mediate the activation of various oncogenes. Following co-treatment, the expression of the genes was evaluated using qRT-PCR, which depicted a decrease in the expression level of TCF by 5-fold and 4.03-fold in MDA-MB-231 **(Figure 3.4.19: A)** and MDA-MB-468 **(Figure 3.4.19: C)** cells, respectively. Similarly, LEF was downregulated by 3.5-fold in MDA-MB-468 **(Figure 3.4.19:C)** cells. However, co-treatment in MDA-MB-231 increases the expression of LEF genes by 1.5-fold **(Figure 3.4.19: A),** the underlying reason remains obscure.

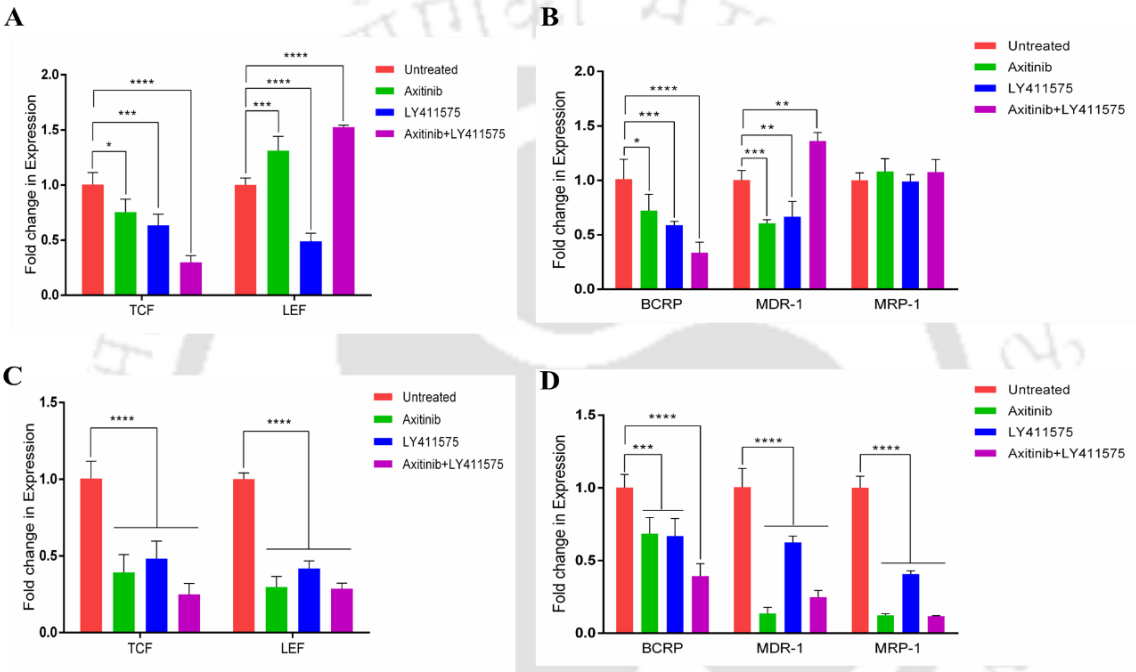

Figure 3.4.19: *Graphical depiction of the alteration in the gene expression profile of TCF and LEF* ***(A),*** *and ABC transporter genes such as BCRP, MRP-1 and MDR-1* ***(B)*** *in MDA-MB-231cells, obtained by qRT-PCR analysis. Similarly, the graphical depiction of the alteration in the gene expression profile of TCF and LEF* ***(C),*** *and ABC transporter genes such as BCRP, MRP-1 and MDR-1* ***(D)*** *in MDA-MB-468 cells, obtained by qRT-PCR analysis. The results are expressed as the mean ± SEM based on three independent experiments. The statistical significance was assessed in comparison to the untreated cells. The significance level was set at $p < 0.05$ (*), $p < 0.01$ (**), $p < 0.001$ (***) and $p < 0.0001$ (****).*

Further, the role of co-therapy on the ABC transporters genes (such as BCRP, MRP-1and MDR-1) was assessed by qRT-PCR analysis. The combination treatment successfully reduced the protein expression profile in MDA-MB-468 **(Figure 3.4.19: D)**, while not many changes were observed in the case of MDA-MB-231 (except for BCRP, which was downregulated by 2.94-fold after co-treatment, depicted in **Figure 3.4.19: B**). Moreover, we also ventured into the protein expression profile of the MDR-1 gene, which endowed us with a similar expression profile of the MDR-1 proteins in both TNBC cells. Altogether, combination treatment somehow enhanced the expression of the MDR-1 protein by 1.4-fold and 1.54-fold in MDA-MB-231 **(Figure 3.4.18: B and F)** and MDA-MB-468 **(Figure3.4.18: J and O)** cells, respectively.

Table 3.4.4: *Gene expression profile of the Wnt downstream TFs and multi-drug resistance genes*

Genes	MDA-MB-231			MDA-MB-468		
	Axitinib	LY411575	Ax + Ly	Axitinib	LY411575	Ax + Ly
Wnt transcription factors						
LEF-1	*** 1.3	**** 2.04	**** 1.52	**** 3.36	**** 2.4	**** 3.5
TCF	* 1.33	*** 1.58	**** 5.01	**** 2.56	**** 2.08	**** 4.02
Multi-drug resistance genes						
BCRP	* 1.38	*** 1.69	**** 2.94	*** 1.46	*** 1.5	**** 2.54
MDR-1	*** 1.66	** 1.49	** 1.25	**** 7.3	**** 1.6	**** 4.03
MRP-1	- 1.08	- 1.01	- 1.07	**** 8.2	**** 2.46	**** 8.55

 # Red depicts upregulation in the expression level, while green depicts downregulation in the expression level
The significance level was set at $p < 0.05$ (*), $p < 0.01$ (**), $p < 0.001$ (***) and $p < 0.0001$ (****)

NF-κB lies downstream of the PI3K/AKT signalling axis and possesses numerous crosstalk with multiple cancer signalling pathways. The activation of NF-κB regulates the process of DNA repair, hence protecting cells from apoptosis. Here, we observed that the expression of NF-κB was substantially reduced following co-therapy **(Figure 3.4.20).**

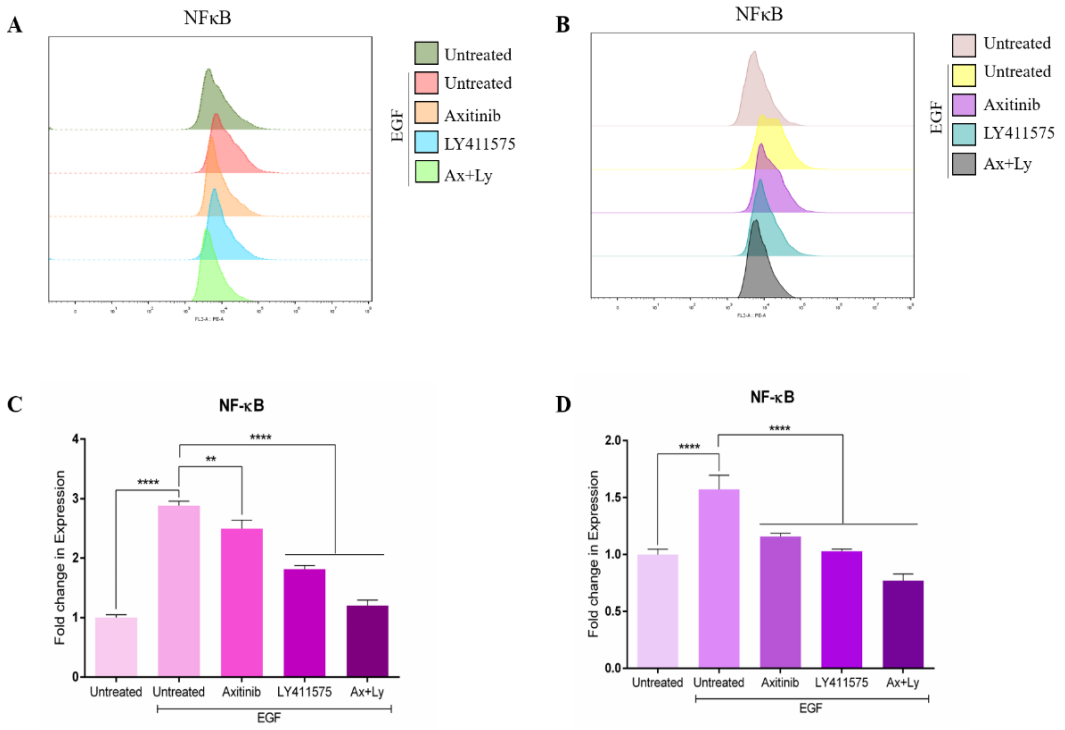

Figure 3.4.20: *Representative histograms depicting the alteration in expression of NF-κB assessed by immune-flow cytometry in MDA-MB-231* ***(A)*** *and MDA-MB-468* ***(B)*** *cells. Graphical representation of fold-change in the protein expression profile of NF-κB in* ***(C)*** *MDA-MB-231 and* ***(D)*** *MDA-MB-468 cells. The results are expressed as the mean ± SEM based on three independent experiments. The statistical significance was assessed in comparison to the untreated cells. The significance level was set at $p < 0.05$ (*), $p < 0.01$ (**), $p < 0.001$ (***) and $p < 0.0001$ (****).*

3.4.8 Co-treatment reduces the expression profile of the VEGFR pathway genes, along with the reduction in RTKs

The associations of the VEGFRs with the Notch pathway has been elucidated in detail in section 3.4.1 and 3.4.2. Therefore, to assess the expression profile of the RTK genes after treatment in breast cancer, qRT-PCR analysis was performed. Interestingly, it was observed that combination treatment reduced the gene expression levels of the aforementioned RTKs significantly in both MDA-MB-231 and MDA-MB-468 cells **(Figure 3.4.21 and Table 3.4.5).** However, the expression profile of VEGFR1 was found to be upregulated in both TNBC cells. From the literature, it is evident that in endothelial cells, VEGFA induces VEGFR2-mediated DLL4 activation. This results in the upregulation of the Notch target protein HES-1 that downregulates VEGFR3 [144].

It is interesting to note that besides the acquisition of mesenchymal properties, EMT also imparts pericyte-like properties to the TNBC cells. This in turn gives rise to a phenomenon known as epithelial-to-pericyte transition. Pericytes regulate blood flow, maintain vascular permeability, and provide mechanical support to the endothelial cells (ECs). They are extremely extended, and branched cells, which are characterized by the expression of α-SMA, desmin, CD146, PDGFRβ, and NG2 proteoglycan [145]. Therefore, to assess the role of pericyte markers, qRT-PCR analysis was performed.

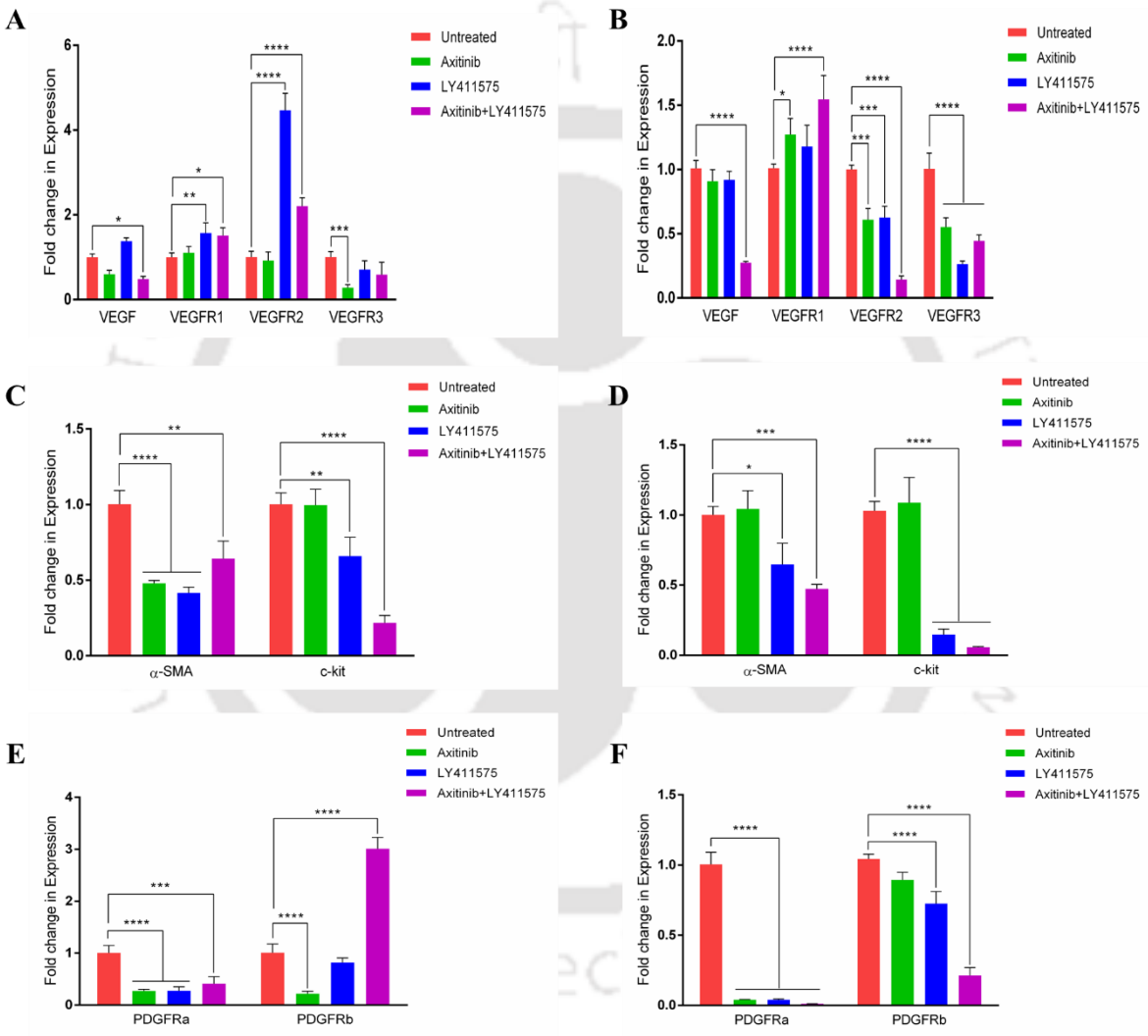

Figure 3.4.21: *Graphical depiction of the alteration in the gene expression profile of* ***(A)*** *VEGF and VEGFRs, alongwith RTKs such as* ***(C)*** *α-SMA and c-Kit,* ***(E)*** *PDGFRα and PDGFRβ in treated MDA-MB-231 cells, obtained byqRT-PCR analysis. Similarly, a graphical depiction of the alteration in the gene expression profile of* ***(B)*** *VEGF andVEGFRs, along with RTKs such as* ***(D)*** *α-SMA and c-Kit,* ***(F)*** *PDGFRα and PDGFRβ in treated MDA-MB-468 cells, obtained by qRT-PCR analysis. Based on three independent experiments, the results are represented as mean ± SEM, along with a statistical significance denoting p < 0.5 (*), p < 0.1 (**), p < 0.01 (***) and p < 0.001 (****).*

It was observed that besides the expression levels of PDGFR receptors, the gene expression level of α-SMA along with c-kit also reduced significantly after combination treatment. In MDA-MB-231 there was a significant reduction of 1.56-fold change in α-SMA, 4.54-fold change in c-Kit, 2.44-fold change in PDGFRα and 2.74-fold change in PDGFRβ after co-therapy **(Figure 3.4.21: C and E)**. Similarly, in MDA-MB-468 there was a significant reduction of 2.11-fold change in α-SMA, 17.85-fold change in c-Kit, 9.89-fold change in PDGFRα and 4.76-fold change in PDGFRβ after co-therapy **(Figure 3.4.21: D and F)**.

Table 3.4.5: *Gene expression profile of the RTKs*

Genes	MDA-MB-231			MDA-MB-468		
	Axitinib	LY411575	Ax + Ly	Axitinib	LY411575	Ax + Ly
RTKs						
VEGF	- 1.67	- 1.38	* 2.08	- 1.1	- 1.08	**** 3.7
VEGFR1	- 1.1	** 1.57	* 1.5	* 1.27	- 1.17	**** 1.54
VEGFR2	- 1.08	**** 1.26	**** 2.2	*** 1.64	*** 1.61	**** 7.14
VEGFR3	*** 3.57	- 1.41	- 1.69	**** 1.82	**** 3.85	**** 2.27
α-SMA	**** 2.08	**** 2.44	** 1.56	- 1.04	* 1.54	* 2.11
C-KIT	- 1.01	** 1.54	**** 4.54	- 1.09	**** 6.8	**** 17.85
PDGFR-α	**** 3.70	**** 3.57	*** 2.44	**** 2.56	**** 2.4	**** 9.89
PDGFR-β	**** 1.72	- 1.34	**** 2.74	- 1.12	**** 1.38	**** 4.76

 # Red depicts upregulation in the expression level, while green depicts downregulation in the expression level

The significance level was set at $p < 0.05$ (*), $p < 0.01$ (**), $p < 0.001$ (***) and $p < 0.0001$ (****)

Therefore, looking into the molecular profile of the pericyte markers, the protein expression pattern of NG2 after subsequent treatments, using immune flow cytometry **(Figure 3.4.22: A and B)** and immunocytochemistry analysis **(Figure 3.4.22: C; Figure 3.4.23: B and G)** were examined. NG2 is a primary pericyte marker, which mediates pericyte activation, thereby acting as a regulator of angiogenic sprouting. It is evident from theprotein expression profile that there was a significant increase in the expression of NG2 following EMT induction. However, after the administration of co-therapy, there was a substantial reduction in the expression of NG2 proteins in both TNBC cells. Moreover, the cytoplasmic domain of NG2 is known to activate numerous effector molecules such as PI3K, AKT, FAK, etc. [146]. The study provides ample evidence of the downregulation of the phosphorylation (or activation) status of these pro-survival pathways after combination therapy. Hence, providing a subtle explanation of the decrease in NG2 proteins. Altogether, it was observed that the combination of a VEGF pathway blocker and a Notch pathway inhibitor successfully abrogated the metastatic propensity at the molecular level.

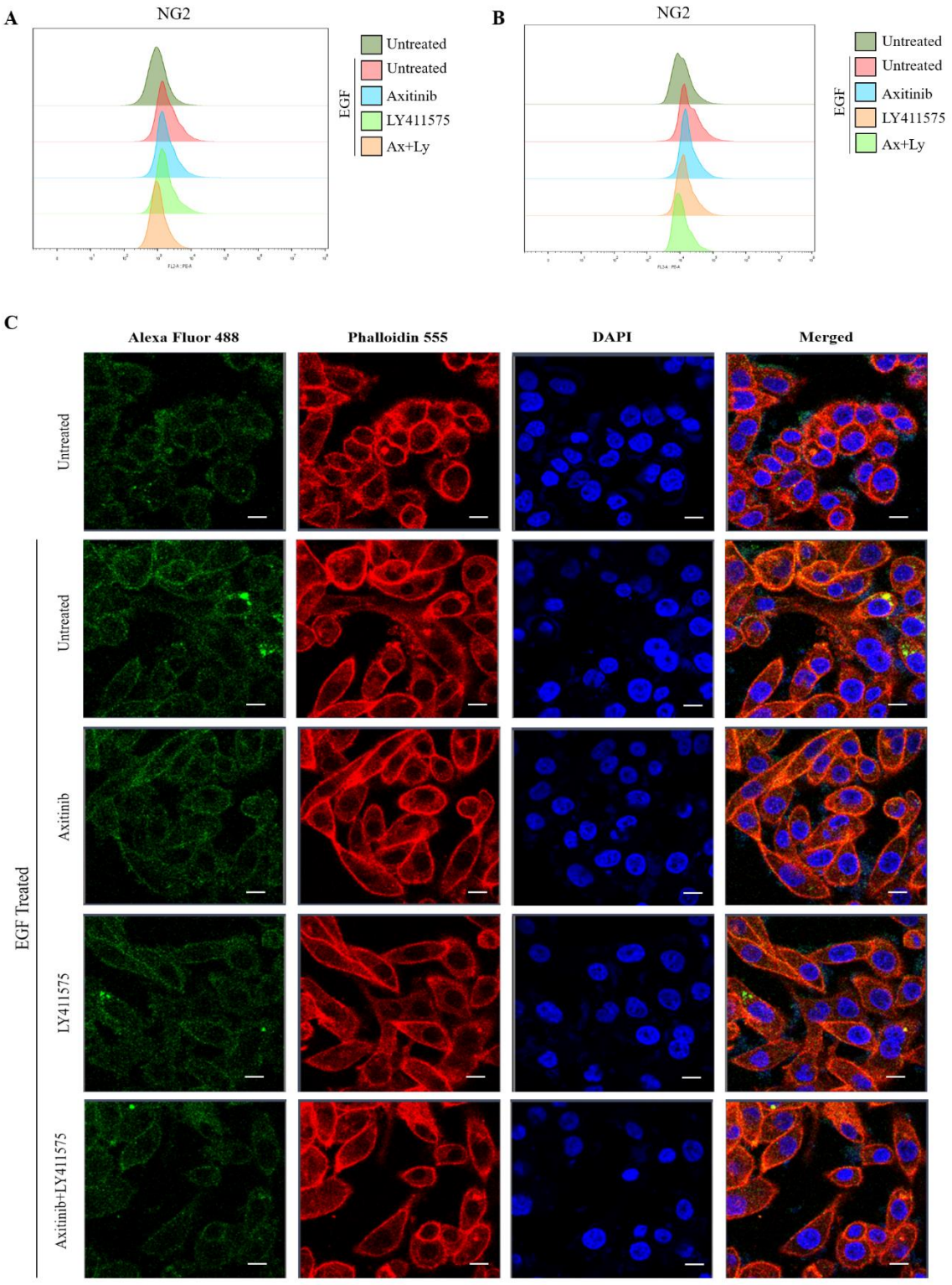

Figure 3.4.22: *Representative histograms depicting the alteration in expression of NG2 assessed by immune-flow cytometry in MDA-MB-231* ***(A)*** *and MDA-MB-468* ***(B)*** *cells.* ***(C)*** *Immune staining of MDA-MB-468 cellswith anti-NG2 antibody as visualized by Alexa Fluor 488. The actin cytoskeletons were counterstained with Phalloidin-555, while the nuclei were stained with DAPI. Cells were treated with the aforementioned inhibitors andtheir combinations for 48 h. The scale bar represents 20 μm.*

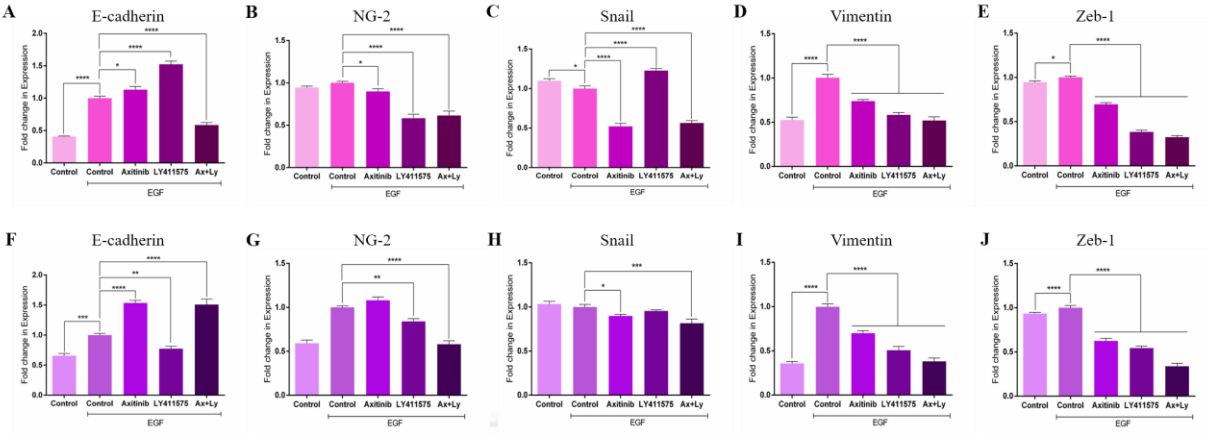

Figure 3.4.23: *Graphical depiction in the fold change alteration in the expression profile (following ICC) of epithelial marker (such as E-cadherin* ***(A)*** *and* ***(F)****), pericyte marker (such as NG2* ***(B)*** *and* ***(C)****) and mesenchymal marker (such as Snail* ***(C)*** *and* ***(H)****, Viemntin* ***(D)*** *and* ***(I)*** *and Zeb-1* ***(E)*** *and* ***(F)****) in MDA-MB-231 and MDA-MB-468, respectively. Based on three independent experiments, the results are represented as mean ± SEM, along with a statistical significance denoting p < 0.5 (*), p < 0.1 (**), p < 0.01 (***) and p < 0.001 (****).*

Table 3.4.6: *Protein expression profile of the treated cells in comparison to the EGF-treated control cells, analyzed by immunoblot analysis*

Genes	MDA-MB-231				MDA-MB-468			
	Untreated	Axitinib	LY411575	Ax + Ly	Untreated	Axitinib	LY411575	Ax + Ly
EMT markers and EMT-TFs								
E-cadherin	- 1.10	*** 1.62	**** 1.73	**** 2.2	- 1.14	**** 1.63	**** 2.1	**** 2.51
Vimentin	- 1.04	- 1.02	- 1.17	- 1.03	- 1.82	* 1.34	* 1.32	* 1.90
Snail	- 1.13	* 1.22	**** 2.78	**** 5.26	- 1.08	*** 2.21	** 1.62	**** 4.66
Twist	- 1.30	- 1.01	* 1.28	**** 2.22	- 1.04	- 1.33	** 1.14	* 1.34
Notch ligand and downstream proteins								
Jagged-1	**** 1.85	* 1.25	*** 1.89	**** 2.56	- 1.21	- 1.06	*** 1.79	**** 3.75
Hes1	- 2.86	- 1.01	** 1.49	**** 2.89	- 1.07	* 1.23	**** 1.89	**** 3.16
p21	- 1.39	** 1.52	**** 1.83	- 1.11	- 1.77	** 1.75	** 1.64	**** 2.38

 # Red depicts upregulation in the expression level, while green depicts downregulation in expression level
The significance level was set at p < 0.05 (*), p < 0.01 (**), p < 0.001 (***) and p < 0.0001 (****)

Table 3.4.7: *Protein expression profile of the treated cells in comparison to the EGF-treated control cells, analyzed by immunoblot analysis*

Stemness markers								
MDR-1	* 1.26	** 1.1	- 1.29	**** 1.4	- 1.05	*** 1.78	- 1.22	* 1.54
CD-9	- 1.24	- 1.27	*** 2.24	* 1.51	** 1.35	- 1.03	* 1.3	*** 1.93
Pro-oncogenic proteins								
p-AKT	** 1.50	* 1.36	*** 1.54	** 1.41	- 1.52	**** 2.31	- 1.14	* 1.46
p-EGFR	**** 1.95	** 1.4	- 1.15	*** 1.82	*** 2.34	**** 1.76	- 1.07	** 1.65
p-FAK	*** 1.31	*** 1.37	* 1.21	- 1.12	- 1.05	*** 1.39	** 1.45	*** 1.85
p-MAPK	** 1.33	- 1.27	- 1.05	* 1.3	** 1.45	*** 1.66	- 1.15	** 1.72

 # Red depicts upregulation in the expression level, while green depicts downregulation in expression level
The significance level was set at $p < 0.05$ (*), $p < 0.01$ (**), $p < 0.001$ (***) and $p < 0.0001$ (****)

Conclusion

The role of Notch in regulating cell fate determination has greatly improved our concept of differentiation and dissemination. It is seen that Notch promotes the differentiation between the leading 'tip' endothelial cells and the growing 'stalk' cells, along with mural cell functions. Interestingly, various research reveals that inactivation and/or blocking Notch functions in tumour vasculature inhibits tumour growth, metastasis and angiogenesis. Besides Notch, the VEGF signalling pathway is vital in facilitating tumour progression. Therefore, it is not surprising that inhibition of the VEGF pathway is considered an attractive strategy to combat aggressiveness in numerous cancers. However, the signalling axis (or cross talk) between Notch and VEGF has been established to combat the enhanced metastatic propensity and angiogenic sprouting in numerous malignancies.

Besides, Notch also facilitates numerous other hallmarks of cancer such as epithelial to mesenchymal transition, maintenance of stem cells, etc. One such hallmark is the Epithelial-to-pericyte transition (EPT), where mesenchymal cells also exhibit pericyte-like properties and possess pericyte markers. Further, it can be portrayed that upon induction of EMT, not only do the cells acquire mesenchymal properties but also pericyte properties. As a result of which they could easily traverse the body on account of chemotaxis, thereby forming additional tumours or blood vessels. The recruitment of pericytes to nascent blood vessels involves a variety of signalling pathways such as TGFβ, PDGF and angiopoietin-Tie2. During angiogenesis, the sprouting endothelial cells secrete PDGF-B to promote the migration and invasion of PDGFR-β expressed mural cells. It is seen that PDGFR-β is a target gene of the Notch pathway. It is seen that Notch1-ICD (intracellular domain) binds to the promoter of PDGFR-β, thereby inducing its expression in a CSL-dependent manner. Moreover, Notch1 signalling is essential for mural cell recruitment, while Notch3 aids in pericyte maturation upon reaching the desired place [147].

In this study, it was hypothesized that a functional link existing between the VEGF and Notch pathway could be a major mediator of epithelial-to-pericyte transition (EPT) in TNBC cells. Since the preliminary study suggests that VEGF and Notch pathways are activated in the TNBC cells, therefore, it was proposed that simultaneous targeting of these pathways might synergistically decrease the aggressiveness of TNBC. Moreover, a deeper understanding of the molecular profile of the TNBC cells upon induction of EMT was also assessed. It was found that TNBC cell lines treated with sub-toxic doses of Axitinib (a second-generation RTK inhibitor) and LY411575 (a potent γ-secretase inhibitor) successfully inhibited the viability of cells. However, when administered in combination, there was an efficient inhibition of cell viability at a substantially lower dose in both monolayers as well as in 3D tumour spheroids.

Moreover, the combination index reveals the synergistic interaction of the two inhibitors at higher doses, which was ascertained by their outcome in various cellular assays. For example, combination treatment synergistically induced apoptosis, decreased the sphere-forming ability and reduced the stemness of TNBC cells. Furthermore, it also resulted in the successful inhibition of mesenchymal markers and upregulation of epithelial markers, thereby abrogating EMT. Furthermore, co-treatment also resulted in successful downregulation in the molecular profile of the pericyte marker, which ultimately hints towards the inhibition of epithelial to pericyte transition. A vital phenomenon that facilitates angiogenesis, therefore providing a hint for further research in animalmodels, Altogether, the results demonstrate that downregulation of the VEGF pathway along with theNotch pathway not only affects the major cross-talks in the EMT and EPT dynamics of the TNBC cells but also provides a novel therapeutic modality to deal with aggressive TNBC.

\

Section 4

Conclusion and Future Prospects

Conclusions and Future Prospects

To elucidate the molecular mechanisms involved in cancer development, it is becoming increasingly important to identify the cellular factors that facilitate the oncogenic properties of the developmental pathways.The intriguing probability of Notch having either oncogenic or tumour suppressive effect in a particular malignancy is highly controversial. However, the Notch pathway is known to potentiate various hallmarks of cancer such as angiogenesis, drug resistance, metastasis, invasion, and maintenance of cancer stem cells, which is attributed to its established crosstalk with several downstream pathways and transcription factors. Therefore, it is crucial to tweak the aberrant activation of this pathway effectively and efficiently to abrogate the aggressive characteristics imparted to various malignancies. The current study focuses on the determination and targeting of the Notch pathway in the metastatic domain of TNBC cells.

The salient features of the current work are as follows:

- Initially, the ADAM was determined to be the crucial node in enhancing the aggressiveness of numerous malignancies. It mediates the proteolytic cleavage of the major pro-oncogenic type-I transmembrane receptors such as Notch, ERBB, EGFR, TNF-α, etc. that facilitates tumour progression and dissemination.
- Besides ADAM, γ-secretase was determined to be a pivotal protease in the activation of the Notch pathway. Therefore, a Polypharmacology approach was utilized to target these major proteases.
- Furthermore, due to the unavailability of a suitable drug, a library of an FDA-approved drugs was screened against the ADAM17 and γ-secretase to obtain a drug that could be repurposed in the treatment of metastatic TNBC.
- From *in silico* screening, Lomitapide, a cholesterol-lowering drug was obtained, which possesses remarkable anti-tumour properties in TNBC cells.
- Further, it was observed that the Notch pathway inhibitor (or the γ-secretase inhibitor, LY411575) enhances the efficacy of SAHA (an HDAC inhibitor), thereby resulting in the abrogation of EMT in TNBC cells.
- Since the Notch pathway and the VEGF signalling pathway facilitate various hallmarks of cancer, the crosstalk of the Notch and VEGF pathway was targeted using Axitinib in combination with LY411575. A synergistic therapeutic outcome was obtained, which successfully abrogated EMT, tumour progression and survival.
- Furthermore, the effectiveness of combination treatment on monolayer cultures, and complex tumour spheroids illustrate the therapeutic significance of combination treatment as an attractive alternative in cancer therapeutics.

Future Prospects

The potential scopes of the present findings include:

- Based on our preliminary studies, ADAM inhibitors can be developed and their consecutive mechanism can be determined from further *in vitro* and *in vivo* studies.
- Since the majority of ADAM inhibitors failed to surpass the clinical trials, therefore a nanomaterial could be designed to therapeutically target the tumour microenvironment, along with enhanced retention timeand efficacy of the inhibitors in the body.
- This study also ascertains the potential role of Notch in tweaking cancer metabolism. Hence, opening a new avenue to assess the variations in molecular response in detail.
- Cancer is a metabolic disease! Thus, the use of a repurposed FDA-approved drug enhances the effectiveness of the outcome at the cellular level. Hence, further studies could be implemented in clinicaltrials after determining their *in vivo* efficacy.
- Moreover, the cholesterol-lowering drug, Lomitapide, which was selected through rigorous screening also depicts the role of tweaking the altered metabolism in cancer. This further opens up new avenues to utilize these drugs in the treatment modalities of TNBC in combination with systemic therapies.
- Additionally, the role of Notch in epigenetic regulation and enhancement of pro-oncogenic and EMT signalling axis, also depicts that this signalling nodule could be an interesting target to circumscribe the metastatic propensity of TNBC.
- This study also endows with information related to the aberrant activation of the Notch and its effect on the metastatic domain of TNBC cells. Therefore, the efficacy of combination treatment could be further examined for its translation potential.

References

[1]. Iglesias, V. S., Giuranno, L., Dubois, L. J., Theys, J., & Vooijs, M. Drug Resistance in Non-Small Cell Lung Cancer: A Potential for NOTCH Targeting? *Frontiers in oncology*. **2018**, *8* (267). https://doi.org/10.3389/fonc.2018.00267

[2]. Antifolk, D., Sjoqyist, M., Cheng, F., Isoniemi, K., Duran, C. L., Muller, A. R., Antlia, C., Niemi, R., Landor, S., Bouten, C. V. C., Bayless, K. J., Eriksson, J. E., Sahlgren, C. M. Selective regulation of Notch ligands during angiogenesis is mediated by vimentin. *PNAS.* **2017**, *114* (23). https://doi.org/10.1073/pnas.1703057114

[3]. Demarest, R. M., Ratti, F. & Capobianco, A. J. It's T-ALL about Notch. *Oncogene.* **2008**, *2*, 5082–5091. https://doi.org/10.1038/onc.2008.222

[4]. Greenwald, I. & Seydoux, G. Analysis of gain-of-function mutations of the lin-12 gene of Caenorhabditis elegans. *Nature*. **1990**, 346(6280), 197–199. https://doi.org/10.1038/346197a0

[5]. Olsauskas-kuprys, R., Zlobin, A. & Osipo, C. Gamma secretase inhibitors of Notch signalling. *OncoTargets and therapy*. **2013**, 6. https://doi.org/10.2147/OTT.S33766943–955

[6]. Huang, Q., Li, J., Zheng, J. & Wei, A. The carcinogenic role of the notch signalling pathway in the development of hepatocellular carcinoma. *Journal of Cancer*. **2019**, *10* (6), 1570–1579. https://doi.org/10.7150/jca.26847

[7]. Galluzzo, P. & Bocchetta, M. Notch signalling in lung cancer. *Expert review of anticancer therapy*. **2011**, *11* (4), 533–540. https://doi.org/10.1586/era.10.158

[8]. Wei, P., Walls, M., Qiu, M., Ding, R., Denlinger, R. H., Wong, A., Tsaparikos, K., Jani, J. P., Hosea, N., Sands, M., Randolph, S., & Smeal, T. Evaluation of selective gamma-secretase inhibitor PF-03084014 for its antitumor efficacy and gastrointestinal safety to guide optimal clinical trial design. *Molecular cancer therapeutics.* **2010**, *9* (6), 1618–1628. https://doi.org/10.1158/1535-7163.MCT-10-0034

[9]. Keyghobadi, F., Medhipour, M., Nekoukar, V., Firouzi, J., Kheimeh, A., Lahrood, F. N., Zavared, V. A., Azimi, M., Mohammadi, M., Sodeifi, N., & Ebrahimi, M. Long-Term Inhibition of Notch in A-375 Melanoma Cells Enhances Tumor Growth Through the Enhancement of AXIN1, CSNK2A3, and CEBPA2 as Intermediate Genes in Wnt and Notch Pathways. *Frontiers in Oncology*. **2020**, *10*, 1–13. https://doi.org/10.3389/fonc.2020.00531

[10]. Mittal, S., Sharma, A., Balaji, S. A., Gowda, M. C., Dighe, R. R., Kumar, R. V., & Rangarajan, A. Coordinate hyperactivation of notch1 and Ras/MAPK pathways correlates with poor patient survival: Novel therapeutic strategy for aggressive breast cancers. *Molecular cancer therapeutics*. **2014**, *13* (12), 3198–3209. https://doi.org/10.1158/1535-7163.MCT-14-0280

[11]. Maniati, E., Bossard, M., Cook, N., Candido, J. B., Emami-Shahri, N., Nedospasov, S. A., Balkwill, F. R., Tuveson, D. A., & Hagemann, T. Crosstalk between the canonical NF-κB and Notch signalling

pathways inhibits Pparγ expression and promotes pancreatic cancer progression in mice. *The Journal of clinical investigation*. **2011**, *121* (12), 4685–4699. https://doi.org/10.1172/JCI45797

[12]. Meurette, O., Stylianou, S., Rock, R., Collu, G. M., Gilmore, A. P., & Brennan, K. Notch activation induces Akt signalling via an autocrine loop to prevent apoptosis in breast epithelial cells. *Cancer Research*. **2009**, *69* (12), 5015–5022. https://doi.org/10.1158/0008-5472.CAN-08-3478

[13]. Braune, E. B., Seshire, A., & Lendahl, U. Notch and Wnt Dysregulation and Its Relevance for Breast Cancer and Tumor Initiation. *Biomedicines*. **2018**, *6* (4), 101. https://doi.org/10.3390/biomedicines6040101

[14]. Andersen, P., Uosaki, H., Shenje, L. T., & Kwon, C. Non-canonical Notch signalling: emerging role and mechanism. *Trends in cell biology*. **2012**, *22* (5), 257–265. https://doi.org/10.1016/j.tcb.2012.02.003

[15]. Sundaram, M. V. The love-hate relationship between Ras and Notch. *Genes & development*. **2005**, *19* (16), 1825–1839. https://doi.org/10.1101/gad.1330605

[16]. Wei Tagami, S., Okochi, M., Yanagida, K., Ikuta, A., Fukumori, A., Matsumoto, N., Ishizuka-Katsura, Y., Nakayama, T., Itoh, N., Jiang, J., Nishitomi, K., Kamino, K., Morihara, T., Hashimoto, R., Tanaka, T., Kudo, T., Chiba, S., & Takeda, M. Regulation of Notch Signalling by Dynamic Changes in the Precision of S3 Cleavage of Notch-1. *Molecular and cellular biology*. **2008**, *28* (1), 165–176. https://doi.org/10.1128/MCB.00863-07

[17]. Belle, V. A., McDermott, N., Meunier, A., & Marignol, L. NUMB inhibition of NOTCH signalling as a therapeutic target in prostate cancer Victoria. *Nature Reviews Urology*. **2014**, *11* (9), 499–507. https://doi.org/10.1038/nrurol.2014.195

[18]. Shou, J., Ross, S., Koeppen, H., De Sauvage, F. J. & Gao, W. Q. Dynamics of Notch expression during murine prostate development and tumorigenesis. *Cancer Research*. **2001**, *61* (19), 7291–7297.

[19]. Sriuranpong, V., Borges, M. W., Ravi, R. K., Arnold, D. R., Nelkin, B. D., Baylin, S. B., & Ball, D. W. Notch signalling induces cell cycle arrest in small cell lung cancer cells. *Cancer Research*. **2001**, *61* (7), 3200–3205.

[20]. Leong, K. G., & Karsan, A. Recent insights into the role of Notch signalling in tumorigenesis. *Blood*. **2006**, *107*(6), 2223–2233. https://doi.org/10.1182/blood-2005-08-3329

[21]. Tohda, S., Murata-Ohsawa, M., Sakano, S. & Nara, N. Notch ligands, Delta-1 and Delta-4 suppress the self-renewal capacity and long-term growth of two myeloblastic leukemia cell lines. *International journal of oncology*. **2003**, *22* (5), 1073–1079.

[22]. Morimura, T., Goitsuka, R., Zhang, Y., Saito, I., Reth, M., & Kitamura, D. Cell cycle arrest and apoptosis induced by Notch1 in B cells. *The Journal of biological chemistry*. **2000**, *275* (47), 36523–36531. https://doi.org/10.1074/jbc.M006415200

[23]. Nefedova, Y., Cheng, P., Alsina, M., Dalton, W. S. & Gabrilovich, D. I. Involvement of Notch-1 signalling in bone marrow stroma-mediated de novo drug resistance of myeloma and other malignant lymphoid cell lines. *Blood.* **2004**, *103* (9), 3503–3510. https://doi.org/10.1182/blood-2003-07-2340

[24]. Roy, M., Pear, W. S. & Aster, J. C. The multifaceted role of Notch in cancer. *Current Opinion in Genetics and Development*. **2007**, *17* (1), 52–59. https://doi.org/10.1016/j.gde.2006.12.001

[25]. Chiaramonte, R., Basile, A., Tassi, E., Calzavara, E., Cecchinato, V., Rossi, V., Biondi, A., & Comi, P. A wide role for NOTCH1 signalling in acute leukemia. *Cancer Letters*. **2005**, *219* (1), 113–120. https://doi.org/10.1016/j.canlet.2004.07.022

[26]. Previs, R. A., Coleman, R. L., Harris, A. L. & Sood, A. K. Molecular pathways: Translational and therapeutic implications of the notch signalling pathway in cancer. *Clinical cancer research*. **2015**, *21* (5), 955–961. https://doi.org/10.1158/1078-0432.CCR-14-0809

[27]. Penton, A. L., Leonard, L. D., & Spinner, N. B. Notch signalling in human development and disease. *Seminars in cell & developmental biology*. **2012**, *23* (4), 450–457. https://doi.org/10.1016/j.semcdb.2012.01.010

[28]. Parmigiani, E., Taylor, V., & Giachino, C. Oncogenic and Tumor-Suppressive Functions of NOTCH Signalling in Glioma. *Cells.* **2020**, *9*(10), 2304. https://doi.org/10.3390/cells9102304

[29]. Tao, J., Jiang, M. M., Jiang, L., Salvo, J. S., Zeng, H. C., Dawson, B., Bertin, T. K., Rao, P. H., Chen, R., Donehower, L. A., Gannon, F., & Lee, B. H. Notch activation as a driver of osteogenic sarcoma. *Cancer cell*. **2014**, *26* (3), 390–401. https://doi.org/10.1016/j.ccr.2014.07.023

[30]. Augert, A., Eastwood, E., Ibrahim, A. H., Wu, N., Grunblatt, E., Basom, R., Liggitt, D., Eaton, K. D., Martins, R., Poirier, J. T., Rudin, C. M., Milletti, F., Cheng, W. Y., Mack, F., & MacPherson, D. Targeting NOTCH activation in small cell lung cancer through LSD1 inhibition. *Science signalling.* **2019**, *12* (567), eaau2922. https://doi.org/10.1126/scisignal.aau2922

[31]. Xie, M., Zhang, L., He, C. S., Xu, F., Liu, J. L., Hu, Z. H., Zhao, L. P., & Tian, Y. Activation of Notch-1 enhances epithelial-mesenchymal transition in gefitinib-acquired resistant lung cancer cells. *Journal of cellular biochemistry*. **2012**, *113* (5), 1501–1513. https://doi.org/10.1002/jcb.24019

[32]. Anjanappa, M., Hao, Y., Simpson, E. R., Bhat-Nakshatri, P., Nelson, J. B., Tersey, S. A., Mirmira, R. G., Cohen-Gadol, A. A., Saadatzadeh, M. R., Li, L., Fang, F., Nephew, K. P., Miller, K. D., Liu, Y., & Nakshatri, H. A system for detecting high impact-low frequency mutations in primary tumors and metastases. *Oncogene*. **2018**, *37* (2), 185–196. https://doi.org/10.1038/onc.2017.322

[33]. Mollen, E. W. J., Ient, J., Tjan-Heijnen, V. C. G., Boersma, L. J., Miele, L., Smidt, M. L., & Vooijs, M. A. G. G. Moving Breast Cancer Therapy up a Notch. *Frontiers in oncology*. **2018**, *8*, 518. https://doi.org/10.3389/fonc.2018.00518

[34]. Demehri, S., Turkoz, A., & Kopan, R. Epidermal Notch1 loss promotes skin tumorigenesis by impacting the stromal microenvironment. *Cancer cell*. **2009**, *16* (1), 55–66. https://doi.org/10.1016/j.ccr.2009.05.016

[35]. Hanlon, L., Avila, J. L., Demarest, R. M., Troutman, S., Allen, M., Ratti, F., Rustgi, A. K., Stanger, B. Z., Radtke, F., Adsay, V., Long, F., Capobianco, A. J., & Kissil, J. L. Notch1 functions as a tumor suppressor in a model of K-ras-induced pancreatic ductal adenocarcinoma. *Cancer research.* **2010**, *70* (11), 4280–4286. https://doi.org/10.1158/0008-5472.CAN-09-4645

[36]. Luiken, S., Fraas, A., Bieg, M., Sugiyanto, R., Goeppert, B., Singer, S., Ploeger, C., Warsow, G., Marquardt, J. U., Sticht, C., De La Torre, C., Pusch, S., Mehrabi, A., Gretz, N., Schlesner, M., Eils, R., Schirmacher, P., Longerich, T., & Roessler, S. NOTCH target gene HES5 mediates oncogenic and tumor suppressive functions in hepatocarcinogenesis. *Oncogene*. **2020**, *39* (15), 3128–3144. https://doi.org/10.1038/s41388-020-1198-3

[37]. Yeh, CH., Bellon, M. & Nicot, C. FBXW7: a critical tumor suppressor of human cancers. *Molecular Cancer*. **2018**, *17*, 115. https://doi.org/10.1186/s12943-018-0857-2

[38]. Li, L., Zhang, J., Xiong, N., Li, S., Chen, Y., Yang, H., Wu, C., Zeng, H., & Liu, Y. Notch-1 signalling activates NF-κB in human breast carcinoma MDA-MB-231 cells via PP2A-dependent AKT pathway. *Medical oncology (Northwood, London, England).* **2016**, *33* (4), 33. https://doi.org/10.1007/s12032-016-0747-7

[39]. Caliceti, C., Nigro, P., Rizzo, P., and Ferrari, R. ROS, Notch, and Wnt Signalling Pathways: Crosstalk between Three Major Regulators of Cardiovascular Biology. *BioMed Research International*. **2014**, 318714, 8. https://doi.org/10.1155/2014/318714

[40]. Zeng, Q., Li, S., Chepeha, D. B., Giordano, T. J., Li, J., Zhang, H., Polverini, P. J., Nor, J., Kitajewski, J., & Wang, C. Y. Crosstalk between tumor and endothelial cells promotes tumor angiogenesis by MAPK activation of Notch signalling. *Cancer cell.* **2005,** *8*(1), 13–23. https://doi.org/10.1016/j.ccr.2005.06.004

[41]. Izrailit, J., Berman, H. K., Datti, A., Wrana, J. L., & Reedijk, M. High throughput kinase inhibitor screens reveal TRB3 and MAPK-ERK/TGFβ pathways as fundamental Notch regulators in breast cancer. *PNAS.* **2013**, *110* (5), 1714–1719. https://doi.org/10.1073/pnas.1214014110

[42]. Koveitypour, Z., Panahi, F., Vakilian, M., Peymani, M., Seyed Forootan, F., Nasr Esfahani, M. H., & Ghaedi, K. Signalling pathways involved in colorectal cancer progression. *Cell & bioscience.* **2019**, *9*, 97. https://doi.org/10.1186/s13578-019-0361-4

[43]. Zavadil, J., & Böttinger, E. P. TGF-beta and epithelial-to-mesenchymal transitions. *Oncogene.* **2005**, *24*(37), 5764–5774. https://doi.org/10.1038/sj.onc.1208927

[44]. Klüppel, M., & Wrana, J. L. Turning it up a Notch: cross-talk between TGF beta and Notch signalling. *BioEssays: news and reviews in molecular, cellular and developmental biology.* **2005**, *27*(2), 115–118. https://doi.org/10.1002/bies.20187

[45]. Nakano, T., Fukuda, D., Koga, J., & Aikawa, M. Delta-Like Ligand 4-Notch Signalling in Macrophage Activation. *Arteriosclerosis, thrombosis, and vascular biology*. **2016,** *36* (10), 2038–2047. https://doi.org/10.1161/ATVBAHA.116.306926

[46]. Tam, S. Y., Wu, V. W. C., & Law, H. K. W. Hypoxia-Induced Epithelial-Mesenchymal Transition in Cancers: HIF-1α and Beyond. *Frontiers in oncology*. **2020**, 10, 486. https://doi.org/10.3389/fonc.2020.00486

[47]. Hanahan D. Hallmarks of Cancer: New Dimensions. *Cancer discovery*. **2022**, *12*(1), 31–46. https://doi.org/10.1158/2159-8290.CD-21-1059

[48]. De Francesco, E. M., Maggiolini, M., & Musti, A. M. Crosstalk between Notch, HIF-1α and GPER in Breast Cancer EMT. *International journal of molecular sciences.* **2018,** *19* (7), 2011. https://doi.org/10.3390/ijms19072011

[49]. Min, C., Eddy, S. F., Sherr, D. H., & Sonenshein, G. E. NF-kappaB and epithelial to mesenchymal transition of cancer. *Journal of cellular biochemistry*. **2008**, *104*(3), 733–744. https://doi.org/10.1002/jcb.21695

[50]. Jiang, Y. G., Luo, Y., He, D., Li, X., Zhang, L., Peng, T., Li, M. C., and Lin, Y. H. Role of Wnt/β-catenin signalling pathway in epithelial-mesenchymal transition of human prostate cancer induced by hypoxia-inducible factor-1α. *International Journal of Urology*. **2007**, *14* (11) 1034–1039. https://doi.org/10.1111/j.1442-2042.2007.01866.x

[51]. Hao, Y., Baker, D., & Ten Dijke, P. TGF-β-Mediated Epithelial-Mesenchymal Transition and Cancer Metastasis. *International journal of molecular sciences*. **2019**, *20* (11), 2767. https://doi.org/10.3390/ijms20112767

[52]. Cao, Y. W., Wan, G. X., Sun, J. P., Cui, X. B., Hu, J. M., Hu, J. M., Liang, W. H., Zheng, Y. Q., and Li, F. Implications of the Notch1-Snail / Slug-epithelial to mesenchymal transition axis for lymph node metastasis in infiltrating ductal carcinoma. The *Kaohsiung Journal of Medical Sciences*. **2015**, *31* (2), 70–76. https://doi.org/10.1016/j.kjms.2014.11.008

[53]. Timmerman, L. A., Grego-Bessa, J., Raya, A., Bertrán, E., Pérez-Pomares, J. M., Díez, J., Aranda, S., Palomo, S., McCormick, F., Izpisúa-Belmonte, J. C., & de la Pompa, J. L. Notch promotes epithelial-mesenchymal transition during cardiac development and oncogenic transformation. *Genes & development*. **2004**, *18* (1), 99–115. https://doi.org/10.1101/gad.276304

[54]. Sahlgren, C., Gustafsson, M. V., Jin, S., Poellinger, L., & Lendahl, U. Notch signalling mediates hypoxia-induced tumor cell migration and invasion. *PNAS*. **2008**, *105* (17), 6392–6397. https://doi.org/10.1073/pnas.0802047105

[55]. Leong, K. G., Niessen, K., Kulic, I., Raouf, A., Eaves, C., Pollet, I., & Karsan, A. Jagged1-mediated Notch activation induces epithelial-to-mesenchymal transition through Slug-induced repression of E-cadherin. *The Journal of experimental medicine*. **2007**, *204*(12), 2935–2948. https://doi.org/10.1084/jem.20071082

[56]. Yuan, X., Wu, H., Han, N., Xu, H., Chu, Q., Yu, S., Chen, Y., & Wu, K. Notch signalling and EMT in non-small cell lung cancer: biological significance and therapeutic application. *Journal of hematology & oncology*. **2014**, *7*, 87. https://doi.org/10.1186/s13045-014-0087-z

[57]. Wang, J., Fu, L., Gu, F., & Ma, Y. Notch1 is involved in migration and invasion of human breast cancer cells. *Oncology reports.* **2011**, *26*(5), 1295–1303. https://doi.org/10.3892/or.2011.1399

[58]. Zhou, J., Jain, S., Azad, S., Azad, A. K., Xu, X., Yu, H. C., Xu, Z., Godbout, R., and Fu, Y. Notch and TGFβ form a positive regulatory loop and regulate EMT in epithelial ovarian cancer cells. *Cellular Signalling.* **2016**, *28* (8), 838–849. https://doi.org/10.1016/j.cellsig.2016.03.016

[59]. Kar, R., Jha, N. K., Jha, S. K., Sharma, A., Dholpuria, S., Asthana, N., Chaurasiya, K., Singh, V. K., Burgee, S., & Nand, P. A "NOTCH" Deeper into the Epithelial-To-Mesenchymal Transition (EMT) Program in Breast Cancer. *Genes.* **2019**, *10* (12), 961. https://doi.org/10.3390/genes10120961

[60]. Chen, J., Imanaka, N., Chen, J., & Griffin, J. D. Hypoxia potentiates Notch signalling in breast cancer leading to decreased E-cadherin expression and increased cell migration and invasion. *British journal of cancer.* **2010**, *102* (2), 351–360. https://doi.org/10.1038/sj.bjc.6605486

[61]. Rangarajan, A., Syal, R., Selvarajah, S., Chakrabarti, O., Sarin, A., & Krishna, S. Activated Notch1 signalling cooperates with papillomavirus oncogenes in transformation and generates resistance to apoptosis on matrix withdrawal through PKB/Akt. *Virology.* **2001**, *286* (1), 23–30. https://doi.org/10.1006/viro.2001.0867

[62]. Pastushenko, I., Brisebarre, A., Sifrim, A., Fioramonti, M., Revenco, T., Boumahdi, S., Van Keymeulen, A., Brown, D., Moers, V., Lemaire, S., De Clercq, S., Minguijón, E., Balsat, C., Sokolow, Y., Dubois, C., De Cock, F., Scozzaro, S., Sopena, F., Lanas, A., D'Haene, N., … Blanpain, C. Identification of the tumour transition states occurring during EMT. *Nature.* **2018**, *556*(7702), 463–468. https://doi.org/10.1038/s41586-018-0040-3

[63]. Bailey, P. C., & Martin, S. S. Insights on CTC Biology and Clinical Impact Emerging from Advances in Capture Technology. *Cells.* **2019**, *8*(6), 553. https://doi.org/10.3390/cells8060553

[64]. Boareto, M., Jolly, M. K., Goldman, A., Pietilä, M., Mani, S. A., Sengupta, S., Ben-Jacob, E., Levine, H., & Onuchic, J. N. Notch-Jagged signalling can give rise to clusters of cells exhibiting a hybrid epithelial/mesenchymal phenotype. *Journal of the Royal Society, Interface.* **2016**, *13*(118), 20151106. https://doi.org/10.1098/rsif.2015.1106

[65]. Ratajczak, M. Z., Bujko, K., Mack, A., Kucia, M., & Ratajczak, J. Cancer from the perspective of stem cells and misappropriated tissue regeneration mechanisms. *Leukemia.* **2018**, *32*(12), 2519–2526. https://doi.org/10.1038/s41375-018-0294-7

[66]. De Francesco, E. M., Sotgia, F., & Lisanti, M. P. Cancer stem cells (CSCs): metabolic strategies for their identification and eradication. *The Biochemical journal.* **2018**, *475*(9), 1611–1634. https://doi.org/10.1042/BCJ20170164

[67]. Agliano, A., Calvo, A., & Box, C. The challenge of targeting cancer stem cells to halt metastasis. *Seminars in cancer biology.* **2017**, *44*, 25–42. https://doi.org/10.1016/j.semcancer.2017.03.003

[68]. Shang, C., Lang, B., & Meng, L. R. Blocking NOTCH pathway can enhance the effect of EGFR inhibitor through targeting CD133+ endometrial cancer cells. *Cancer biology & therapy*. **2018**, *19* (2), 113–119. https://doi.org/10.1080/15384047.2016.1250985

[69]. Xiao, W., Gao, Z., Duan, Y., Yuan, W., & Ke, Y. Notch signalling plays a crucial role in cancer stem-like cells maintaining stemness and mediating chemotaxis in renal cell carcinoma. *Journal of experimental & clinical cancer research: CR*. **2017**, *36* (1), 41. https://doi.org/10.1186/s13046-017-0507-3

[70]. Chen, Y., Sun, W., He, R., Zhang, F., Wang, H., Li, P., Shao, R. G., & Xu, X. Lidamycin decreases CD133 expression in hepatocellular carcinoma via the Notch signalling pathway. *Oncology letters*. **2017**, *14*(6), 7889–7895. https://doi.org/10.3892/ol.2017.7248

[71]. Shaya, O., & Sprinzak, D. From Notch signalling to fine-grained patterning: Modeling meets experiments. *Current opinion in genetics & development*. **2011**, *21*(6), 732–739. https://doi.org/10.1016/j.gde.2011.07.007

[72]. Li, J. L., & Harris, A. L. Notch signalling from tumor cells: a new mechanism of angiogenesis. *Cancer cell*. **2005**, *8* (1), 1–3. https://doi.org/10.1016/j.ccr.2005.06.013

[73]. Mungamuri, S. K., Yang, X., Thor, A. D., & Somasundaram, K. Survival signalling by Notch1: mammalian target of rapamycin (mTOR)-dependent inhibition of p53. *Cancer research*. **2006**, *66* (9), 4715–4724. https://doi.org/10.1158/0008-5472.CAN-05-3830

[74]. Cho, S., Lu, M., He, X., Ee, P. L., Bhat, U., Schneider, E., Miele, L., & Beck, W. T. Notch1 regulates the expression of the multidrug resistance gene ABCC1/MRP1 in cultured cancer cells. *PNAS*. **2011**, *108* (51), 20778–20783. https://doi.org/10.1073/pnas.1019452108

[75]. Choi, Y. I., Jeon, S. H., Jang, J., Han, S., Kim, J. K., Chung, H., Lee, H. W., Chung, H. Y., Park, S. D., & Seong, R. H. Notch1 confers a resistance to glucocorticoid-induced apoptosis on developing thymocytes by down-regulating SRG3 expression. *PNAS*. **2001**, *98* (18), 10267–10272. https://doi.org/10.1073/pnas.181076198

[76]. Farah, E., Li, C., Cheng, L., Kong, Y., Lanman, N. A., Pascuzzi, P., Lorenz, G. R., Zhang, Y., Ahmad, N., Li, L., Ratliff, T., & Liu, X. NOTCH signalling is activated in and contributes to resistance in enzalutamide-resistant prostate cancer cells. *The Journal of biological chemistry*. **2019**, *294* (21), 8543–8554. https://doi.org/10.1074/jbc.RA118.006983

[77]. Rizzo, P., Osipo, C., Foreman, K., Golde, T., Osborne, B., & Miele, L. Rational targeting of Notch signalling in cancer. *Oncogene*. **2008**, *27* (38), 5124–5131. https://doi.org/10.1038/onc.2008.226

[78]. Sen, P., and Ghosh, S. S. The Intricate Notch Signalling Dynamics in Therapeutic Realms of Cancer. *ACS Pharmacology and Translational Science*. **2023**, *6* (5), 651–670. https://doi.org/10.1021/acsptsci.2c00239

[79]. Franceschini, A., Szklarczyk, D., Frankild, S., Kuhn, M., Simonovic, M., Roth, A., Lin, J., Minguez, P., Bork, P., von Mering, C., & Jensen, L. J. STRING v9.1: protein-protein interaction networks,

with increased coverage and integration. *Nucleic acids research.* **2013**, *41*(Database issue), D808–D815. https://doi.org/10.1093/nar/gks1094

[80]. Morris, G. M., Huey, R., Lindstrom, W., Sanner, M. F., Belew, R. K., Goodsell, D. S., & Olson, A. J. Software news and updates AutoDock4 and AutoDockTools4: Automated docking with selective receptor flexibility. *Journal of Computational Chemistry.* **2009**, *30*(16), 2785–2791. https://doi.org/10.1002/jcc.21256

[81]. Abraham, M. J., Murtola, T., Schulz, R., Páll, S., Smith, J. C., Hess, B., & Lindahl, E. Gromacs: High performance molecular simulations through multi-level parallelism from laptops to supercomputers. *SoftwareX*. **2015**, 1–2, 19–25. https://doi.org/10.1016/j.softx.2015.06.001

[82]. Lemkul, J. From proteins to perturbed hamiltonians: A suite of tutorials for the GROMACS-2018 molecular simulation package. *Living Journal of Computational Molecular Science*. **2019**, 1(1), 1–53. https://doi.org/10.33011/livecoms.1.1.5068

[83]. Kumari, R., Kumar, R., & Lynn, A. g_mmpbsa-a GROMACS tool for high-throughput MM-PBSA calculations. *Journal of Chemical Information and Modeling*. **2014**, *54* (7), 1951–1962. https://doi.org/10.1021/ci500020m

[84]. Kollman, P. A., Massova, I., Reyes, C., Kuhn, B., Huo, S., Chong, L., Lee, M., Lee, T., Duan, Y., Wang, W., Donini, O., Cieplak, P., Srinivasan, J., Case, D. A., and Cheatham, T. E. Calculating structures and free energies of complex molecules: combining molecular mechanics and continuum models. *Accounts of Chemical Research*. **2000**, *33* (12), 889–897, https://doi.org/10.1021/ar000033j

[85]. Riccardi, C., and Nicoletti, I. Analysis of apoptosis by propidium iodide staining and flow cytometry. *Nature Protocol.* **2006**, *1* (3), 1458–1461. https://doi.org/10.1038/nprot.2006.238

[86]. Sivandzade, F., Bhalerao, A., and Cucullo, L. Analysis of the Mitochondrial Membrane Potential Using the Cationic JC-1 Dye as a Sensitive Fluorescent Probe. *Bio-Protocol.* **2019**, *9* (1), 1–13. https://doi.org/10.21769/bioprotoc.3128

[87]. Livak, K. J., & Schmittgen, T. D. Analysis of relative gene expression data using real-time quantitative PCR and the 2(-Delta Delta C(T)) Method. *Methods (San Diego, Calif.)*. **2001**, *25* (4), 402–408. https://doi.org/10.1006/meth.2001.1262

[88]. Wu, H., Wang, S., Weng, D., Xing, H., Song, X., Zhu, T., Xia, X., Weng, Y., Xu, G., Meng, L., Zhou, J., & Ma, D. Reversal of the malignant phenotype of ovarian cancer A2780 cells through transfection with wild-type PTEN gene. *Cancer letters.* **2008**, *271* (2), 205–214. https://doi.org/10.1016/j.canlet.2008.06.018

[89]. Chen, W. L., Kuo, K. T., Chou, T. Y., Chen, C. L., Wang, C. H., Wei, Y. H., & Wang, L. S. The role of cytochrome c oxidase subunit Va in non-small cell lung carcinoma cells: association with migration, invasion and prediction of distant metastasis. *BMC cancer.* **2012**, *12*, 273. https://doi.org/10.1186/1471-2407-12-273

[90]. Crowley, L. C., Christensen, M. E., and Waterhouse, N. J. Measuring survival of adherent cells with the Colony-forming assay. *Cold Spring Harbour Protocol.* **2016**, 8, 721–724, https://doi.org/10.1101/pdb.prot087171

[91]. Mullooly, M., McGowan, P. M., Kennedy, S. A., Madden, S. F., Crown, J., O' Donovan, N., & Duffy, M. J. ADAM10: a new player in breast cancer progression? *British journal of cancer*. **2015**, *113* (6), 945–951. https://doi.org/10.1038/bjc.2015.288

[92]. Mittal, S., Sharma, A., Balaji, S. A., Gowda, M. C., Dighe, R. R., Kumar, R. V., & Rangarajan, A. Coordinate hyperactivation of Notch1 and Ras/MAPK pathways correlates with poor patient survival: Novel therapeutic strategy for aggressive breast cancers. *Molecular Cancer Therapeutics*. **2014**, *13*(12), 3198–3209. https://doi.org/10.1158/1535-7163.MCT-14-0280

[93]. Voudouri, K., Berdiaki, A., Tzardi, M., Tzanakakis, G. N., & Nikitovic, D. Insulin-like growth factor and epidermal growth factor signalling in breast cancer cell growth: Focus on endocrine resistant disease. *Analytical Cellular Pathology*. **2015**, 975495. https://doi.org/10.1155/2015/975495

[94]. Heath, E. I., Burtness, B. A., Kleinberg, L., Salem, R. R., Yang, S. C., Heitmiller, R. F., Canto, M. I., Knisely, J. P. S., Topazian, M., Montgomery, E., Tsottles, N., Pithavala, Y., Rohmiller, B., Collier, M., and Forastiere, A. A. Phase II, parallel-design study of preoperative combined modality therapy and the matrix metalloprotease (Mmp) inhibitor prinomastat in patients with esophageal adenocarcinoma. *Investigational New Drugs*. **2006**, *24* (2), 135–140. https://doi.org/10.1007/s10637-006-5934-5

[95]. Witters, L., Scherle, P., Friedman, S., Fridman, J., Caulder, E., Newton, R., and Lipton, A. Synergistic inhibition with a dual epidermal growth factor receptor/HER-2/Neu tyrosine kinase inhibitor and a disintegrin and metalloprotease inhibitor. *Cancer Research*. **2008**, *68* (17), 7083–7089. https://doi.org/10.1158/0008-5472.CAN-08-0739

[96]. Xue, C. B., He, X., Corbett, R. L., Roderick, J., Wasserman, Z. R., Liu, R. Q., Jaffee, B. D., Covington, M. B., Qian, M., Trzaskos, J. M., Newton, R. C., Magolda, R. L., Wexler, R. R., & Decicco, C. P. Discovery of macrocyclic hydroxamic acids containing biphenylmethyl derivatives at P1', a series of selective TNF-alpha converting enzyme inhibitors with potent cellular activity in the inhibition of TNF-alpha release. *Journal of Medicinal Chemistry*. **2001**, *44* (21), 3351–3354. https://doi.org/10.1021/jm0155502

[97].Levin, J.I., Chen, J.M., Laakso, L.M., Du, M., Schmid, J., Xu, W., Cummons, T., Xu, J., Jin, G., Bar one, D., & Skotnicki, J. S. Acetylenic TACE inhibitors. Part 3: Thiomorpholine sulfonamide hydroxamates. *Bioorganic & Medicinal Chemistry Letters*. **2006**, *16* (6), 1605–1609. https://doi.org/10.1016/j.bmcl.2005.12.020

[98]. Niu, X., Umland, S., Ingram, R., Beyer, B. M., Liu, Y.-H., Sun, J., Lundell, D., & Orth, P. IK682, a tight binding inhibitor of TACE. *Archives of Biochemistry and Biophysics*. **2006**, *451*(1), 43–50. https://doi.org/10.1016/j.abb.2006.03.034

[99]. Lu, H. Y., Zu, Y. X., Jiang, X. W., Sun, X. T., Liu, T. Y., Li, R. L., Wu, Q., Zhang, Y.S., and Zhao, Q. C. Novel ADAM-17 inhibitor ZLDI-8 inhibits the proliferation and metastasis of chemo-resistant non-small-cell lung cancer by reversing notch and epithelial mesenchymal transition in vitro and in vivo. *Pharmacological Research.* **2019**, *148*, 104406. https://doi.org/10.1016/j.phrs.2019.104406

[100]. Zhang, Y., Li, D., Jiang, Q., Cao, S., Sun, H., Chai, Y., Li, X., Ren, T., Yang, R., Feng, F., Li, B.-A., & Zhao, Q. Novel ADAM-17 inhibitor ZLDI-8 enhances the in vitro and in vivo chemotherapeutic effects of sorafenib on hepatocellular carcinoma cells. *Cell Death & Disease*. **2018**, *9* (7), 743. https://doi.org/10.1038/s41419-018-0804-6

[101]. Elad, N., De Strooper, B., Lismont, S., Hagen, W., Veugelen, S., Arimon, M., Horré, K., Berezovska, O., Sachse, C., & Chávez-Gutiérrez, L. The dynamic conformational landscape of gamma-secretase. *Journal of cell science.* **2019**, *128* (3), 589–598. https://doi.org/10.1242/jcs.164384

[102]. Carroll, C. M., & Li, Y. M. Physiological and pathological roles of the γ-secretase complex. *Brain research bulletin.* **2016**, *126* (Pt 2), 199–206. https://doi.org/10.1016/j.brainresbull.2016.04.019

[103]. Selkoe, D., & Kopan, R. Notch and Presenilin: regulated intramembrane proteolysis links development and degeneration. *Annual review of neuroscience*. **2003**, *26*, 565–597. https://doi.org/10.1146/annurev.neuro.26.041002.131334

[104]. Golde, T. E., Koo, E. H., Felsenstein, K. M., Osborne, B. A., & Miele, L. γ-Secretase inhibitors and modulators. *BBA: Biomembranes.* **2013**, *1828* (12), 2898–2907. https://doi.org/10.1016/j.bbamem.2013.06.005

[105]. Saad, M. I., Rose-John, S., & Jenkins, B. J. ADAM17: An Emerging Therapeutic Target for Lung Cancer. *Cancers.* **2019**, *11* (9), 1218. https://doi.org/10.3390/cancers11091218

[106]. Sen, P., Kandasamy, T., & Ghosh, S. S. *In-silico* evidence of ADAM metalloproteinase pathology in cancer signalling networks. *Journal of biomolecular structure & dynamics*. **2022**, *40* (22), 11771–11786. https://doi.org/10.1080/07391102.2021.1964602

[107]. Curry, C. L., Reed, L. L., Golde, T. E., Miele, L., Nickoloff, B. J., & Foreman, K. E. Gamma secretase inhibitor blocks Notch activation and induces apoptosis in Kaposi's sarcoma tumor cells. *Oncogene.* **2005**, *24* (42), 6333–6344. https://doi.org/10.1038/sj.onc.1208783

[108]. Levin, J. I., Chen, J. M., Laakso, L. M., Du, M., Schmid, J., Xu, W., Cummons, T., Xu, J., Jin, G., Barone, D., & Skotnicki, J. S. Acetylenic TACE inhibitors. Part 3: Thiomorpholine sulfonamide hydroxamates. *Bioorganic & medicinal chemistry letters*. **2006**, *16* (6), 1605–1609. https://doi.org/10.1016/j.bmcl.2005.12.020

[109]. C.T. Walsh, R.D. Schwartz-bloom, Levine's Pharmacology, **2004**.

[110]. Goulooze, S.C., Cohen, A. F., and Rissmann, R. Lomitapide. *British Journal of Clinical Pharmacolology*. **2015**, *80* (2), 179–181. https://doi.org/10.1111/bcp.12612

[111]. Xie, Y., Newberry, E. P., Young, S. G., Robine, S., Hamilton, R. L., Wong, J. S., Luo, J., Kennedy, S., & Davidson, N. O. Compensatory increase in hepatic lipogenesis in mice with conditional

intestine-specific Mttp deficiency. *The Journal of biological chemistry*. **2006**, *281* (7), 4075–4086. https://doi.org/10.1074/jbc.M510622200

[112]. Listenberger, L. L., & Brown, D. A. Fluorescent detection of lipid droplets and associated proteins. *Current protocols in cell biology*. **2007**,*24*. https://doi.org/10.1002/0471143030.cb2402s35

[113]. Niklaus, N. J., Tokarchuk, I., Zbinden, M., Schläfli, A. M., Maycotte, P., & Tschan, M. P. The Multifaceted Functions of Autophagy in Breast Cancer Development and Treatment. *Cells*. **2021**, *10*(6), 1447. https://doi.org/10.3390/cells10061447

[114]. Xie, Y., Li, J., Kang, R., & Tang, D. Interplay Between Lipid Metabolism and Autophagy. *Frontiers in cell and developmental biology*. **2020**, *8*, 431. https://doi.org/10.3389/fcell.2020.00431

[115]. Zuo, Q., Liao, L., Yao, Z. T., Liu, Y. P., Wang, D. K., Li, S. J., Yin, X. F., He, Q. Y., & Xu, W. W. Targeting PP2A with lomitapide suppresses colorectal tumorigenesis through the activation of AMPK/Beclin1-mediated autophagy. *Cancer letters.* **2021**, *521*, 281–293. Advance online publication. https://doi.org/10.1016/j.canlet.2021.09.010

[116]. Babaei, G., Aziz, S. G., & Jaghi, N. Z. Z. EMT, cancer stem cells and autophagy; The three main axes of metastasis. *Biomedicine & pharmacotherapy*. **2021**, *133*, 110909. https://doi.org/10.1016/j.biopha.2020.110909

[117]. Sun, P. C., Tzao, C., Chen, B. H., Liu, C. W., Yu, C. P., & Jin, J. S. Suberoylanilide hydroxamic acid induces apoptosis and sub-G1 arrest of 320 HSR colon cancer cells. *Journal of biomedical science*. **2010**, *17*(1), 76. https://doi.org/10.1186/1423-0127-17-76

[118]. Wawruszak, A., Borkiewicz, L., Okon, E., Kukula-Koch, W., Afshan, S., & Halasa, M. Vorinostat (SAHA) and Breast Cancer: An Overview. *Cancers.* **2021**, *13*(18), 4700. https://doi.org/10.3390/cancers13184700

[119]. Xiu, M. X., Liu, Y. M., & Kuang, B. H. The oncogenic role of Jagged1/Notch signalling in cancer. *Biomedicine & pharmacotherapy*, **2020,** *129*, 110416. https://doi.org/10.1016/j.biopha.2020.110416

[120]. Li, C. Y., Miao, K. L., Chen, Y., Liu, L. Y., Zhao, G. B., Lin, M. H., & Jiang, C. Jagged2 promotes cancer stem cell properties of triple negative breast cancer cells and paclitaxel resistance via regulating microRNA-200. *European review for medical and pharmacological sciences*. **2018**, *22* (18), 6008–6014. https://doi.org/10.26355/eurrev_201809_15936

[121]. Wu, S., Luo, Z., Yu, P. J., Xie, H., & He, Y. W. Suberoylanilide hydroxamic acid (SAHA) promotes the epithelial mesenchymal transition of triple negative breast cancer cells via HDAC8/FOXA1 signals. *Biological chemistry*. **2016**, *397*(1), 75–83. https://doi.org/10.1515/hsz-2015-0215

[122]. Ansieau, S., Collin, G., & Hill, L. EMT or EMT-Promoting Transcription Factors, Where to Focus the Light? *Frontiers in oncology*. **2014**, *4*, 353. https://doi.org/10.3389/fonc.2014.00353

[123]. Rädler, P. D., Wehde, B. L., Triplett, A. A., Shrestha, H., Shepherd, J. H., Pfefferle, A. D., Rui, H., Cardiff, R. D., Perou, C. M., & Wagner, K. U. Highly metastatic claudin-low mammary cancers can

originate from luminal epithelial cells. *Nature communications.* **2021**, *12* (1), 3742. https://doi.org/10.1038/s41467-021-23957-5

[124]. Ghuwalewala, S., Ghatak, D., Das, P., Dey, S., Sarkar, S., Alam, N., Panda, C. K., & Roychoudhury, S. CD44(high)CD24(low) molecular signature determines the Cancer Stem Cell and EMT phenotype in Oral Squamous Cell Carcinoma. *Stem cell research.* **2016**, *16* (2), 405–417. https://doi.org/10.1016/j.scr.2016.02.028

[125]. Sheridan, C., Kishimoto, H., Fuchs, R. K., Mehrotra, S., Bhat-Nakshatri, P., Turner, C. H., Goulet, R., Jr, Badve, S., & Nakshatri, H. CD44+/CD24- breast cancer cells exhibit enhanced invasive properties: an early step necessary for metastasis. *Breast cancer research.* **2006,** *8* (5), R59. https://doi.org/10.1186/bcr1610

[126]. Imrich, S., Hachmeister, M., & Gires, O. EpCAM and its potential role in tumor-initiating cells. *Cell adhesion & migration.* **2012**, *6*(1), 30–38. https://doi.org/10.4161/cam.18953

[127]. Chen, W., Bai, Y., Patel, C., & Geng, F. Autophagy promotes triple negative breast cancer metastasis via YAP nuclear localization. *Biochemical and biophysical research communications*. **2019**, *520* (2), 263–268. https://doi.org/10.1016/j.bbrc.2019.09.133

[128]. Fröhlich, L. F., Mrakovcic, M., Smole, C., & Zatloukal, K. Molecular mechanism leading to SAHA-induced autophagy in tumor cells: evidence for a p53-dependent pathway. *Cancer cell international.* **2016**, *16* (1), 68. https://doi.org/10.1186/s12935-016-0343-0

[129]. Soliman, H., Khalil, F., & Antonia, S. PD-L1 expression is increased in a subset of basal type breast cancer cells. *PloS one.* **2014**, *9* (2), e88557. https://doi.org/10.1371/journal.pone.0088557

[130]. Hegedűs, L., Rittler, D., Garay, T., Stockhammer, P., Kovács, I., Döme, B., Theurer, S., Hager, T., Herold, T., Kalbourtzis, S., Bankfalvi, A., Schmid, K. W., Führer, D., Aigner, C., & Hegedűs, B. HDAC Inhibition Induces PD-L1 Expression in a Novel Anaplastic Thyroid Cancer Cell Line. *Pathology oncology research: POR.* **2020**, *26* (4), 2523–2535. https://doi.org/10.1007/s12253-020-00834-y

[131]. Mansour, F. A., Al-Mazrou, A., Al-Mohanna, F., Al-Alwan, M., & Ghebeh, H. PD-L1 is overexpressed on breast cancer stem cells through notch3/mTOR axis. *Oncoimmunology*. **2020**, *9* (1), 1729299. https://doi.org/10.1080/2162402X.2020.1729299

[132]. Armenta-Castro, E., Reyes-Vallejo, T., Máximo-Sánchez, D., Herrera-Camacho, I., López-López, G., Reyes-Carmona, S., Conde-Rodríguez, I., Ramírez-Díaz, I., Aguilar-Lemarroy, A., Jave-Suárez, L. F., Milflores-Flores, L., Santos-Lopez, G., Reyes-Leyva, J., & Vallejo-Ruiz, V. Histone H3K9 and H3K14 acetylation at the promoter of the LGALS9 gene is associated with mRNA levels in cervical cancer cells. *FEBS open bio.* **2020**, *10*(11), 2305–2315. https://doi.org/10.1002/2211-5463.12973

[133]. Wada, T. T., Araki, Y., Sato, K., Aizaki, Y., Yokota, K., Kim, Y. T., Oda, H., Kurokawa, R., & Mimura, T. Aberrant histone acetylation contributes to elevated interleukin-6 production in

rheumatoid arthritis synovial fibroblasts. *Biochemical and biophysical research communications.* **2014**, *444* (4), 682–686. https://doi.org/10.1016/j.bbrc.2014.01.195

[134]. Al-Roub, A., Al Madhoun, A., Akhter, N., Thomas, R., Miranda, L., Jacob, T., Al-Ozairi, E., Al-Mulla, F., Sindhu, S., & Ahmad, R. IL-1β and TNFα Cooperativity in Regulating IL-6 Expression in Adipocytes Depends on CREB Binding and H3K14 Acetylation. *Cells.* **2021**, *10* (11), 3228. https://doi.org/10.3390/cells10113228

[135]. Jiang, G. M., Wang, H. S., Zhang, F., Zhang, K. S., Liu, Z. C., Fang, R., Wang, H., Cai, S. H., & Du, J. Histone deacetylase inhibitor induction of epithelial-mesenchymal transitions via up-regulation of Snail facilitates cancer progression. *BBA: Molecular Cell Research.* **2013**, *1833* (3), 663–671. https://doi.org/10.1016/j.bbamcr.2012.12.002

[136]. Liu, Z. J., Shirakawa, T., Li, Y., Soma, A., Oka, M., Dotto, G. P., Fairman, R. M., Velazquez, O. C., & Herlyn, M. Regulation of Notch1 and DLL4 by vascular endothelial growth factor in arterial endothelial cells: implications for modulating arteriogenesis and angiogenesis. *Molecular and cellular biology*. **2003**, *23*(1), 14–25. https://doi.org/10.1128/MCB.23.1.14-25.2003

[137]. Hellström, M., Phng, L. K., & Gerhardt, H. VEGF and Notch signalling: the yin and yang of angiogenic sprouting. *Cell adhesion & migration.* **2007**, *1* (3), 133–136. https://doi.org/10.4161/cam.1.3.4978

[138]. Holderfield, M. T., & Hughes, C. C. Crosstalk between vascular endothelial growth factor, notch, and transforming growth factor-beta in vascular morphogenesis. *Circulation research.* **2008**, *102*(6), 637–652. https://doi.org/10.1161/CIRCRESAHA.107.167171

[139]. Stehle, F., Schulz, K., Fahldieck, C., Kalich, J., Lichtenfels, R., Riemann, D., & Seliger, B. Reduced immunosuppressive properties of axitinib in comparison with other tyrosine kinase inhibitors. *The Journal of biological chemistry*. **2013**, *288* (23), 16334–16347. https://doi.org/10.1074/jbc.M112.437962

[140]. Lin, C. W., Liao, M. Y., Lin, W. W., Wang, Y. P., Lu, T. Y., & Wu, H. C. Epithelial cell adhesion molecule regulates tumor initiation and tumorigenesis via activating reprogramming factors and epithelial-mesenchymal transition gene expression in colon cancer. *The Journal of biological chemistry*. **2012**, *287*(47), 39449–39459. https://doi.org/10.1074/jbc.M112.386235

[141]. Sen, P., Kandasamy, T., & Ghosh, S. S. Multi-targeting TACE/ADAM17 and gamma-secretase of notch signalling pathway in TNBC via drug repurposing approach using Lomitapide. *Cellular signalling*. **2023**, *102*, 110529. https://doi.org/10.1016/j.cellsig.2022.110529

[142]. Murayama, Y., Oritani, K., & Tsutsui, S. Novel CD9-targeted therapies in gastric cancer. *World journal of gastroenterology*. **2015**, *21*(11), 3206–3213. https://doi.org/10.3748/wjg.v21.i11.3206

[143]. Rappa, G., Green, T. M., Karbanová, J., Corbeil, D., & Lorico, A. Tetraspanin CD9 determines invasiveness and tumorigenicity of human breast cancer cells. *Oncotarget.* **2015**, *6*(10), 7970–7991. https://doi.org/10.18632/oncotarget.3419

[144]. Thomas, J. L., Baker, K., Han, J., Calvo, C., Nurmi, H., Eichmann, A. C., & Alitalo, K. Interactions between VEGFR and Notch signalling pathways in endothelial and neural cells. *Cellular and molecular life sciences: CMLS*. **2013**, *70* (10), 1779–1792. https://doi.org/10.1007/s00018-013-1312-6

[145]. Ribeiro, A. L., & Okamoto, O. K. Combined effects of pericytes in the tumor microenvironment. *Stem cells international*. **2015**, 868475. https://doi.org/10.1155/2015/868475

[146]. Nicolosi, P. A., Dallatomasina, A., & Perris, R. Theranostic impact of NG2/CSPG4 proteoglycan in cancer. *Theranostics*. **2015**, *5* (5), 530–544. https://doi.org/10.7150/thno.10824

[147]. Kofler, N. M., Shawber, C. J., Kangsamaksin, T., Reed, H. O., Galatioto, J., & Kitajewski, J. Notch signalling in developmental and tumor angiogenesis. *Genes & cancer*. **2011**, *2* (12), 1106–1116. https://doi.org/10.1177/1947601911423030

भारतीय प्रौद्योगिकी संस्थान गुवाहाटी
Indian Institute of Technology Guwahati

Publications and Patents

Publications from thesis work:

1. **Plaboni Sen,** Thirukumaran Kandasamy, Siddhartha Sankar Ghosh (2021). *In-silico* evidence of ADAM metalloproteinase pathology in cancer signalling networks. ***Journal of Biomolecular Structure and Dynamics,*** 2021, 1-16. DOI: 10.1080/07391102.2021.1964602 **[Taylor & Francis publishing group, IF-5.235].**
2. **Plaboni Sen**, Thirukumaran Kandasamy, Siddhartha Sankar Ghosh (2023). Multi-targeting TACE/ADAM17 and gamma-secretase of notch signalling pathway in TNBC via drug repurposing approach using Lomitapide. ***Cellular Signalling***, 2023, DOI: 10.1016/j.cellsig.2022.110529 **[Elsevier, IF-4.85].**
3. **Plaboni Sen**, Siddhartha Sankar Ghosh (2023). The Intricate Notch Signalling Dynamics in Therapeutic Realms of Cancer. ***ACS Pharmacology and Translational Science***, 2023. 6, 5, 651−670. DOI: 10.1021/acsptsci.2c00239 **[ACS Publication, IF-6.0]**.
4. **Plaboni Sen**, Siddhartha Sankar Ghosh (2023). The γ-secretase inhibitor, LY411575 potentiates the activity of Suberoylanilide hydroxamic acid (SAHA) by inhibiting its ability to induce EMT via the activation of the Notch signalling pathway in TNBC cells. ***ACS Pharmacology and Translational Science***, 2023. **[ACS Publication, IF-6.0]**.
5. **Plaboni Sen**, Siddhartha Sankar Ghosh (2023). Targeting Cross-talks of Notch and VEGF in the Realm of EMT and EPT Dynamics in Triple Negative Breast Cancer Cells. *(Manuscript communicated)*

Other Publications:

6. **Plaboni Sen**, Muktashree Saha, Siddhartha Sankar Ghosh (2020). Nanoparticle mediated alteration of EMT dynamics: an approach to modulate cancer therapeutics. ***Materials Advances***, 2020,1, 2614-2630. DOI: 10.1039/D0MA00455C **[RSC publishing group, IF-5.0].**
7. **Plaboni Sen,** Suchandra Roy Acharyya, Arisha Arora, Siddhartha Sankar Ghosh (2023). An *in-silico* approach to understand the potential role of Wnt Inhibitory Factor-1 (WIF-1) in the inhibition of the Wnt signalling pathway. ***Journal of Biomolecular Structure and Dynamics,*** 2023, **[Taylor & Francis publishing group, IF-5.235].**

Publications from collaborative work:

8. Thirukumaran Kandasamy, **Plaboni Sen**, and Siddhartha Sankar Ghosh (2021). Multi-targeted Drug Repurposing Approach for Breast Cancer via Integrated Functional Network Analysis. ***Molecular Informatics***. DOI: 10.1002/minf.202100300. **[Wiley, IF-4.03]**
9. Suchandra Roy Acharyya, **Plaboni Sen**, Thirukumaran Kandasamy, Siddhartha Sankar Ghosh (2022). Dual therapeutic approach to modulate Glycogen Synthase kinase-3 beta (GSK-3B) and inhibitor of nuclear factor kappa kinase-beta (IKK-β) receptors by in silico designing of inhibitors. ***Journal of Molecular Graphics and Modelling,*** 115 (2022) 108225, DOI: 10.1016/j.jmgm.2022.108225 **[Elsevier, IF-2.94]**
10. Suchandra Roy Acharyya, **Plaboni Sen**, Thirukumaran Kandasamy, Siddhartha Sankar Ghosh (2022). Designing of disruptor molecules to restrain the protein–protein interaction network of VANG1/SCRIB/NOS1AP using fragment-based drug discovery techniques. ***Molecular Diversity,*** DOI: 10.1007/s11030-022-10462-0 **[Springer, IF-3.364].**
11. Rajib Shome, **Plaboni Sen**, Siddhartha Sankar Ghosh (2022). Regulating SQSTM1/P62 and Wnt/β-catenin signalling of EMT to constrain TNBC invasiveness. DOI: 10.21203/rs.3.rs-1630401/v1
12. Subhasis Dey, **Plaboni Sen**, Anjali Patel, Biswa Mohan Prusty, Siddhartha Sankar Ghosh and Debasis Manna (2022). A photo-responsive fluorescent amphiphile for target-specific and image-guided drug delivery applications. ***Organic & Biomolecular Chemistry***. 20, 7803, DOI: 10.1039/d2ob01332k **[Royal Society of Chemistry, IF-3.876].**

13. Gloria Narayan, Akriti Agrawal, **Plaboni Sen,** Shirisha Nagotu, and Rajkumar P Thummer (2023). Production of bioactive recombinant human PAX4 protein from *E. coli*. ***The Protein Journal.*** DOI: 10.1007/s10930-023-10143-3 **[Springer Publications, IF-3.0].**
14. Gloria Narayan, **Plaboni Sen**, Ronima KR, Shirisha Nagotu, and Rajkumar P Thummer (2023). Biological activity of recombinant human PDX1 protein produced from *Escherichia coli. (Manuscript Communicated)*
15. Niraj k prasad, **Plaboni Sen**, Rajib Shome, Siddhartha Sankar Ghosh and Amaresh Dalal (2023). Understanding the migration tendency of cancer cell membrane derived nanovesicles through network of micron sized channels. *(Manuscript Communicated)*
16. Parijat Dutta, Thirukumaran Kandasamy, **Plaboni Sen**, and Siddhartha Sankar Ghosh (2023). Targeting AR-positive Breast Cancer Cells via drug repurposing approach. *(Manuscript Communicated)*

National Patent:

1. Monica Naorem, Plaboni Sen, Rajan Singh, Roy P. Paily, Siddhartha S. Ghosh, Lactate dehydrogenase (LDH) sensing device comprising SiO2 trench embedded sensor-based sensing device incorporating GO/Ag NPs, Application No: **202231008246**, Date: February 16,2022.

Conferences

1. **Participated** in Translational research and biomarker discovery, September 4th, 2018; organised by the Department of Bioscience and Bioengineering, IIT Guwahati
2. **Participated** as a member of the organizing committee in the DBT Program Support Sponsored Workshop on Therapeutic Materials: Techniques and Applications by Department of Biosciences and Bioengineering, IIT Guwahati, 19th-20th January, 2019.
3. **Poster presentation** in Research conclave, 14th-17th March 2019, organised by IIT Guwahati
4. **Participated** as a volunteer in ICANN 2019, organized by Centre for Nanotechnology, IIT Guwahati, 18th-21st December 2019.
5. **Speaker** during the one-day offline workshop titled "*Real-Time Based Molecular Disease Diagnostic*" conducted by BioNEST IIT Guwahati, 14th July, 2022.
6. **Virtual (Oral) presentation** on "*Polypharmacological approach to target the oncogenic proteins to tweak the developmental pathways for inhibiting TNBC progression and dissemination*" at **7th World Congress on "Breast Cancer, Cancer Research & Therapy"** held during October 20 - 22, 2022 at Las Vegas, NV, USA
7. **Oral presentation** on *"multi-Targeted therapeutic approach to tweak the Notch Signalling Pathway in EMT induced TNBC"* in **7th World Cancer Congress (Bangalore Healthcare summit)** held on 19 - 20 November, 2022, Yelahanka, Bangalore. [**Asima Chatterjee Memorial Award for *Best Researcher*]**.
8. **Resource person** in the one-day offline workshop on "Hands-on workshop on basic flow cytometry" conducted by BioNEST IIT Guwahati Technological Innovation and Development Foundation on January 18th,2023.
9. **Participated** in 3-minute Thesis presentation on "*Targeting Notch Signalling in EMT Dynamics of Triple-negative Breast cancer cells*" in **Research and Industrial Conclave 2023**, organised by IIT Guwahati (14th to 16th May, 2023).
10. **Participated** in Poster presentation on *"Polypharmacology approach to tweak the Notch Signalling Pathway in metastatic TNBC cells"* in **Research and Industrial Conclave 2023**, organised by IIT Guwahati (14th to 16th May, 2023).

Appendix

Buffers and Their Compositio

4 X protein loading dye (10 ml)	2 ml 1M Tris-HCl (pH 6.8), 0.8 g SDS, 4.0 ml 100 % glycerol, 0.4 ml 14.7 M β- mercaptoethanol, 8 mg bromophenol blue in water
30% Acrylamide solution	29.2 % (w/w) Acrylamide, 0.8 % (w/w) N, N' -methylenebisacrylamide
Blocking buffer for Western blot	4 % (w/v) BSA in PBST/ TBST
Gel running buffer (10x)	250 mM Tris base, 1.92 M glycine, and 1 % SDS
Phosphate buffer saline	137 mM NaCl, 2.68 mM KCl, 7.98 mM Na2HPO4, 1.4 mM KH2PO4, pH 7.4
Tris buffered saline	Tris-HCl (50Mm), NaCl (150 mM), pH 7.5
Tris buffered saline Tween - 20 (TBST)	Tris-HCl (50Mm), NaCl (150 mM), Tween 20 (0.1% v/v) pH 7.5
Tris acetate EDTA (TAE) 50X (100 ml)	24.2 g Tris base, 5.71 ml of glacial acetic acid, 10 ml of 0.5 EDTA (pH 8)
Towbin Buffer (5X)	25 mM Tris base, 192 mM glycine, and 20 % methanol